University of Sheffield

Department of Mechanical Engineering

Simulation of Transition and Roughness Effects
on Micro Air Vehicle Aerodynamics

by

Sheng Liu

Supervised by Prof Ning Qin

A thesis submitted to the University of Sheffield in partial fulfilment of the
requirements for the degree of Doctor of Philosophy

October 2014

To my parents

Abstract

Accurate simulations on smooth and rough surfaces are of practical importance for micro air vehicle (MAV) design. This work includes the investigations of the models' capability used in the aerodynamic simulation, and the numerical investigations of roughness effects on low Reynolds number aerodynamics for rough aerofoils and an MAV platform.

Firstly, the low Re SST, γ-Re_θ SST and low Re DDES-SST models are compared with an experiment on the smooth NACA 2415 aerofoil at $Re = 1 \times 10^5$. It is found that both low Re SST and γ-Re_θ SST models have a reasonably good capability to predict lift, drag and bubble between $4^\circ \leq \alpha \leq 8^\circ$. The low Re DDES-SST model performs better at $\alpha = 12^\circ$ than 4°, predicting the best matched lift and resolving more transitional flow features.

Secondly, the low Re SST and γ-Re_θ SST models incorporated with the equivalent sand grain roughness method are compared with an experiment on a rough NACA 0012 aerofoil at $Re = 1.5 \times 10^5$. The roughness result shows, while the low Re SST model predicts the correct trend of the roughness effects, the γ-Re_θ SST model fails to predict the transition on the rough aerofoil surface, resulting in inaccurate lift and drag prediction.

Thirdly, the investigations on rough aerofoils between $Re = 2 \times 10^4 \sim 2 \times 10^5$ shows the beneficial roughness effects only occur under an appropriate combination of Reynolds number, roughness height, incidence and aerofoil. A detailed guidance and suggestions of the application of roughness are proposed. The study also enriches the understanding of roughness effects at very low Reynolds numbers.

Finally, the roughness investigation on the MAV platform shows better lift to drag ratios due to the rough thin wing are small at the lowest Reynolds number. A higher aspect ratio wing and better wing-fuselage integration may obtain more benefits from roughness.

Acknowledgements

My biggest thank you goes to my parents. They provide the financial support and tolerate the loneliness without their only son being around.

My second thank you goes to my supervisors. The opportunity of this study and the academic guidance are provided by the main supervisor, Prof Ning Qin. His profound knowledge in aerodynamics and computational methods enrich my understandings, and his advice and patient on the language support improves my English writing. Other support on the doctoral training programme from the second supervisor, Dr A. F. Nowakowski, is also acknowledged.

Dr Zhaolin Chen in the aerodynamic research group provides the MAV geometry and useful discussions throughout the time for this doctoral study. Other group members are acknowledged for their attention and suggestion on this study, including Gabriele L Mura, Benjamin L Hinchliffe, Veronica Palma Gonzalez Garcia, Hao Chen, Muhammad Al Hakim bin Naziruddin, Ho-chun Yu, Drs Spiros Siouris, Mathew Harris, Feng Zhu, Wei Wang, Yibin Wang, Feng Deng, and Wenhua Wu.

During the study of roughness modelling, Luís Eça from Instituto Superior Técnico, Portugal, is acknowledged for fruitful discussions. Hemant Punekar and Balasubramanyam Sasanapuri from ANSYS Technical Support are also acknowledged for the information on the implementation of the γ-Re_θ SST model and the related roughness model.

The resource for the computation and the use of ANSYS and MATLAB software are provided by the computing service in the University of Sheffield. Dr Deniz Savas is particularly acknowledged.

My last thank you goes to the people I have met in this country, those I know or do not know their names, who add colours to the dull days.

Table of Contents

List of Tables

List of Figures

Nomenclature

B	= the universial law-of-the-wall contant
c	= aerofoil chord length
C_l	= lift coefficient, $C_l = L/(0.5\rho U_{ref}^2 S_{ref})$
C_{lf}	= the skin friction component in the total lift
C_{lp}	= the pressure component in the total lift
C_d	= drag coefficient, $C_d = D/(0.5\rho U_{ref}^2 S_{ref})$
C_{df}	= the skin friction component in the total drag
C_{dp}	= the pressure component in the total drag
C_f	= skin friction coefficient, $C_f = \tau_w/(0.5\rho U_{ref}^2)$
C_p	= pressure coefficient, $C_p = (p - p_\infty)/(0.5\rho U_{ref}^2)$
c_v	= specific heat at constant volumne
e	= internal energy
h	= roughness height
h^+	= nondimensional roughness height, $h^+ = \rho u_\tau h/\mu$
$\bar{h}$	= average roughness height
k	= turbulence kinetic energy in k-ω model
p	= pressure
R	= universal gas contant, 287.05 J/(kg · K)
Re	= Reynolds number, $Re = \rho U_{ref} L_{ref}/\mu$
Re_θ	= momentum thickness Reynolds number, $Re_\theta = \rho U_{ref}\theta/\mu$
S	= strain rate magnitude, $S = \sqrt{0.5 S_{ij} S_{ij}}$
S_{ij}	= strain rate tensor, $S_{ij} = \frac{1}{2}\left(\frac{\partial u_i}{\partial x_j} + \frac{\partial u_j}{\partial x_i}\right)$
q-criterion	= q vortex identification, the second invariant of the velocity gradient tensor, $$q = 0.5 \times (\Omega^2 - S^2)$$ $$= -0.5 \times \left(\left(\frac{\partial u}{\partial x}\right)^2 + \left(\frac{\partial v}{\partial y}\right)^2 + \left(\frac{\partial w}{\partial z}\right)^2\right)$$ $$- \frac{\partial u}{\partial y}\frac{\partial v}{\partial x} - \frac{\partial u}{\partial z}\frac{\partial w}{\partial x} - \frac{\partial v}{\partial z}\frac{\partial w}{\partial y}$$
Tu	= Turbulence intensity, %
T	= Temperature
$\vec{U}$	= velocity vector
u	= x velocity
v	= y velocity

w	= z velocity
$-\overline{u'v'}/U_\infty^2$	= normalized Reynolds shear stress
x	= position in x-coordinate
y^+	= nondimensional cell wall distance, $y^+=\rho u_\tau y/\mu$
y	= cell wall distance, y-coordinate
z	= spanwise coordinates, z-coordinate

Greek Symbols

α	= angle of attack
Γ	= diffusion coefficient
ε	= dissipation rate for k-ε model
γ	= intermittency factor
δ	= boundary layer thickness
δ_{ij}	= kronecker delta, δ=1 when i=j, otherwise δ=0
θ	= momentum thickness
κ	= von Karman constant
μ_t/μ	= viscosity ratio
μ_t	= turbulence viscosity (eddy viscosity)
μ	= viscosity
u_τ	= friction velocity, $u_\tau=\sqrt{\tau_w/\rho}$
ρ	= air density
τ	= shear stress
τ_w	= wall shear stress
ω	= specific dissipation rate for k-ω model
Ω	= vorticity tensor magnitude, $\Omega = \sqrt{0.5\Omega_{ij}\Omega_{ij}}$
Ω_{ij}	= vorticity tensor, $\Omega_{ij} = \frac{1}{2}\left(\frac{\partial u_i}{\partial x_j} - \frac{\partial u_j}{\partial x_i}\right)$

Subscript

∞	= freestream
g	= geometrical
$inlet$	= inlet values
ref	= reference values
s	= sand grain

Superscript

| ' | = fluctuation |
| + | = normalisation |

Acronyms

2D	= Two dimensional
3D	= Three dimensional
CFD	= Computational Fluid Dynamics
DES	= Detached Eddy Simulation
DDES	= Delayed Detached Eddy Simulation
DNS	= Direct Numerical Simualtion
FFT	= Fast Fourier Transform
IDDES	= Improved Delayed Detached Eddy Simulation
K-H	= Kelvin-Helmholtz
LES	= Large Eddy Simulation
LSB	= Laminar Separation Bubble
MAV	= Micro Air Vehicle
NASA	= National Aeronautical and Space Administration
RANS	= Reynolds Averaged Navier Stokes
RSM	= Reynolds Stress Model
SST	= Shear Stress Transport
T-S	= Tollmien-Schlichting

Chapter 1 Introduction

1.1 Motivation

Over a hundred years of development, human beings now are able to build large aeroplanes that are capable of carrying hundreds of passengers across oceans, as well as small unmanned aeroplanes that are flying at lower speeds and lower altitudes. In the spectrum of aeroplanes, the two ends are interesting, i.e. the smallest and the largest. The serious research efforts to build small ever aircraft emerged in mid-1990s, according to Mueller[1]. This led to the birth of micro air vehicle (MAV). The main task of MAV is military and civilian surveillance. MAV may look similar in the size to model aeroplanes flying in model competitions, or even in parks, and it was not uncommon MAV builders used material and electronic equipment that could be purchased directly from model shops. In fact, the development of light material and electronic equipment in the aeromodel community facilitated the development of MAV at the early stage. However, MAV has more stringent design requirements, such as cruise range, payload and portability. MAV also uses more sophisticated manufacturing method, e.g., 3D printing[2], and more advanced numerical method to obtain more in-depth aerodynamic analysis, e.g., Reynolds Averaged Navier Stokes (RANS) simulation[3] and Large Eddy Simulation (LES)[4]. The development of MAV research reflects many aspects of the state-of-the-art of aeronautical studies. For example, the research in the configuration extends beyond fixed-wing to rotary wing[5], flapping wing[6], and even some special types of configuration, e.g., cyclocopter[7]. In addition, the research includes laminar to turbulence transition at low Reynolds numbers at low speeds[8], as well as the realisation of morphing aircraft[9–11].

Among the broad scope of MAV research, this thesis investigates the simulation of transitional flows and roughness effects for MAV. This includes the investigation for the simulation on smooth and rough surfaces.

For an aerodynamic simulation of MAV on smooth surfaces, the capability of the tool to reproduce the low Reynolds number effects is one important aspect. This is in fact the main challenge for the simulation. The challenge is

due to separation and transition in the flow at low Reynolds numbers, and there is lack of knowledge of suitable models. The Reynolds number is defined as,

$$Re = \frac{\rho V L}{\mu} \tag{1-1}$$

and it physically refers to the ratio of inertial force and viscous force. The range for low Reynolds numbers is approximately limited between 1×10^4 and 2×10^5. This range is reasonable for MAV studies, as shown in Table 1-1.

Table 1-1. The range of Reynolds numbers*

Type of flying object	Mean chord (m)	Velocity (m/s)	Re
Transonic transports			$>1\times10^7$
Model aeroplanes			
Indoor models	0.05	2	7×10^3
Small models	0.1	5	3.4×10^4
Medium models	0.2	10	1.4×10^5
Large and fast models	0.3	20	4.1×10^5
MAV[12]			
NRL MITE			$5\times10^4 \sim 1\times10^5$
Flexible wing MAV University of Florida			$\approx 1\times10^5$
Adaptive wing MAV University of Arizona			$5\times10^4 \sim 2\times10^5$
Birds and insects[13]			
Albatross	0.2	16	2.2×10^5
Gull	0.14	10	1.4×10^5
Swift	0.03	$6.1 \sim 39$	$1.3\times10^4 \sim 8.2\times10^4$
Butterfly (gliding)	0.05	2	7×10^3

* The Reynolds numbers are approximately accurate. The air condition is sea level standard.

The low Reynolds number effects are not unfamiliar for wind tunnel measurement. In the low speed testing, the Reynolds number in testing is always of the first priority to match the one in operations. If the two Reynolds numbers are different, the measured data is expected to be incomparable with that for the flying vehicle in real scales.

The low Reynolds number effects can be also understood from the variation of aerodynamic characteristics with respect to the decreasing Reynolds number. Generally, for a given aerofoil, maximum lift, minimum drag, and maximum lift to drag ratio degrade as Reynolds number decreases. Furthermore, nonlinearity, e.g., nonlinear lift growth, and hysterias loop may happen, e.g., lift needs to go back to a lower incidence to recover from stall. In the range of MAV

flight Reynolds number, the degradation becomes more and more severe to the decreasing Reynolds number. Given a particular incidence, the lift may abruptly drop; meanwhile the drag may abruptly increase at some Reynolds numbers, defined as the "critical Reynolds number". The systematic work by Schmitz[13] provided a good example to illustrate this. In this series of wind tunnel measurements, the N60 aerofoil showed a critical Reynolds number of 6.3×10^4 at $\alpha = 6°$. The lift coefficient dropt approximately from 0.97 to 0.6, the drag increased approximately from 0.08 to 0.097. The measurement further included four other profiles, i.e., Gö 625, N60R, flat plate and cambered plate 417a. Other than the thin flat plate and cambered plate 417a, other aerofoils all showed a critical Reynolds number. The reason for the superiority of thin profiles to others was believed that, the sharper the leading edge, the earlier does the laminar separation bubble reach the leading edge, also for the transition point. Thin profiles with sharp nose are easier to attach turbulently at lower Reynolds numbers.

Schmitz[13] also believed that surface roughness, as a technique for artificial turbulence, could play the same effects as the sharp nose of the thin plates. The artificial turbulence was referred to the turbulence created artificially, for example by sound waves, or turbulence-inducing wires. Schmitz[13] cited the experimental data by Hooker[14]. The experimental study was conducted at Reynolds numbers from 1.18×10^5 to 3.55×10^6. It was observed that the surface roughness generally had detrimental effects, such as reducing the lift slope and reducing the maximum C_l. However, the detrimental effects were less severe at lower Reynolds numbers. The evidences for the beneficial effects of surface roughness were reported in the studies in the subsequent decades, such as Kraemer[15], Lyon et al.[16], and Althaus[17].

It is therefore interesting to investigate the potential of beneficial roughness effects on the aerodynamic performance of the MAV platform developed in the author's research group. This also requires an investigation for suitable roughness model at low Reynolds numbers.

1.2 Objective

The main objective is the simulation of aerodynamic performance and the roughness effects. This includes the investigation for the simulation on smooth and rough surfaces at low Reynolds numbers including transition (*objective A*), and then the investigation on the roughness effect (*objective B*).

Objective A leads to the investigation on simulation methods. As mentioned earlier, the capability of reproducing low Reynolds number effects is crucial, and thus a suitable simulation should properly deal with the flow features in low Reynolds number boundary layer flows. The key flow features are separation and transition. Carmichael[18] and Mueller *et al.*[19] provided a good survey of low Re flows over aerofoils. Generally, at low Reynolds number and operating lift condition, the flow is very likely to separate before it reaches the trailing edge on the upper surface. Sometimes, a laminar separation bubble (LSB) occurs. Prior to the separation, because of a relatively low Reynolds number, the flow remains laminar. After the separation, the flow commonly transits towards turbulence in the separated shear layer above the wall, and because of enhanced mixing and momentum transfer of the turbulent flow, the stream gains more energy and attaches back onto the upper surface. This region between separation and reattachment is often termed as LSB. The existence of the LSB alters the boundary layer shape, affects the attached/separated flow region on the upper surface, therefore it dictates aerofoil aerodynamic performance.

On the aspect of roughness modelling, the simulation method depends on the type of roughness. The type of roughness may be categorised as single/isolated roughness and distributed roughness. For the former type, the exact roughness geometrical description is possible to present in the geometrical model in numerical simulations, and thus it is relatively easy to deal with. For the latter type, the detailed description of the roughness geometry is usually impossible to retain in simulations, and thus a model is required. One challenge of roughness modelling is that, when using distributed roughness to mimic real life rough surfaces, it is of certain difficulty to convert the real surface to an equivalent surface. Another challenge is to reproducing the effects of this

4

equivalent surface. In the context of the low Reynolds number boundary layer flow, the effects should include those on laminar, transitional, and turbulent flows.

Instead of investigating "how to model" aforementioned flow features and effects, this thesis investigates "how well the models model". The focus is on the comparison between numerical prediction and experimental data on lift, drag, and bubble locations. The pressure distribution and skin friction distribution are compared when the experimental data is available. Two fundamental questions are raised:

(1) How well the transitional flow over aerofoils, wings and full MAV is modelled, as compared to the experimental data?

(2) How well the flow influenced by surface roughness is modelled, as compared to the experimental data?

Apparently, a complete answer to the two questions requires considerable investigations on all methods available today. This is impossible to accomplish within a single thesis. Particularly, below methods are investigated:

(1) RANS simulation. RANS method uses Reynolds-average (commonly time-average) to model the statistical behaviour of turbulence. The flow field (velocity field) is represented by a mean flow plus a fluctuation. During the procedure of Reynolds-averaging on the flow governing equations (Navier-Stokes equations), unknown Reynolds shear stress terms require additional equations to close the system, known as "closure problem". In the historical development, various numbers of turbulence models, whether or not based on Boussinesq Approximation, i.e., eddy viscosity concept, have been proposed. Different turbulence models have various degrees of sophistication in the formulation, as well as different ranges of applications. In the context of external flow around aerial vehicles, Spalart-Allarmas (SA) and Shear Stress Transport (SST) model are of the most popularity. Comparing to Direct Numerical Simulation (DNS) and LES, RANS requires much less mesh points, as detailed turbulent fluctuation are "modelled", and therefore it is an economical engineering method. The primary focus in this thesis is on

the variants of SST models that can model flow transition. Two models are investigated:

- SST + low Reynolds number correction (viscous correction), designated as "low Re SST" model, and

- SST + two additional transport equations of intermittency factor γ and transition momentum thickness Reynolds number $Re_{\theta t}$, designated as "γ-Re_θ SST" model.

(2) Delayed detached eddy simulation (DDES). DDES belongs to the variant of detached eddy simulation (DES) method, while DES method is known as a hybrid RANS-LES approach, with the aim to take the advantage of both the good capability of LES on resolving separated and the economic cost of RANS on attached flows. This is realised by using RANS for attached boundary layer flows and switching to LES for separated flows and the region outside boundary layers. Although the idea and formulation for DES is proposed concisely at the beginning, i.e., using a simple blending function, after years of development, the blending function becomes more and more sophisticated. The original blending function uses the wall distance as the RANS length scale, and the local grid spacing as the LES length scale. When the LES length scale is larger than the RANS length scale, the model switches to LES mode. When the opposite happens, the model switches to RANS mode. The transition process between these two modes is rapid, and is controlled via the blending functions. It is known such formulation suffers grid-induced separation. In some region (grey area) even inside the boundary layer these two length scales may be ambiguous, and the model may switch LES mode on for attached flows. When mesh becomes finer, the grey area grows and the problem becomes more evident. Improvement has been developed, such as delayed detached eddy simulation (DDES). The blending function for DDES includes flow field information to ensure RANS mode to be active in attached boundary layers. This thesis investigates a DDES formulation with low Re correction for transitional flow simulation:

- DDES (SST) + low Re correction.

(3) The equivalent sand grain approach for roughness modelling. The realistic surface is simplified to a surface with closely packed spheres, i.e., sand grains, and the roughness height is the diameter of the sphere. The major effects of surface roughness are simplified to roughness induced transition and enhanced turbulent skin friction due to the equivalent sand grain roughness. The third simplification is that, the effects of surface roughness are represented by altering the wall boundary condition, instead of resolving the complex flow behind individual roughness elements. In the context of SST model, the wall boundary condition of ω is required to change accordingly. The two variants of SST model mentioned in (1) can be modified correspondingly to model roughness and roughness induced transition. The two models become:

- SST + low Re correction + rough wall boundary condition, and
- SST + γ-Re$_\theta$ + rough wall boundary condition + modified transition correlations due to roughness.

In addition, a literature review on LSB, methods for RANS transition, DDES transition, and roughness modelling at low Reynolds number is provided.

Objective B leads to the simulation on rough surfaces, rough aerofoils and the MAV platform are included. The investigation on aerofoils is included due to the relatively ample 2D experimental data for validations and relatively cheap computational expenses. In addition, a literature review on roughness effects is provided.

Based on above discussion, the following objectives are refined:
(1) Literature review on LSB, RANS transition methods, DDES transition methods, roughness effects, and roughness modelling methods,
(2) Evaluation of the capability of low Re SST model and γ-Re$_\theta$ SST model against the experimental lift, drag, bubble location, pressure distribution, and skin friction distribution (if available),
(3) Evaluation of the capability of the two models with roughness modifications against the experimental lift, drag, bubble location,

pressure distribution, and skin friction distribution (if available),

(4) Evaluation of the capability of low Re SST DDES model against the experimental lift, drag, bubble location, pressure distribution, and skin friction distribution (if available),

(5) Investigation of the roughness effects on rough aerofoils at low Reynolds numbers, including the effects on lift and drag characteristics, the change in the flow field due to the roughness, the roughness effects under different roughness height, and the Reynolds number effects on the roughness effects,

(6) Investigation of the roughness effects of the MAV platform, including the effects on lift and drag characteristics and the change in the flow field due to the roughness.

1.3 Outline

This introduction provides the motivation, objective, and outline of the current research. The second chapter reviews the literature on LSB, RANS and DDES transition methods, roughness effects, and roughness modelling at low Reynolds numbers. The third chapter describes the numerical method and turbulence models. The fourth chapter compares the prediction of low Re SST, γ-Re_θ SST and low Re DDES-SST models on NACA 2415 aerofoil, and also compares the result with an experiment. The fifth chapter compares the prediction of rough low Re SST and γ-Re_θ SST models on the rough NACA 0012 aerofoil, and compares the result with an experiment. The sixth chapter investigates the roughness effects on rough aerofoils at low Reynolds numbers. The seventh chapter investigates the roughness effects on the MAV platform. The eighth chapter presents the overall conclusion and future work.

Chapter 2 Literature Review

The literature is reviewed on: LSB, RANS transition methods, DDES transition methods, roughness effects and roughness modelling. The literature review on LSB establishes a physical foundation for the investigation of the capability of RANS and DDES transition methods on relevant flows. The research on transition methods is very broad. The focus here is limited to those used on the LSB flow related to MAV. The review on the roughness effects provides more details on the improvements in aerodynamics. For roughness modelling methods and transition methods, it is found the field of MAV provides insufficient literature. The scope therefore extends to the field of small wind turbines and low pressure gas turbines, because they also operate at low Reynolds numbers. Especially for the roughness modelling, the recently important advances primarily appear in turbomachinery applications.

2.1 Laminar Separation Bubble

The study of laminar separation bubbles can be traced back to 1920s. Tani[20] provided a good historical description with illustrative examples on this matter. Tani[20] mentioned, the laminar separation bubble, or the bubble, was firstly discovered in aerofoil stall studies. At that time, stall could be categorised as leading edge stall, trailing edge stall, and thin aerofoil stall. The bubble appeared for the thin aerofoil stall. The apparent influence of the bubble was on the pressure distribution on an aerofoil, i.e., a constant pressure region named as pressure plateau. Nevertheless, it was also noted, in some cases, the presence of bubbles was not accompanied by a constant pressure region.

The bubbles discussed in Tani[20] were mostly at $Re\sim O(10^6)$, which are beyond the range of low Reynolds numbers. At low Reynolds numbers, currently considerable amount of literature owe the first systematic work to Schmitz[13] during 1930s in Germany. The experimental measurements were conducted on four distinct profiles with various thickness and Reynolds numbers between 20000 and 200000. In the NASA version of English translation, LSB was termed as "transition vortex", probably due to the fact that LSB "trips" the boundary layer state to turbulent. Schmitz's measurements

continued after the Second World War and further results were published in Kraemer[15], Schmitz[21], and Schmitz[22]. The additional results included the data on rough surface finish (denoted as "paper model"), "turbulence wires", bird wings, and the data from free flights.

However, Schmitz's work gave no much insight on the fundamental flow and transition process associated to the bubble. By comparison, the experimental data cited in Tani[20], Gaster[23] and Horton[24] were the basis for the development of semi-empirical model for bubble prediction in the following decades, see Meara and Mueller[25] for an example.

Among the relevant literature on the bubble, the main aspect of the study may be regarded as follows:

(1) A "natural" bubble. It refers to the bubble that forms without forcing environmental disturbances. The study belongs to this catalogue has a wide range of focuses, mainly fundamental flow[26–28], transition process[29–31], bubble bursting[23,32], and bubble dynamics influenced by incidence[33], Reynolds number[18] and stall hysteresis[34]. It is impossible to find a single piece of work covering all these problems. The fundamental flow and vortex evolvement in the transition process are currently of substantial interest.

(2) The bubble subjected to environmental disturbances, for instance, elevated freestream turbulence intensity[35], wake effects[36], acoustic disturbances[37], surface roughness[37,38], and cross flows[39]. For each type of environmental disturbance, all the problems mentioned in (1) should be investigated.

(3) The bubble on 3D geometries, such as wings or full MAVs. In (1) and (2) the studies are conducted on 2D geometries, e.g., flat plates and aerofoils. No DNS or well controlled experimental results have been published for 3D geometries. Recently, Chen et $al.$[40] simulated the LSB on a wing using the γ-Re$_\theta$ SST model, and Makino[41] conducted experiments on wings at low Reynolds numbers. However, these results provide no detailed information for the transition process.

The following material provides more details about the fundamental flow and transition process. A schematic of a short bubble, viewed in a time-averaged manner, is depicted in Fig. 2-1.
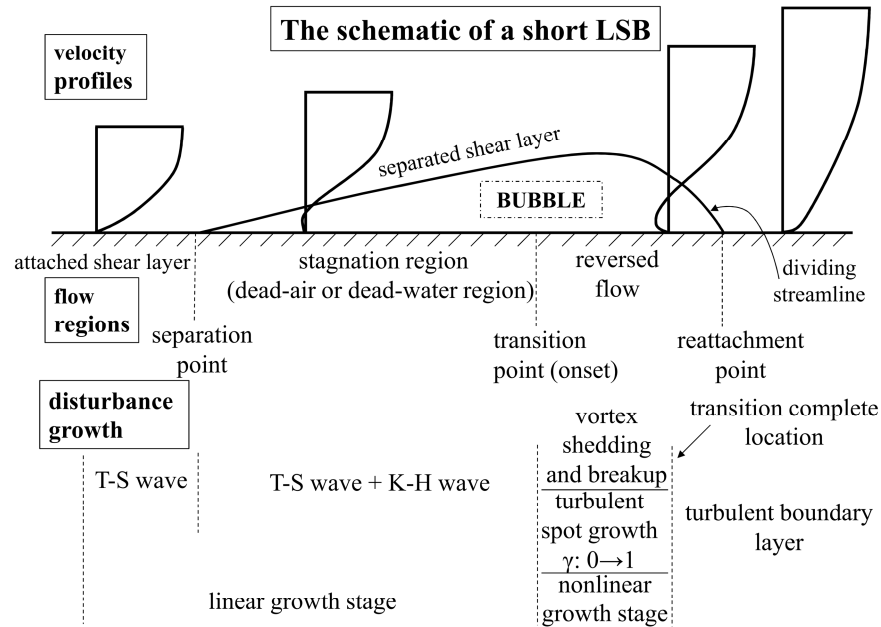
Fig. 2-1. The schematic of a separation bubble

The laminar separation is due to the adverse pressure gradient. After some distance downstream, the separated flow reattaches to the surface. The flow region between separation and reattachment refers to the bubble. In smoke wire flow visualisations[42], smoke lines bends upwards at the point of separation and dispersed downstream. Near the time averaged reattachment point, smoke line indicates the flow reattaches. This vivid picture may give rise to the name "bubble".

The study on the bubble developed some glossary when describing the flow. Fig. 2-1 shows a separated shear layer, a dead-air region, and a reversed flow region. The dead air region has a relatively low velocity, nearly stagnation, and this behaviour gives rise to the constant pressure region. Above the dead air region, it is so-called separated shear layer, which is believed to be related to the transition process. The reversed flow region has the relatively large reversed flow. In the instantaneous flow, the complex vortex evolvement can be

11

observed, and no general agreement can be found so far. Above description applies on short bubbles. For long bubbles, there are insufficient flow pictures. Besides, the picture described here is only meaningful when viewing from a time averaged manner. Arena and Mueller[42] demonstrated a case that even the dead air region changed in size with respect to time, i.e., the dead-air was not really "dead". The observation was the bubble continuously shrank and grew in size. Transition was not fixed in a point over time, changing with time instead. Smoke lines also showed the transition location was different spanwise, as well as the bubble size.

A qualitative description on the transition process is summarised for a natural short bubble, with the absence of environmental disturbance. It is acceptable that the transition is related to flow shear. For a bubble, the attached shear layer and separated one are all responsible for the transition process. Here three scenarios may happen. Scenario *A* is the transition happens before separation point and then finishes within the bubble region. Scenario *B* is the transition happens and finishes within the bubble region. Scenario *C* is the transition happens within the bubble region and finishes after time averaged reattachment point (beyond the bubble region). Hatman and Wang[43] provided a comprehensive model using empirical correlations to determine transition location and reattachment location for each scenario. Nevertheless, the correlations are primarily based on flat plate results, and their use on more practical aerofoil was believed to be "limited". Mayle[36] in 1991 provided empirical correlations for transition onset and transition onset and transition complete location based on the momentum thickness Reynolds number at the separation point Re_{θ_s}. As further evaluated in Walker[44] in 1993, Mayle 1991 correlation was believed to be of practical importance in the context of gas turbine applications, and Walker[44] provided some refinement on the correlations. Afterwards, Malkiel and Mayle[29] conducted experiments on a long bubble, and the results support Mayle 1991 correlations. Walker[44] in addition criticised the determination of transition end locations, pointed out that it may not coincide with the end of the constant pressure region, and it may lie well before that (evidence: the long bubble case in Malkiel and Mayle[29]) or even after the reattachment point (mentioned in Walker[44]). This thesis only takes

account of *Scenario B*.

In this scenario, there is ample evidence to describe the disturbance amplification as linear and subsequent nonlinear stages. Brinkerhoff and Yaras[31] demonstrated a good example. Based on their DNS results, it was vividly to see the flow was unstable to T-S waves in the attached boundary layer at first, and the separated shear layer was then unstable to K-H waves. The vortical structures developed in the attached boundary layer were convected into the separated shear layer, and they interacted with the shed vortices that due to K-H instability, resulting in a facilitated transition .The shed vortices are the result of the "roll-up" of separated shear layer. Up to the roll up, the disturbance described from the linear stability theory agrees with the reality well. The roll up is also termed as "vortex formation" in some literature, e.g., Marxen[26]. From both visualisations in DNS and experiments, this shed vortex lost its spanwise uniformity and eventually disintegrates into vortical structures in small scales. The transition process is mentioned as "vortex breakup", or "breakdown to turbulence" in some literature, and it is frequently mentioned as a rapid process. Malkiel and Mayle[29] mentioned it was completed within one wavelength of the shed vortex. It is found that there is no general agreement on explaining this process. The aforementioned Brinkerhoff and Yaras[31] believed the interaction of the vortices originated in both attached and separated shear layers was responsible, whereas Marxen[26] proposed 3 types of instability mechanism. The flow picture in this process is also not universal. McAuliffe and Yaras[45] found, only below $Re_{\theta s}$ (momentum thickness Reynolds number at the separation point) about 100, a vortex paring process existed. Marxen[26] found the spanwise non-uniformity already existed in the vortex formation. Serna and Lázaro[30] found the shed vortex moved towards the solid wall and then broke up. Burgmann[27] found a process that the vortex transformed from C-vortex to "screwdriver" vortex. Freestream turbulence was also believed to have influences. To sum up, it is only safe to generally say the final transition process is a "vortex formation and breakup process", and this is sufficient for the purpose for current study.

2.2 Transition Modelling for Reynolds Averaged Navier Stokes Simulation

The review introduces a comprehensive framework of RANS transition modelling. The models reviewed here are more than the two used in this work.

Standard RANS is incapable of resolving transition because Reynolds-averaging masks all spectrum of turbulence. To model transition, additional empirical information must be transferred to the turbulence model, either through re-formulation of the model, or through additional model calibrations. RANS turbulence models till now develop a great number of models. It is noticeable that difference models will require distinct formulation for transition, and will lead to different conclusions. The subsequent discussion is limited to $k - \omega$ based SST models.

Apparently, in the perspective of flow, if turbulence models can only model turbulent boundary layer, transition models should model both laminar and turbulent boundary layer. The first task is to predict the border of these two types of flow, i.e., the transition location. In realistic flows, the transition process is completed via a finite length of a region, instead of a point, so that the flow state gradually changes from laminar to turbulent. Consequently, the modelling of transition process is another task of transition models. Furthermore, because the coupling with the flow equations is realised via eddy viscosity, and the modelling of laminar boundary layer and transitional boundary layer must eventually reflect on the eddy viscosity, the second task is actually the correction on the eddy viscosity according to particular flow state. To sum up, transition models should accomplish two tasks:

(1) Transition location prediction, and

(2) Transitional flow modelling (via eddy viscosity).

2.2.1 Transition Location Prediction

For this task, below methods can be found in literature:

(1) Methods based on stability analysis

The classic introduction to stability theory may be referred to Schlichting

and Gersten[46], and White[47]. Simply put, the stability theory concerns whether the disturbance grows or decays when supplied to a laminar flow. If the disturbance grows or amplifies, the flow will evolve to turbulence. If the disturbance decays, the flow will remain laminar. In analyses, the linear stability equation is common, i.e., Orr-Sommerfeld equation. The problem then becomes the analysis of the Eigen values of the equation. The application of this method on the MAV-related laminar separation bubble flow may be referred to Windte et al.[48] The stability analysis concerns nonlinear stability may be referred to Stuart[49]. However nonlinear stability analysis has no relevant application in LSB flow modelling.

Among stability analysis method, a semi-empirical method has been developed, i.e., e^N method, proposed by Smith and Gamberoni[50] and van Ingen[51]. The method analyses the growth of the amplification factor N along the aerofoil chord length, instead of directly analysing the stability equation. An example of the application on laminar separation bubble flow may be referred to Windte et al.[48] At the first step, a flow solution is obtained from RANS simulations, and the boundary layer parameters are extracted, e.g., boundary layer momentum thickness, shape factors, etc. Then, the distribution of N is determined from empirical correlations or a linear stability solver. When N grows to a number provided from the user, the corresponding chord location is determined as the transition location, from which the turbulence production term is activated. Windte et al.[48] applied e^N with BSL model on the separation bubble flow on SD7003 aerofoil. The distribution of Reynolds stresses and the prediction in the lift and drag were in a reasonably agreement with the experiment, with some empiricism on the choice on the critical N. Another example is Lian and Shyy[52], which applied e^N on the same SD7003 case. Using a different correlation and turbulence models, it also obtained satisfactory results.

The application on unsteady transition onset at low Reynolds numbers may be referred to Radespiel et al.[53] and Windte et al.[54]. The application on 3D boundary layers at low Reynolds numbers has not appeared. The most relevant studies are Cebeci et al.[55] and Stock[56]: the former does not combine e^N with

RANS, and the latter concerns high Reynolds number laminar wing.

The last method presented couples mathematically the stability analysis and RANS models. The coupling is possible, because the starting point of stability theory and RANS models is similar, i.e., the flow field is decomposed to a mean flow plus a fluctuation (disturbance). The stability theory deals with whether the disturbance causes the flow to be unstable, whereas RANS turbulence model deals with the influence of the turbulent fluctuation on the eddy viscosity. Wilcox and Traci[57] proposed a complete model approximately 40 years ago. Fu and Wang[58] reviewed this model recently, and believed that the work was still a significant development on a physically sound alternative to linear stability/e^N method. However, the application on separation bubble flow at low Reynolds numbers has not appeared.

(2) Methods based on empirical correlations

The empirical correlations are generally obtained from systematic experiments, and they are commonly the correlations between critical boundary layer momentum thickness Reynolds number and freestream turbulence intensity, pressure gradient, and even roughness. The use of this method requires the integral parameters such as momentum thickness Reynolds number and non-local information such as the critical momentum thickness Reynolds number, and this is incompatible with the requirement of modern CFD (see the definition by Menter *et al.*[59]), because non-local operations are not compatible with massively paralleled computations. However, this method has a breakthrough in the recent decade. The new model is formulated via local variables.

The important localisation is described as follows. The local variable transition model developed by Menter and Langtry[60], Langtry and Menter[61] and Langtry and Menter[62] is discussed as an example. The existing non-local correlation may have the form: $Re_{\theta_t} = f(Tu, dp/ds)$. Based on that, the local $Re_{\theta_{t,local}}$ can be calculated at each grid point. For the local variable model, Re_{θ_t} is transported from farfield boundary throughout the flow field. The value on the farfield boundary is obtained from the correlation with zero pressure gradients. Re_{θ_t} at every grid point, termed as $\widetilde{Re_{\theta_t}}$, is solved by the transport

equation, which is designed to force $\widetilde{Re_{\theta_t}} = Re_{\theta_{t,local}}$ outside the boundary layer, and to determine $\widetilde{Re_{\theta_t}}$ from upstream boundary layer together with the one diffused from the outside of the boundary layer. Once the field of $\widetilde{Re_{\theta_t}}$ is obtained, a relationship $Re_c = f(\widetilde{Re_{\theta_t}})$ based on numerical experiments is used to calculate the local critical Reynolds number Re_c. The local momentum thickness Reynolds number $Re_{\theta,local}$ is also necessary, which is calculated at each grid point via a relationship between vorticity Reynolds number Re_v and $Re_{\theta,local}$. The transition onset is then evaluated on the comparison between Re_c and $Re_{\theta,local}$. When $Re_{\theta,local}{>}Re_c$, the transition onset occurs, and when $Re_{\theta,local}{<}Re_c$, the transition onset does not occur. It is noticed that the proposal by Menter and Langtry[60] and Langtry and Menter[62] defines the transition onset criterion rather complicated than just using $Re_{\theta,local}{>}Re_c$. By comparison the proposal by Zhang and Gao[63] is relatively simple.

The complete framework of Menter and Langtry[60] and Langtry and Menter[62] has additional relationship $F_{legnth} = f(\widetilde{Re_{\theta_t}})$ to control the transition length and a transport equation of a intermittency factor γ, known as γ-Re$_\theta$ model. Menter and Langtry[60] provided a complete model coupled with SST turbulence model. Langtry and Menter[62] further provided the missing $Re_{\theta_c} = f(\widetilde{Re_{\theta_t}})$ and $F_{legnth} = f(\widetilde{Re_{\theta_t}})$ in their first publication, re-calibrated the model constant, and modified the relationship $Re_{\theta_t} = f(Tu, dp/ds)$. Medida and Baeder[64] coupled the γ-Re$_\theta$ model with SA turbulence model.

The intermittency factor γ physically means the portion of turbulent state in the total time measured at a given point. Before the γ-Re$_\theta$ model was proposed, there were models based on solely γ. However because the empirical information is nonlocal, the application is limited, see the review by Pasquale *et al.*[65]. The concept of intermittency is important and common in transition modelling.

(3) Low Reynolds number model

Some studies believe low Reynolds number model at best can only model bypass transition. The reason is that, the viscous correction used for the

modelling of the viscous sublayer is difficult to be calibrated further for the laminar to turbulent transition. In other words, low Reynolds number models are lack of generality.

This perspective is not adopted here. The supporting evidence is the low Re $k - \omega$ model by Wilcox[66]. The reason for its success may be simply that, it is easier to calibrate the $k - \omega$ model for the purpose of transition, as the model already has the ability to model viscous sublayer. More detailed explanation can be found in Wilcox[66]. However, the work has not been received sufficient attention. It is believed here that, the answer to the capability of the low Reynolds number model should consider the difference between base turbulence models.

In the context of this thesis, the low Re $k - \omega$ model's transition prediction is explained as follows, which is interpreted from the comprehensive explanation by Wilcox[66] and Fu and Wang[58]. The formulation of such model is based on two observations. Firstly, in the transport equation of turbulence kinetic energy k, the source terms have both production and destruction. It is a reasonable assumption that k can represent the flow in laminar state, turbulence state and those in between. Then the location where net production, i.e., the production subtracts the destruction, starts to be positive can be regarded transition onset. Similarly, the location where the net production of ω starts to be positive can be regarded as transition complete. Apparently, the former moment must happen before the latter moment to ensure the occurrence of transition. Secondly, in the numerical experiment on a flat plate, two asymptote relationships are used for the calibration for transition onset and transition complete. The abovementioned two points also indicate the transition process from onset to complete is modelled.

The low Re models have an advantage that confirmed widely: it is easy to implement in general purpose CFD codes and it is compatible with modern CFD codes.

(4) Artificial judgment

There are two proposals by Tang[67] and Catalano and Tognaccini[68].

Although these methods are seemingly lack of a physical foundation, their accuracy is surprisingly good. These artificial experiences may indicate something that has not been understood.

Tang[67] assumed that the transition onset location coincides with the attachment point of the first vortex in the laminar flow solution. This judgment was based on the observation of C_p distribution fluctuates with the number of iterations, leading to a difficulty to obtain steady state solution (note Tang[67] used a steady solver). Before the determined point, the turbulence production term was deactivated, after which the turbulence production term was activated. Tang[67] applied this method on three turbulence models on the SD7003 aerofoil case, and satisfactory comparisons on $\overline{u'v'}$ were obtained between simulations and experiments. Three additional aerofoil applications also showed reasonably good comparison on C_p. However, the comparisons on the transition location and drag were not reported.

Catalano and Tognaccini[68] assumed the transition onset location lied at 10%c after the minimum C_f after the laminar separation. Although not clearly stated, the minimum C_f referred to the minimum $|C_f|$, instead of the point with most negative values. In the practice, the flow field was firstly solved using RANS with a very low freestream turbulence intensity and viscosity ratio, where a laminar separation bubble could be obtained. The transition location was determined from the C_f, and then the flow field was solved again with prescribed turbulence intensity, viscosity ratio, and the transition point just determined, after which the turbulence production term was activated. In the results by Catalano and Tognaccini[68] and Catalano and Tognaccini[69], the comparison on the drag polar between the experimental data and simulation results was even weirdly better than their LES results.

2.2.2 Transitional Flow Modelling

This task refers to the modelling of the transition process. Regarding this problem, three common approaches can be found: (1) not modelling the transition process: (2) modelling via intermittency; (3) modelling via laminar fluctuation energy.

(1) No modelling

The common way is to deactivate the turbulence production before the transition point. If without modelling the transition process, sufficient accurate results can be still obtained, and then this is at least valuable from an engineering perspective. In real practices, the application is limited by the complexity of the flow, especially when the influence of the transitional length is not negligible.

The aforementioned examples of the e^N method, i.e., Radespiel *et al.*[53], and Windte *et al.*[54] and the artificial judgment, i.e., Tang[67], and Catalano and Tognaccini[68] in Section 2.2.1 belong to this genre. These studies are all simulating the challenging laminar separation bubble flow. However, there are a lot of problems.

One problem is the reattachment point of the separation bubble predicted lies behind the one in the experiment, leading to a longer bubble. This problem was discovered in Radespiel *et* al.[53] Fu and Wang[58] believed that the cause may be the incapability of RANS turbulence models to reproduce the much higher turbulent spot production rate in the transition process for bubbles than that for natural transition. The recent attempt to approach this problem is referred to Probst *et al.*[70] Their proposal used a Reynolds stress model, with an added Reynolds stress distribution at the transition location predicted by the e^N method. The added Reynolds stress was determined from both e^N and DNS results. A "vast improvement" was claimed for the proposal.

A different perspective is discussed here. Obviously, the procedure is relatively trivial because it requires the information from DNS results. In addition, it is not valid for the argument that the development of Reynolds stress is too slow and too less, resulting in a longer predicted bubble. Probst *et al.*[70] only rely on their own results that are favourable to them. The results by both Catalano and Tognaccini[68] and Lian and Shyy[52] are the opposite examples. Lian and Shyy[52] obtained even a better result, in terms of a better understanding on the choice of the critical factor N linked to the freestream turbulence intensity and a better agreement on the bubble length.

Therefore other unknowns may exist to explain the problem that Radespiel *et al.*[53] had. Lian and Shyy[52] used a low Re $k - \omega$ model, the transition length was controlled via an intermittency factor γ, and a different empirical correlation for e^N method was used. The exact cause deserves further investigation.

(2) The concept of intermittency factor

The physical meaning of intermittency factor γ represents the turbulent portion during the total time sampled at a given point. Apparently, it is possible to define a process of γ growing from 0 to 1, corresponding to the transition process from laminar to fully turbulent flows.

Lian and Shyy[52] presented an example of combining the e^N method and the intermittency factor γ. γ is used to control the eddy viscosity: $\mu_t = \begin{cases} 0 & x \leq x_T \\ \gamma\mu_t & x > x_T \end{cases}$, where x_T is the transition location. Note γ here is only treated as a one dimensional variable along the aerofoil chord.

In the aforementioned method using empirical correlations, e.g., γ-Re$_\theta$ model, γ is used to adjust the production and destruction of turbulence kinetic energy k: $\widetilde{P_k} = \gamma_{eff}P_k, \widetilde{D_k} = \min(\max(\gamma_{eff}, 0.1), 1.0) D_k$. It is noteworthy that, the numerical usage of γ by Menter and Langtry[60] apparently violates the physical meaning of γ. For example, outside the boundary layer, γ is designed as always equal to 1, with the justification to better modelling freestream turbulence effects. Also for example, in the relevant separation bubble transition case, γ is designed so as it can grow more than 1, with the justification to better reproduce the rapid turbulent spot production rate. Moreover, this violation is believed by the authors of the model as an evidence of the flexibility of the model of dealing with complex transitional flows. However, a neutral perspective is held towards this here.

In the laminar fluctuation energy related methods, γ can be used for the weighted average of laminar fluctuation energy and turbulent fluctuation energy: $K = (1 - \gamma)k_L + \gamma k_T$, where K is the total fluctuation energy, subscript L stands for laminar, and subscript T stands for turbulent.

It is foreseeable that, as a useful tool, the intermittency factor will be continually used for transition model design.

(3) The concept of laminar fluctuation energy

Mayle and Schulz[71] firstly proposed the concept of laminar fluctuation energy k_L and a related model. The fluctuation in pre-transitional region is different from the turbulent fluctuation. The frequency is relatively low, and the energy is contained by streamwise vortices. It is linked with the freestream turbulence in bypass transition. The recent proposal is referred to Walters and Cokjat[72]. Another model by Fu and Wang[58] propose a formulation without the individual transport equation for the laminar fluctuation energy, and the formulation incorporated boundary layer stability without a direct stability analysis. However, the capability of the models using this concept for the modelling of LSB at low Reynolds numbers are not yet completely understood.

The concept of laminar fluctuation energy may be categorised into a method of transition location prediction in Section 2.2.1, because the model by Walters and Cokjat[72] has such ability. However, it is difficult to make a clear categorisation, because the models following this concept differ greatly from Walters and Cokjat[72], such as the model by Fu and Wang[58].

2.2.3 Numerical Aspect

The numerical aspects of transition models are reviewed, including inflow condition, mesh influence, and interpolation scheme. A sufficient understanding on these aspects is the preamble to properly use transition models. The review is limited to SST models, and it is not a full catalogue of numerical aspect. Only problems sufficiently discussed in the literature are presented.

(1) Inflow condition

The inflow condition is the boundary condition specified by the user at flow inlet. For external flow problems, users usually need to specify the value of variables at the farfield. In the generation of the initial field, i.e., initialisation of the solution, it is also convenient to assign the value specified at the inlet to every mesh point throughout the flow domain. In the review by Batten *et al.*,[73]

the guidance on a suitable inflow condition was believed to be insufficient, as one reason for the slow development of transition models.

In this aspect, the research for turbulence models in recent year refers to Rumsey et al.[74], Spalart and Rumsey[75] and Rumsey[76]. The research is related to the unphysical laminar region predicted by the model in the flow field. Such behaviour was found when set relatively low inflow turbulence, and applied to fully turbulent $k - \varepsilon$, SST, and SA models. The reason was associated with the near wall function for turbulence models. Modifying this function or choosing higher inflow turbulence was found possible to avoid this problem. Additionally, Spalart and Rumsey[75] found a "relaminarisation phenomenon", which was more profound at low Reynolds numbers. However, insufficient discussion about this problem is found for transition models at low Reynolds number.

Rumsey and Spalart[77] observed the turbulence intensity specified at inlet continuously decayed in the flow domain for turbulence models at low Reynolds numbers. The decay was due to numerical reasons instead of a physical reason. The flow problem they dealt with was an external flow, with the farfield boundary placed at 50c and 100c away, and the turbulence intensity decayed to 0 before reaching the aerofoil leading edge. This was believed to be the cause for the "pseudo laminar region" problem just mentioned, and it could reduce the accuracy of the result. On the other hand, even if the turbulence decay indeed happened in the reality, it was likely to be under-resolved in the simulation, because the mesh spacing was coarse towards farfield in external flow problems. Rumsey and Spalart[77] proposed a method to control this decay.

For transition models, inflow turbulence decay is also observed. Langtry[78] proposed a practice to ensure the decayed value in front of the simulated object equals to the desired one. The practice requires a series of attempts on the combinations of turbulence intensity and viscosity ratio, and then the one with desired decayed values is chosen. This obviously increases the total computational time, because more than one simulation is necessary. By comparison, Fu and Wang[58] is an example of combining Rumsey and Spalart method with a transition model, in order to control the decay.

(2) Mesh influence

Langtry[78] provided a relative comprehensive recommendation for the use of γ-Re$_θ$ SST model within the framework of ANSYS CFX and with a bounded central differencing scheme. It was found, in a boundary layer at least 100 grid points were required streamwise, the normal growth ratio within a boundary layer were required to be less than 1.1 to 1.15, the first layer height y^+ was required to be no greater than 5, and the region representing the separation bubble was preferable to be refined.

(3) Interpolation scheme

The accuracy of the interpolation scheme influences the numerical dissipation. It is common to see a second order accuracy being used, in all transition model work cited. Nevertheless, only Langtry[78] has made a clear recommendation, stating a second order accuracy scheme for momentum equations are mandatory for the γ-Re$_θ$ SST model.

2.2.4 Combination: Complete Transition Models

The methods mentioned in Section 2.2.1 transition location prediction and Section 2.2.2 transitional flow modelling may be combined to formulate complete models. The emerged models for low Reynolds number laminar separation bubble flow simulation can be summarised in Table 2-1. Three further notes are made on these models.

(1) Low Re SST

The SST model uses a switch function F_1 to ensure $k - \omega$ formulation is activated inside the boundary layer. It also contains a switch function F_2, adjusting the eddy viscosity calculation according to Bradshaw assumption, to improve the prediction in adverse pressure gradient boundary layer flow. In the recent result by Catalano and Tognaccini[68], the second switch function, i.e., F_2 function, was ineffective at low Reynolds number; it activated at a wrong condition, and contaminated the flow in the reattached boundary layer. Catalano and Tognaccini[68] thus proposed a corrected F_2 function based on flow Reynolds number, received plausible improvement, and named the new model as SST low Reynolds number, or SST-LR for short.

There are two points to clarify. Firstly, their model is not a genuine model for transition, because it only modifies F_2 function, instead of using the viscous correction that is commonly relevant to transition modelling. Secondly, the low Re SST model used in this thesis is a genuine model for transition, because it combines the low Re viscous correction for $k - \omega$ model with high Reynolds number SST model. In the following chapters this model is shown to be capable of producing satisfactory results.

(2) γ-Re_θ SST

This model received a great attention in recent years. The recent applications are presented as follows. Chen *et al.*[40] validated the model on bubbles on a cambered plate. The result showed a good agreement with experiments on the lift, especially for the nonlinear change of the lift. However, the discrepancy on the drag at low incidences was notable. Chen and Qin[79] demonstrated another validation of the model for 3D flows over MAV, and a good agreement on the lift and drag with the experiment was obtained before stall. However, these applications provided no information for the accuracy of bubble predictions.

(3) Unsteady RANS

The use of URANS can be found for some transition models. However, many problems have not been clearly answered.

The results by Windte *et al.*[48] and Counsil and Boulama[80,81] raise the first question about the capability of URANS on laminar separation bubble simulations. Although they used distinct ways to deal with transition, the periodic vortex shedding could be found in some of their results. Windte *et al.*[48] believed those vortex shedding were resolved K-H instabilities. This is an interesting conclusion. If this can be resolved, it is interesting to investigate further whether or not URANS can replace the transition model for separation bubble simulations.

Table 2-1. RANS transition models for LSB flows at low Re

Publication	Model	LSB test case	Note
Windte, *et al.*[48]	1. e^N(approximate envelope) + BSL 2. e^N(linear stability solver) + BSL	SD7003 aerofoil, $Re = 6\times10^4$, $\alpha = 4^\circ, 8^\circ, 11^\circ$	URANS
Radespiel *et al.*[53]	e^N(linear stability solver) + BSL	SD7003 aerofoil, $Re = 6\times10^4$ steady: $\alpha = 4^\circ, 8^\circ, 11^\circ$ unsteady: plunging motion	URANS
Probst *et al.*[70]	e^N(linear stability solver) + low Re ε^h RSM + insertion of Reynolds stress profile and dissipation rate profile	SD7003 aerofoil, $Re = 6\times10^4$, $\alpha = 4^\circ$	
Lian and Shyy[52]	e^N(approximate envelope) + low Re $k-\omega$	1. SD7003 aerofoil, $Re = 6\times10^4$, $\alpha = 4^\circ, 8^\circ, 11^\circ$ 2. SD7003 aerofoil, $Re = 6\times10^4$, drag polar	FSI
Langtry and Menter[61]	γ-Re_θ SST, 2004	1. Pratt & Whitney Pak B cascade, $Re = 5\times10^4$, 7.5×10^4, 1×10^5 2. Zierke and Deutsch compressor, $Re = 4.7\times10^5$ 3. Flat plates: T3LB, T3LC, T3LD 4. T106, $Re = 91077$	Unsteady wake/blade interaction for T106 case
Langtry and Menter[62]	γ-Re_θ SST, 2009	1. Pratt & Whitney Pak B cascade, $Re = 5\times10^4$, 7.5×10^4, 1×10^5 2. Zierke and Deutsch compressor, $Re = 4.7\times10^5$ 3. Flat plates: T3C4	No clear improvements for separation induced transition
Counsil and Boulama[80,81]	γ-Re_θ SST, 2009	1. NACA 0012 aerofoil, $Re = 1\times10^5$, $\alpha = 4^\circ$ 2. NACA 0012 aerofoil, $Re = 5\times10^4$, $\alpha = 5^\circ$ 3. NACA 0012 aerofoil, $Re = 4.8\times10^4$, $\alpha = 6^\circ$ 4. NACA 0012 aerofoil, $Re = 2.5\times10^5$, $\alpha = 4^\circ$ 5. SD7003 aerofoil, $Re = 6\times10^4$, $\alpha = 4^\circ, 8^\circ$	URANS
Tang[67]	1. Artificial judgement + SA 2. Artificial judgement + BSL 3. Artificial judgement + JL	1. SD7003 aerofoil, $Re = 6\times10^4$, $\alpha = 4^\circ$ 2. Eppler 387 aerofoil, $Re = 1\times10^5$, $\alpha = 7^\circ$ 3. LA203A aerofoil, $Re = 2.5\times10^5$, $\alpha = 4^\circ$ 4. LNV109A aerofoil, $Re = 3.75\times10^5$, $\alpha = 8^\circ$	
Catalano and Tognaccini[68] Catalano and Tognaccini[69]	artificial judgement + modified SST	1. SD7003 aerofoil, $Re = 6\times10^4$, $\alpha = 4^\circ, 6^\circ, 8^\circ, 9^\circ$ 2. SD7003 aerofoil, $Re = 6\times10^4$, drag polar	

BSL: Baseline model
RSM: Reynolds stress model
FSI: Fluid-Structure Interaction

The second question is about the rigorousness about URANS itself, which can be reflected in Counsil and Boulama[80]. The γ-Re_θ SST model was used in an unsteady flow solver. However the contradictive fact is, the empirical correlations for γ-Re_θ SST were all measured and refined in stationary cases (a steady transition location with respect to a definite Re_θ, Tu_∞, and pressure gradient). A closer examination of the result at 4 degree undergoing flow unsteadiness actually showed a deviation from the experiment on the transition location prediction, although not noticed by Counsil and Boulama[80]. The review by Batten et al.[73] also believed it is necessary to develop a genuine (mathematically and physically sound) unsteady transition model.

The last question about URANS is the capability to deal with flow with unsteady transition onset. The relevant flow is found for the gas turbine blades, see the review by Mayle[36]. For MAV related flows, the similar circumstance may be the unsteady separation and transition on the wing subjected to the propeller wake. However, insufficient studies can be found.

2.3 Transition Modelling for Detached Eddy Simulation

Based on existing literature, it is found that without a specific transition modification, DES or hybrid RANS-LES method is incapable of predicting transitional flow well. An example may be Magagnato et al.[82] The original DES97 model was used to simulate the flow on the VKI turbine blades. The simulation result showed the suction side was almost attached laminar flow, whereas a separation bubble and turbulent fluctuation were observed in the experiment. The same circumstance repeated in Alam et al.,[83] in which DDES result showed attached flow and never separated. In the review by Fujii[84], the poor capability of DES in the plasma flow control at low Reynolds number cases was mentioned, and the recommendation was that LES was more preferable than hybrid RANS-LES methods.

The efforts to incorporate transition models to hybrid RANS-LES methods are reviewed as follows. Sørensen et al.[85] combined γ-Re_θ model with DES method and tested the new method on a cylinder and a thick aerofoil cases. The result showed the new model gave better drag prediction for the cylinder case

over a wide range of Reynolds numbers. However, the result showed the new model gave no clear improvement for the aerofoil case. For example, the lift and drag were not well predicted at the same time. The discrepancy between simulations and experiments was attributed to the wind tunnel wall effects. The aerofoil test case in Sørensen et al.[85] was at $Re = 3 \times 10^6$ without separation bubbles. Alam et al.[83] incorporated a transition sensitive $k - k_L - \omega$ model into the "dynamic hybrid RANS-LES" method they developed. The new model demonstrated the capability of capturing LSB on PAK-B aerofoil at $Re = 2.5 \times 10^4$ and 1×10^5, with $Tu_\infty = 0.5\%$ or 9%. However, while a clear improvement was found compared to the DDES result, a notable discrepancy was found on the pressure distribution and velocity profiles compared to the experiment. Gross and Fasel[86] incorporated several types of RANS eddy viscosity models to their hybrid models, and investigated the capability of them. The relevant test case was NACA64$_3$-618 at $Re = 3 \times 10^5$. The model incorporated a modified $k - \omega$ model predicted a bubble. However, a notable discrepancy on lift and drag compared to the referred DNS result was found. Arvidson et al.[87] incorporated a low Reynolds number $k - \omega$ model to their hybrid models. It focused on the calibration on the correction function and provided no relevant results on the LSB simulation.

Based on above discussions, the topic of DDES transition is an under-researched field. There is no universal approach. All of the test cases are 2D geometries (the simulation is 3D, while the case are cylinders, aerofoils, etc.). None of them discusses the vortex motion evolved in the transition process of the separation bubble.

2.4 Roughness Effects

For different types of surface roughness, the influence on the aerodynamic performance is different. The studies generally can be categorised into two groups, i.e., trip wires and distributed roughness. The trip wire roughness is usually a wire attached to the aerofoil's surface, in order to trip transition. Sometimes, it is also called isolated roughness. The diameter or the height of the wire is the main parameter correlated to the criterion of transition. The distributed roughness contains a number of roughness elements distributed in an

area of surface. The roughness elements can be man-made or those existing in the nature. A sandpaper, or a machined surface before polishing can be regarded as distributed roughness. The geometrical information of the roughness elements that is important for the roughness modelling includes the mean height and the spacing, for instances. Langtry[78] used the geometrical height of the roughness elements in their transition correlations.

The study on the effects of trip wires was relatively complete and well-documented in Lyon et al.[15], Selig et al.[85] and Selig et al.[86] Gopalarathnam et al.[88] made a conclusive remark on the possibility of using trip wires in low Re aerofoil design. The primary conclusion was that single trip wire on aerofoils (SA7024, 7025, and 7026) showed no clear advantage over their performance in the clean condition ($10^5 < Re < 3 \times 10^5$). Recently, the work by Zhou and Wang[38] on roughness bump can be seen as an analogy to trip wires, reporting that the lift to drag ratio of SD7003 aerofoil was improved by 29% when $Re = 6 \times 10^4$.

The application of trip wires on MAV is found in Kellog[89]. The MAV flight test used trip wire roughness to deal with the sensitivity in pitch control. However, the overall performance was found degraded at the same time.

The distributed surface roughness can have either detrimental or beneficial effects, depending on the operating condition and the roughness condition. Only the study showing beneficial effects is presented as follows. Kraemer[15] reported that Gö 801 aerofoil with paper covering showed better lift and drag characteristics below Reynolds number of 7.5×10^4. Althaus[17] found rough aerofoils, covered by paper or balsa wood, could obtain better aerodynamic performance at sufficient low Reynolds numbers. Bloch and Mueller[90] found the distributed grit roughness on the FX 63-137 aerofoil at $Re = 8 \times 10^4$ produced a more gradual stall and lower drag at low incidences. Lyon et al.[16] reported the experiments on SD7037 and RG15 aerofoils with rough fibre glass weave or rough wood-grain finish had less drag at low incidences when $Re = 2 \times 10^5$. Huebsch et al.[91] found the dynamic roughness was effective in eliminating separation at $\alpha = 12°$ for NACA0012 aerofoil at $Re = 6 \times 10^4$, based on both computational and experimental results. Zhang et al.[92] found the leading edge roughness on GA(W)-1 aerofoil could delay the stall and eliminating hysteresis

loop in the stall, although the performance degradation (reduction in lift coefficients) was also found. Finally, McMaster and Henderson's diagram[93] as an aerofoil data survey is widely cited for the roughness effects.

The application of distributed roughness on MAV is not found, while there are some applications on model aeroplanes. Simons[94] provided a qualitatively conclusion, believing that roughness could be useful to deal with the "subcritical problem", whereas maintaining accurate shape was of importance when without such problems. The "subcritical problem" was related to the minimum critical Reynolds number, below which the aerofoil worked under the subcritical state.

Kramer[15] presented a good definition of the critical Reynolds number and the sub/super critical state flow over aerofoil surfaces. Based on experimental observations, the flow on either side of an aerofoil might have a portion of turbulent attached flow (supercritical state), or not at all (subcritical state). The supercritical state could have better lift and drag characteristics than the subcritical state, because the turbulent boundary layer could overcome more adverse pressure gradient. For a give aerofoil, a minimum critical Reynolds number could exist, below which flows were subcritical state at all incidences, and aircrafts usually had insufficient lift to drag ratio to sustain good performances for the flight.

The above cited work all agrees the benefit of surface roughness can be attributed to its effects on the laminar separation bubble. Surface roughness can promote boundary layer transition and reduce pressure drag as the separation bubble can be reduced or eliminated.

The roughness needs to be sufficient large to take effects and the limit may be defined as the minimum effective roughness, which is of practical importance. When the roughness tends to have detrimental effects, this minimum may be the upper limit for the surface finishing. On the other hand, when the roughness has beneficial effects, this minimum may be the lower limit.

Schlichting[95] defined such limit as "admissible roughness". For turbulent boundary layer, the roughness increases the skin friction and a simple

relationship is deduced from the observation on the resistance formula of sand-roughened plates:

$$h_{adm} \leq l \times \frac{100}{Re_l}$$ (2-1)

For laminar boundary layer, the roughness induces boundary layer transition, and a simple relationship based on Feindt's experiment[96] on roughened pipes is available:

$$Re_{crit} = \frac{\rho U_{ref} h_{crit}}{\mu} = 120$$ (2-2)

2.5 Roughness Modelling

The equivalent sand grain roughness method is reviewed. The method is based on Nikuradse's early rough pipe experiments[97], from which the universal law-of-the-wall for rough walls was proposed. By embedding this into the near wall treatment in the turbulence modelling, roughness effects can then be simulated, e.g., Eça and Hoekstra[98] and Knopp *et al.*[99] On the other hand, through certain correlations in the shape and density of roughness elements to Nikuradse's sand grains, real life roughness can eventually be simulated to some degree, such as Dirling's correlation[100].

Compared to the universal smooth law-of-the-wall, the universal rough law-of-the-wall is not free from criticism, as noted by Bradshaw[101] and the reference therein. The basic roughness effects are the change of the constant in the logarithmic velocity profile, which is decreasing as to the nondimensional roughness height. The range of roughness height is divided into hydrodynamically smooth, transitional rough and fully rough regions depending on the effects. Bradshaw[101] argued there was no absolute lower limit for the roughness height to take effects, so that the concept of the critical roughness height was erroneous. The note on the other hand argued the correlation on transitional roughness data by Nikuradse represented only rare cases.

The proposal for incorporating the rough law-of-the-wall for $k - \omega$ based SST model is discussed in Eça and Hoekstra[98] and Knopp *et al.*[99] Knopp *et al.*[99]

believed that, the proposal by Wilcox[102] originally for $k - \omega$ model had two shortcomings: (1) a very fine near wall mesh for the mesh convergence are required and (2) the unsatisfactory prediction for transitional roughness. An improvement was then proposed. Hellsten and Laine[103] pointed out that a shortcoming for the SST model and proposed an extension to ensure proper modelling on fully rough surfaces. Eça and Hoekstra[98] investigated the mesh requirement for the three proposals to the SST model: (1) Wilcox proposal plus Hellsten and Laine extension, (2) Knopp *et al.* proposal and (3) "automatic wall functions" proposed by Apsley[104]. The result agreed that Wilcox proposal required very fine mesh to reduce numerical error, whereas Knopp *et al.* proposal was less sensitive. Additionally, the Apsley wall function approach was necessary to locate the first grid node large than roughness height.

The universal law-of-the-wall for rough walls deals with turbulent boundary layers. For the transitional flow at low Reynolds numbers, the modelling for roughness induced transition needs to be taken into account. This can be realized through either low Reynolds number correction for a particular turbulence model, or through a correlation based model. The early experimental data by Feindt[96] has been widely used to devise these approaches. Recent advances on the modelling for roughness induced transition at low Reynolds numbers is found in the turbomachinery application. Stripf *et al.*[105] developed new correlations from experiments, and Elsner and Warzecha[106,107] implemented the correlations into the γ-Re$_\theta$ SST model. The correlation requires the information of the ratio between the roughness height and the boundary layer displacement thickness. However, the transition onset location prediction was not satisfactory for their high pressure turbine test case. Dassler *et al.*[108] developed an approach to avoid the aforementioned requirement by including an additional transport equation of an amplification roughness variable. Langel *et al.*[109] extended this proposal to the γ-Re$_\theta$ SST model, while the test case was at high Reynolds numbers. The above work just mentioned in the application of turbomachinery provides validation cases at neither low freestream turbulence nor low Reynolds numbers.

On the characterisation of the real surface roughness to the simulated

equivalent sand grain roughness, Bons and Christensen[110] provided a recent review in the context of turbomachinery application. The review highlighted the difference between real and simulated rough surfaces, and suggested that more geometry information should be known instead of simply using an equivalent height. Pailhas[111] found the Dirling's correlation was insufficient to determine the equivalent height, and the flow field information was suggested to be taken into account, such as the pressure gradient. The characterisation is challenging work.

2.6 Conclusion

The review provides essential background information for the topic:

(1) The understanding of the fundamental flow simulated. That is, the laminar separation bubble at low Reynolds numbers.

(2) The understanding and the usage of the transition models for RANS and DDES used in this work.

(3) The roughness effects.

(4) The understanding of the roughness model used.

The review explains the necessity of this work:

(1) The capability of RANS methods for the bubble simulation is not fully understood.

(2) There is lack of understanding of the DDES method for the bubble simulation.

(3) The method for low Re roughness simulation requires more studies.

(4) There is no result on roughness simulations published at low Reynolds numbers for MAV.

Chapter 3 Methodology

Computational Fluid Dynamics (CFD) method is used for obtaining all the data. The flow is described by the governing equations, and commercial code ANSYS FLUENT is used to solve these equations. Turbulence models and roughness models are incorporated to deal with flows associated with transition and surface roughness. The technique to post-processing the raw data is also described.

3.1 Governing Equation

The flow governing equation is derived from mass conservation, momentum conservation, and energy conservation. The conservation form is described as follows, neglecting body forces:

$$\frac{\partial \rho}{\partial t} + \nabla \cdot (\rho \vec{U}) = 0 \tag{3-1}$$

$$\frac{\partial \rho u}{\partial t} + \nabla \cdot (\rho u \vec{U}) = -\frac{\partial p}{\partial x} + \frac{\partial \tau_{xx}}{\partial x} + \frac{\partial \tau_{yx}}{\partial y} + \frac{\partial \tau_{zx}}{\partial z} \tag{3-2}$$

$$\frac{\partial \rho v}{\partial t} + \nabla \cdot (\rho v \vec{U}) = -\frac{\partial p}{\partial y} + \frac{\partial \tau_{xy}}{\partial x} + \frac{\partial \tau_{yy}}{\partial y} + \frac{\partial \tau_{zy}}{\partial z} \tag{3-3}$$

$$\frac{\partial \rho w}{\partial t} + \nabla \cdot (\rho w \vec{U}) = -\frac{\partial p}{\partial z} + \frac{\partial \tau_{xz}}{\partial x} + \frac{\partial \tau_{yz}}{\partial y} + \frac{\partial \tau_{zz}}{\partial z} \tag{3-4}$$

$$\frac{\partial}{\partial t}\left[\rho\left(e + \frac{U^2}{2}\right)\right] + \nabla \cdot \left[\rho\left(e + \frac{U^2}{2}\right)\vec{U}\right]$$

$$= \rho \dot{q} - p\nabla \cdot \vec{U} + \nabla \cdot (\Gamma \nabla T) + u\left(\frac{\partial \tau_{xx}}{\partial x} + \frac{\partial \tau_{yx}}{\partial y} + \frac{\partial \tau_{zx}}{\partial z}\right)$$

$$+ v\left(\frac{\partial \tau_{xy}}{\partial x} + \frac{\partial \tau_{yy}}{\partial y} + \frac{\partial \tau_{zy}}{\partial z}\right) + w\left(\frac{\partial \tau_{xz}}{\partial x} + \frac{\partial \tau_{yz}}{\partial y} + \frac{\partial \tau_{zz}}{\partial z}\right) \tag{3-5}$$

Γ is the thermal conductivity of the fluid. A value of 0.0242 W/(m·K). Two addition equations are supplement, i.e., the equations of state for perfect gas:

$$e = c_V T \tag{3-6}$$

$$p = \rho R T \tag{3-7}$$

For the low speed flow problems investigated in this thesis, the Mach number is at an order of $O(10^{-2})$. The effect of the compressibility should be negligible. Therefore the use of the energy equation is unnecessary. It is still

solved because of the software. When the farfield boundary condition is used, the software enables the energy equation by default. The farfield boundary condition is used for the external flow problems studied in this thesis.

The stress terms are described as follows, assumed Newtonian fluid:

$$\tau_{xx} = \lambda \left(\frac{\partial u}{\partial x} + \frac{\partial v}{\partial y} + \frac{\partial w}{\partial z} \right) + 2\mu \frac{\partial u}{\partial x} \tag{3-8}$$

$$\tau_{yy} = \lambda \left(\frac{\partial u}{\partial x} + \frac{\partial v}{\partial y} + \frac{\partial w}{\partial z} \right) + 2\mu \frac{\partial v}{\partial y} \tag{3-9}$$

$$\tau_{zz} = \lambda \left(\frac{\partial u}{\partial x} + \frac{\partial v}{\partial y} + \frac{\partial w}{\partial z} \right) + 2\mu \frac{\partial w}{\partial z} \tag{3-10}$$

$$\tau_{xy} = \tau_{yx} = \mu \left(\frac{\partial v}{\partial x} + \frac{\partial u}{\partial y} \right) \tag{3-11}$$

$$\tau_{xz} = \tau_{zx} = \mu \left(\frac{\partial w}{\partial x} + \frac{\partial u}{\partial z} \right) \tag{3-12}$$

$$\tau_{zy} = \tau_{yz} = \mu \left(\frac{\partial w}{\partial y} + \frac{\partial v}{\partial z} \right) \tag{3-13}$$

where $\lambda = -\frac{2}{3}\mu$.

Above equations are general forms. The Reynolds averaged momentum equation is as follows, written in the tensor format:

$$\rho \frac{\partial U_i}{\partial t} + \rho U_j \frac{\partial U_i}{\partial x_j} = -\frac{\partial p}{\partial x_i} + \frac{\partial}{\partial x_j} (2\mu S_{ji} - \overline{\rho u_i' u_j'}) \tag{3-14}$$

The unknown Reynolds stress terms are modelled via Boussinesq eddy viscosity assumptions:

$$\tau_{ij} = -\overline{\rho u_i' u_j'} = 2\mu_t S_{ij} - \frac{2}{3}\rho k \delta_{ij} \tag{3-15}$$

μ_t is calculated from turbulence models.

The energy equation used is derived from the Reynolds analogy to the momentum equations. The energy equation used includes no terms for kinetic energy, pressure work, heat flux and viscosity terms for the incompressible cases, as follows:

$$\frac{\partial}{\partial t}(\rho e) + \nabla \cdot (\rho e \vec{U}) = \nabla \cdot (\Gamma_{eff} \nabla T) \tag{3-16}$$

$$\Gamma_{eff} = \Gamma + \frac{c_p \mu_t}{Pr_t} \qquad\qquad (3\text{-}17)$$

Pr_t is the turbulent Prandtl number. A value of 0.85 is used, which is the Fluent's default value, instead of the textbook's value of 0.91. c_p is the specific heat at constant pressure. A value of 1006.43 J/(kg·K) is used.

3.2 Solver and Solution Strategy

ANSYS FLUENT v14.0 is used for solving both steady and unsteady state compressible Reynolds-Averaged Navier-Stokes (RANS) equations using the finite volume method. The pressure-based coupled solver is chosen, which couples continuity and momentum equations with Rhie-Chow's pressure interpolation mehod[112] for the cell face velocity. Compared to the segregated pressure based solvers, the coupled solver is a more recent development, see for example Chen and Prezekwas,[113] where the coupled solver demonstrates excellent numerical convergence and significant computational time reductions. In this work, the coupled solver is found to be more robust and converging better than the segregated solvers in the cases at low Reynolds numbers.

The second order upwind difference scheme is used for the convective terms in the momentum, k, ω and energy equations, except for the momentum equation in DDES. A bounded central difference scheme is used instead. The temporal scheme is the second order Euler backward difference scheme. The gradient is evaluated via the Green-Gauss node based scheme.

The wall boundary is defined as no-slip condition and adiabatic walls. The farfield boundary is defined as Riemann farfield, which is a non-reflection freestream boundary that receives freestream values at flow inlets and extrapolates values from the interior domain at flow outlets. In DDES calculations, the two sides of the domain are treated as periodic conditions. In the simulation for the MAV platform, a half model is used. The mid-plane is treated as a symmetry boundary.

A pseudo time formulation is used for steady state calculations. The formulation requires pseudo time step as an input, which is chosen based on the flow and the chord length. The value used in this work is at an order of $O(10^{-3})$.

The unsteady calculation for URANS and DDES uses a dual-time stepping scheme. The physical time step Δt for DDES is constant 2×10^{-4}s. This time step is considered suitable as it gives $U_\infty \frac{\Delta t}{\Delta x} < 1$ thoughout the region of interest in the flow field, such as the boundary layer flow on the aerofoils surfaces. A calculation with 1×10^{-4}s shows no apparent difference.

The starting solution for steady RANS calculations is generated as follows. The k and ω field is constantly assigned by the values specified in the farfield. The velocity field is generated by solving Laplacian equations, as the built-in capability of the solver. The starting solution for unsteady DDES is the nearly converged RANS solution using the low Re SST model, where a separation bubble already exists.

The residuals in each governing equation, the lift and drag histories are monitored for judging convergence. For steady calculations, a convergence criterion of 10^{-6} for residuals or a total number of iterations of 1500 is used. This is found to be necessary to have negligible lift and drag coefficient variation between iterations. In separation bubble related cases, this criterion is sufficient to ensure the bubble location remains steady. The steady calculation, if possible to converge, usually has lift and drag flattened after 500 iterations. The threshold for the variation can be chosen depending on the desired accuracy. For unsteady calculations, a convergence criterion of 10^{-5} for residuals is used for inner iterations, and the residuals can usually drop three or more orders of magnitude. This criterion usually takes 20 to 30 inner iterations to reach, checked at every 10th iteration number. For DDES calculations, the solution runs for a sufficient time to reach a statistically converged state, and the total physical time is no more than 1.8s. For the case showing periodic changes, only 7 cycles are included in the solution due to the limited data storage.

3.3 Mesh Generation

All sets of mesh are generated in ANSYS ICEM CFD program. The multi-block structure mesh generator is used. The mesh is exported as an unstructured data format to the solver.

The built-in structured mesh refinement function is used for generating the refined mesh for mesh sensitivity studies. Once a refinement ratio is specified, the mesh spacing will reduced approximately by that ratio. It is found this function is not robust. Adjustments must be undertaken to ensure the mesh required is generated.

3.4 Turbulence Model

All turbulence models use underlying shear stress transport (SST) model[114]. The model uses following transport equations for k and ω:

$$\frac{\partial \rho k}{\partial t} + \nabla \cdot \left(\rho \vec{U} k\right) = \nabla \cdot [(\mu + \sigma_k \mu_t)\nabla k] + P_k - D_k \tag{3-18}$$

$$\frac{\partial \rho \omega}{\partial t} + \nabla \cdot \left(\rho \vec{U} \omega\right) = \nabla \cdot [(\mu + \sigma_\omega \mu_t)\nabla \omega] + \alpha \frac{\rho}{\mu_t} P_k + \text{CD} - D_\omega \tag{3-19}$$

μ_t is given by:

$$\mu_t = \rho \frac{a_1 k}{\max(a_1 \omega, F_2 S)} \tag{3-20}$$

P_k is the production of turbulence kinetic energy k:

$$P_k = \min(\mu_t S^2, 10\beta^* \rho k \omega) \tag{3-21}$$

S is the magnitude of the strain rate tensor. The strain rate tensor is defined as:

$$S_{ij} = \frac{1}{2}\left(\frac{\partial u_i}{\partial x_j} + \frac{\partial u_j}{\partial x_i}\right) \tag{3-22}$$

D_k is the dissipation of k:

$$D_k = \beta^* \rho \omega k \tag{3-23}$$

D_ω is the dissipation of specific dissipation rate ω:

$$D_\omega = \beta \rho \omega^2 \tag{3-24}$$

The cross diffusion term is described as:

$$\text{CD} = 2(1 - F_1)\rho \sigma_{\omega 2} \frac{\nabla k \cdot \nabla \omega}{\omega} \tag{3-25}$$

F_1 is the blending function that controls whether $k - \omega$ formulation or $k - \varepsilon$ formulation switches on. A value of 1 switches $k - \omega$ formulation on. It is defined as follows:

$$F_1 = \tanh(\text{arg}_1^4) \tag{3-26}$$

$$\text{arg}_1 = \min\left(\max\left(\frac{\sqrt{k}}{0.09\omega y}, \frac{500\nu}{y^2\omega}\right), \frac{4\rho\sigma_{\omega2}k}{CD_{k\omega}y^2}\right) \tag{3-27}$$

$$CD_{k\omega} = \max(2\rho\sigma_{\omega2}\frac{\nabla k \cdot \nabla\omega}{\omega}, 10^{-10}) \tag{3-28}$$

F_2 is the blending function that controls the way to calculate μ_t. A value of 1 is for boundary layer flows. It is defined as follows:

$$F_2 = \tanh(\text{arg}_2^2) \tag{3-29}$$

$$\text{arg}_2 = \max\left(\frac{2\sqrt{k}}{0.09\omega y}, \frac{500\nu}{y^2\omega}\right) \tag{3-30}$$

y is the distance nearest to the wall surface.

σ_k and σ_ω are defined as:

$$\sigma_k = F_1\sigma_{k1} + (1 - F_1)\sigma_{k2} \tag{3-31}$$

$$\sigma_\omega = F_1\sigma_{\omega1} + (1 - F_1)\sigma_{\omega2} \tag{3-32}$$

α is defined as:

$$\alpha = F_1\alpha_1 + (1 - F_1)\alpha_2 \tag{3-33}$$

$$\alpha_1 = \frac{\beta_1}{\beta^*} - \frac{\sigma_{\omega1}\kappa^2}{\sqrt{\beta^*}} \tag{3-34}$$

$$\alpha_2 = \frac{\beta_2}{\beta^*} - \frac{\sigma_{\omega2}\kappa^2}{\sqrt{\beta^*}} \tag{3-35}$$

β is defined as:

$$\beta = F_1\beta_1 + (1 - F_1)\beta_2 \tag{3-36}$$

The rest model constants are defined as follows:

$$\sigma_{k1} = 0.85, \ \sigma_{\omega1} = 0.5, \ \beta_1 = 0.075$$

$$\sigma_{k2} = 1, \ \sigma_{\omega2} = 0.856, \ \beta_2 = 0.0828$$

$$\beta^* = 0.09, \ a_1 = 0.31, \ \kappa = 0.41$$

The boundary condition for k is a user specified value at the farfield and zero normal gradient at walls. The boundary condition for ω is a user specified value at the farfield and a wall value calculated from the following formula:

$$\omega = 10\frac{6\mu}{\rho\beta_1 y^2} \tag{3-37}$$

Eq (3-37) requires $y^+ < 3$. It is noted ANSYS FLUENT uses "enhanced wall

function". When a low enough y^+ is realised, such as $y^+ \sim O(1)$ or less, Eq (3-37) is used, meanwhile the wall shear stress is calculated from:

$$\tau_w = \mu \frac{\partial u}{\partial y}\bigg|_{y=0} \tag{3-38}$$

3.4.1 Low Re SST

The low Reynolds number SST model is an extension to the above described standard SST model. The turbulence viscosity μ_t is modified as:

$$\mu_t = \frac{\rho k}{\omega} \frac{1}{\max[\frac{1}{\alpha^*}, \frac{SF_2}{a_1 \omega}]} \tag{3-39}$$

The coefficient α^* is calculated from:

$$\alpha^* = \alpha_\infty^* \left(\frac{\alpha_0^* + Re_t/R_k}{1 + Re_t/R_k} \right) \tag{3-40}$$

The coefficient α is modified as follows:

$$\alpha = \frac{\alpha_\infty}{\alpha^*} \left(\frac{\alpha_0 + Re_t/R_\omega}{1 + Re_t/R_\omega} \right) \tag{3-41}$$

$$\alpha_\infty = F_1 \alpha_{\infty 1} + (1 - F_1)\alpha_{\infty 2} \tag{3-42}$$

$$\alpha_{\infty 1} = \frac{\beta_1}{\beta_\infty^*} - \frac{\sigma_{\omega 1} \kappa^2}{\sqrt{\beta_\infty^*}} \tag{3-43}$$

$$\alpha_{\infty 2} = \frac{\beta_2}{\beta_\infty^*} - \frac{\sigma_{\omega 2} \kappa^2}{\sqrt{\beta_\infty^*}} \tag{3-44}$$

The coefficient β^* is modified as follows:

$$\beta^* = \beta_\infty^* \left(\frac{4/15 + (Re_t/R_\beta)^4}{1 + (Re_t/R_\beta)^4} \right) \tag{3-45}$$

Re_t is known as turbulent Reynolds number, defined as:

$$Re_t = \rho k/\mu\omega \tag{3-46}$$

The model constants are defined as follows:

$R_k = 6$, $R_\omega = 2.95$, $R_\beta = 8$, $\alpha_0 = 1/9$, $\alpha_0^* = 0.024$, $\alpha_\infty^* = 1$, $\beta_\infty^* = 0.09$

3.4.2 γ-Re$_θ$ SST

The γ-Re$_θ$ SST model[62] is a local correlation based transition model, which additionally solves the transport equations for the intermittency factor and the transition momentum thickness Reynolds number. The general idea is to localize the traditional empirical onset criteria via the vorticity Reynolds

number, and use intermittency factor to correct the turbulence production. Three correlations are required to complete the formulation. The Langtry-Menter correlation[62] is used.

The additional two transport equations for the intermittency factor γ and the transition momentum thickness Reynolds number $\widetilde{Re}_{\theta t}$ are described as follows:

$$\frac{\partial \rho \gamma}{\partial t} + \nabla \cdot (\rho \vec{U} \gamma) = \nabla \cdot [(\mu + \sigma_\gamma \mu_t)\nabla\gamma] + P_\gamma - E_\gamma \qquad (3\text{-}47)$$

$$\frac{\partial \rho \widetilde{Re}_{\theta t}}{\partial t} + \nabla \cdot (\rho \vec{U} \widetilde{Re}_{\theta t}) = \nabla \cdot [\sigma_{\theta t}(\mu + \mu_t)\nabla\widetilde{Re}_{\theta t}] + P_{\theta t} \qquad (3\text{-}48)$$

The two transport equation interacts with original SST model via γ. The modified transport equation for k is described as follows:

$$\frac{\partial \rho k}{\partial t} + \nabla \cdot (\rho \vec{U} k) = \nabla \cdot [(\mu + \sigma_k \mu_t)\nabla k] + \widetilde{P_k} - \widetilde{D_k} \qquad (3\text{-}49)$$

with

$$\widetilde{P_k} = \gamma_{eff} P_k \qquad (3\text{-}50)$$

$$\widetilde{D_k} = \min(\max(\gamma_{eff}, 0.1), 1) D_k \qquad (3\text{-}51)$$

P_k and D_k follows the original SST model, and

$$F_1 = \max(F_1, F_3) \qquad (3\text{-}52)$$

$$F_3 = e^{-(R_y/120)^8} \qquad (3\text{-}53)$$

$$R_y = \frac{\rho y \sqrt{k}}{\mu} \qquad (3\text{-}54)$$

F_1 in the right hand side of Eq (3-52) is the original SST F_1 blending function.

For the transport equation for γ:

$$P_\gamma = F_{legnth} c_{a1} \rho S [\gamma F_{onset}]^{0.5} (1 - c_{e1}\gamma) \qquad (3\text{-}55)$$

$$E_\gamma = c_{a2} \rho \Omega \gamma F_{turb} (c_{e2}\gamma - 1) \qquad (3\text{-}56)$$

The constants are:

$$c_{e1} = 1, c_{a1} = 2, c_{e2} = 50, c_{a2} = 0.06, \sigma_\gamma = 1$$

Ω is the magnitude of the vorticity tensor:

$$\Omega_{ij} = \frac{1}{2}\left(\frac{\partial u_i}{\partial x_j} - \frac{\partial u_j}{\partial x_i}\right) \qquad (3\text{-}57)$$

F_{turb} is defined as:

$$F_{turb} = e^{-(Re_t/4)^4} \tag{3-58}$$

F_{legnth} requires a correlation:

$$F_{legnth} = \begin{cases} [39.8189 - 1.1927 \cdot 10^{-2}\widetilde{Re}_{\theta t} \\ \quad -1.32567 \cdot 10^{-4}\widetilde{Re}_{\theta t}^2] & \widetilde{Re}_{\theta t} < 400 \\ [263.404 - 1.23939\widetilde{Re}_{\theta t} \\ \quad +1.94548 \cdot 10^{-3}\widetilde{Re}_{\theta t}^2 \\ \quad -1.01695 \cdot 10^{-6}\widetilde{Re}_{\theta t}^3] & 400 \le \widetilde{Re}_{\theta t} < 596 \\ [0.5 - (\widetilde{Re}_{\theta t} - 596) \cdot 3 \cdot 10^{-4}] & 596 \le \widetilde{Re}_{\theta t} < 1200 \\ 0.3188 & 1200 \le \widetilde{Re}_{\theta t} \end{cases} \tag{3-59}$$

The modification for the sublayer is:

$$F_{legnth} = F_{legnth}(1 - F_{sublayer}) + 40F_{sublayer} \tag{3-60}$$

$$F_{sublayer} = e^{-(R\omega/0.4)^4} \tag{3-61}$$

$$R_\omega = \frac{\rho y^2 \omega}{500\mu} \tag{3-62}$$

F_{onset} controls the production of γ, and indirectly affects the production of k. It is defined as follows:

$$F_{onset} = \max(F_{onset2} - F_{onset3}, 0) \tag{3-63}$$

$$F_{onset2} = \min[\max(F_{onset1}, F_{onset1}^4), 2.0] \tag{3-64}$$

$$F_{onset1} = \frac{Re_v}{2.193 \cdot Re_{\theta c}} \tag{3-65}$$

$$F_{onset3} = \max\left[1 - \left(\frac{Re_t}{2.5}\right)^3, 0\right] \tag{3-66}$$

$$Re_v = \frac{\rho y^2 S}{\mu} \tag{3-67}$$

$Re_{\theta c}$ requires the second correlation:

$$Re_{\theta c} = \begin{cases} [\widetilde{Re}_{\theta t} - (3.96035 - 1.20656 \cdot 10^{-2}\widetilde{Re}_{\theta t} \\ \quad +8.6823 \cdot 10^{-4}\widetilde{Re}_{\theta t}^2 - 6.96506 \cdot 10^{-7}\widetilde{Re}_{\theta t}^3 \\ \quad +1.74105 \cdot 10^{-10}\widetilde{Re}_{\theta t}^4)] & \widetilde{Re}_{\theta t} \le 1870 \\ \\ [\widetilde{Re}_{\theta t} - (593.11 + (\widetilde{Re}_{\theta t} - 1870) \cdot 0.482)] & \widetilde{Re}_{\theta t} > 1870 \end{cases} \tag{3-68}$$

The modification for predicting separation induced transition is:

$$\gamma_{sep} = \min(s_1 F_{reattach} \max\left(0, \frac{Re_v}{3.235 \cdot Re_{\theta c}} - 1\right), 2)F_{\theta t} \qquad (3\text{-}69)$$

$$F_{reattach} = e^{-(Re_t/20)^4} \qquad (3\text{-}70)$$

$$\gamma_{eff} = \max(\gamma, \gamma_{sep}) \qquad (3\text{-}71)$$

$$s_1 = 2 \qquad (3\text{-}72)$$

For the transport equation for $\widetilde{Re}_{\theta t}$:

$$P_{\theta t} = c_{\theta t} \frac{\rho}{t} (Re_{\theta t} - \widetilde{Re}_{\theta t})(1.0 - F_{\theta t}) \qquad (3\text{-}73)$$

$$t = \frac{500\mu}{\rho U^2} \qquad (3\text{-}74)$$

$$F_{\theta t} = \min\left\{\max\left[F_{wake}e^{-(y/\delta)^4}, 1.0 - \left(\frac{\gamma - 1/c_{e2}}{1.0 - 1/c_{e2}}\right)^2\right], 1\right\} \qquad (3\text{-}75)$$

$$\theta_{BL} = \frac{\widetilde{Re}_{\theta t}\mu}{\rho U} \qquad (3\text{-}76)$$

$$\delta_{BL} = \frac{15}{2}\theta_{BL} \qquad (3\text{-}77)$$

$$\delta = \frac{50\Omega d}{U}\delta_{BL} \qquad (3\text{-}78)$$

$$F_{wake} = e^{-(Re_\omega/10^5)^2} \qquad (3\text{-}79)$$

$$Re_\omega = \frac{\rho\omega y^2}{\mu} \qquad (3\text{-}80)$$

The constants for the equation are:

$$c_{\theta t} = 0.03, \ \sigma_{\theta t} = 2$$

$Re_{\theta t}$ in the $P_{\theta t}$ requires the third empirical correlation of this model:

$$Re_{\theta t} = \left[1173.51 - 589.428Tu + \frac{0.2196}{Tu^2}\right]F(\lambda_\theta), \ Tu \leq 1.3 \qquad (3\text{-}81)$$

$$Re_{\theta t} = 331.5[Tu - 0.5658]^{-0.671}F(\lambda_\theta), \ Tu > 1.3 \qquad (3\text{-}82)$$

with

$$F(\lambda_\theta) = 1 - \left[-12.986\lambda_\theta - 123.66\lambda_\theta^2 - 405.689\lambda_\theta^3\right]e^{-\left(\frac{Tu}{1.5}\right)^{1.5}}, \ \lambda_\theta \leq 0 \quad (3\text{-}83)$$

$$F(\lambda_\theta) = 1 + 0.275[1 - e^{-35\lambda_\theta}]e^{-\left(\frac{Tu}{0.5}\right)}, \ \lambda_\theta > 0 \qquad (3\text{-}84)$$

and

$$\lambda_\theta = \frac{\rho \theta^2}{\mu} \frac{dU}{ds} \qquad (3\text{-}85)$$

$$Tu = 100 \frac{\sqrt{2k/3}}{U} \qquad (3\text{-}86)$$

$$U = \sqrt{u^2 + v^2 + w^2} \qquad (3\text{-}87)$$

$$\frac{dU}{ds} = \frac{u}{U}\frac{dU}{dx} + \frac{v}{U}\frac{dU}{dy} + \frac{w}{U}\frac{dU}{dz} \qquad (3\text{-}88)$$

$$\frac{dU}{dx} = \frac{u}{U}\frac{du}{dx} + \frac{v}{U}\frac{dv}{dx} + \frac{w}{U}\frac{dw}{dx} \qquad (3\text{-}89)$$

$$\frac{dU}{dy} = \frac{u}{U}\frac{du}{dy} + \frac{v}{U}\frac{dv}{dy} + \frac{w}{U}\frac{dw}{dy} \qquad (3\text{-}90)$$

$$\frac{dU}{dz} = \frac{u}{U}\frac{du}{dz} + \frac{v}{U}\frac{dv}{dz} + \frac{w}{U}\frac{dw}{dz} \qquad (3\text{-}91)$$

dU/ds is the derivative of velocity magnitude with respect to the streamline direction. λ_θ is a pressure gradient parameter. Tu is the turbulence intensity.

The limiters are set for λ_θ, Tu, and Re_t:

$$-0.1 \leq \lambda_\theta \leq 0.1, \ Tu \geq 0.027, \ Re_t \geq 20$$

In Eq (3-81) and (3-82), θ presents on both sides and therefore the equation must be solved iteratively. An initial guess can be made using zero pressure gradient.

The boundary condition for γ equation is 1 at the flow inlet and zero normal gradient at walls. Physically, the intermittency factor equals 0 for laminar flows and 1 for turbulent flows. Obviously, this numerical usage does not follow the physical meaning. The treatment here is stated to preserve the original turbulence model's freestream turbulence decay rate[62].

The boundary condition for $\widetilde{Re}_{\theta t}$ equation is a value calculated from the correlation at the flow inlet that assumes $F(\lambda_\theta) = 1$ and zero normal gradient at walls.

3.4.3 Delayed Detached Eddy Simulation

The DDES formulation used in this work is based on the aforementioned low Re SST model. It modifies k equations by adding a length scale in the

dissipation term:

$$\frac{\partial \rho k}{\partial t} + \nabla \cdot (\rho \vec{U} k) = \nabla \cdot [(\mu + \sigma_k \mu_t)\nabla k] + P_k - \rho \sqrt{k^3}/l_{DDES} \quad \text{(3-92)}$$

The DDES length scale is defined as follows[115]:

$$l_{DDES} = l_{RANS} - f_d \max(0, l_{RANS} - l_{LES}) \tag{3-93}$$

$$l_{RANS} = \frac{\sqrt{k}}{\beta^* \omega} \tag{3-94}$$

$$l_{LES} = C_{DES}\Delta_{max} \tag{3-95}$$

$$C_{DES} = C_{DES1} \cdot F_1 + C_{DES2} \cdot (1 - F_1) \tag{3-96}$$

$$f_d = 1 - \tanh[(20r_d)^3] \tag{3-97}$$

$$r_d = \frac{\mu_t + \mu}{\rho \kappa^2 y^2 \sqrt{0.5(S^2 + \Omega^2)}} \tag{3-98}$$

where $C_{DES1} = 0.78$, and $C_{DES2} = 0.61$.

Δ_{max} is the maximum edge length of a cell:

$$\Delta_{max} = \max(\Delta x, \Delta y, \Delta z) \tag{3-99}$$

$\Delta x, \Delta y, \Delta z$ are grid spacing in x, y and z directions.

It is clear here that the low Re correction does not change the definition of l_{DDES}. It indirectly influences the calculation of l_{DDES} via μ_t.

3.5 Roughness Model

The law-of-the-wall for rough walls used is briefly described as follows, according to Ioselevich and Pilipenko[116]:

$$u^+ = \frac{1}{\kappa} \ln y^+ + B - \Delta B \tag{3-100}$$

and the downshift ΔB is formulated as follows:

(1) $h_s^+ \leq 2.25$, the hydraulically smooth, $\Delta B = 0$;   (3-101)

(2) $2.25 < h_s^+ \leq 90$, the transitional region,

$$\Delta B = \frac{1}{\kappa} \ln\left(\frac{h_s^+ - 2.25}{87.75} + C_s h_s^+\right) \times \sin[0.4258(\ln h_s^+ - 0.811)]; \tag{3-102}$$

(3) $h_s^+ > 90$, the fully rough region, $\Delta B = \frac{1}{\kappa} \ln(1 + C_s h_s^+);$ (3-103)

where C_s is the roughness constant (= 0.5 for uniform sand grain surface).

In the detailed implementation to the underlying SST model, an automatic

wall treatment[117] is used to model roughness effects via the ω boundary condition, which optimally blends the wall value of ω in the viscous sublayer and the log layer based on the near wall grid density. In the case of roughness, according to Langtry and Menter[118], the blending of sublayer and log layer value is not physically sensible when the sublayer is greatly disturbed, such as the fully rough cases. To overcome this deficiency, as well as to account for the blockage effects of the sand grain roughness, the cell wall distance is shifted by half of the roughness height, i.e., $y_{rough} = y + 0.5h_s$. In this way, u_τ and ω wall values are primarily determined from their log law formulations when the roughness height is sufficiently greater than the first layer height.

For the γ-Re_θ SST model, when roughness is simulated, the model uses an additional empirical correlation for roughness induced transition. It corrects the local transition momentum thickness, i.e., $\widetilde{Re}_{\theta t,rough} = f(\widetilde{Re}_{\theta t,smooth}, h_g)$, relying on the geometrical roughness height rather than the equivalent sand grain height, and then the obtained $\widetilde{Re}_{\theta t,rough}$ is used to calculate the new $Re_{\theta c}$ and F_{length} [119]. According to Langtry and Menter[118], it is improved from the correlation by Mayle[36] and validated against Pimenta's flat plat data[120] and Karlsruhe's roughened turbine blade data[121]. However, the validations for low Reynolds number external flow with low freestream turbulence intensities are not available.

Two more points are discussed here for the two SST models. First, it is known that the original high Reynolds number SST model tends to underestimate the skin friction, especially in fully rough cases, and an additional blending function by Hellsten and Laine[103] may be required. The two SST models used in this work have no such blending function. To investigate the consequence, a user defined function is written and implemented into the low Re SST model in the software. The results on the rough NACA 0012 aerofoil, which is investigated in Chapter 5, show 0.9% increase in the drag coefficient at $\alpha = 0°$ when $Re = 5 \times 10^4$ and $\alpha = 4°$ when $Re = 1.5 \times 10^5$. The results on skin friction coefficients also show no significant changes.

3.6 Post-Processing Technique

General post-processing, such as x-y plots, contour plots, vortex visualisations, and animations are generated through the built-in functions of ANSYS FLUENT, CFD-Post, Tecplot, MATLAB, and Gnuplot. For the non-general post-processing, substantial programming work is required, as described in the following sections.

3.6.1 Extraction of Transition Location

The low Re SST and γ-Re$_\theta$ SST model are able to model transitional flows, so that there is a region in the flow field that begins with transition onset and ends with transition complete. Because the two models deal with transition distinctly, a general approach is required to accomplish the comparison between the two. In the software's framework, it is possible to implement a same criterion for the transition onset that is used in the experimental study on laminar separation bubbles, as in Radespiel $et\ al.$[53]

The transition onset location is approximated by the location where normalised Reynolds shear stress reaches the threshold of 0.1% and shows a clear rise. For RANS results, the Reynolds shear stress is approximately as follows, via Boussinesq approximations:

$$\tau_{xy} = -\rho\overline{u'v'} = \mu_t \left(\frac{\partial u}{\partial y} + \frac{\partial v}{\partial x}\right) \tag{3-104}$$

DDES results directly use resolved $u'v'$ Reynolds shear stress. The normalised Reynolds shear stress is defined as $-\frac{\overline{u'v'}}{U_\infty^2}$, and $\overline{u'v'}$ is obtained via averaging processes described as follows.

3.6.2 Averaging process for DDES results

For a generic variable ϕ, for example instantaneous u, v, w, p, long-time averaging is used to obtain the mean:

$$\bar{\phi} = \frac{1}{t}\int_0^t \phi\,dt \tag{3-105}$$

The fluctuation component of velocity is defined as:

$$u' = u - \bar{u} \tag{3-106}$$

$$v' = v - \bar{v} \tag{3-107}$$

$$w' = w - \bar{w} \tag{3-108}$$

The resolved Reynolds shear stresses are defined as:

$$\overline{u'v'} = \frac{1}{t} \int_0^t u'v' \, dt \tag{3-109}$$

$$\overline{u'w'} = \frac{1}{t} \int_0^t u'w' \, dt \tag{3-110}$$

$$\overline{v'w'} = \frac{1}{t} \int_0^t v'w' \, dt \tag{3-111}$$

The resolved turbulence kinetic energy and turbulence intensity are defined as:

$$k = \frac{1}{2} (\overline{u'^2} + \overline{v'^2} + \overline{w'^2}) \tag{3-112}$$

$$Tu = 100 \frac{\sqrt{2k/3}}{U_\infty} \tag{3-113}$$

$$\overline{u'^2} = \frac{1}{t} \int_0^t u'u' \, dt \tag{3-114}$$

$$\overline{v'^2} = \frac{1}{t} \int_0^t v'v' \, dt \tag{3-115}$$

$$\overline{w'^2} = \frac{1}{t} \int_0^t w'w' \, dt \tag{3-116}$$

The result for DDES is 3D. Spanwise averaging is performed by arithmetically averaging the data on the 40 spanwise locations extracted.

The flow variables are saved in every time step. The raw data is exported to Tecplot and processed via a dedicated macro script, which performs the operations described above.

Chapter 4 RANS and DDES comparison for NACA 2415 Aerofoil with Experiment

RANS and DDES results are obtained on the NACA 2415 aerofoil with comparison to the experiment. The RANS models investigated are low Re SST and γ-Re_θ SST models, and the DDES model investigated is the low Re DDES-SST model. The investigation provides understanding for the capability of RANS models and DDES models for the simulation of laminar separation bubble at low Reynolds numbers.

4.1 Introduction

It is of importance to find a reliable method for low Re flow simulation subjected to LSB. The LSB involves separation and transition, so that the corresponding understanding on the models with the capability of transition modelling is necessary. In this work, the low Re SST and γ-Re_θ SST models for RANS models and the DDES-SST model with a low Re correction for DDES models are investigated. The test case is the NACA 2415 aerofoil with the experiment.

In this investigation the DDES model is proposed to incorporate a simple low Re correction (Eq 3-39 to Eq 3-46 and corresponding model constants on page 40) to the RANS part of the DDES-SST model. There are three reasons for this. Firstly, it is reasonable to hypothesis a DDES model to predict transition requires a transition sensitive RANS part. Secondly, no relevant results with such proposal have been published. Thirdly, the low Re correction is relatively simple and compatible with modern CFD codes.

The current work in this paper primarily presents RANS and DDES results on the NACA 2415 aerofoil at $Re = 1 \times 10^5$, and the comparison with the experiment by Genç[122]. The result using the DDES model is performed at $\alpha = 4°$ and 12°. From the comparison, the pros and cons of RANS and DDES models are discussed, as well as the importance of the low Re correction. The suggestions for the model improvements are also provided.

4.2 Mesh and Inflow Condition

The mesh has an overall C-type structured block plus an additional block for the blunt trailing edge. The RANS simulations use 2D meshes, with a farfield boundary located 20c away from the aerofoil. The total mesh elements is 66002, with mesh points of 100 in the wall normal direction and a total number of 411 on upper and lower surfaces. Fig. 4-1a shows the mesh near the aerofoil.

DDES uses 3D mesh that is generated by extruding spanwise the 2D RANS mesh. The spanwise length is 0.2c, with 40 mesh points distributed. The mesh includes total 2640080 elements. Fig. 4-1b shows the 3D mesh.

Both 2D mesh and 3D mesh satisfy $\Delta y^+ < 1$, checked after calcualtions. For DDES result at 12º, Δx^+ is less than 10, and Δz^+ reaches 48 on the leading edge and then reaches 25 near the reattachment line.

Table 4-1 shows the inflow condition. It is noted the two transition RANS models have distinct turbulence decay behaviour, and thus two different set of conditions are used. The Tu_∞ and μ_t/μ values are chosen to produce $Tu_\infty = 0.41\%$ near the aerofoil leading edge, which falls inside the range of 0.3% ~ 0.7% reported in the experiment. The DDES model adopts the same values for the low Re SST model. It is noted that, firstly the contours lines are in a half circular shape because a half circular upstream boundary is used, and secondly a change of 0.7% to 0.55% in Tu_{inlet} only results in a slight change on the bubble location for the γ-Re_θ SST model, because the turbulence intensity decayed only varies in a small amount (from 0.46% to 0.41%). The turbulence decay in the computational result may not represent the realistic. This is not a problem here as long as a same basis for numerical comparisons is established.
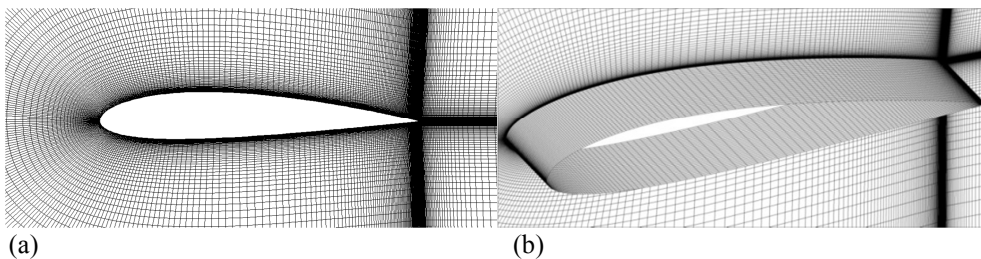

(a)   (b)
Fig. 4-1. (a) 2D mesh for RANS calculations, (b) 3D mesh for DDES calculations

Table 4-1. Inflow condition

Case	Tu	μ_t/μ	k	ω	U_∞(m/s)
Low Re SST DDES	0.5%	10	2.5×10^{-3}	17	8.1
γ-Re$_\theta$ SST	0.55%	10	3×10^{-3}	20	

4.3 Referred Experimental Data

In the experiment by Genç[122], a wing with a chord length of 180 mm and a span length of 290 mm was manufactured. The wing was composed of a foam core and a glass fibre shell. The accuracy for aerofoil coordinates was 0.1 mm. In the test, two end plates made from plexi-glass were attached to the wing. The pressure distribution and force measurement were conducted at four Reynolds numbers of 5×10^4, 1×10^5, 2×10^5, and 3×10^5. The pressure data was collected for 4 angles of attack, i.e., 0º, 4º, 8º, 12º. The pressure transducer took 1000 samples per second, and the mean pressure was processed by software. The force data was collected between angles of attack of −12º to 20º for 16.4s for each test, using a 3 components load cell system that located outside the wind tunnel. The sampling frequency was 1000 Hz, and the sampling time was 120s in each test. Mean forces, lift and drag were worked out after the measurement. Oil flow visualisations were conducted at the last three Reynolds numbers for angles of attack of 4º, 8º, 12º, and 15º. The separation bubble location and transition location were reported. The hot-wire measurement was further performed to understand the velocity fluctuation. The reported freestream turbulence intensity was about 0.3% at highest speeds and 0.7% at lowest speeds. The experiment estimated the blockage was less than 10% and no correction was performed on the data. However, Figure 7 in Genç[122] clearly shows the tested wing had a higher aspect ratio than reported. The interpretation on the experimental data, especially at high incidences, may need care.

4.4 RANS Result

4.4.1 Mesh Sensitivity

Table 4-2 shows the mesh sensitivity for RANS calculations. The refined 2D mesh is generated by reducing the mesh spacing uniformly by 2, leading to a total number of mesh points of 264008.

The result shows a clear difference between the two models, i.e., C_l by the γ-Re$_\theta$ SST model is 19% higher than the one by the low Re SST model. This is attributed to the different flow feature modelled, which is also presented Table 4-2: on the upper surface, although the low Re SST model predicts a similar separation location as to the γ-Re$_\theta$ SST model, the flow has no reattachment to form a bubble. The separation and reattachment locations vary by 1% chord length due to the mesh refinement, and this is satisfactory.

On the other hand, the low Re SST model shows 4% change on C_l and 7% change on C_d, compared to 1% and −1% for the γ-Re$_\theta$ SST model, due to mesh refinement. Therefore the low Re SST model shows a larger sensitivity on the mesh size than the γ-Re$_\theta$ SST model. These sensitivities are still acceptable for the current investigation.

Table 4-2. Mesh sensitivity for RANS at $\alpha=2°$

	Mesh elements	C_l	C_d	Separation	Reattachment
Low Re SST	66002	0.3963	0.0182	0.42	No
	264008	0.3800	0.0195	0.41	No
γ-Re$_\theta$ SST	66002	0.4704	0.0187	0.40	0.80
	264008	0.4729	0.0186	0.41	0.79

4.4.2 Lift and Drag

The computed lift and drag are compared to the experiment in Fig. 4-2. The general trend for lift and drag curves predicted by the two models shows an agreement.

The drag curve shows the two models predict similar drag in a wide range of incidence. The data between $\alpha = 2°$ and $12°$ shows a good correlation with the experimental data. At negative incidence and higher incidence, the deviation from the experimental data gradually becomes large.

By comparison, the lift curves predicted by the two models only follow the experiment data well between $\alpha = 2°$ and $8°$. At higher incidences, the lift is under-predicted. At lower incidences, the lift is also under-predicted. The lift predicted by the γ-Re$_\theta$ SST model is obviously larger than that for the low Re

SST model between $\alpha = -2°$ and 14° by 0.04 ~ 0.07. However, this difference shows no superiority for the γ-Re$_\theta$ SST model over the low Re SST model, because it is not closer to the experimental data.
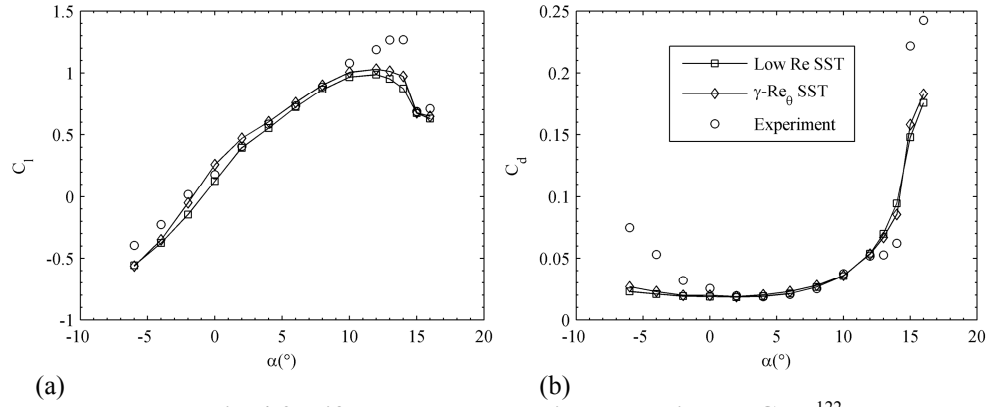

(a)   (b)

Fig. 4-2. Lift and drag comparison, experiment: Genç[122]

4.4.3 Bubble Location

The discrepancy between the numerical result and the experimental result at lower and higher incidences is expected to be the limited capability of the two models on the bubble location prediction, as can be shown in Table 4-3 at the two highest incidences. The difference between the two models may be explained from the fundamental formulation. The γ-Re$_\theta$ SST model incorporates a correction to intensify the turbulence production after a separation, see Eq. (3-69) to Eq. (3-72), so that the model is more likely to predict a reattachment and maintain a bubble to higher incidences.

Table 4-3. Bubble location comparison

Case	α (°)	Separation	Reattachment
Experiment[122]	4	0.3	0.72
	8	0.2	0.6
	12	0.1	0.42
	15	0.05	0.2
Low Re SST	4	0.34	0.65
	8	0.18	0.43
	12	0.04	0.2
	15	0.03	No
γ-Re$_\theta$ SST	4	0.33	0.67
	8	0.23	0.56
	12	0.03	0.2
	15	0.02	No

4.5 DDES and RANS: $\alpha = 4°$

4.5.1 Lift and Drag History and RANS Convergence

Fig. 4-3 shows the lift and drag history for DDES simulations. It is clear that after approximately 0.4s the flow field becomes statistically converged, and this part of data is averaged for the comparisons in succeeding sections.
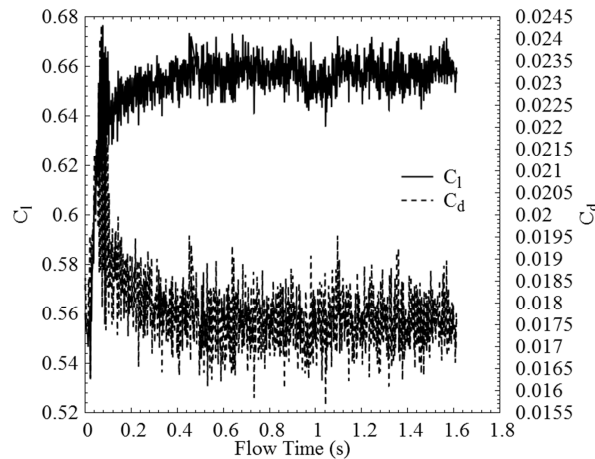

Fig. 4-3. The time history of lift and drag coefficients, DDES, α=4º

The calculation using the low Re SST model is found difficult to converge. A series of attempts have been performed using various combinations of pseudo time steps and pressure-velocity under relaxation factors. It is observed that the solution is likely to appear periodically oscillations in residual, lift, or drag histories, when using lower pseudo time steps. On the other hand, lower pressure-velocity under relaxation factors in some cases can smooth out oscillations. However, a well-converged steady state solution has not been obtained. Then, unsteady calculations have been performed. Three different time steps, i.e., 0.0008s, 0.0004s, and 0.0002s have been tested. It is found the solution of the 0.0008s case eventually converges to steady state, and it is selected for the comparison. The other two produce oscillations of large amplitude. Averaging may be necessary to obtain the mean.

Although not presented, the calculations at many other incidences have a similar difficulty to converge. URANS results are obtained for the comparisons. In some of the URANS results, vortex shedding is resolved, and averaging the flow field provides a bubble.

By comparisons, the calculation using the γ-Re$_θ$ SST model shows no such difficulties. A converged steady state solution is obtained, as well as for other incidences.

4.5.2 Mean Lift and Drag

The mean lift and drag by the DDES model are obtained by time-averaging the lift and drag from 0.4s to 1.6s in the flow time, as shown in Table 4-4. The results are compared to the 2D RANS result and the experimental data. The 5% uncertainty reported in the experiment is included in the comparison.

The results by the DDES model deviate the farthest from the experimental lift, whereas the drag prediction is acceptable. The low Re SST model produces the best drag, whereas the γ-Re$_θ$ SST model produces the best lift. No model predicts the best lift and the best drag at the same time. The experimental data is uncorrected for the blockage and wind tunnel wall effects. The close match in the drag may be coincidence.

Table 4-4. (Mean) C_l and C_d comparison, $α$=4º

Case	C_l	C_d
Experiment[122]	0.5856 (0.5563~0.6149)	0.01859 (0.01766~0.01952)
Low Re SST	0.5531 (-6%)	0.01902 (+2%)
γ-Re$_θ$ SST	0.6029 (+3%)	0.02013 (+8%)
DDES	0.6572 (+12%)	0.01759 (-5%)

4.5.3 Mean C_p and C_f comparison

Fig. 4-4a shows the comparison on the pressure distribution. It is clear that a kink shape exists on the experimental curve near approximately 0.3c where the expected laminar separation is. The curve afterwards does not level off perfectly to present a well-known plateau shape for laminar separation bubbles.
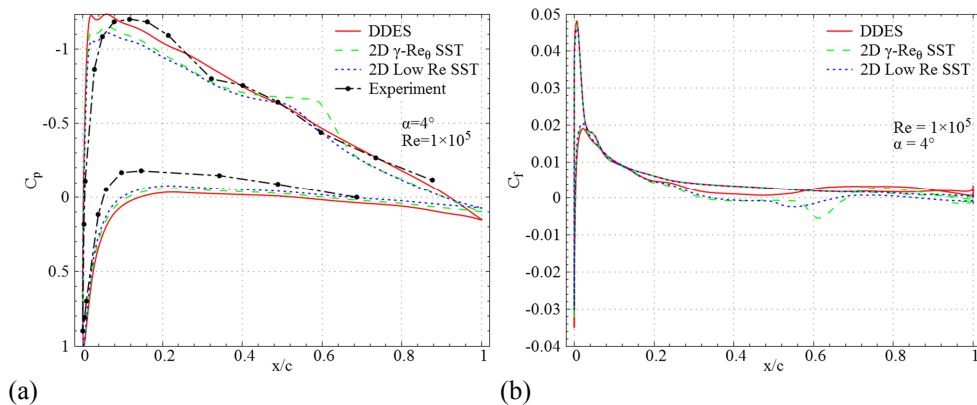

(a)　　　　　　　　　　　　　　　　(b)

Fig. 4-4. Comparisons on C_p and C_f, $α$=4º

The result by the γ-Re$_\theta$ SST model predicts a lower suction peak and a more upstream peak location, as compared to the experiment. The curve also deviates from the experimental data after approximately 0.42c where the plateau for the γ-Re$_\theta$ SST model occurs. The comparison for the data on the lower surface shows also a deviation.

The result by the low Re SST model predicts an overall similar pressure and skin friction distribution to those by the γ-Re$_\theta$ SST model. Nevertheless, the pressure plateau is less notable.

The result by the DDES model shows a similar shape and no much deviation from the result from RANS on the lower surface, whereas a clear difference is noted on the upper surface. The suction peak predicted is higher and closer to the experimental data, whereas the peak location remains the same as RANS. More importantly, neither a kink nor a plateau occurs on the pressure distribution.

The skin friction distribution is analysed further, see Fig. 4-4b. No experimental data is available for comparison. It is clear the result by the DDES model predicts no separation and reattachment, as there is no change of sign in skin friction. Nevertheless, the result does show a clear rise after approximately 0.5c, which mimics the natural transition on a flat plate. By comparisons, separation and reattachment are predicted by the two RANS models with a distinct "tick" shape, and the one for the low Re SST model is less notable than that for the γ-Re$_\theta$ SST model.

Obviously, skin friction data correlates pressure data on the influence of the bubble. Besides the bubble, the two RANS models further predict a clear trailing edge separation, which is not predicted by the DDES model. The separation should be a turbulent separation.

4.5.4 Mean Laminar Separation Bubble

The bubble location is compared with the experimental data in Table 4-5. The beginning of the bubble, where the laminar separation occurs, is over-predicted by 0.04c and 0.03c for the low Re SST and γ-Re$_\theta$ SST models,

respectively. The end of the bubble, where the reattachment occurs, is under-predicted by 0.07c and 0.05c, respectively. The trailing edge separation occurs respectively at 0.87c and 0.97c for low Re SST and γ-Re$_\theta$ SST models. No experimental data is available. As mentioned earlier, the DDES model predicts neither a bubble nor a trailing edge separation.

In terms of bubble prediction, the comparison in Fig. 4-4a, Fig. 4-4b, and Table 4-5 show a consistency. This is also expected to explain the difference on the lift and drag comparison, shown earlier in Table 4-4.

Table 4-5. (Mean) bubble location comparison, α=4°

Case	Laminar separation	Transition	Reattachment	Turbulent separation
Experiment[122]	0.30	0.62	0.72	Not provided
Low Re SST	0.34	0.5	0.65	0.87
γ-Re$_\theta$ SST	0.33	0.54	0.67	0.97
DDES	no	≈ 0.5	no	no

4.5.5 Mean Flow Field

The mean flow field of the DDES result is compared with those using low Re SST and γ-Re$_\theta$ SST models from Fig. 4-5 to Fig. 4-7. Flow streamlines are plotted to visualise flow features such as separation bubbles. Normalised resolved Reynolds shear stress and turbulence kinetic energy are plotted to aid the comparison on the development of turbulence. It is found the Reynolds shear stress and turbulence kinetic energy grows from a location near mid-chord on the upper surface, which is similarly predicted by all three models.

On the bubble prediction, it is found that the DDES model predicts no bubble, which is consistent with previous interpretation from pressure and skin friction results. Both low Re SST and γ-Re$_\theta$ SST models predict a bubble, and the one predicted by the γ-Re$_\theta$ SST model shows a larger height and shorter distance from the maximum height location to the reattachment point. The height of the bubble is much smaller than the streamwise length, approximately 2.8% of that. The bubble is also asymmetry about the maximum height location. The length from the separation point to the transition onset is longer than that from the transition onset to the reattachment. A similar trend is reported from the experiment, see Table 4-5.
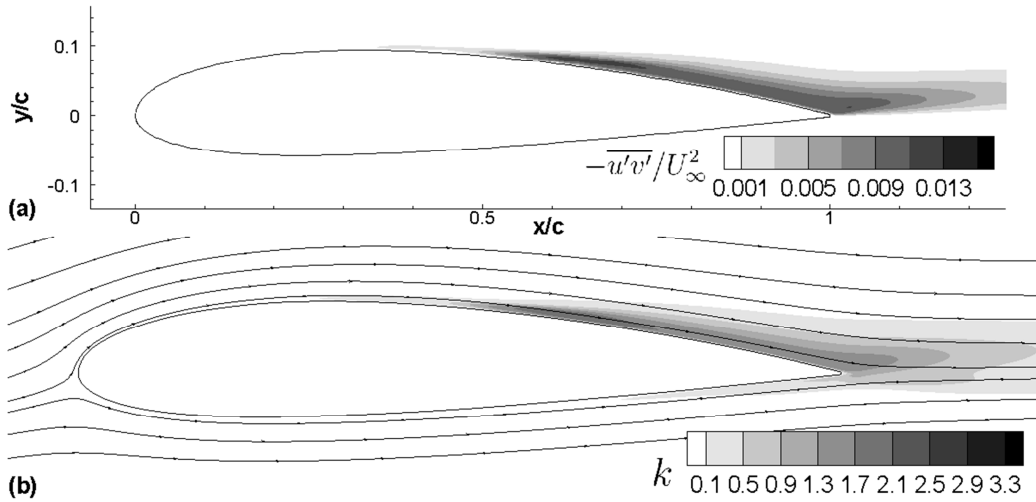
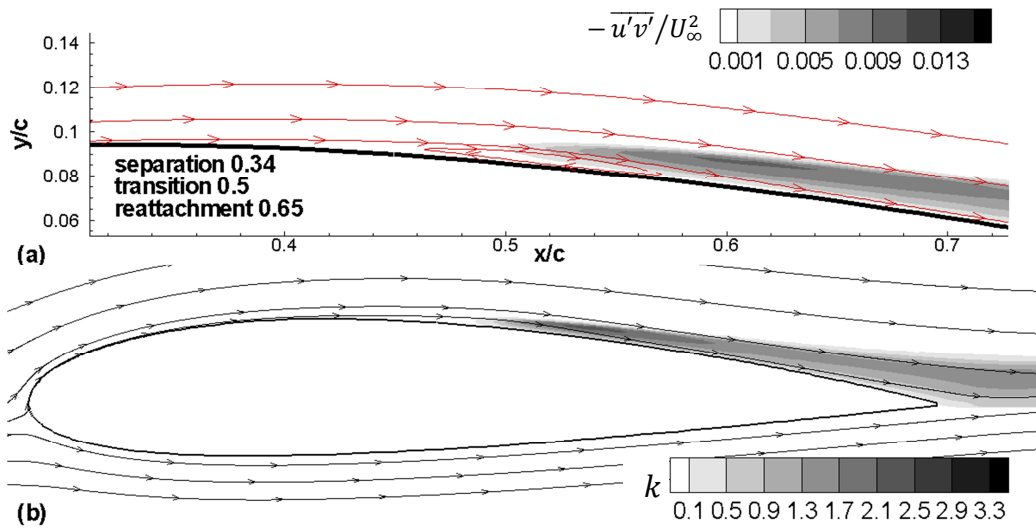**Fig. 4-5. The mean flow field for DDES at $\alpha=4°$, (a) resolved $-\overline{u'v'}/U_\infty^2$, (b) resolved k**

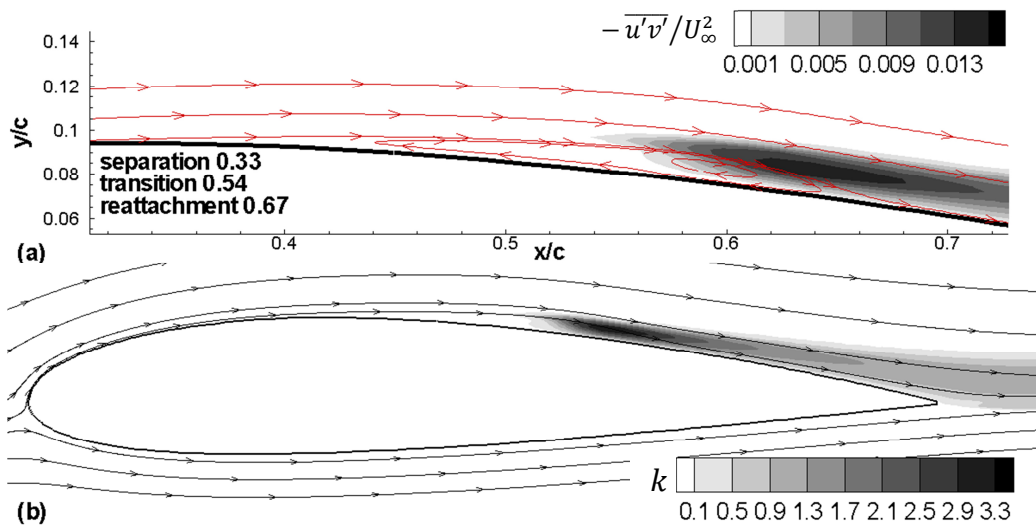**Fig. 4-6. The flow field for low Re SST at $\alpha=4°$, (a) $-\overline{u'v'}/U_\infty^2$, (b) k**

Fig. 4-7. The flow field for γ-Re$_\theta$ SST at $\alpha=4°$, (a) $-\overline{u'v'}/U_\infty^2$, (b) k

4.5.6 Instantaneous Flow Field

Overall, the flow undergoes periodic changes on the upper surface and the lower surface. The representative motion of vortex structures is shown in Fig. 4-8.

On the upper surface, a spanwise extended vortex A can be found after the 2D attached boundary layer, as shown in Fig. 4-8a. This vortex A presents a spanwise non-uniformity, and it is shed from the upstream shear layer. In the following time increment, this vortex travels gradually downstream and disintegrates gradually into smaller vortex structures, as marked from Fig. 4-8a to Fig. 4-8d. In Fig. 4-8c, a new vortex A' can be identified upstream. Then in Fig. 4-8e, the flow recovers to the state shown in Fig. 4-8a. The vortex A refers to the vortex A_1 in Fig. 4-8a, and again a new vortex A'' can be identified upstream. Based on the time evolving from Fig. 4-8a to Fig. 4-8e, the period of the shedding of vortex A is approximately 0.004s. This is checked by examining the flow pictures in a smaller time interval of 0.0002s between Fig. 4-8a and Fig. 4-8c.

The vortex A_1 is better to be described as vortex groups, because the vortices shows three dimensionality and randomness in shapes, which is the sign for turbulent flow. The vortex A_1 continues travelling downstream. In Fig. 4-8e, it becomes the vortex A_2 in Fig. 4-8a. The vortex A_2 keeps travelling downstream-wise and becomes more and more scattered. Once again, in Fig. 4-8e, it becomes the vortex A_3 in Fig. 4-8a. The vortex A_3 then travels downstream and finally moves into the wake. Through the evolvement of vortex structures, the flow on the upper surface clearly undergoes laminar, turbulent states, and the transitional state in between.

The instantaneous flow pictures for the DDES result shows a transition process. The region that the vortex structures become scattered, 3D and randomness correlates with the location where resolved turbulence kinetic energy and resolved normalised u'v' stress grow significantly in Fig. 4-5.
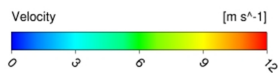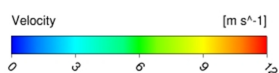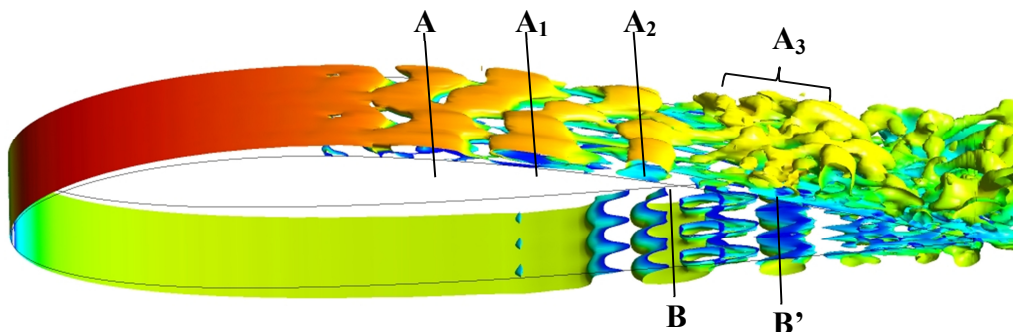
(a)

(b)

(c)

(d)
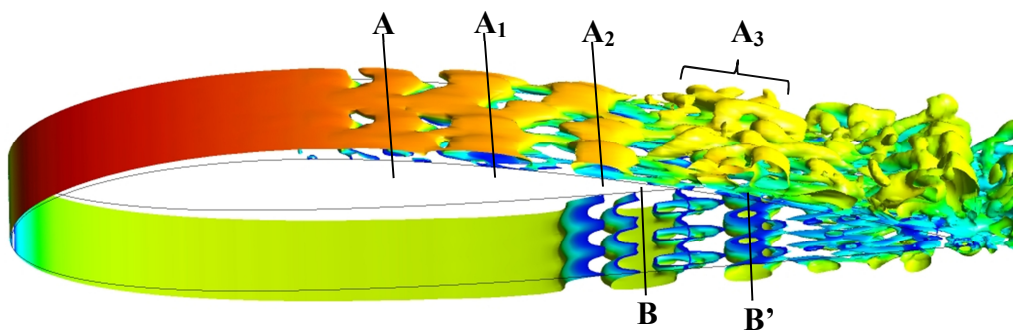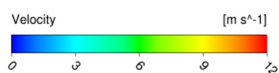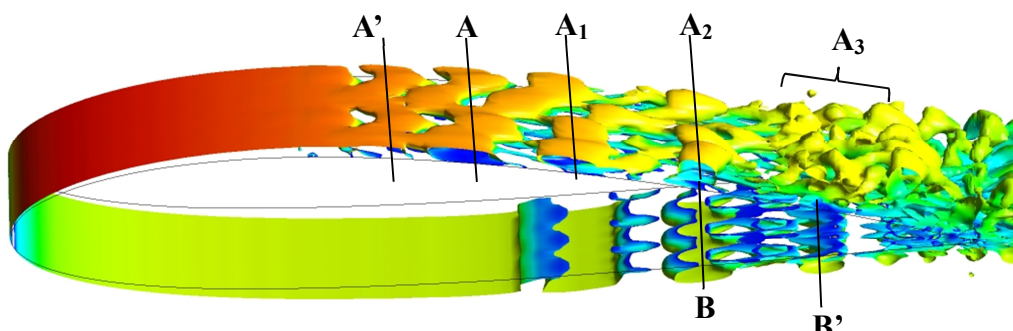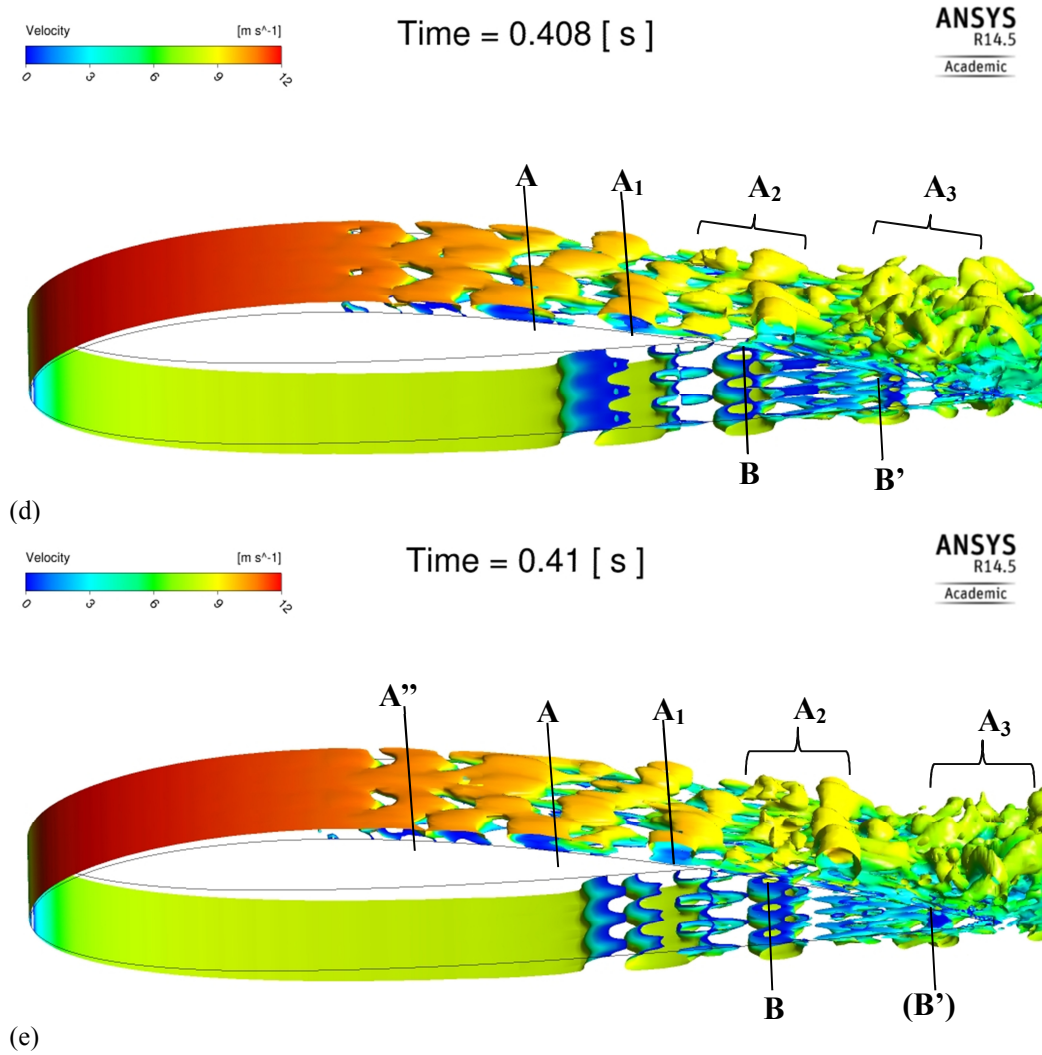
(e)

Fig. 4-8. Vortex structures visualised by q-criterion iso-surfaces, q ≈ 0.5, coloured by velocity magnitude, α=4°

On the lower surface, a similar scenario happens. Vortex *B* is identified in Fig. 4-8a. It also shows spanwise non-uniformity. In Fig. 4-8a, the vortex *B'* is the vortex *B* travelled downstream from Fig. 4-8e. It then disintegrates and can hardly be found in In Fig. 4-8e. One difference from vortex *A* is that, vortex *B* shows a larger period of shedding. The time from Fig. 4-8a to Fig. 4-8e gives a period of 0.008s.

The instantaneous flow pictures on the lower surface are again consistent with the resolved turbulence kinetic energy and resolved normalised u'v' stress in Fig. 4-5.

It is interesting to note the vortex shedding found in the instantaneous flow is responsible for the transition process. Fig. 4-9 further shows the instantaneous

and mean x-wall-shear-stress. It can be found although the vortex shedding leads to small areas of negative x-wall-shear-stress, its effects are averaged out in the mean result, as well as the spanwise averaged result. On the other hand, it is also found that the location where the vortex shedding occurs is approximately 0.32c, similar to the separation location for other models in Table 4-5.

Overall at $\alpha = 4º$, for DDES results, although an acceptable prediction on lift and drag is also obtained, the incapability on the prediction of the separation bubble desires further improvements and investigations for the model.
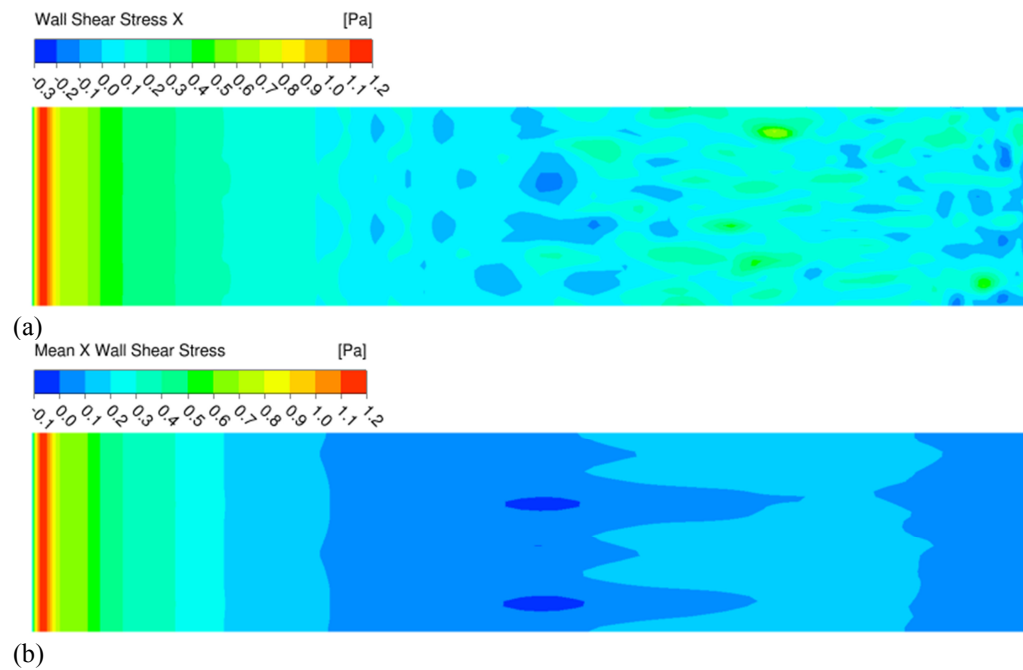

(a)

(b)

Fig. 4-9. Instantaneous (a) and mean (b) x wall shear stress, $\alpha=4º$

4.6 DDES and RANS: $\alpha = 12°$

4.6.1 Lift and Drag History and RANS Convergence

Fig. 4-10 shows the lift and drag history for DDES simulations. It is clear that for 12°, there is no apparent starting process. Comparing to 4°, the time history of lift and drag evolvement in the first 0.4s show no clear influence of the starting solution. Time-averaging statistics are still collected after the initial 0.4s. The end of time-averaging has been carefully tested at various locations, and the test shows the ending location only leads to insignificant change on the mean statistics. The final choice is the moment when 5 periods can be just included.
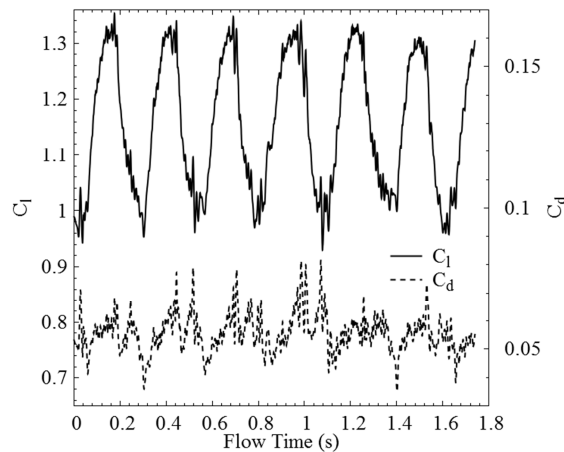
Fig. 4-10. The time history of lift and drag coefficients, DDES, α=12º

Fig. 4-11 shows the Fast Fourier Transform (FFT) analysis on lift and drag histories from 0.4s to 1.74s flow time. A peak frequency of 3.8 Hz is observed for both lift and drag analysis.
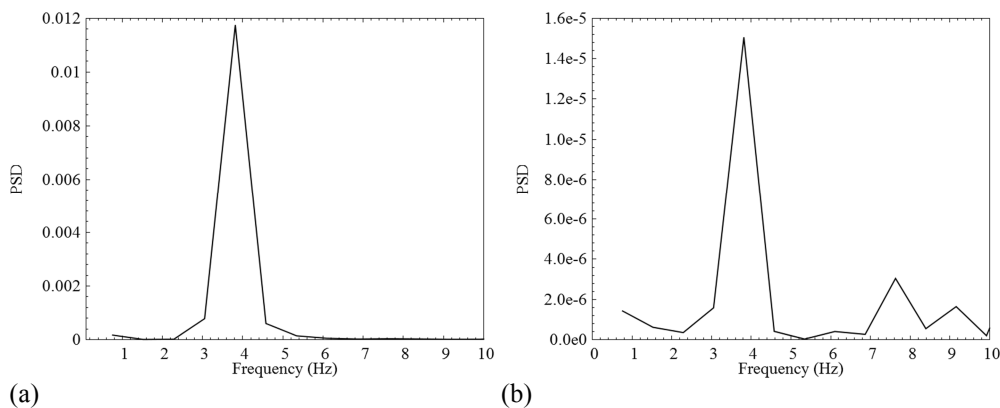

(a)   (b)

Fig. 4-11. FFT results of (a) C_l and (b) C_d, α=12º, PSD: Power Spectral Density

63

At $\alpha = 12°$, the RANS calculation by low Re SST and γ-Re$_\theta$ SST models all converges to steady state.

4.6.2 Mean Lift and Drag

The mean lift and drag are obtained by time-averaging lift and drag from 0.4s to 1.74s flow time, as shown in Table 4-6, compared to the 2D RANS result and the experimental data.

At this angle of attack, the DDES model predicts the best lift whereas the worst drag, different to the case at 4°. Comparing to low Re SST and γ-Re$_\theta$ SST models, the DDES model at this higher angle of attack justifies itself from the lift prediction. However, similar to the cases at 4°, none of the models predict the best lift and drag at the same time.

Table 4-6. (Mean) C_l and C_d comparison, α=12°

Case	C_l	C_d
Experiment[122]	1.1889 (1.1271~1.2507)	0.05191(0.04921~0.05461)
Low Re SST	0.9866 (-17%)	0.05392 (+4%)
γ-Re$_\theta$ SST	1.03 (-13%)	0.05348 (+3%)
DDES	1.1552 (-3%)	0.05607 (+8%)

4.6.3 Mean C_p and C_f Comparison

Fig. 4-12a shows the C_p and C_f comparisons at $\alpha = 12°$. The prediction by low Re SST and γ-Re$_\theta$ SST models are nearly the same other than the bubble location, while the DDES model predicts a suction peak 0.4 higher. All simulation results seem to predict a higher suction peak than the experimental data, however the measured data in the experiment may be insufficiently dense near the leading edge, which can be observed in Fig. 4-12a.

The kink shape is observed on the upper surface pressure curve for all simulations. This implies the prediction of laminar separation bubbles. Similar to the cases at $\alpha = 4°$, the low Re SST model predicts a less notable pressure plateau than the γ-Re$_\theta$ SST model, the experimental data presents no perfect plateau shape, and the simulation results for the lower surface curve imperfectly match the experimental data, although better than the cases at $\alpha = 4°$.

The results on the skin friction in Fig. 4-12b confirm the existent of laminar separation bubbles, based the observation of the "tick" shape. The result by the γ-Re_θ SST model is distinct once again for its deep valley of the tick.

Other than the bubble, the results also indicate a separation occurs near the mid-chord. This should be a turbulent separation and is predicted in all three cases.
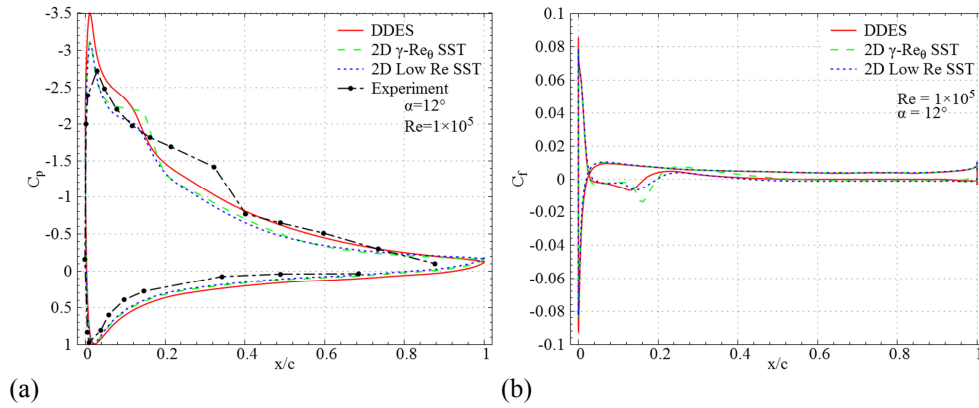

Fig. 4-12. C_p and C_f comparison, α=12°

4.6.4 Mean Laminar Separation Bubble

Table 4-7 shows the comparison on the bubble location. It is notable that, different to the case at $\alpha = 4°$, the DDES model predicts a bubble, and the bubble location is close to those predicted by low Re SST and γ-Re_θ SST models. This leads to the interpretation that the DDES model may only predicted bubble at sufficiently high incidences.

Table 4-7. (Mean) bubble location comparison, α=12°

Case	Laminar separation	Transition	Reattachment	Turbulent separation
Experiment[122]	0.12	0.3	0.42	Not provided
Low Re SST	0.04	0.11	0.20	0.41
γ-Re_θ SST	0.03	0.12	0.20	0.53
DDES	0.03	N/A	0.16	0.51

The low Re SST model once again shows an overall consistent result with the γ-Re_θ SST model with the difference on the final turbulent separation location. It can be concluded that for both 4° and 12° cases, the simulations by low Re SST and γ-Re_θ SST models are consistent, while their difference from the experimental data always exists and becomes larger at $\alpha = 12°$.

The reason for the difference between simulations and the experiment on the bubble prediction may be the discrepancy on the prediction of laminar separation near the leading edge. From Table 4-7, the experimental data shows flow separates at 0.12c, whereas all simulations show 0.03c or 0.04c. This location is much earlier than the experimental one, subsequently earlier transition, and a shorter bubble.

It is impossible to obtain the transition location from the DDES result using the normalised Reynolds shear stress, as discussed in the next section.

4.6.5 Mean Flow Field

Similar to the 4° cases, Fig. 4-13 to Fig. 4-15 compares the normalised Reynolds shear stress and turbulence kinetic energy predicted by the three models. It is clear all three simulations show consistent flow field features: a small separation bubble occurs near the leading edge and a turbulent separation occurs at approximately mid-chord.

The shape of the bubble is overall shorter than that for 4°. The height remains almost the same. The distance between the separation and the transition onset remains larger than that between the transition onset and the reattachment. The bubble predicted by the γ-Re_θ SST model remains taller than that for the low Re SST model. The bubble predicted by the DDES model is a result through time-averaging. The instantaneous flow changes in each time moment, as shown in the next section.

The low Re SST and γ-Re_θ SST models predict similar distribution of Reynolds shear stress and turbulence kinetic energy, while the γ-Re_θ SST model predicts higher Reynolds shear stress and turbulence kinetic energy near the transition location. The result by the DDES model is not possible to be compared to that for the RANS models. It is found that, through the long-time averaging, the resolved Reynolds shear stress near the bubble is negative, whereas positive for RANS result. The method to define the transition location is not applicable for the negative Reynolds shear stress. The transition location for DDES is thus not available in Table 4-7.

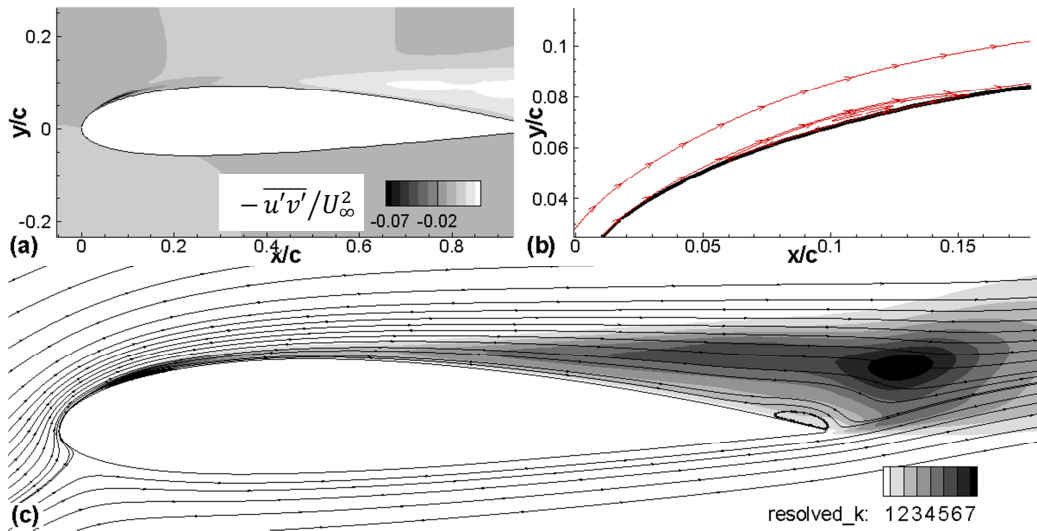**Fig. 4-13. The mean flow field* for DDES at α=12º, (a) resolved $-\overline{u'v'}/U_\infty^2$, (b) zoomed view of the bubble, (c) resolved k**

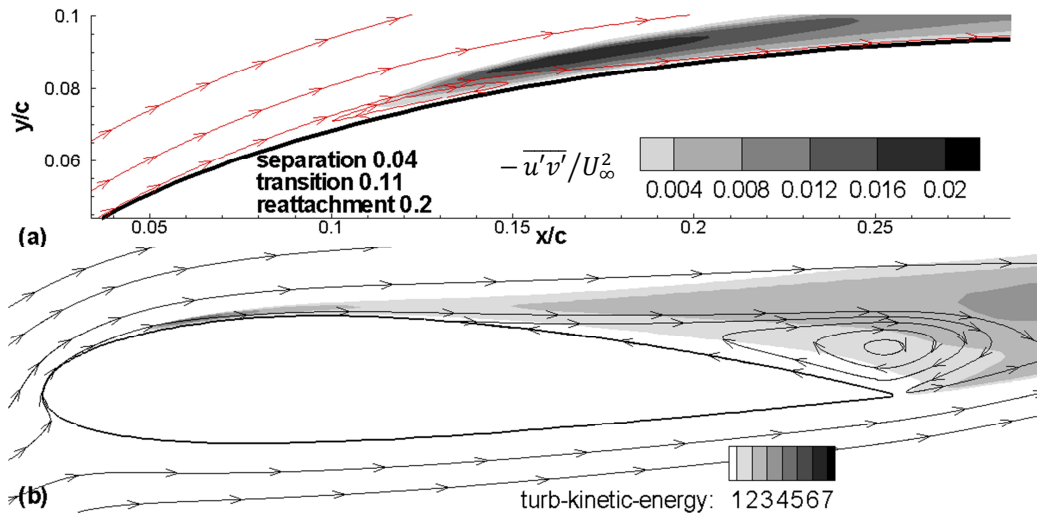* long time averaged result

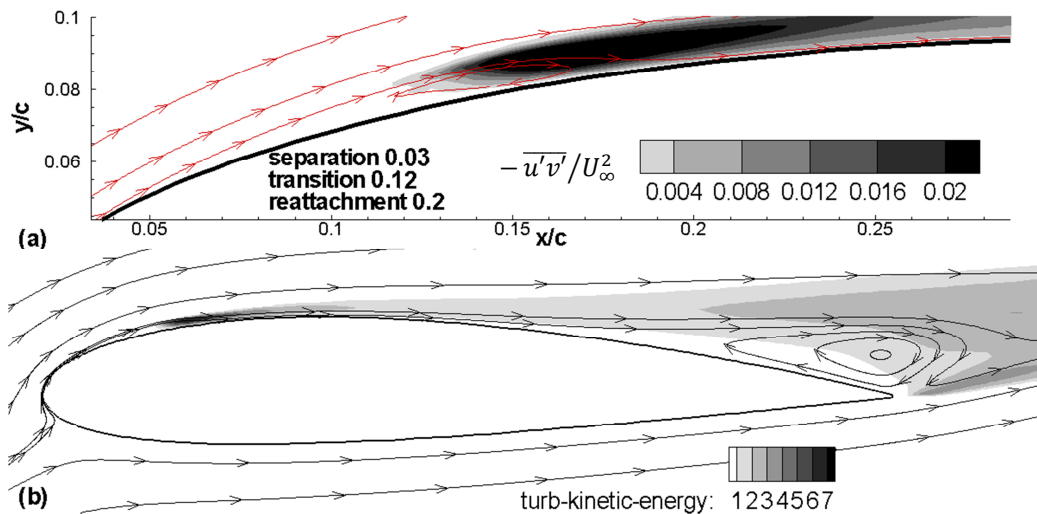**Fig. 4-14. The flow field for low Re SST at α=12º, (a) $-\overline{u'v'}/U_\infty^2$, (b) k**

Fig. 4-15. The flow field for γ-Re$_\theta$ SST at α=12º, (a) $-\overline{u'v'}/U_\infty^2$, (b) k

A more appropriate averaging may be phase-averaging. According to the instantaneous results presented in the next section, the flow undergoes periodic change. However, this operation is impossible due to the shortage in the hard disk storage to store sufficient samples.

The turbulent separation from approximately mid-chord has a much larger scale than the separation bubble. It occupies the entire region after the mid-chord and greatly thickens the boundary layer thickness. While the result by low Re SST and γ-Re_θ SST models shows a consistency, the result by the DDES model obviously presents a much shallower recirculated separation. A closer examination at the skin friction plot in Fig. 4-12b shows although negative skin friction values are observed, the magnitude for the DDES model is only at an order of $O(10^{-4})$. Comparing to the order of $O(10^{-3})$ by low Re SST and γ-Re_θ SST models, the DDES model obviously predicts weaker reversed flow. The higher lift for the DDES model can be the result of this weaker separation, as can be found in Table 4-6.

4.6.6 Instantaneous Flow Field

The instantaneous flow field is more complex than that for 4º. The difference is the vortex shedding process and the vortex evolvement. The vortex shed can be in two- or three- dimensional forms. When travelling downstream-wise, the vortex initially spanwise extends and then disintegrates into scattered vortices, i.e., becomes 3D. The area of separation and attachment also changes as to time, leading to a periodic change in the flow, as well as in the lift and drag shown earlier in Fig. 4-10.

Flow pictures in one period (i.e., physical time 1.11s-1.364s) are presented in Fig. 4-16. The flow in Fig. 4-16k recovers to the state in Fig. 4-16a. Vortex *A* is marked as the identification of periodic flow features. Approximately, Fig. 4-16k recovers the location of vortex *A* in Fig. 4-16a. The 9 moments in between, i.e., 1/10 to 9/10 of a period, are presented from Fig. 4-16b to Fig. 4-16j. The observations may be summarised as follows:
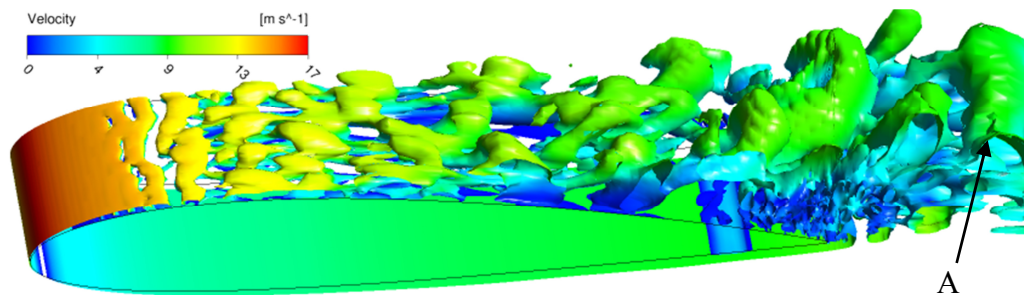
(1) The flow on a portion of upper surface near the leading edge and the whole lower surface presents as attached flows. The flow on the lower surface

shows steady and attached, whereas the attached flow on the upper surface near the leading edge shows a substantial change in chordwise length with respect to the flow time.
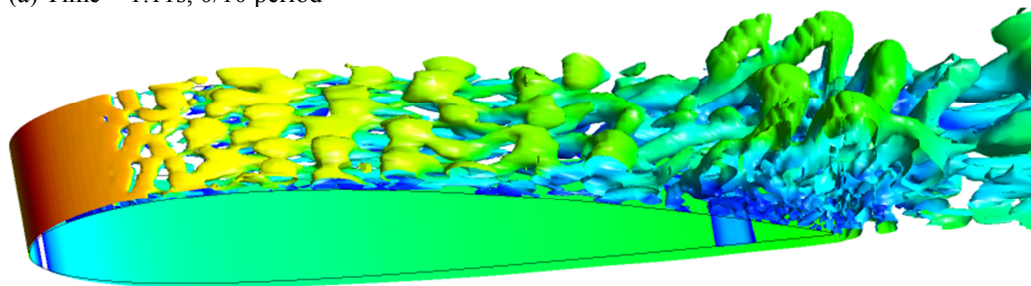
(2) 3D and fine vortex structures always present in the location near the upper surface trailing edge.

(3) The common features for these flow pictures are the vortex shedding from the vortex sheet near the leading edge and the evolvement from 2D to 3D of these vortices.

(4) The periodic change occurs in the upper surface flow. From Fig. 4-16a to Fig. 4-16e, the vortex shed travels downstream from approximately 0.19c to 0.6c, and behaves 3D. Then in Fig. 4-16e and Fig. 4-16f, a vortex sheet grows. In the following Fig. 4-16f to Fig. 4-16h, two vortex sheets and two vortex shedding zone can be found. From Fig. 4-16i to Fig. 4-16k, the second vortex sheet disappears, and the vortices shed becomes 3D. The vortex sheet is believed to be the identification for attached boundary layer or the steady part of separated shear layer.

(a) Time = 1.11s, 0/10 period

(b) Time = 1.126s, 1/10 period

(c) Time = 1.152s, 2/10 period

(d) Time = 1.178s, 3/10 period

(e) Time = 1.1206s, 4/10 period

(f) Time = 1.232s, 5/10 period

(g) Time = 1.258s, 6/10 period

(h) Time = 1.284s, 7/10 period

(i) Time = 1.31s, 8/10 period

(j) Time = 1.336s, 9/10 period

A
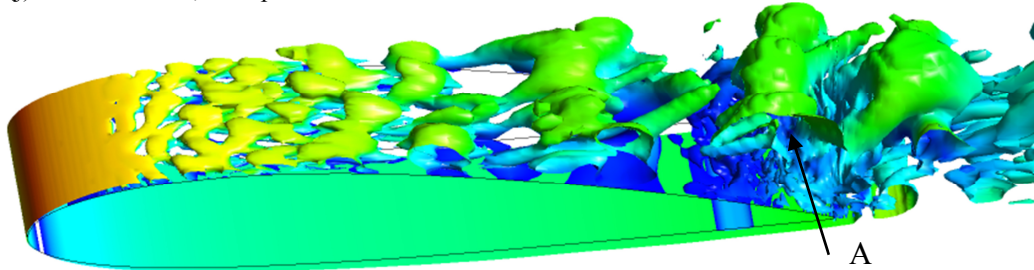
(k) Time = 1.364s, 10/10 period

Fig. 4-16. Vortex structures visualised by q-criterion iso-surfaces, q ≈ 5, coloured by velocity magnitude, α=12º

The period for the vortex shedding is found to be 0.0014s. Another observation is that the laminar to turbulent transition is accompanied with the change from 2D vortices to 3D vortices.

The streamlines plotted in Fig. 4-17 on the mid-span plane offers a better representation of the flow separation and attachment. A safe interpretation of the result should be based on the streamlines outside the near wall region. The observation may be summarised as follows:

(1) Two flow separation regions co-exist on the upper surface. One locates near the leading edge and looks like a separation bubble. Another one locates near the trailing edge and can extend up to mid-chord in some moments.
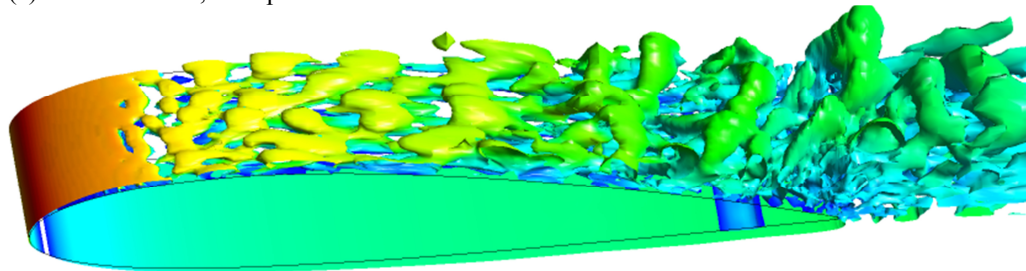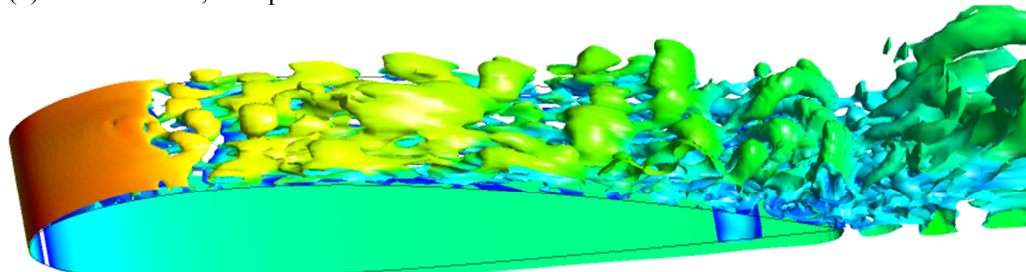
71

(a) Time = 1.11s, 0/10 period

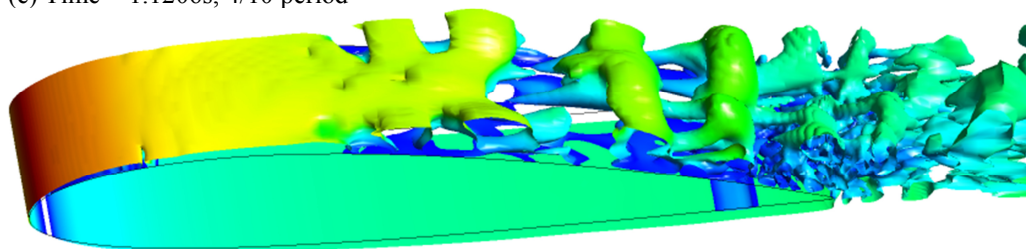(b) Time = 1.126s, 1/10 period

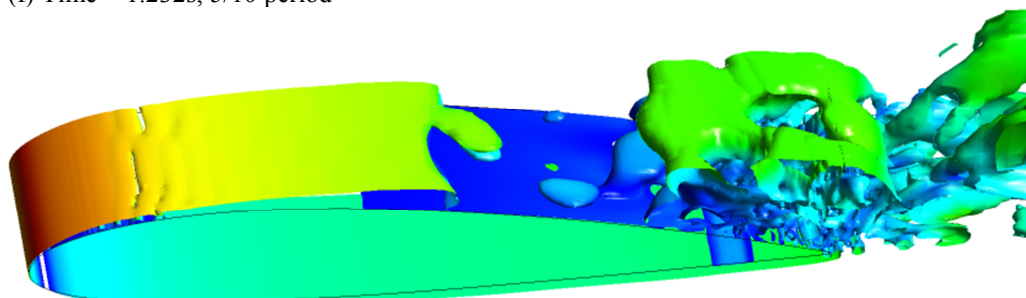(c) Time = 1.152s, 2/10 period
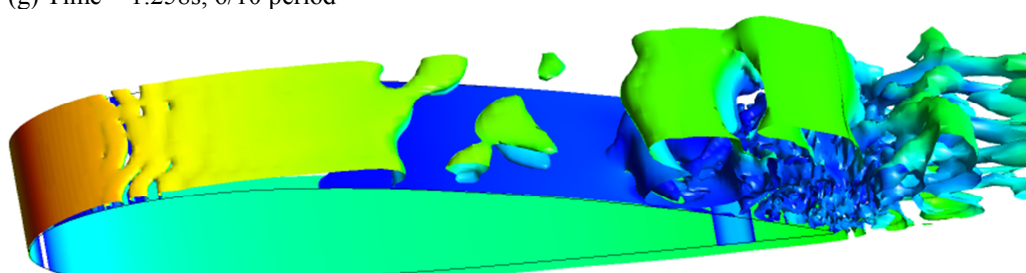
(d) Time = 1.178s, 3/10 period

(e) Time = 1.1206s, 4/10 period

(f) Time = 1.232s, 5/10 period
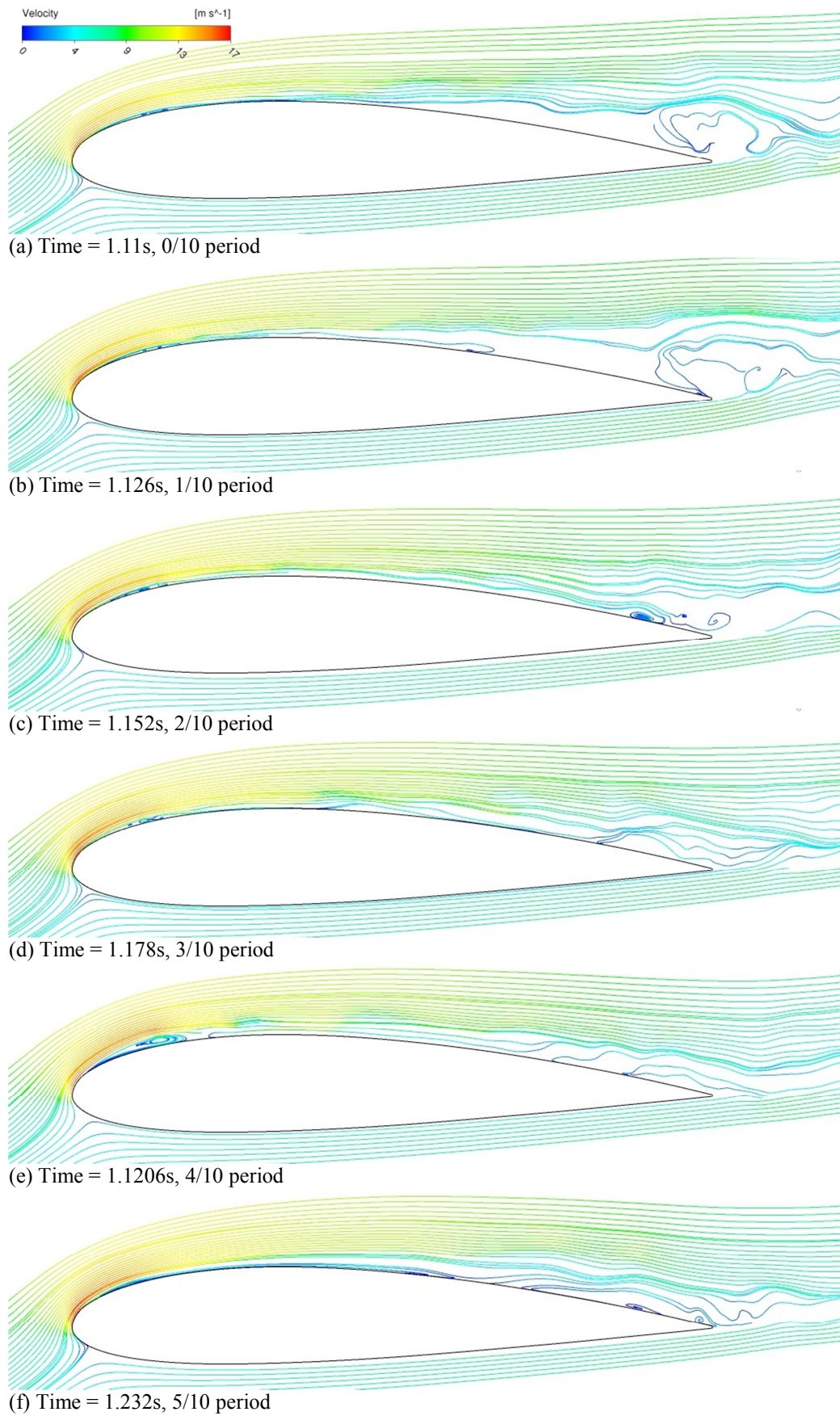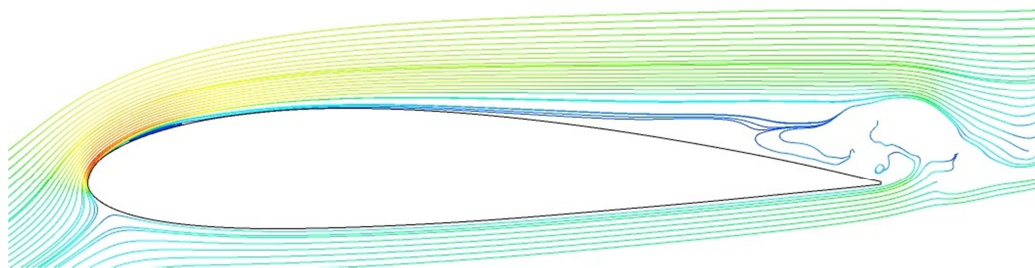
(g) Time = 1.258s, 6/10 period
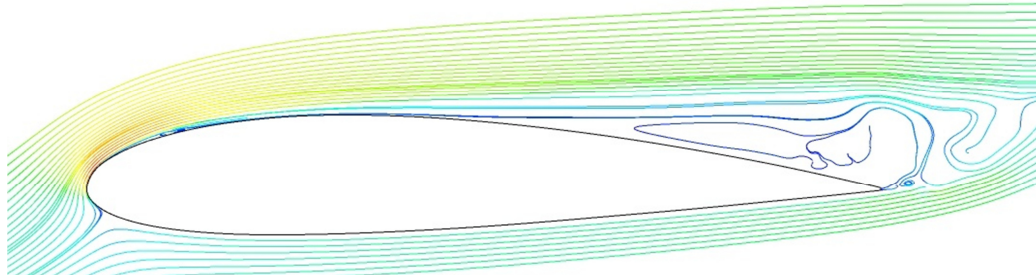
(h) Time = 1.284s, 7/10 period
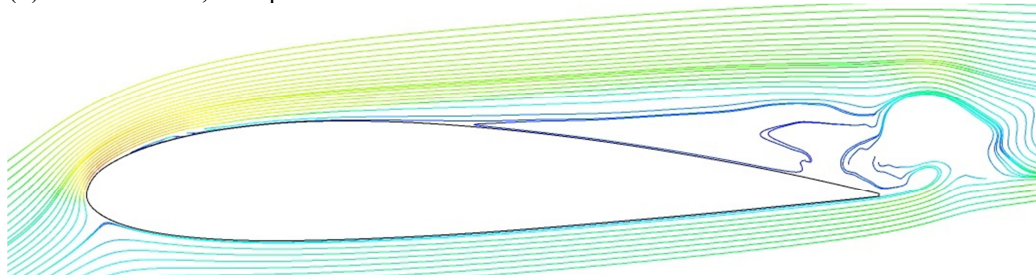
(i) Time = 1.31s, 8/10 period
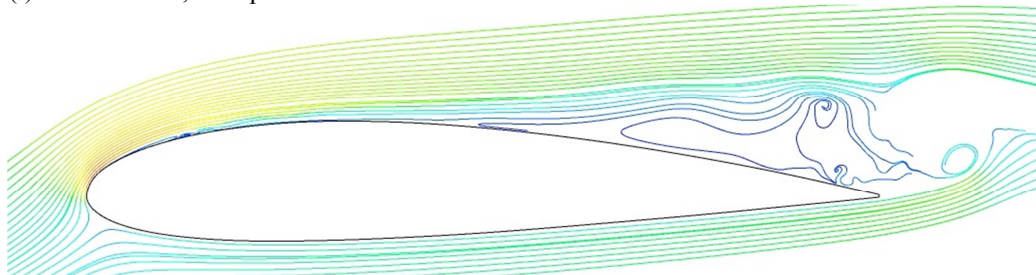
(j) Time = 1.336s, 9/10 period
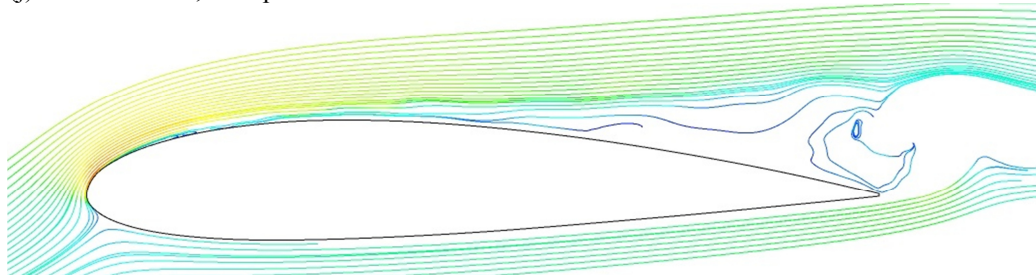
(k) Time = 1.364s, 10/10 period

Fig. 4-17. Streamlines on the mid-span plane, coloured by velocity magnitude, 12º

(2) The size of the two separation region changes periodically according to time. From Fig. 4-17a to Fig. 4-17e, the leading edge separation region grows gradually longer and higher. In Fig. 4-17e, a clear separation bubble can be seen, whereas in other time moments, multiple vortex cores exist. This is

consistent with the evolvement of the vortical structures in Fig. 4-16. The trailing edge separation clearly decreases at the same time, and the streamlines bend gradually towards the upper surface. In the rest time of this period, from Fig. 4-17f to Fig. 4-17k, the two separation regions perform the reversed motion and eventually recover to the state in Fig. 4-17a. Similar to the evolvement of the vortical structure in Fig. 4-16, the recovering process is not identical to the developing process. For example, the two dimensional flow separation features starting from mid-chord that can be found in Fig. 4-17h and j are not repeated in the first half of the period.

Back to the mean flow plotted in Fig. 4-13, it is found there the turbulent separation area is much shallower than the RANS result. Based on the instantaneous result here indeed shows separations, the DDES model is likely not resolving this flow feature well.

4.7 DDES without Low Re Correction

The corresponding lift and drag history, pressure and skin friction result, and instantaneous flow field results for the DDES model without the low Re correction are presented in Fig. 4-18, Fig. 4-19, Fig. 4-20, and Fig. 4-21 respectively.

Apparently, the lift and drag history shows no turbulent flow feature, such as random fluctuations. This can be confirmed from instantaneous flow depicted in Fig. 4-21, from which the flow is observed to be 2D. Although Fig. 4-21b obviously shows the separation occurs on the upper surface, there is no resolved LES content. The pressure and skin friction also show no separation bubble. These observations suggest the DDES model without the low Re correction stays in the URANS mode in the results, even in the separation region where the LES mode of the DDES model is expected to activate. Comparing the result to previous sections, it can be understood that the low Re correction enables more details of turbulent flows to be resolved and thus presents more realistic flows. The correction is therefore responsible for better resolving transitional flows. Without any proper treatment, the DDES model is unable to predict flows subjected to separation bubbles.

(a)   (b)
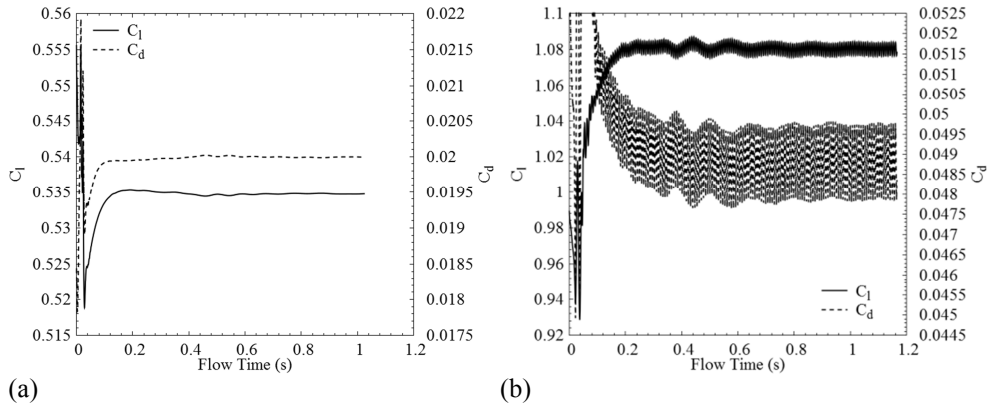
Fig. 4-18. The time history of lift and drag coefficient, DDES without the low Re correction, (a) 4º, (b) 12º

(a)   (b)
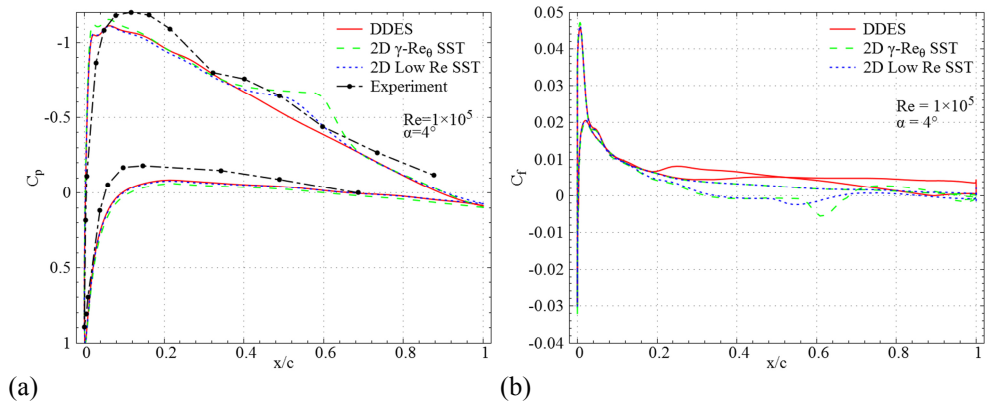
Fig. 4-19. C_p and C_f result for DDES without the low Re correction, 4º

(a)   (b)
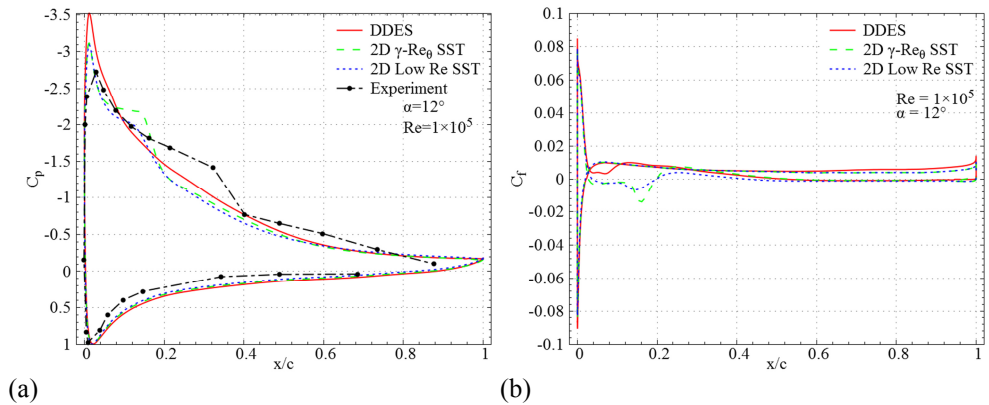
Fig. 4-20. C_p and C_f result for DDES without the low Re correction, 12º

Fig. 4-22 and Fig. 4-23 compares the f_d function (Eq 3-97, pp. 45) distribution with or without the low Re correction at $\alpha = 4º$, while Fig. 4-24 and Fig. 4-25 compares those at $\alpha = 12º$. When the low Re correction is not used, the near wall flow region all remains in the URANS mode, and when the low Re correction is used, part of the near wall flow region performs in the LES mode. Another observation is, at this low Reynolds number, the area for the URANS mode ($f_d < 1$) covers a large area more than necessary (it should just covers the near wall boundary layer region, leaving the rest for the LES mode). Even in

relatively well-performed cases with the low Re correction, f_d increases to 1 near the boundary layer edge, and recovers to 1 at some distance away.

(a)

(b)
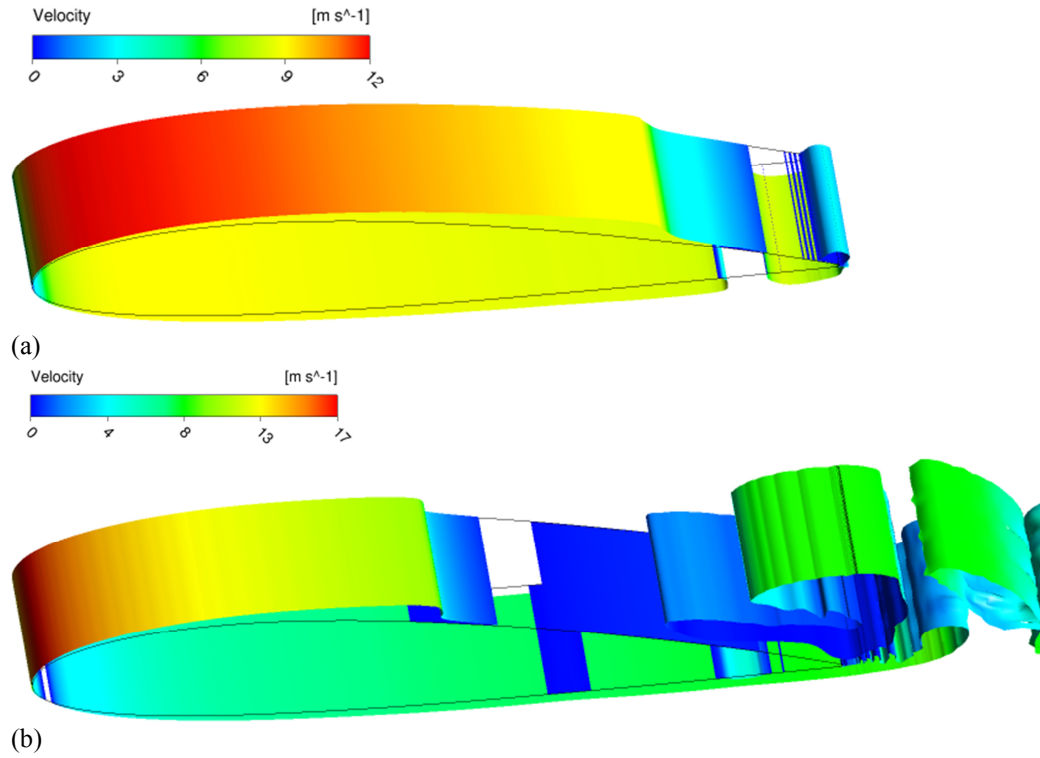
Fig. 4-21. The instantaneous flow for DDES without the low Re correction, (a) 4°, q≈39, (b) 12°, q≈5

(a)

(b)
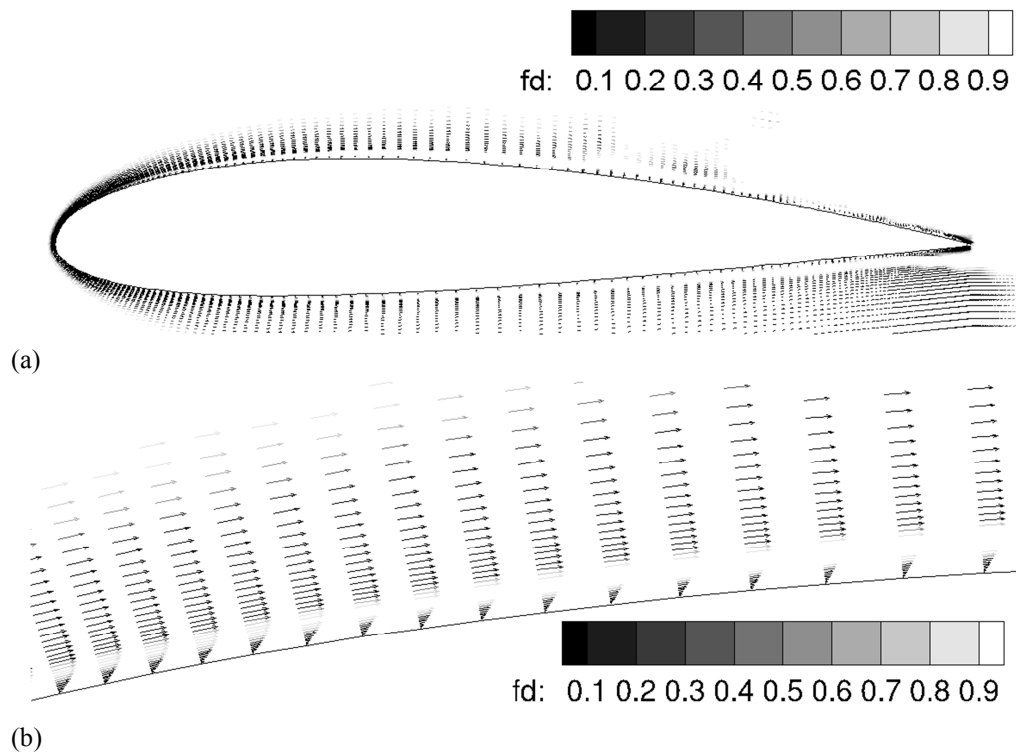
Fig. 4-22. The instantaneous velocity vectors on mid-span plane coloured with fd function, DDES with the low Re correction, $\alpha = 4°$, (a) overall view, (b) zoomed view

(a)

(b)
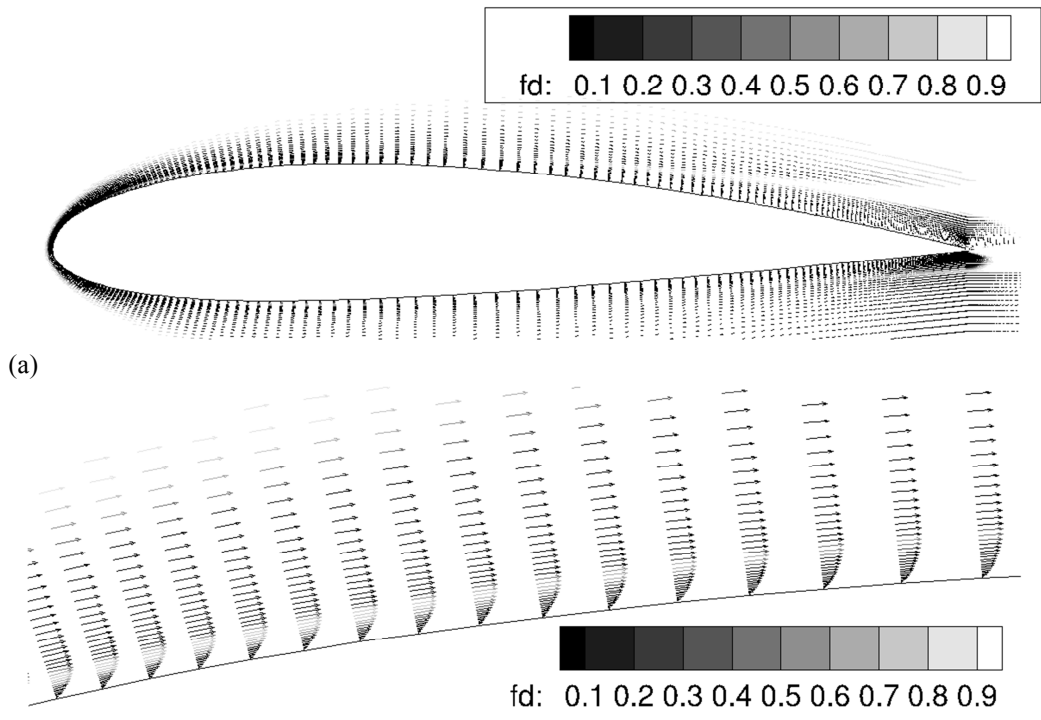
Fig. 4-23. The instantaneous velocity vectors on mid-span plane coloured with fd function, DDES without the low Re correction, $\alpha = 4°$, (a) overall view, (b) zoomed view

(a)

(b)
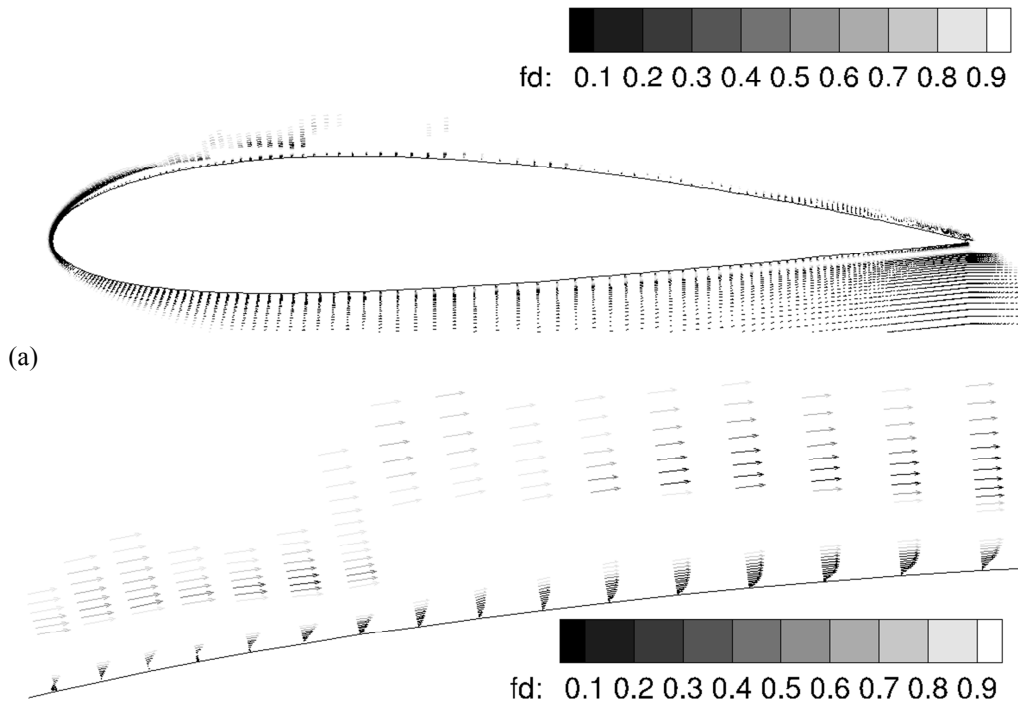
Fig. 4-24. The instantaneous velocity vectors on mid-span plane coloured with fd function, DDES with the low Re correction, $\alpha = 12°$, (a) overall view, (b) zoomed view

(a)

(b)
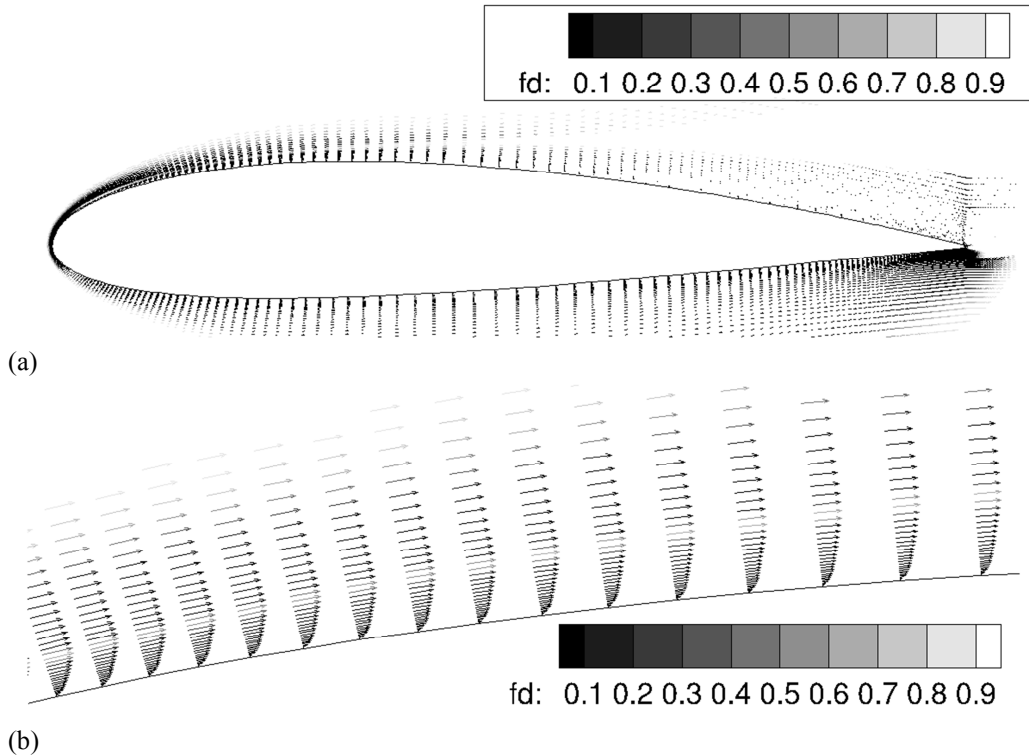
Fig. 4-25. The instantaneous velocity vectors on mid-span plane coloured with fd function, DDES without the low Re correction, α = 12º, (a) overall view, (b) zoomed view

4.8 Conclusion

This work investigates the capability of the low Re SST model, the γ-Re$_\theta$ SST model and a DDES model with a low Re correction, with the comparisons to the experiment.

The low Re SST model and the γ-Re$_\theta$ SST model shows similar predictions, and no one is found superior than the other. Compared to the experiment, the lift and drag coefficients are reasonably predicted at intermediate range of incidences. The γ-Re$_\theta$ SST model, other than the separation induced transition correction, incorporates no transition correlation for separation bubbles. Thus the future work for improvements may incorporate available transition correlations. Compared to the low Re SST model, it is found that the separation induced transition correction produces more turbulence after the transition onset, so that the corresponding bubble reattaches in a shorter distance, as well as a more notable influence in the pressure and skin friction. The low Re SST model, with no dedicated treatment for separation induced transition, performs surprisingly well as compared to the γ-Re$_\theta$ SST model.

Nevertheless, it seems unsteady calculations are the frequent usage for this model.

The DDES model proposed with a low Re correction resolves some large turbulent eddies. It is able to resolve the periodic change in the field and the transition process related to separation bubbles at $\alpha = 12º$. Other than the lift at $\alpha = 12º$, the result on lift and drag shows no superiority over the two RANS models. Compared to the DDES model without the low Re correction, the low Re correction is responsible for resolving transitional flows. The prediction of the separation bubble at $\alpha = 4º$ and the turbulent separation at $\alpha = 12º$ need further investigations.

Chapter 5 Roughness Modelling Comparison between Low Re SST and γ-Re$_θ$ SST Models with Experiment[1]

Roughness modelling at low Reynolds numbers of $O(10^4-10^5)$ is of practical importance for micro air vehicles. Following the understanding already obtained in Chapter 4, the capability of roughness modification to low Re SST and γ-Re$_θ$ SST models is investigated in this chapter. The roughness is modelled as sand grains. A series of simulations using the two models have been performed on NACA0012 aerofoil with comparisons to the experimental data. The understanding obtained from these two models provides the guidance for the simulation of roughness effects in Chapter 6 and Chapter 7.

5.1 Referred Experimental Data

This work compares the results from the two models with the experimental data by Chakroun *et al.*[123]. In the experiment, the measured aerofoil was NACA0012 aerofoil. The lift and drag coefficients data were measured between $-16° \leq α \leq 26°$ on a smooth surface, surfaces with either P80 (200 *μm*) or Grit 36 (500 *μm*) sandpapers at $Re = 1.5 \times 10^5$. These data are compared to assess the overall performance of the two models. To further understand the difference between the two models on the prediction of laminar to turbulent transition, skin friction data are compared. The experiment collected corresponding data between Reynolds number 1.97×10^4 and 7.87×10^4, instead of specifying a clear number. In the simulation, a Reynolds number of 5×10^4 is assumed.

The freestream turbulence intensity was not clearly reported. The same researchers' previous work[124] reported the turbulence intensity less than 0.5% for the same wind tunnel. A value of 0.33% is chosen in the present simulations.

---

[1]The work reported in this chapter has been published in:

Liu, S., and Qin, N., Modelling roughness effects for transitional low Reynolds number aerofoil flows, *Journal of Aerospace Engineering, Proceeding of the Institute of Mechanical Engineers, Part G*, 2014.

Table 5-1 shows the freestream condition used in the simulation. There is some decay for the turbulence intensity from the flow inlet to the aerofoil leading edge. To maintain the prescribed value (0.33%), the input at the flow inlet is adjusted to 0.4% for the low Re SST model and 0.43% for the γ-Re$_\theta$ SST model.

Table 5-1. Freestream properties

Reynolds number	Mach number	$(\mu_t/\mu)_{inlet}$	Tu (%)	T (K)
150000	0.0432	10	0.33	293.15 (μ=1.81e-5
50000	0.0144			Pa·s)

The Grit 36 case in the experiment is simulated. The nominal 500 μm was "roughness thickness" mentioned in the experiment, which can be seen as the geometrical roughness height.

The equivalent sand grain roughness height is difficult to obtain. Ferrer and Munduate[125] estimated a relationship of $h_s/\bar{h}$=2.043 for a grit-40 surface, and Pailhas *et al.*[111] reported an averaged value of $h_s/\bar{h}$=2 based on their experiment for a 3MP40 surface. Considering Grit 36 surface is close to the grit-40 surface in grade, $h_s/\bar{h}$=2 or h_s=1000 μm is assumed in the following simulations. $\bar{h}$ here refers to the nominal grain size of the sandpaper. Ideally, a dedicated experiment should be performed to identify the appropriate height.

The nondimensional roughness height h_s^+ is shown in Fig. 5-1, calculated after the flow is solved. The h_s^+ values indicate this roughness height is in the transitional rough region for the $Re = 5\times10^4$ case and only the leading edge part is in the fully rough region for the $Re = 1.5\times10^5$ case. See Section 3.5 for the definition of transitional rough and fully rough regions.

(a)   (b)
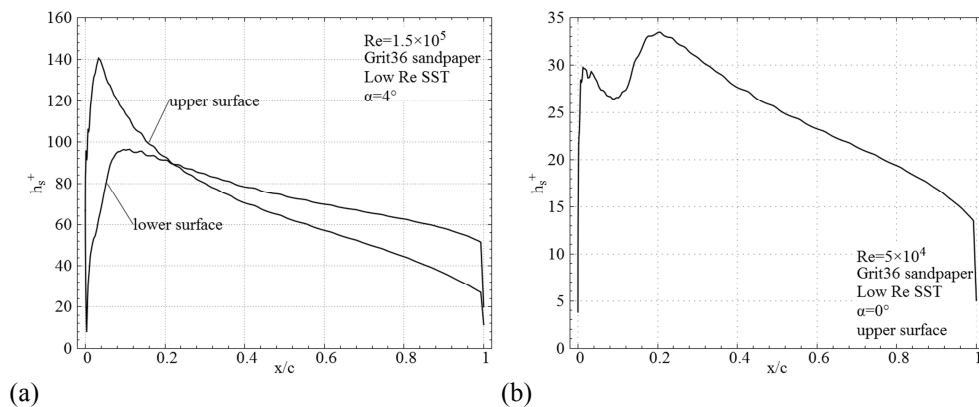
Fig. 5-1. h_s^+ distribution.

5.2 Grid Convergence

Fig. 5-2 (a) shows the geometry of computational domain and the boundary conditions. The farfield boundary is 20 chords away from the aerofoil. A sensitivity study of the farfield boundary location performed by the authors shows this size is appropriate.

The computational grid is generated using ICEM grid generation program. The grid topology is a C-type. Further block splitting is made near the aerofoil to better control the boundary layer mesh and the mesh in the near wake. A base grid is generated at first and then refined or coarsened by a ratio of 1.5 along each axis to check grid convergence. The base grid has a maximum first grid layer's y^{+} of approximately 0.7 ($Re = 1.5 \times 10^{5}$) , (checked after the flow is solved), and a near wall grid expansion ratio of 1.1, chosen according to the suggestion by Menter[60].

The lift and drag coefficients at $\alpha = 4°$ are compared, as shown in Table 5-2, with the Grid Convergence Index (GCI) by Roache[126] shown in Table 5-3. The results show no convergence on drag coefficients in all cases, and no convergence on lift coefficients for the rough case using the γ-Re_{θ} SST model. The converged cases show super-convergence (the observed order of convergence $P_{123\ Cl}$ is much greater than theoretical 2), and a value of 2 is adopted when calculating GCI. All available GCI values are in a satisfactory range. Grid 2 is eventually used as the change in the lift and drag coefficients due to the refinement is sufficiently small for this study.
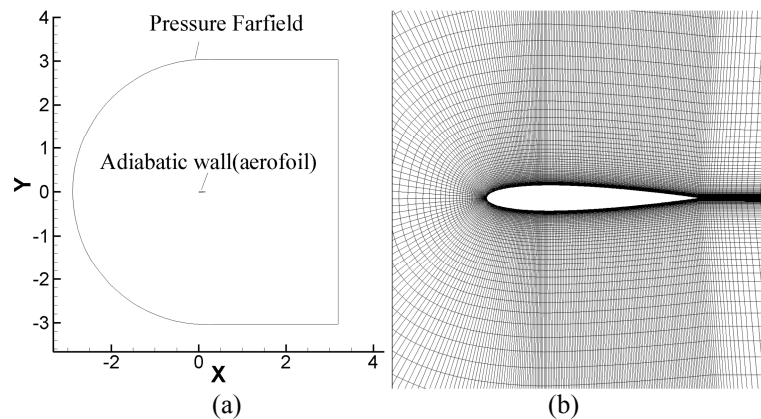
Fig. 5-2. (a) Domain and boundary condition, (b) Grid elements near the aerofoil

Table 5-2 Grid sensitivity results

Grid elements	Smooth				Rough			
	Low Re SST		γ-Re$_\theta$ SST		Low Re SST		γ-Re$_\theta$ SST	
	C_l	C_d	C_l	C_d	C_l	C_d	C_l	C_d
Grid 3: 25706	0.4966	0.01314	0.5110	0.01410	0.3644	0.03216	0.4540	0.01057
Grid 2: 57312	0.4907	0.01315	0.5078	0.01402	0.3652	0.03235	0.4520	0.01075
Grid 1: 129102	0.4888	0.01295	0.5071	0.01387	0.3658	0.03235	0.4559	0.01044

Table 5-3 Grid Convergence Index results for Grid 2

	Smooth		Rough
	Low Re SST	γ-Re$_\theta$ SST	Low Re SST
GCI$_{fine,123}$ C_l	2.90%	1.50%	2.19%
$P_{123\ Cl}$	2.78	3.68	0.62

Roache[126] suggests that the code has something unknown when the grid convergence result showing super-convergence. However, the near wall model used here contains switching functions based on the first cell height. From coarse to fine meshes, the near wall model changes accordingly. This makes the ideal mesh convergence required by the GCI study difficult.

5.3 Result and Discussion

5.3.1 Lift and Drag Comparison at $Re = 1.5 \times 10^5$

The lift and drag coefficients are compared with available experimental data to evaluate the overall performance of the two models. The experimental data shows generally lower lift and higher drag for the Grit36 case, when comparing to the results on smooth surfaces. The experimental observation therefore shows that the roughness deteriorated the aerofoil's lift and drag characteristics.

The lift and drag coefficients on smooth and rough surfaces predicted by the two models are presented Fig. 5-3 and Fig. 5-4. On smooth surfaces, there is little difference on the lift and drag coefficients between the two models, and both lift and drag results before stall are in reasonably good agreement with the experiment.

On rough surfaces, the two models behave rather differently. The γ-Re$_\theta$ SST clearly overpredicts the lift and underpredicts the drag. On the other hand,

the low Re SST model manages to predict the correct trend of the roughness effects, i.e., a decrease in lift coefficients and an increase in drag coefficients. The lift coefficient by the low Re SST model compares well with the experimental data but the drag coefficient underpredicts the experimental data although upward trend from smooth surface drag is correct.
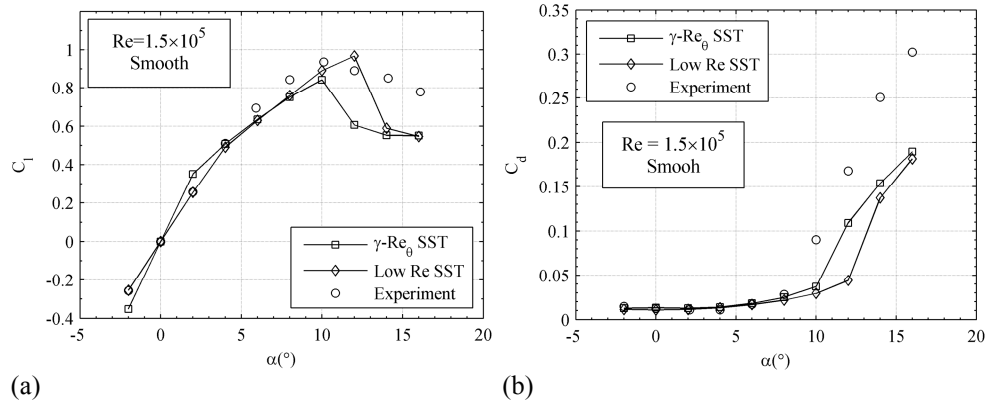
(a)   (b)

Fig. 5-3. Lift and drag coefficients on smooth surfaces, experiment: Chakroun et al.[123]
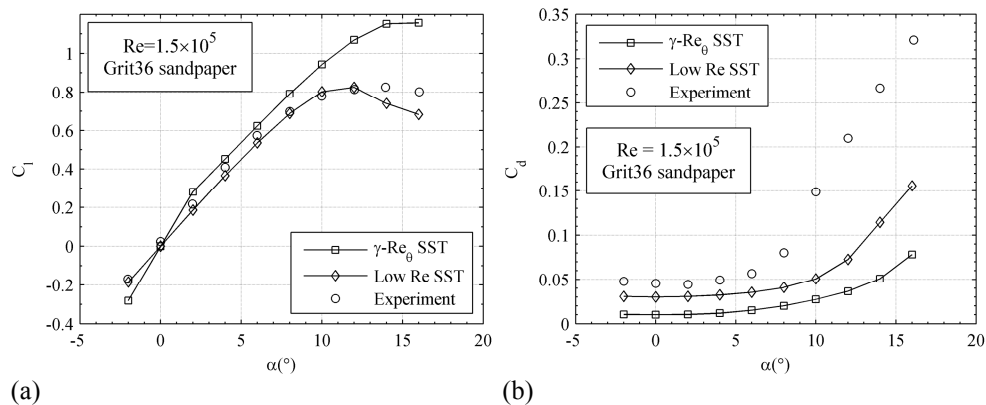
(a)   (b)

Fig. 5-4. Lift and drag coefficients on the Grit 36 surface, experiment: Chakroun et al.[123]

5.3.2 Skin Friction Result at $Re = 5\times10^4$

Fig. 5-5 (a) shows the skin friction predicted by the two models on smooth surfaces, comparing with the experimental data at $\alpha = 0°$. On the smooth surface, the prediction by the two models agrees with the experimental data very well, and the difference between the two models is below 0.1%. It is not surprising that the two models are consistently accurate at this laminar boundary layer condition as the eddy viscosities are negligible.

Fig. 5-5 (b) shows the results on the rough surfaces. It is observed that roughness-induced transition, as observed in the experiment, is predicted by the low Re SST model, while the γ-Re$_\theta$ SST model clearly misses the transition on

the rough aerofoil surface.

The drag coefficient results are compared to investigate the overall effects, as presented in Table 5-4. When the roughness is introduced, the low Re SST model shows a 150% increase in the skin friction drag C_{df}, due to a transitional boundary layer. By comparison, the γ-Re$_\theta$ SST model shows only 2% increase, due to its failure in capturing transition on the rough surface. Although a reduction in the pressure drag C_{dp} is observed from the results by low Re SST, it is overshadowed by the increase in the skin friction and the total drag C_d increases as a result. The decrease in the pressure drag by the low Re SST model can be attributed to the reduction of the trailing edge separation zone, as can be observed in Fig. 5-5(a) and (b). Although the experimental drag coefficients are not available at this Reynolds number for exact comparisons, the prediction in the trend of drag variation is obviously wrong for the γ-Re$_\theta$ SST model at $Re = 1.5\times10^5$.

(a)   (b)
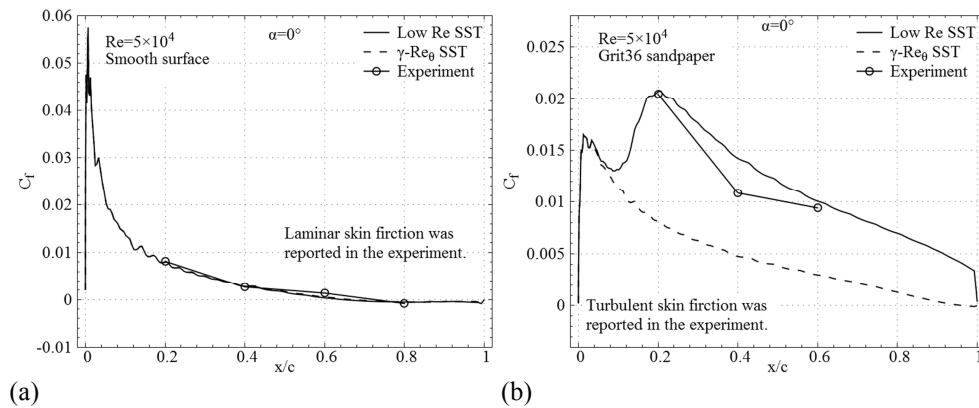
Fig. 5-5. C_f comparisons on the Grit 36 upper surface, experiment: Chakroun et al.[123]

Table 5-4 Drag coefficients comparison at $Re=5\times10^4$

	Smooth		Grit36	
	Low Re SST	γ-Re$_\theta$ SST	Low Re SST	γ-Re$_\theta$ SST
C_{dp}	0.01018	0.01033	0.00645	0.00497
C_{df}	0.00942	0.00957	0.02361	0.00978
C_d	0.01960	0.01989	0.03006	0.01475

5.3.3 Flow Field Result at $Re = 1.5\times10^5$

Fig. 5-6 and Fig. 5-7 show the flow field at a representative $\alpha = 6°$, accompanied with the pressure and skin friction results. The normalized Reynolds shear stress is compared to facilitate understanding.

(a)

(b)

(c)

(d)
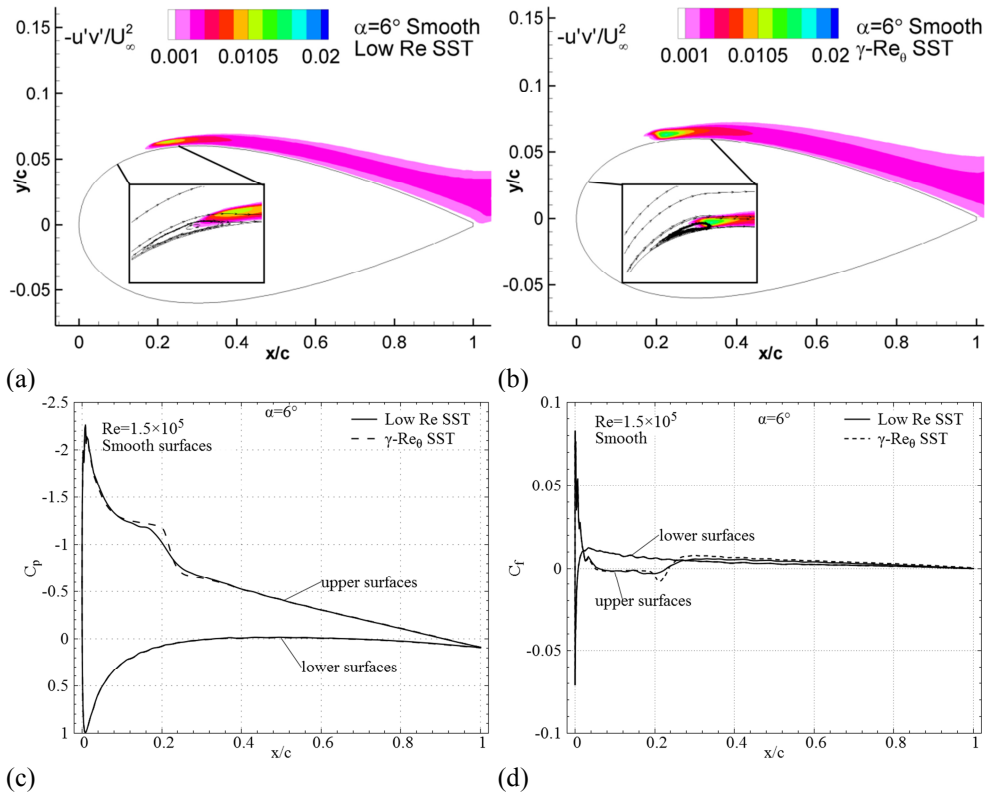
Fig. 5-6. Flow field, pressure, and skin friction results (x to y scale is 0.3 in (a) and (b))

(a)

(b)

(c)

(d)
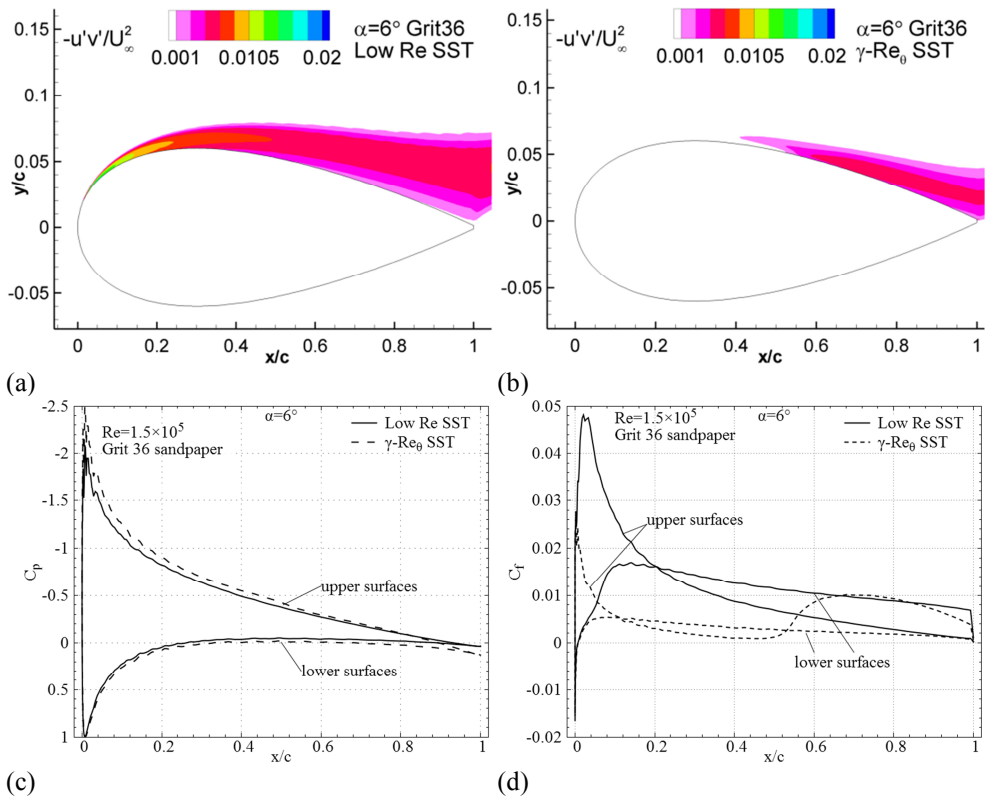
Fig. 5-7. Flow field, pressure, and skin friction results, (x to y scale is 0.3 in (a) and (b))

For the smooth aerofoil, Fig. 5-6 shows that, both models predict a transitional leading edge separation bubble on the upper surface. The prediction

of the two models is generally similar. The bubble location is 0.05c-0.23c and 0.06c-0.23c for the γ-Re$_θ$ SST model and the low Re SST model, respectively. The Reynolds shear stress exceeds the cut-off level 0.001 at 0.16c for both models. Fig. 5-6 (c) and (d) show clear differences in pressure and skin friction distribution in the bubble area, but they are similar, leading to little differences in the total lift and drag coefficients.

On the Grit36 rough surface, both predict no separation bubbles on the upper surface, as shown in Fig. 5-7(a) and (b). The Reynolds shear stresses show that the low Re SST model predicts turbulent boundary layer starting from the leading edge as confirmed by the skin friction results in Fig. 5-7(d) The Reynolds shear stress predicted by the γ-Re$_θ$ SST model exceeds the threshold at 0.41c above the upper surface. This in some degree agrees with the skin friction data, taking the minimum skin friction as the transition onset location (0.46c). The γ-Re$_θ$ SST model's prediction of later transition on the upper surface and lack of transition on the lower surface result in much lower skin friction, as show Fig. 5-7 (d). Obviously, the skin friction magnitude in Fig. 5-7 (d) is directly related to the Reynolds shear stresses in Fig. 5-7 (a) and (b).

The difference in the drag coefficient predicted by the two models is largely attributed to the difference in the skin friction due to different boundary layer status. Additionally, on the upper surface, the γ-Re$_θ$ SST model increases the peak of the pressure coefficient, as shown in Fig. 5-7 (c). This explains the increase of the lift coefficient in Fig. 5-4 (a), inconsistent with the experimental trend.

5.3.4 Further Discussion

The two models predict transition in different ways. In the case of low Re SST model, the point where the production of turbulence kinetic energy overtaking the dissipation is defined as the transition onset and the point where the "near balance is achieved" between the production and the dissipation is defined as the point when the boundary layer becomes fully turbulent. When roughness induced transition is modelled, the boundary condition for $ω$ and some model coefficients are changed, according to rough surface experimental

data. The increase of the roughness height decreases the ω wall value and then decrease the dissipation term in the k transport equation, resulting earlier transition to occur[102].

In the case of γ-Re$_\theta$ SST model, an empirical correlation for transition onset and completion is used. Local critical Reynolds number is calculated through the correlation based on the geometrical roughness height, turbulence intensity and pressure gradient. As mentioned earlier, the correlation was developed for relatively high turbulence intensities (> 1%), and it may not perform well in the low incoming flow intensity as in current cases (< 0.5%). This shortcoming may be one source of the problem attributing to the difficulty of the model for rough surface transition prediction.

5.4 Conclusion

By using the equivalent sand grain approach in RANS simulation for a rough surface aerofoil, this paper investigates the roughness modelling of the γ-Re$_\theta$ SST model and the low Reynolds number SST model for low Reynolds number transitional flows. The primary observed roughness effects are the decrease in lift, the increase in drag, the increase in skin friction and roughness induced transition in boundary layers for the NACA0012 aerofoil at $Re = 1.5 \times 10^5$. The results on smooth surfaces from both models show similar skin friction, pressure, and lift and drag predictions at $Re = 5 \times 10^4$. The results at $Re = 1.5 \times 10^5$ on rough surfaces show that the low Re SST model is capable of modelling the roughness effects in a more consistent way as compared with the experiment. The γ-Re$_\theta$ SST model, on the other hand, fails to give an effective prediction for transitional flow on rough surfaces, resulting in incorrect lift and drag predictions.

Chapter 6 Investigation of Roughness Effects for Aerofoils at Low Reynolds Numbers

From this chapter, the investigation of the roughness effects is presented. A systematic investigation is conducted on three aerofoils, various Reynolds numbers and various roughness heights. The rough low Re SST model is chosen for the simulations, based on the findings from Chapter 5.

6.1 Introduction

As mentioned earlier, the beneficial roughness effects are the motivation for the simulation of roughness effects. In this investigation, following aspects are mainly concerned:

(1) The circumstance that the roughness can have beneficial effects,

(2) The effects by aerofoil, roughness condition, incidence, and Reynolds number on the beneficial effects,

(3) The agreement between the numerical data and available experimental data in the literature.

A systematic investigation on the roughness effects is conducted accordingly. The roughness is modelled as sand grains distributed evenly on aerofoil surfaces. Additionally, to make the investigation representative, the following choices are made:

(1) A few representative aerofoils are investigated, i.e., NACA 0012 aerofoil (symmetry), NACA 2415 aerofoil (thick) and a cambered plate profile (thin). The thin cambered plate profile is defined in Pelletier and Mueller[127]. Thin wing profiles are believed to have better performance over relatively thick profiles at low Reynolds numbers. Including both thin and thick aerofoils is intended for better understanding of roughness effects on aerofoils with different thickness, distinct aerodynamic performance and flow behaviour.

(2) The choice of roughness height covers from hydrodynamically smooth to fully rough region as possible as it can, as shown in Table 6-1. The relative roughness height with respect to the chord length h_s/c is used for comparison. The nondimensional roughness height h_s^+ varies significantly from the leading edge to the trailing edge on a given aerofoil, and the value presented is the

typical maximum.

(3) The range for the Reynolds numbers is limited between 2×10^4 and 2×10^5, which is reasonable for MAV flights. A few Reynolds numbers are selected for simulations, and the results at Reynolds numbers of 2×10^4, 6×10^4 and 1.5×10^5 are presented in detail. At each Reynolds number, the simulation is individually performed at angles of attack ranging from −2º to 16º with 2º interval.

<p align="center">Table 6-1 Roughness heights in the investigation</p>

Name	h_s/c	$h_{s,max}^+$			
		$Re=2\times10^4$	6×10^4	1.5×10^5	2×10^5
Rough a	1.25E-04	0.6	1.3	2.7	3.3
Rough b	2.50E-04	1.1	2.5	4.3	6.2
Rough c	5.00E-04	2.1	4.6	9.3	10.9
Rough d	1.00E-03	3.7	8.0	16.5	22.2
Rough e	2.00E-03	6.5	13.9	35.6	48.1
Rough f	4.00E-03	11.0	27.3	75.1	98.7

6.2 Simulation Setup

The freestream condition for all simulations is shown in Table 6-2. It is chosen to mimic laminar inflows. It is found no significant turbulence intensity decay for this low freestream turbulence setting.

<p align="center">Table 6-2 Freestream condition</p>

Tu_{inlet} (%)	$(\mu_t/\mu)_{inlet}$	Temperature (K)
0.05	1	293.15 (μ=1.81e-5 Pa·s)

Fig. 6-1 shows the aerofoils and the meshes. The meshes use the same blocking configuration for each aerofoil. The total number of elements is 55312 for all simulations, and maximum y^+ of the grids is at an order of O(1). The general rule of the grid generation is the same as the one used in Chapter 5, and the meshes share a large similarity as the one that already demonstrates mesh independence. Thus it is reasonable to assume the new mesh is sufficient fine for present investigations. Because the Reynolds number investigated varies from 2×10^4 to 2×10^5, the mesh is generated to satisfy the highest Reynolds number with appropriate y^+. This ensures the first cell height is also appropriate for other Reynolds numbers and other aerofoils.

The rough low Re SST model is shown in Chapter 5 to be a suitable model

to investigate the roughness effects at low Reynolds numbers, and therefore this model is chosen here. Based on the result in Chapter 5, it should be kept in mind that the model is sufficient to investigate the trend of surface roughness: although at the validated $Re = 1.5 \times 10^5$, the drag increase due to the roughness may be underestimated.

<div align="center">
(a)   (b)   (c)
</div>
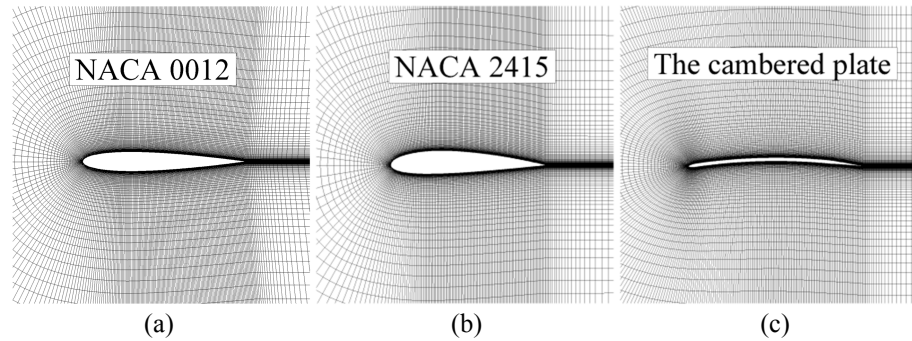
Fig. 6-1. The close-up view of the grids used for the three aerofoils

6.3 Lift and Drag for Rough Aerofoils

The lift, drag and lift to drag ratio results, for each Reynolds number and rough aerofoil, are presented from Fig. 6-2 to Fig. 6-10. In each figure, "a" to "d" show the general effects, and "e" to "f" show the detailed effects on each incidence. The roughness effects is observed for a given aerofoil at a given Reynolds number and incidence with respective to the increase of the roughness height. Generally, the incidences that can have higher C_l/C_d due to the roughness are fewer at higher Reynolds numbers. The NACA 0012 and NACA 2415 aerofoils can only have notable improvements on $C_{l,max}$ and $C_l/C_{d,max}$ at the moderate Reynolds number with a suitable roughness height. The cambered plate can always have $C_{l,max}$ and $C_l/C_{d,max}$ improved, even at the highest Reynolds number.

6.3.1 $Re = 2 \times 10^4$

At this Reynolds number, the general trend for the roughness effects is beneficial. Higher C_l, lower C_d and higher C_l/C_d are observed for almost all incidences, and higher $C_{l,max}$ and $C_l/C_{d,max}$ are observed for the three aerofoils, see Fig. 6-2, Fig. 6-5, and Fig. 6-8. Larger roughness is preferable. Although there is no direct experimental evidence available to accomplish a comparison, it is noted that the experiment by Kraemer[15] showed both increases in lift and

drag coefficients at $Re = 2.1 \times 10^4$ on a Gö 801 aerofoil with paper covering.

Other than the general trend, it is noted some cases show different changes for the lift. For NACA 0012 aerofoil, the incidence 6º shows a continuous reduction in the lift. The cambered plate at $\alpha = 6°$ shows a substantial reduction in C_l for small roughness and then a slowly increase for higher roughness.

6.3.2 $Re = 6 \times 10^4$

At this Reynolds number, generally at a suitable roughness height, higher C_l, lower C_d, higher C_l/C_d can be obtained, see Fig. 6-3, Fig. 6-6, and Fig. 6-9. For NACA 0012 aerofoil, the roughness can be more beneficial for $\alpha \geq 8º$. $C_{l,max}$ can be improved, while the gain in $C_l/C_{d,max}$ is small. It is also noticed that, similar to $Re = 2 \times 10^4$, the incidence 6º again shows a continuous reduction in the lift. For NACA2415 aerofoil, the suitable range of the incidence is $\alpha \geq 0º$, and both $C_{l,max}$ and $C_l/C_{d,max}$ can be improved. For the cambered plate, all incidences can be benefited from the roughness, and both $C_{l,max}$ and $C_l/C_{d,max}$ can be improved.

6.3.3 $Re = 1.5 \times 10^5$

At this Reynolds number, the effects on the three aerofoils are not the same, see Fig. 6-4, Fig. 6-7 and Fig. 6-10. For NACA 0012, higher C_l, lower C_d, higher C_l/C_d can be notably obtained only for $\alpha \geq 12°$. The increase in $C_{l,max}$ is small. Other incidences demonstrate detrimental effects, i.e., an increase in the drag and a reduction in the lift.

For NACA 2415, the roughness has detrimental effects at all incidences. For the cambered plate, similar to that for $Re = 2 \times 10^4$, at a suitable roughness condition, all incidences can obtain beneficial roughness effects. Compared to the other two aerofoils, only the cambered plate obtains higher $C_{l,max}$ and higher $C_l/C_{d,max}$.

For the cambered plate, it is also noted the higher $C_l/C_{d, max}$ obtained at $Re = 1.5 \times 10^5$ is located at a sharp peak when $\alpha = 2°$. At this incidence, C_l is found to have a great increase. This good performance at the "sharp peak" may lead to

a sensitive aerodynamic performance, and therefore this beneficial effect is not robust.

(a)

(b)

(c)

(d)

(e)

(f)

(g)
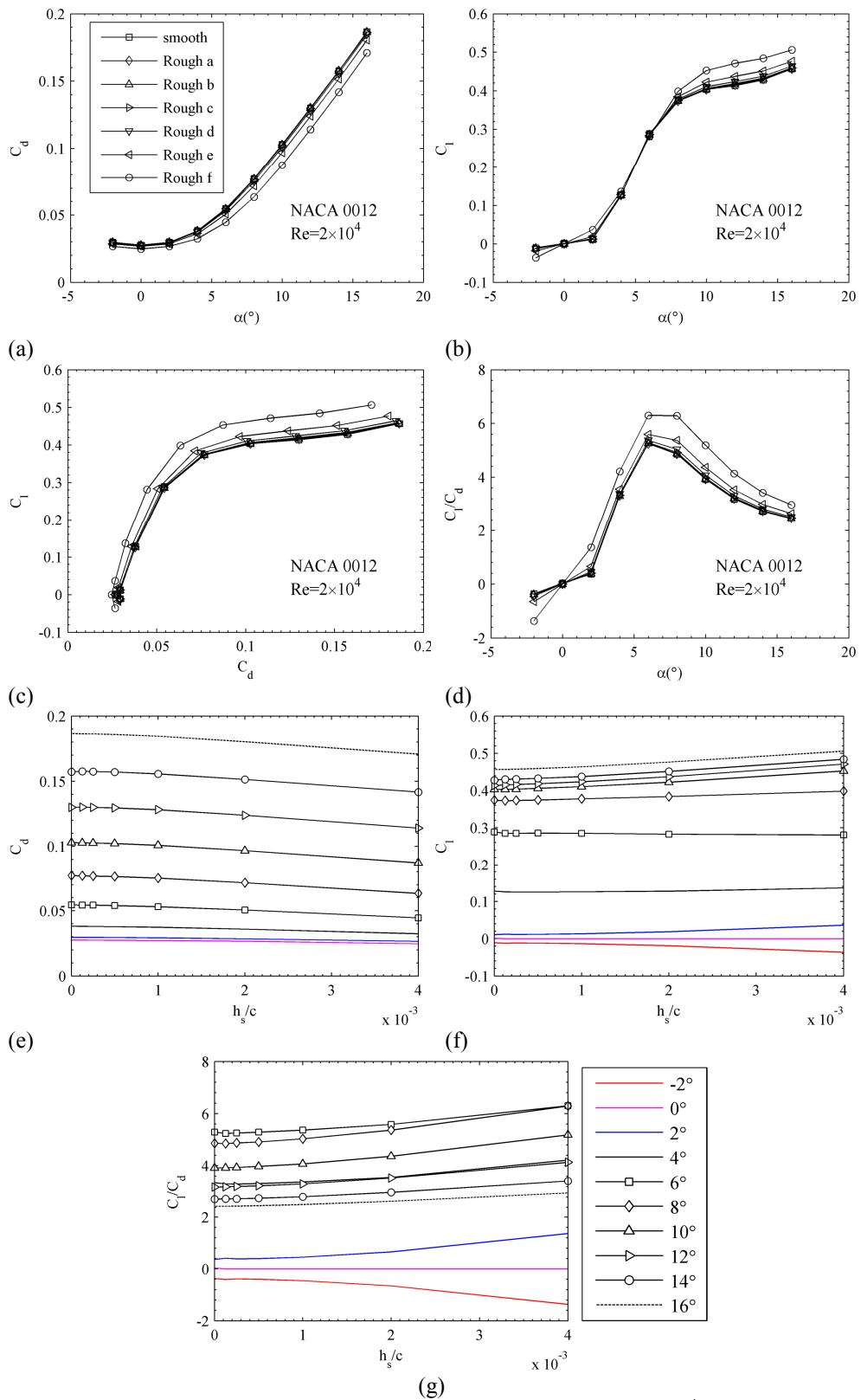
Fig. 6-2. The aerodynamics affected by the roughness at $Re = 2\times10^4$, NACA 0012

(a)

(b)

(c)

(d)

(e)

(f)

(g)
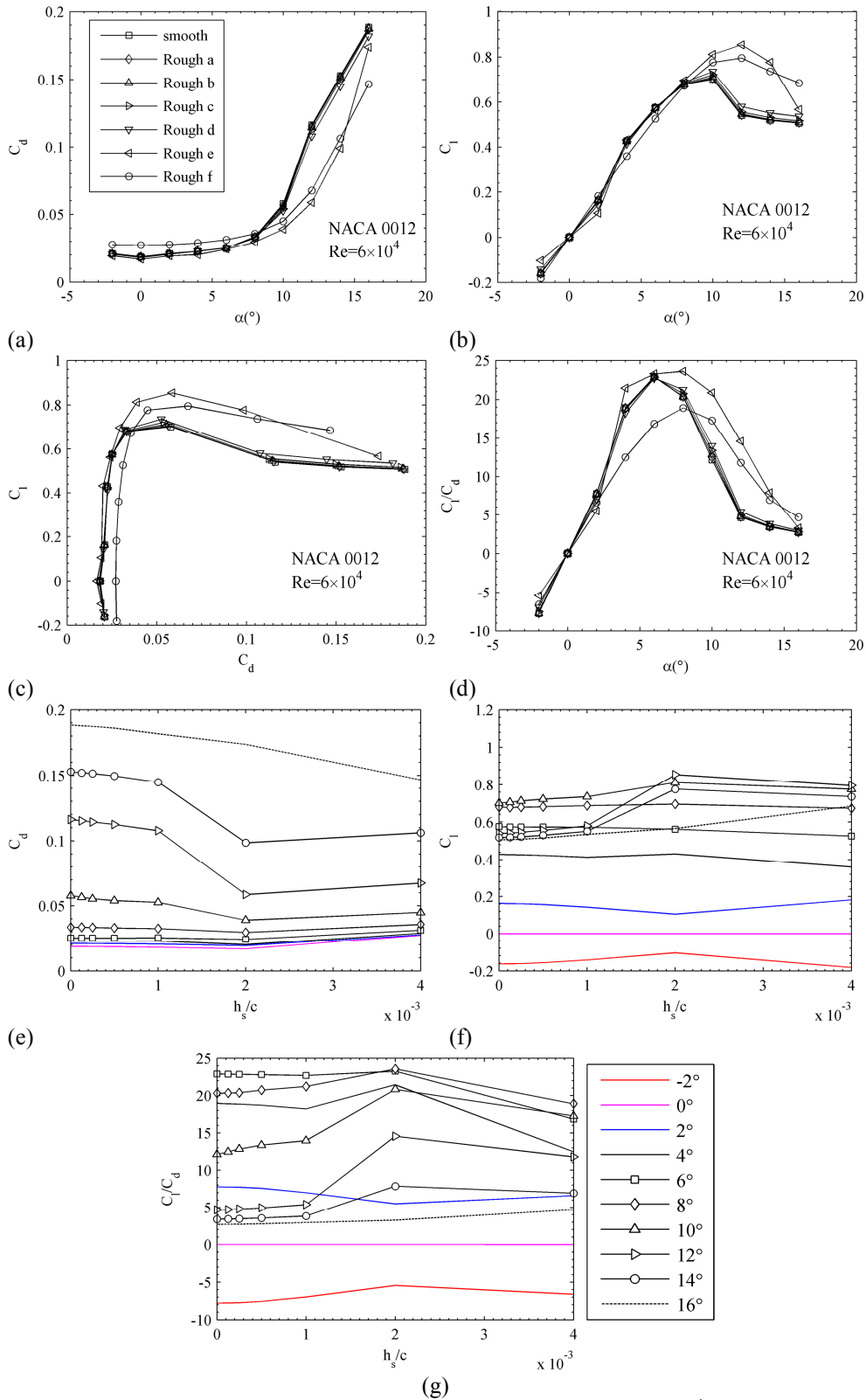
Fig. 6-3. The aerodynamics affected by the roughness at $Re = 6 \times 10^4$, NACA 0012
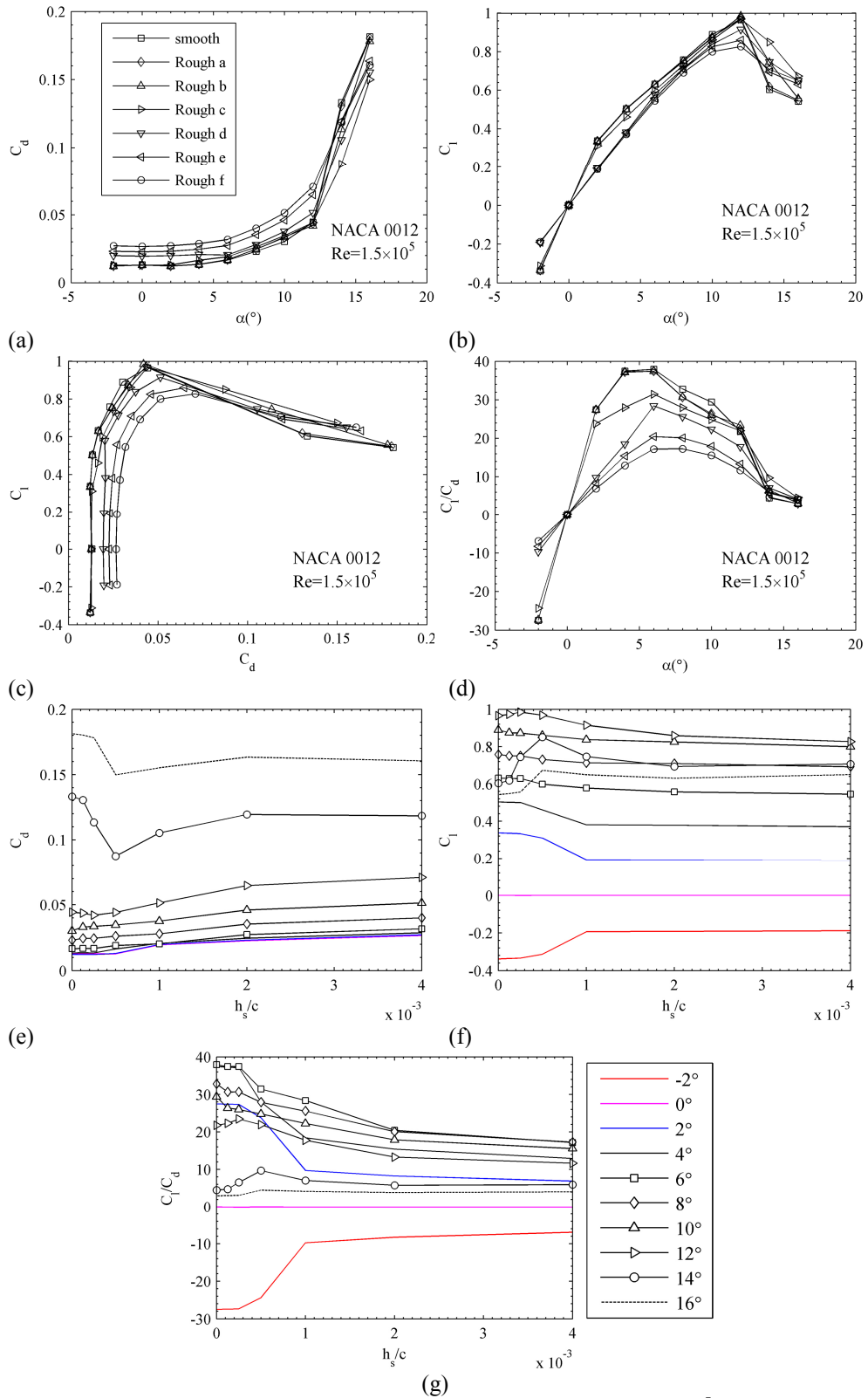
Fig. 6-4. The aerodynamics affected by the roughness at $Re = 1.5×10^5$, NACA 0012

(a)

(b)

(c)

(d)

(e)

(f)

(g)
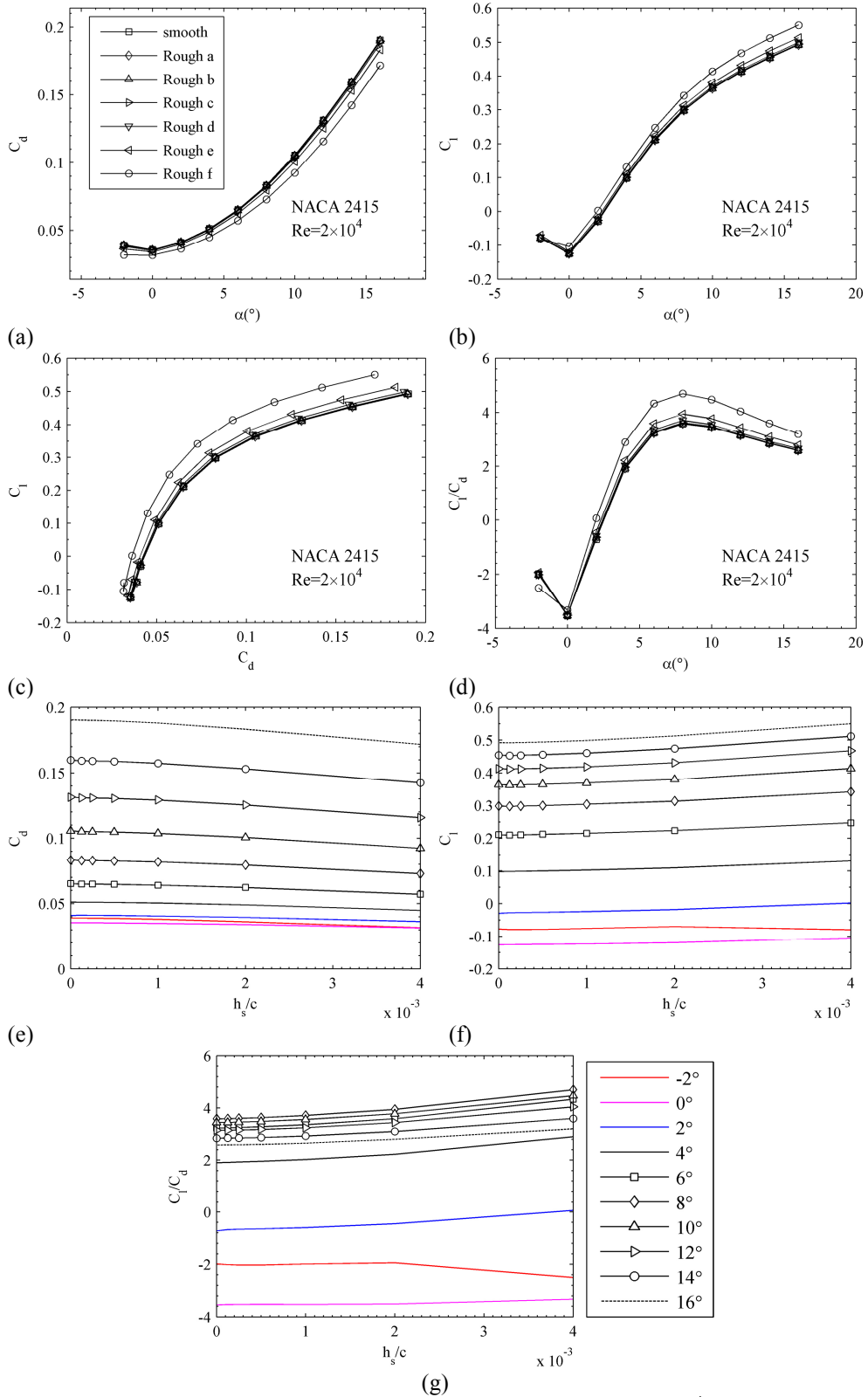
Fig. 6-5. The aerodynamics affected by the roughness at $Re = 2 \times 10^4$, NACA 2415

Fig. 6-6. The aerodynamics affected by the roughness at $Re = 6 \times 10^4$, NACA 2415

(a)

(b)

(c)

(d)

(e)

(f)

(g)
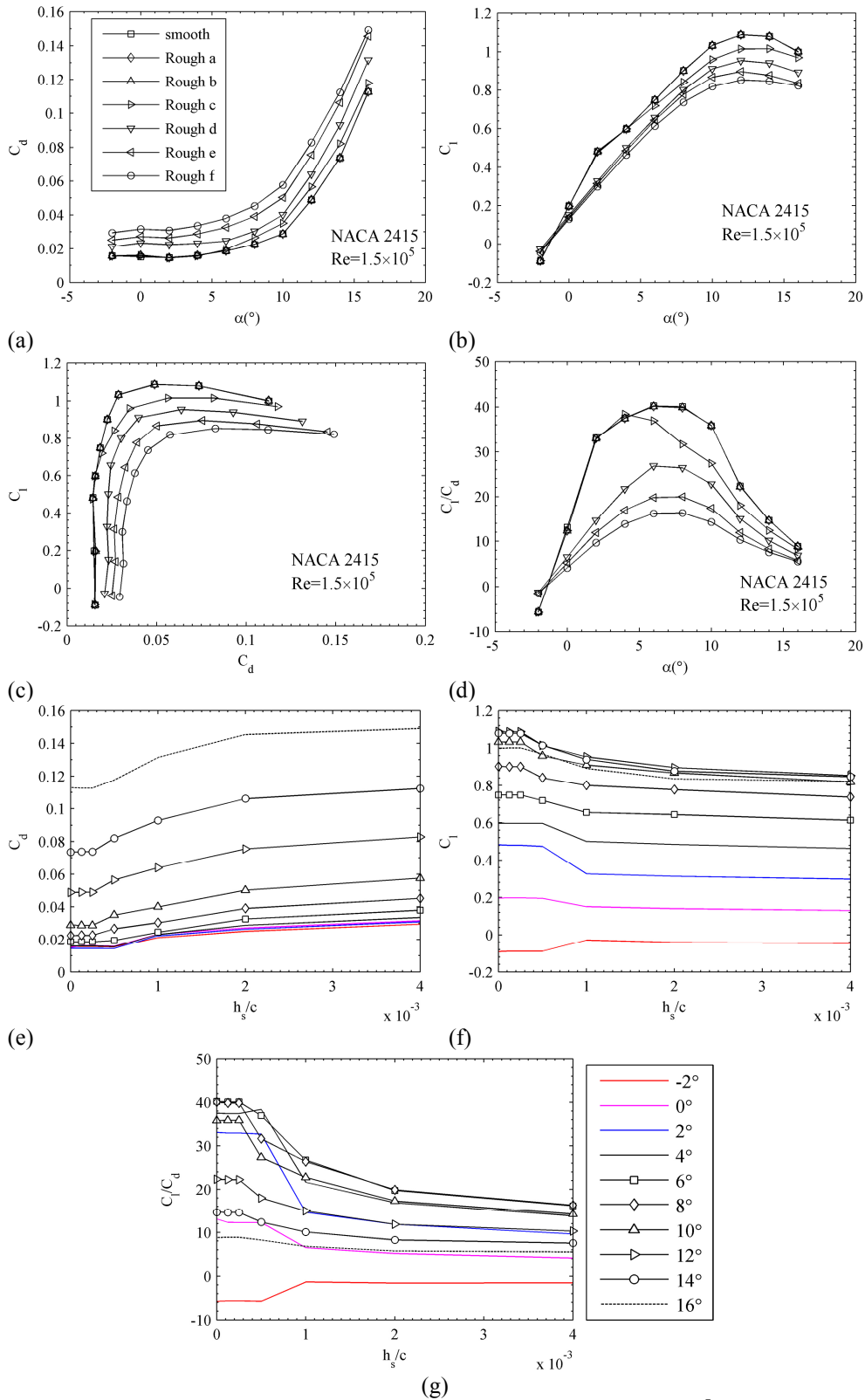
Fig. 6-7. The aerodynamics affected by the roughness at $Re = 1.5 \times 10^5$, NACA 2415
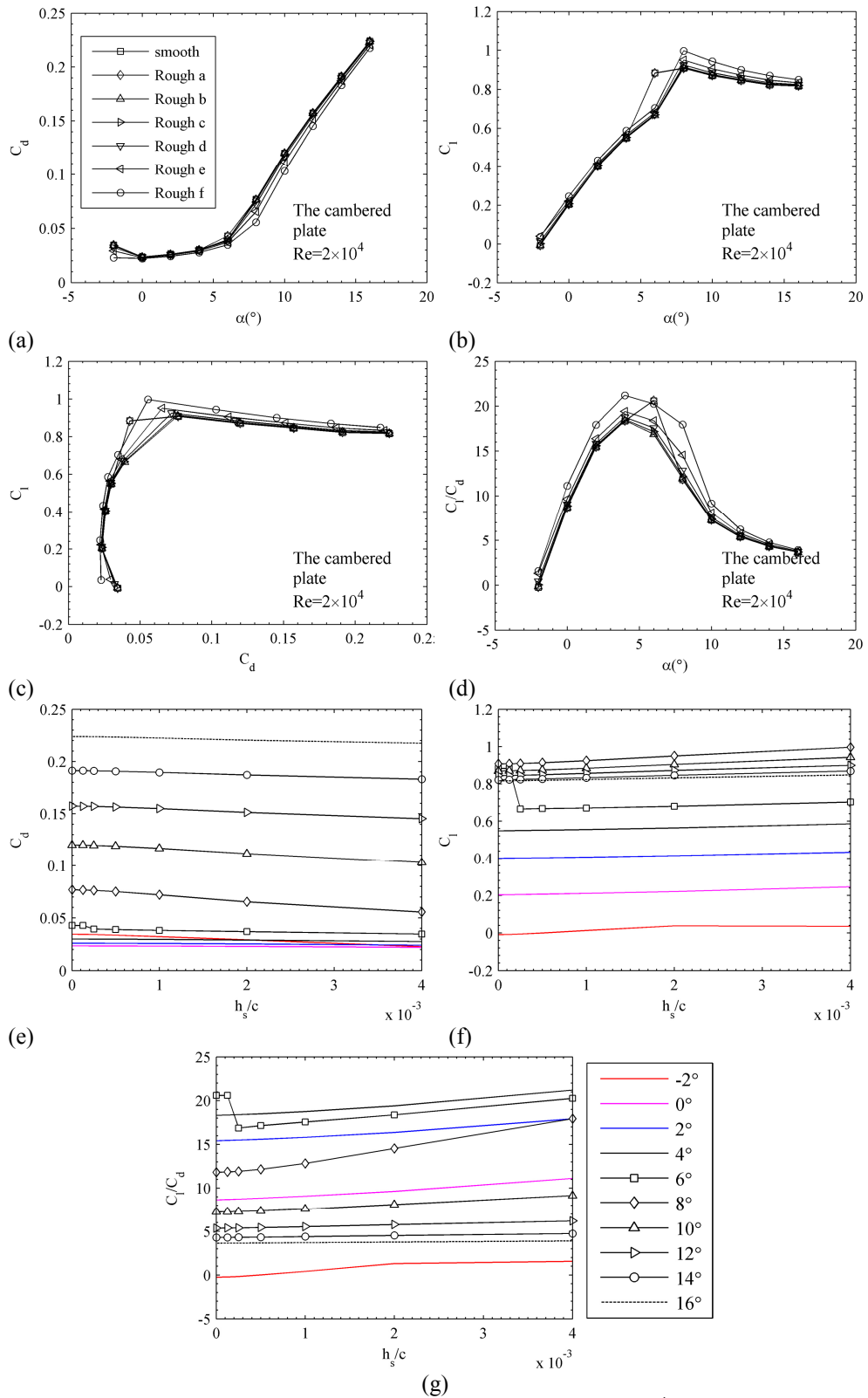
Fig. 6-8. The aerodynamics affected by the roughness at $Re = 2 \times 10^4$, the cambered plate

(a)

(b)

(c)
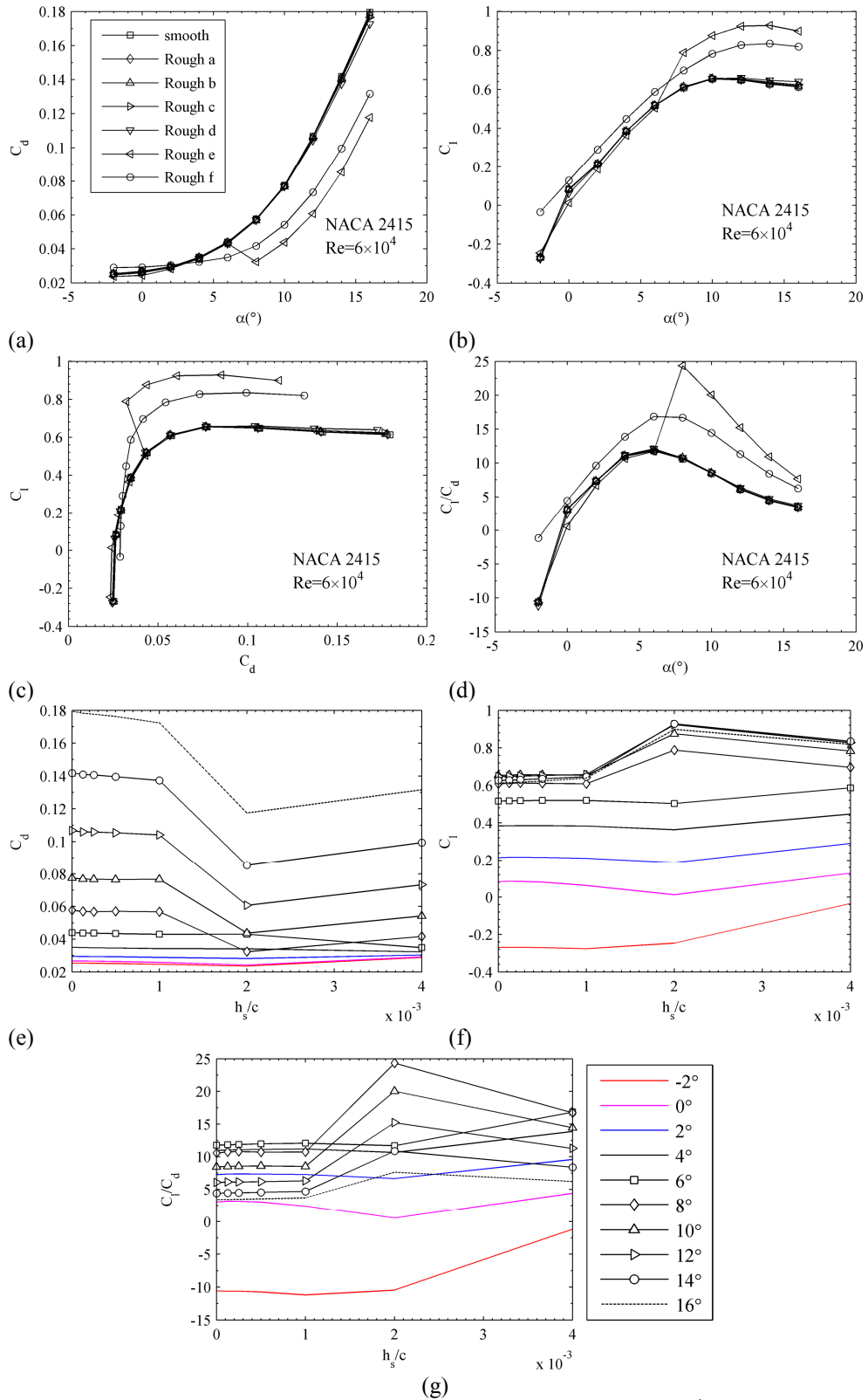
(d)

(e)

(f)

(g)
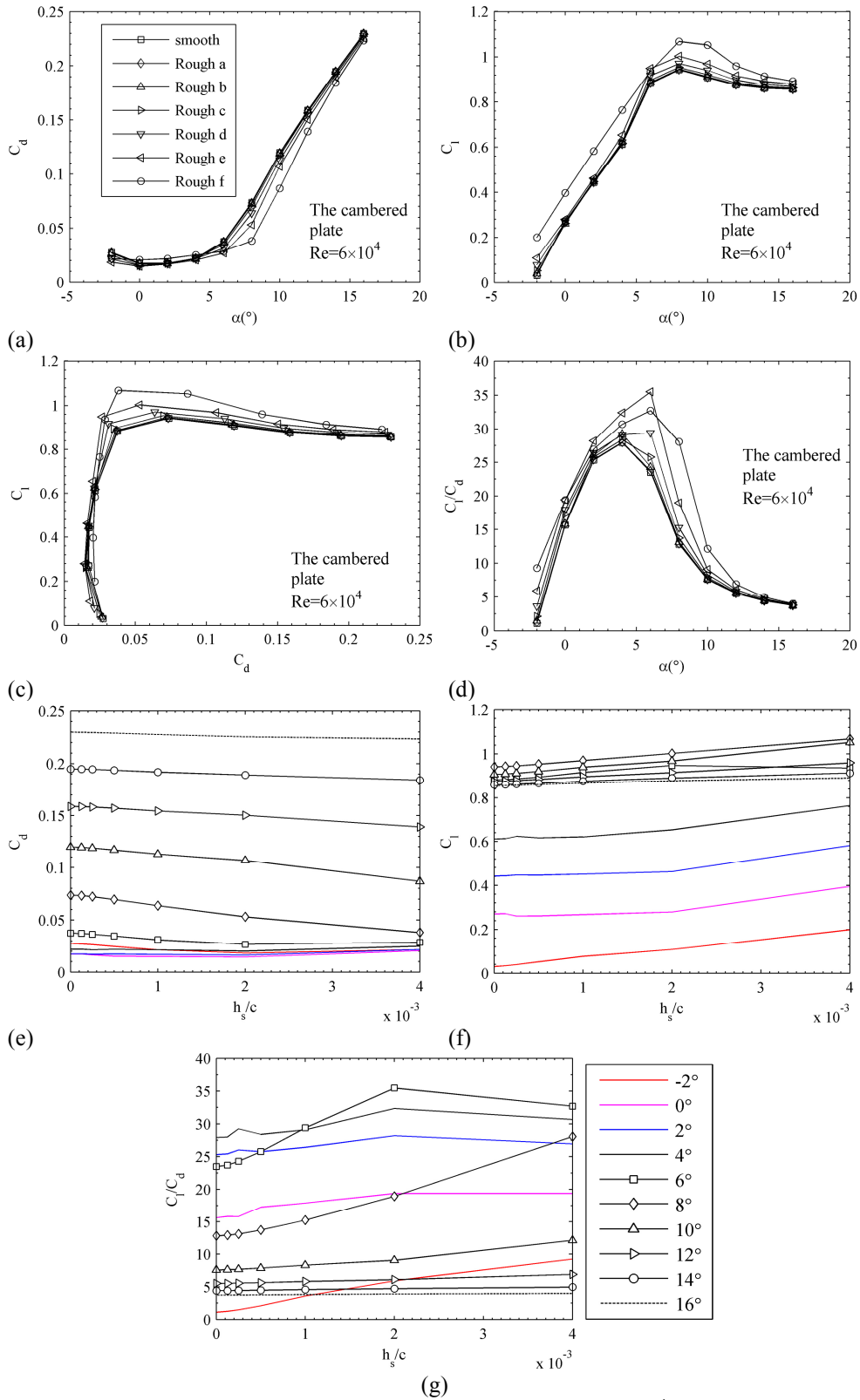
Fig. 6-9. The aerodynamics affected by the roughness at *Re* = 6×10⁴, the cambered plate

(a)

(b)

(c)

(d)

(e)

(f)

(g)
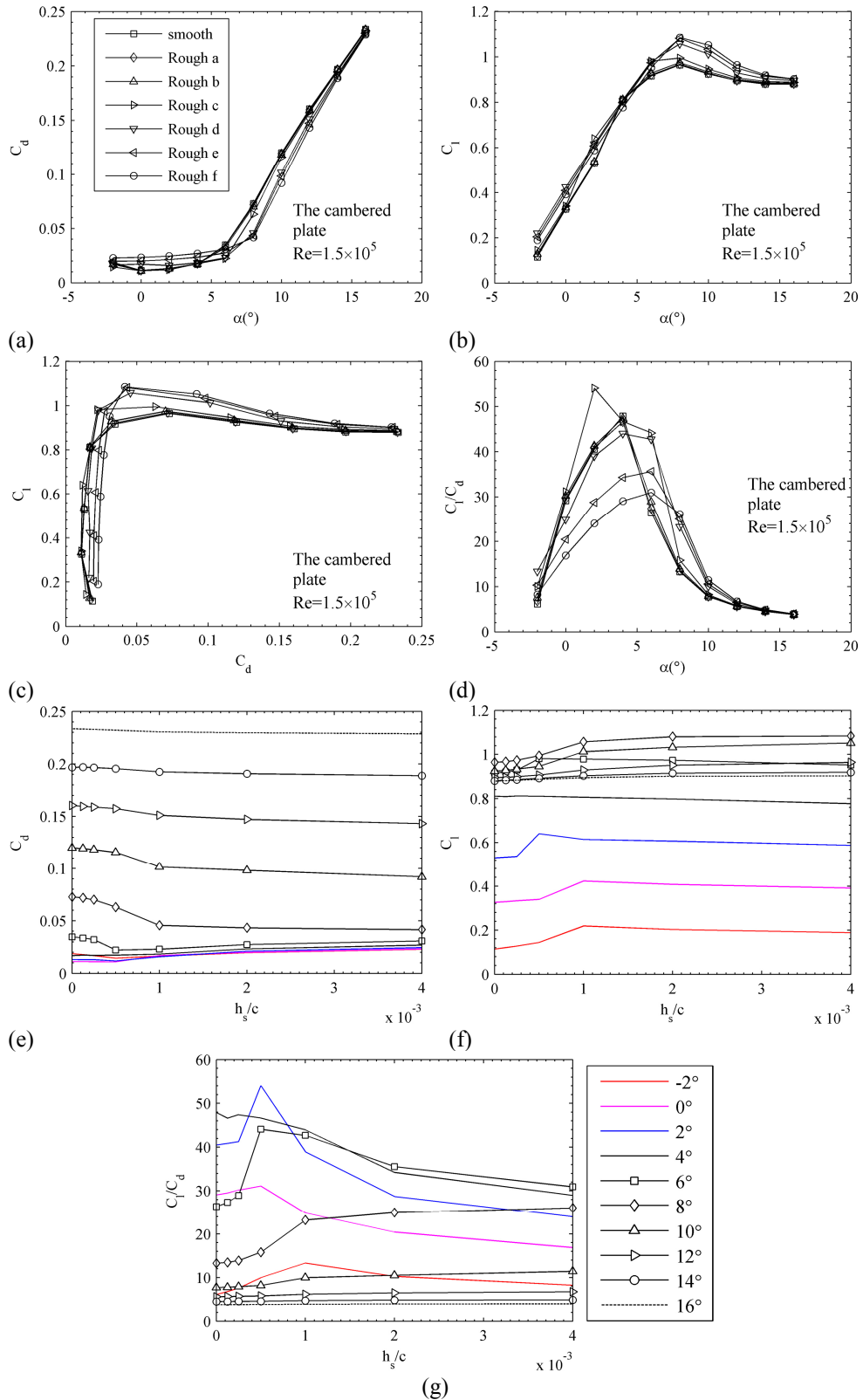
Fig. 6-10. The aerodynamics affected by the roughness at *Re* = 1.5×10⁵, the cambered plate

6.3.4 Minimum Effective Roughness at Low Reynolds Numbers

The results presented demonstrate that the roughness needs to be sufficiently high to take effects. The minimum relative roughness is computed and compared to relation (2-1), as shown in Table 6-3. For the purpose of the comparison, only the drag results for the three aerofoils at $\alpha = 0°$ are taken into account. It can be seen that relation (2-1) matches the simulation result for the most cases, and it is inclined to be conservative.

Table 6-3 Admissive roughness height*

Name	h_s/c	$h_s/c \geq h_{adm}/l$? / notable simulated roughness effects?		
		$Re=2\times10^4$ $h_{adm}/l =5.00\text{E-}03$	6×10^4 1.67E-03	1.5×10^5 6.67E-04
Rough a	1.25E-04	no/no	no/no	no/no
Rough b	2.50E-04	no/no	no/no	no/no
Rough c	5.00E-04	no/no	no/no	no/yes
Rough d	1.00E-03	no/no	no/no	yes/yes
Rough e	2.00E-03	no/no	yes/yes	yes/yes
Rough f	4.00E-03	no/yes	yes/yes	yes/yes

$$*h_{adm}/l \leq \frac{100}{Re}$$

For relation (2-2), it is actually an equivalently loosened relation than relation (2-1). It is noticed that relation (2-2) is satisfied when the roughness induced transition happens. For example for all aerofoils, it is the *Rough f* condition at Re = 6×10^4 and the *Rough d* condition at $Re = 1.5\times10^5$.

These agreements to some degree validate the simulation result, and it should be noted that the admissive roughness could be smaller for higher incidences.

6.4 Flow Field for Rough Aerofoils

The change in the lift and drag presented in Section 6.3 is closely related to the change in the flow field. In the context of flows on aerofoils at low Reynolds numbers, the roughness effects on the lift and drag is determined by the effects on the separation. The following discussions are made on the detailed roughness effect on each incidence.

6.4.1 NACA 0012

When $Re = 2\times10^4$, the flow on the upper surface separates near the mid-chord location at $\alpha = 0°$, and the separation point moves upstream when the incidence increases. The separation is laminar separation without reattachment. When the roughness is increased, this separation point moves downstream. This may indicate that the flow at the separation point is transitional when the roughness is applied. The enhanced turbulence kinetic energy transferred from upstream, due to the roughness, maintains longer attached boundary layers (here uses the turbulence kinetic energy to describe all fluctuation energy in transitional and turbulent flow).

The reduction in the separation explains the general trend for the change in the lift (increase) and drag (reduction). The reduction at $\alpha = 6°$ may be due to the suction loss at all roughness conditions.

When $Re = 6\times10^4$, the flow on the upper surface separates near 0.6c at $\alpha = 0°$, and the separation moves upstream when the incidence increases. From $\alpha = 6°$, a separation bubble forms from 0.08c to 0.45c. Its length shrinks, and its location moves upstream when the incidences increases. From $\alpha = 8°$, a second (turbulent) separation after the reattachment starts from approximately 0.7c. This separation point moves upstream until the flow on the upper surface completely separates ($\alpha \geq 10°$).

For $\alpha \leq 4°$, in small to intermediate roughness conditions, the separation near the trailing edge reduces. This leads to a reduction in the lift and the pressure drag. The lift to drag ratio reduces. When sufficient roughness is applied (*Rough f* for $\alpha = 0°$ and $2°$ and *Rough e* for the rest), the separation is eliminated. This leads to an increase in the lift and a reduction in the pressure drag. The total drag is increased due to the rise in the skin friction drag. For $\alpha = 4°$, more roughness further reduces the lift and increases the pressure drag and the total drag. The rise in the skin friction drag at this Reynolds number is an important contributor for the rise in the total drag.

For $\alpha = 6°$ and $8°$, the bubble can be eliminated by the roughness (*Rough*

e). The lift and the pressure drag reduce for $\alpha = 6º$. The total drag reduces. The lift to drag ratio increases. For $\alpha = 8º$, when the bubble is eliminated, the separation near the trailing edge is also eliminated. This leads to an increase in the lift and reduction in the pressure drag and the total drag. More roughness reduces the lift and increases the pressure drag and total drag for both incidences.

The increase in the lift for $\alpha \geq 10º$ is because of the reduction of the leading edge separation due to the roughness. However, if high roughness is applied, the separation point moves upstream. This upstream movement is believed to be caused by the more thickened boundary layer due to the roughness. Because of this, the suction peak reduces, the lift reduces, and the pressure drag increases. The total drag also increases.

Compare to previous Reynolds number, the reduction in the lift at small to moderate roughness conditions is evident for $\alpha = 2º\sim6º$.

When $Re = 1.5\times10^5$, the flow pictures are similar to $Re = 6\times10^4$, with a more downstream separation point and a bubble formed for $\alpha = 2°\sim12º$. With sufficient roughness (*Rough c*), the bubble can be eliminated, and the lift reduces. The pressure drag reduces, while the total drag increases due to the rise in the skin friction drag. The skin friction drag enhanced by the roughness is more substantial at than the previous Reynolds number.

For $\alpha = 8°$ and $10°$, the flow on the upper surface has a bubble and a trailing edge separation. When the bubble is eliminated, the trailing edge separation remains almost the same location. This results in the reduction in the lift and the pressure drag. The total drag increases due to the rise in the skin friction drag. More roughness moves the separation point upstream. This leads to the increase in the pressure drag and the reduction in the lift.

For $\alpha = 12°$ and above, the roughness reduces the leading edge separation. The change in the lift and drag is similar to that for $Re = 6\times10^4$. The total drag is generally increased due to the excessive skin friction drag. The small rise in the lift for $\alpha = 14°$ and $16º$ is due to the downstream movement of the separation

point.

6.4.2 NACA 2415

When $Re = 2 \times 10^4$, the flow is similar to that for NACA 0012 aerofoil. The flow separates on the upper surface and the separation point moves upstream when the incidence increases. The roughness moves the separation point downstream, resulting in the increase in the lift and the reduction in the pressure drag and total drag at all roughness conditions..

When $Re = 6 \times 10^4$, compared to NACA 0012 aerofoil, the flow never attaches back to the upper surface to form a bubble. For $\alpha \leq 6°$, similar to the NACA 0012 aerofoil, the reduction of the trailing edge separation at small to intermediate roughness conditions leads to the reduction in the lift and the pressure drag, as well as the increase in the total drag due to the rise in the skin friction drag. The highest roughness (*Rough f*) reduces the separation substantially (the separation is not entirely eliminated for $\alpha \geq 4°$), resulting in the increase in the lift and the reduction in the drag.

For $\alpha \geq 8°$, the *Rough e* condition starts to delay the separation point substantially, and the *Rough f* condition moves the separation point again forward. This delay and forward movement of the separation point is similar to the cases $\alpha \geq 10°$ for NACA 0012, as well as the associated change in the lift and the drag.

When $Re = 1.5 \times 10^5$, compared to previous Reynolds numbers, the separation bubble exists for $\alpha = 2°\sim16°$ on the upper surface. The roughness starts to eliminate the separation or the separation bubble from the *Rough d* condition for $0° \leq \alpha < 10°$ or the *Rough c* condition for $\alpha \geq 10°$. The elimination of the bubble leads to the reduction in the lift and pressure drag for $\alpha = 2°\sim8°$. The total drag generally increases due to the rise in the skin friction drag.

From $\alpha = 6°$, a second separation occurs near the trailing edge after the bubble on the smooth surface. After the bubble is eliminated by the roughness, the separation point still remains and locates upstream. This upstream movement is found to be more evident for higher incidences ($\alpha \geq 10°$).

Therefore the lift reduces and the pressure drag increases, also for more roughness.

Compared to NACA 0012 aerofoil, NACA 2415 aerofoil at $Re = 1.5 \times 10^5$ can improve no lift near stall. This may due to the separation bubble exists near the stall incidence. The roughness removes the bubble and reduces the lift.

6.4.3 The Cambered Plate

The flow on the cambered plate at the three Reynolds numbers is similar. At low incidences, a separation occurs near the trailing edge on the upper surface. At intermediate incidences, a separation bubble occurs near the leading edge, and its size increases as the incidence increases. A second separation after the bubble also occurs near the trailing edge. At higher incidences, the full separation of the flow on the upper surface occurs when the separation bubble and the trailing edge separation merges. The incidence for the occurrence of the bubble is 6º for $Re = 2 \times 10^4$ and 6×10^4, and 4º, 6º and 8º for $Re = 1.5 \times 10^5$.

When the roughness is applied, the trailing edge separation at low incidences and the leading edge separation at high incidences reduce, resulting in the increase in the lift and the reduction in the pressure drag. At the *Rough e* condition when $Re = 6 \times 10^4$ and the *Rough c* condition when $Re = 1.5 \times 10^5$, the roughness is sufficient to eliminate the separation. More roughness leads to the reduction in the lift and the increase in the pressure drag. Compared to the other two aerofoils, the cambered plate is different, because the reduction in the trailing edge separation at low incidences leads to an increase in the lift.

The bubble can be eliminated when sufficient roughness is applied, resulting in the reduction in the pressure drag. The related change in the lift is different for different Reynolds numbers. At $Re = 2 \times 10^4$, the *Rough b* condition reduces the length considerably, while the trailing edge separation extends upstream. The lift reduces greatly and the pressure drag reduces. More roughness further reduces the bubble and the separation, resulting in further reduction in the increase the lift and the reduction in the pressure drag. The total drag reduces as the pressure drag reduces. At $Re = 6 \times 10^4$ and 1.5×10^5, the

roughness can eliminate the bubble and the trailing edge separation at the same time. The lift increases, and the pressure drag reduces. More roughness leads to the reduction in the lift and the increase in the pressure drag. The total drag generally increases due to the rise of the skin friction drag.

6.4.4 Summary

The cambered plate may represent thin aerofoils, and the NACA 0012 and NACA 2415 aerofoils may represent aerofoils with moderate thickness. The general roughness effects on aerofoils with thin and moderate thickness are summarised in Table 6-4 and Table 6-5.

In terms of better C_l/C_d, the roughness is generally not recommended for moderate thick aerofoil at low incidences and the incidences with bubbles. For high incidences, the roughness can generally delay the stall and enhance C_l/C_d and $C_{l,max}$. Furthermore, a moderate Reynolds number and a suitable Roughness height are required to have notable beneficial effects. The thin profile is distinct. It can have $C_{l,max}$ improved for all the Reynolds numbers studied.

Table 6-4. The roughness effects for thin aerofoils
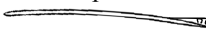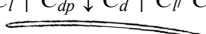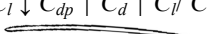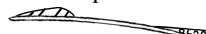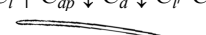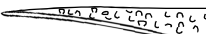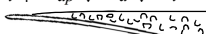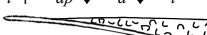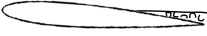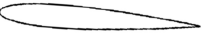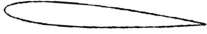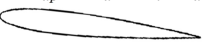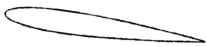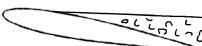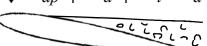
Smooth ($\alpha \uparrow$)	Rough	High roughness
TE separation	The separation is reduced or ellminated. $C_l \uparrow C_{dp} \downarrow C_d \uparrow C_l/C_d \uparrow$	$C_l \downarrow C_{dp} \uparrow C_d \uparrow C_l/C_d \downarrow$
LE bubble + TE separation	1. The bubble is reduced, while the separation extends upstream ($Re=2\times10^4$, $\alpha=6°$ only). $C_l \downarrow C_{dp} \downarrow C_d \downarrow C_l/C_d \downarrow$ 2. The bubble and the separation are reduced or ellminated at the same time. $C_l \uparrow C_{dp} \downarrow C_d \downarrow C_l/C_d \uparrow$	The buble is ellminated, and the separation are reduced $C_l \uparrow C_{dp} \downarrow C_d \downarrow C_l/C_d \uparrow$ $C_l \downarrow C_{dp} \uparrow C_d \uparrow C_l/C_d \downarrow$
LE separation	The separation point is delayed. $C_l \uparrow C_{dp} \downarrow C_d \downarrow C_l/C_d \uparrow$	The separation point is further delayed. $C_l \uparrow C_{dp} \downarrow C_d \downarrow C_l/C_d \uparrow$

Table 6-5. The roughness effects for moderate thick aerofoils

Smooth ($\alpha \uparrow$)	Rough	High roughness
TE separation	1. The separation is reduced for small to moderate roughness. $C_l \downarrow C_{dp} \downarrow C_d \downarrow C_l/ C_d \downarrow$ 2. The separation is ellminated by sufficent roughness. $C_l \uparrow C_{dp} \downarrow C_d \uparrow C_l/ C_d \downarrow$	$C_l \downarrow C_{dp} \uparrow C_d \uparrow C_l/ C_d \downarrow$
TE bubble	The bubble is eliminated. $C_l \downarrow C_{dp} \downarrow C_d \uparrow C_l/ C_d \downarrow$	$C_l \downarrow C_{dp} \uparrow C_d \uparrow C_l/ C_d \downarrow$
LE bubble + TE separation	1. Both the bubble and the separation are ellminated (NACA 0012, Re= 60000). $C_l \uparrow C_{dp} \downarrow C_d \downarrow C_l/ C_d \uparrow$ 2. The bubble is ellminated, while the separation remains almost the same, likely to happen at Re= 150000. $C_l \downarrow C_{dp} \downarrow C_d \uparrow C_l/ C_d \downarrow$	$C_l \downarrow C_{dp} \uparrow C_d \uparrow C_l/ C_d \downarrow$ The separation point moves upstream. $C_l \downarrow C_{dp} \uparrow C_d \uparrow C_l/ C_d \downarrow$
LE separation	The separation point is delayed. $C_l \uparrow C_{dp} \downarrow C_d \downarrow C_l/ C_d \uparrow$ Note: The separation occurs at Re=20000 at all incidences behave like this.	Re=20000 The separation point is further delayed. $C_l \uparrow C_{dp} \downarrow C_d \downarrow C_l/ C_d \uparrow$ Re= 60000 and 150000 The separation point moves upstream. $C_l \downarrow C_{dp} \uparrow C_d \uparrow C_l/ C_d \downarrow$

It is interesting to note the roughness effects on the lift and drag are different at low α between the thin cambered plate and the moderate thick NACA 0012/NACA 2415 aerofoils. This may indicate the trailing edge separations on NACA 0012/NACA 2415 and the cambered plate are different. A clear answer to this difference requires further investigations.

6.5 Reynolds Number Effects for Rough Aerofoils

In the previous results at each Reynolds number, it has been demonstrated that the aerodynamic performance can be improved at some conditions. However, in real applications, MAV may have a range of operating speed, a

fixed roughness height may not introduce the beneficial effects at all Reynolds numbers, and the same for the detrimental effects. The result in this section investigates the roughness effects for a given roughness height under the change in Reynolds numbers. Firstly, the lift and drag results are organised for a given roughness condition. The selected conditions are smooth, *Rough e* and *Rough f*. The latter two demonstrate the most notable roughness effects in previous results. Secondly, the critical Reynolds number is discussed, showing the related roughness effects. Thirdly, the roughness effects with varied Reynolds number on $C_l/C_{d,max}$ *and* $C_{l,max}$, as two important aerodynamic factors, are compared to McMaster and Henderson's diagram[93], which is an aerofoil survey based on experimental data.

6.5.1 Comparison of Smooth and Two Roughness Conditions

Fig. 6-11, Fig. 6-12 and Fig. 6-13 show the lift and drag coefficients of NACA 2415 aerofoil at various Reynolds numbers under given roughness conditions (Smooth, *Rough e* and *Rough f*). The aerodynamics on the smooth surface is highly dependent on the magnitude of the Reynolds number, i.e. low Reynolds number effects. By comparison, when the roughness is applied, especially at the largest roughness height, the difference in the aerodynamic performance is eliminated for $Re \geq 6 \times 10^4$. In other words, rough aerofoils with sufficient roughness can have little change in aerodynamic performance within a range of Reynolds number.

Fig. 6-14, Fig. 6-15, Fig. 6-16 and Fig. 6-17 further show the results on NACA0012 aerofoil and the cambered plate profile under the smooth and *Rough f* conditions. The lesser dependence on the Reynolds number for the aerodynamic performance is similarly observed at the *Rough f* condition. It should be noted the lesser dependence on the Reynolds number is not necessarily a beneficial effects for higher Reynolds numbers, because the previous good performance deteriorates to a lower level. Although there is no direct comparable literature, the simulation by Xia[128] on an aerofoil with corrugated skin showed similar Reynolds number effects.

(a)

(b)

(c)

(d)

(e)

(f)

(g)
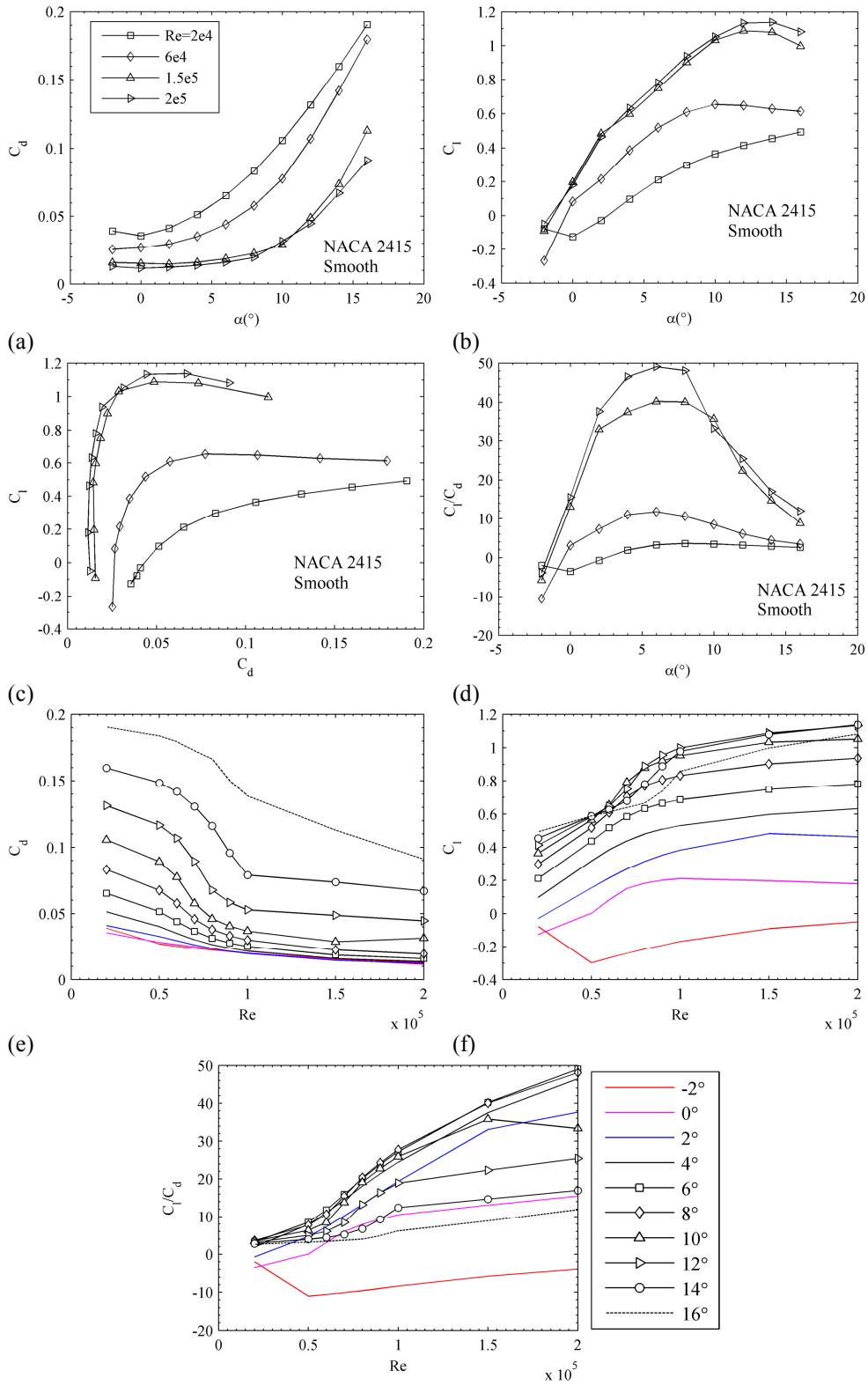
Fig. 6-11. Reynolds number effects on smooth NACA 2415
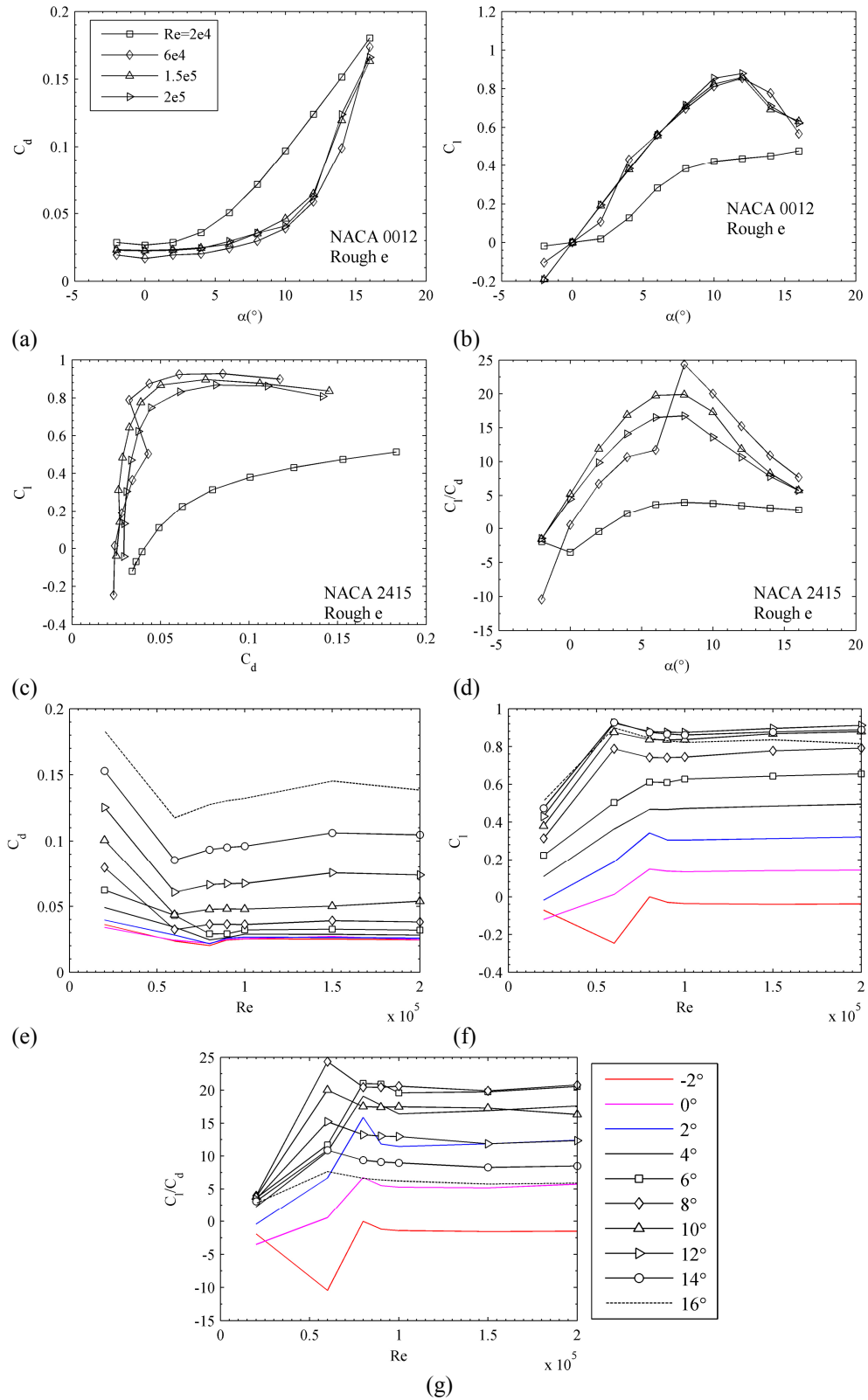
Fig. 6-12. Reynolds number effects on rough NACA 2415, *Rough e* condition

111

(a)

(b)

(c)

(d)

(e)

(f)

(g)
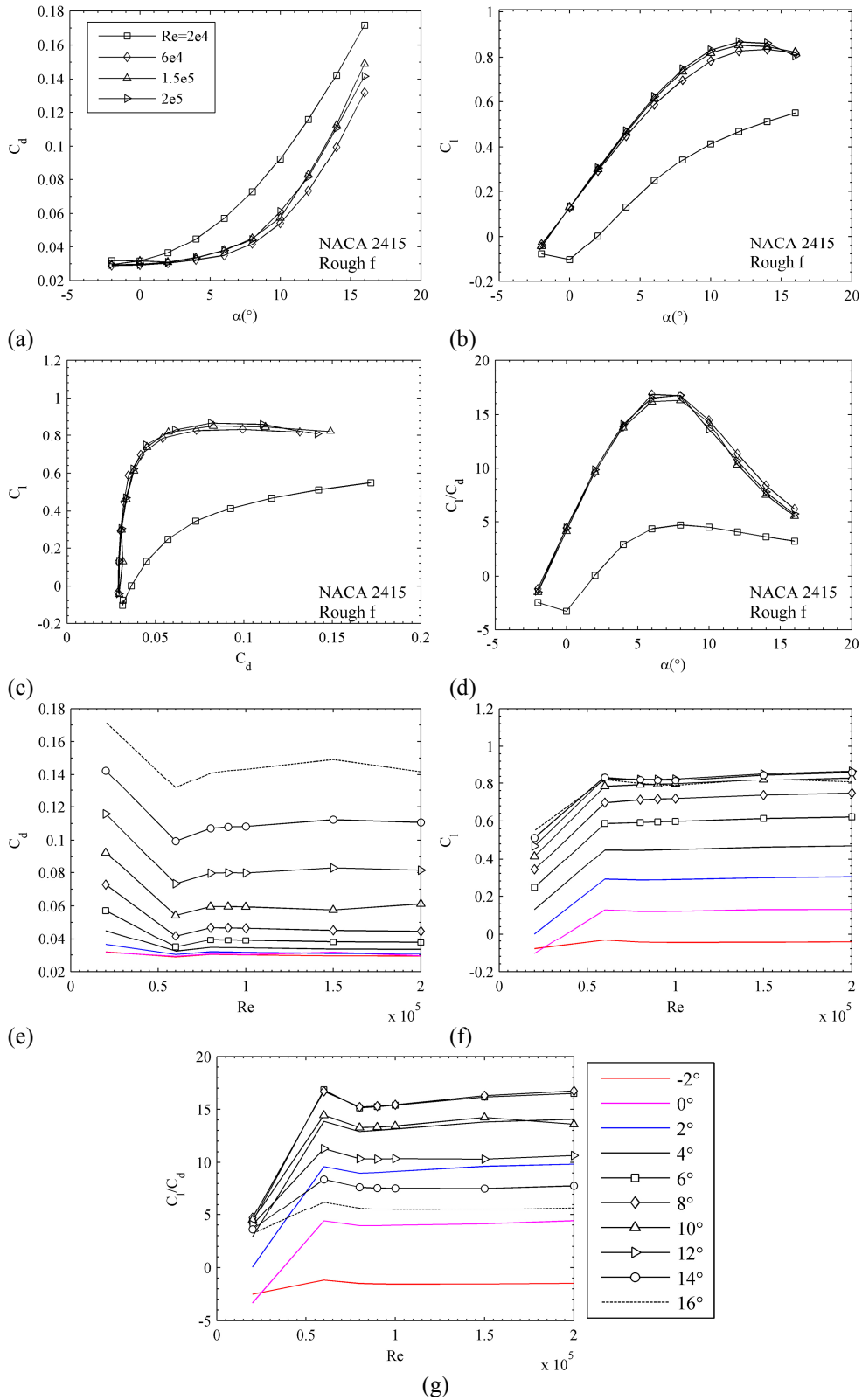
Fig. 6-13. Reynolds number effects on rough NACA 2415, *Rough f* condition
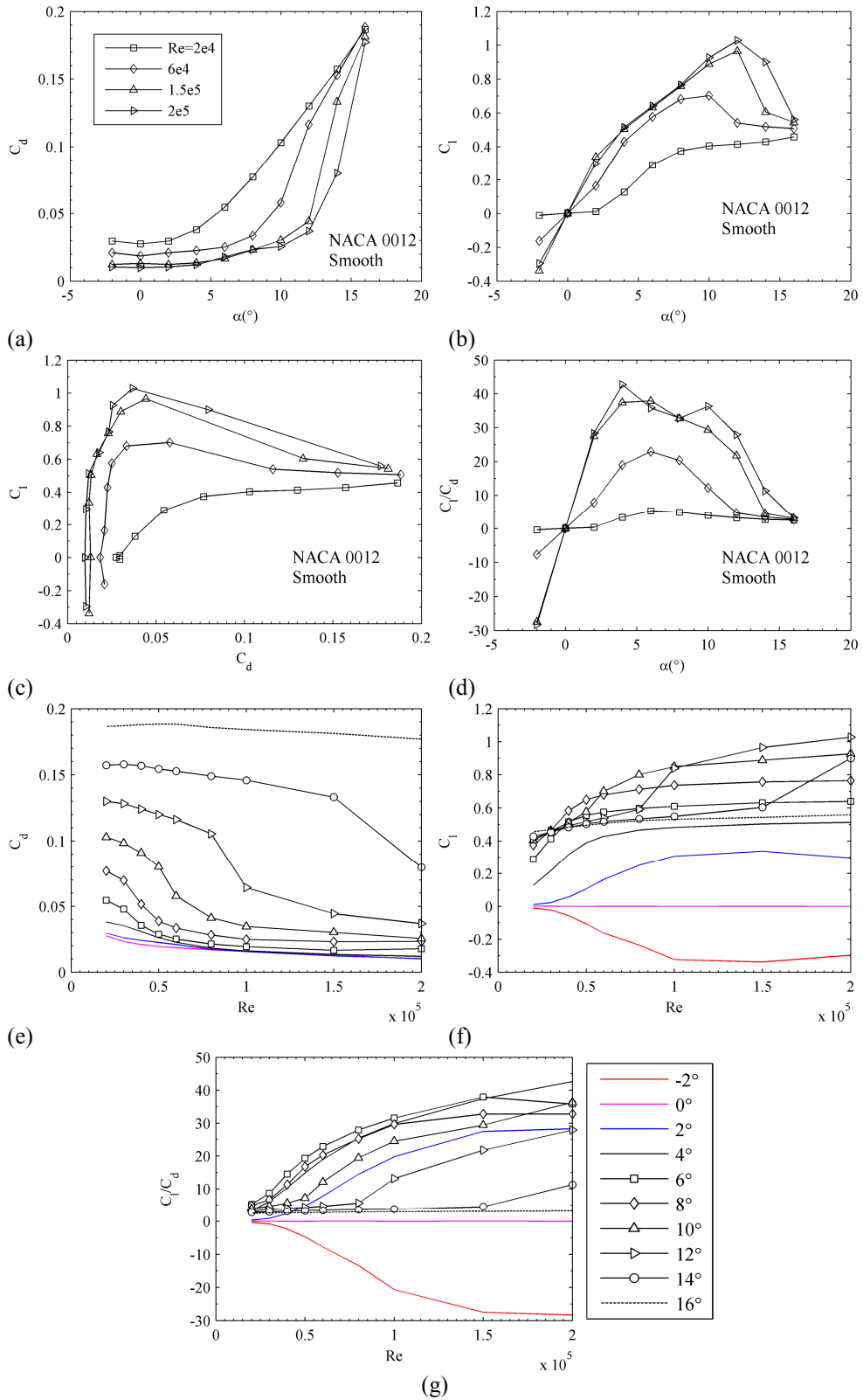
Fig. 6-14. Reynolds number effects on smooth NACA 0012

(a)

(b)

(c)

(d)

(e)

(f)

(g)
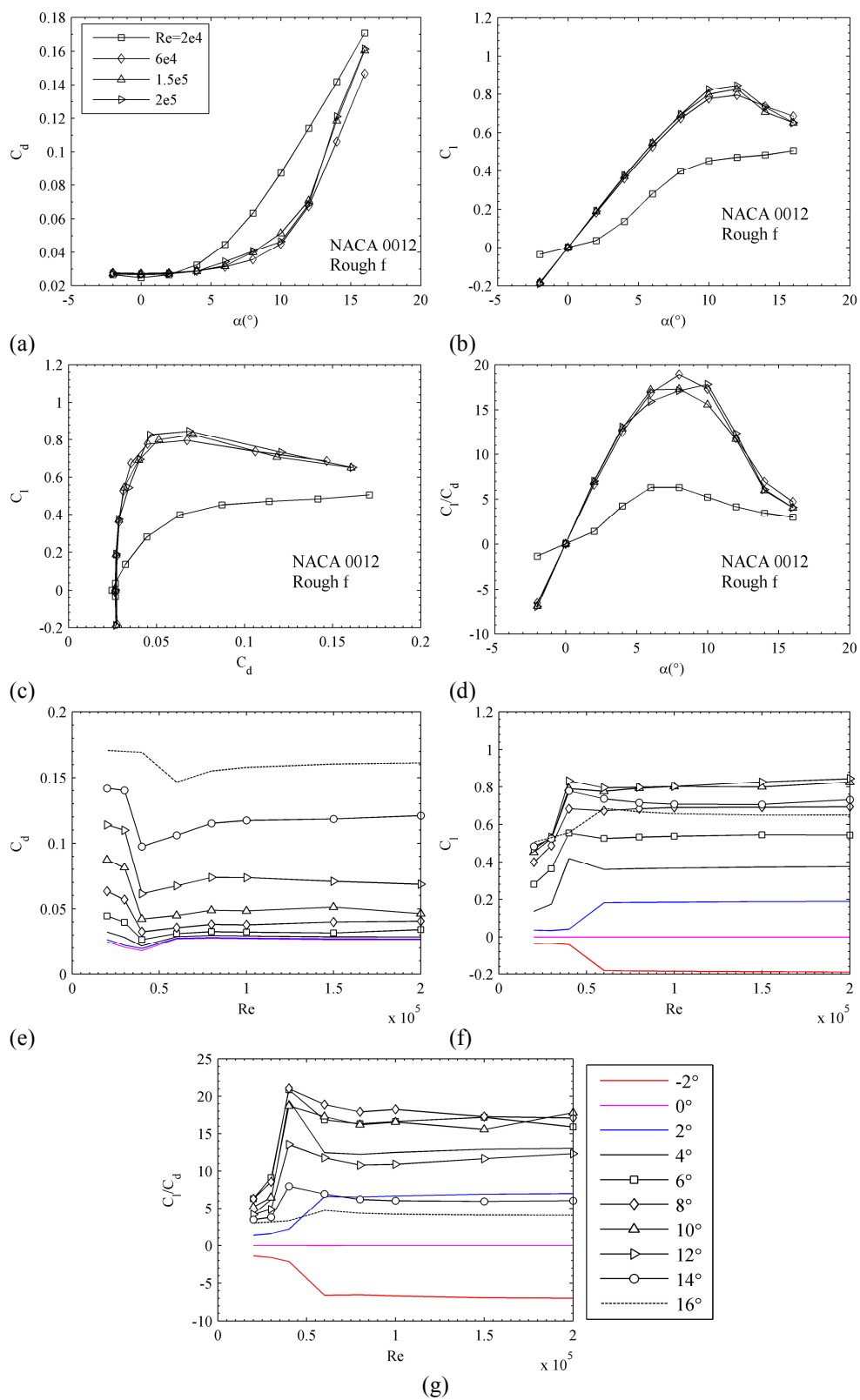
Fig. 6-15. Reynolds number effects on rough NACA 0012, *Rough f* condition

114

(a)

(b)

(c)

(d)

(e)

(f)

(g)
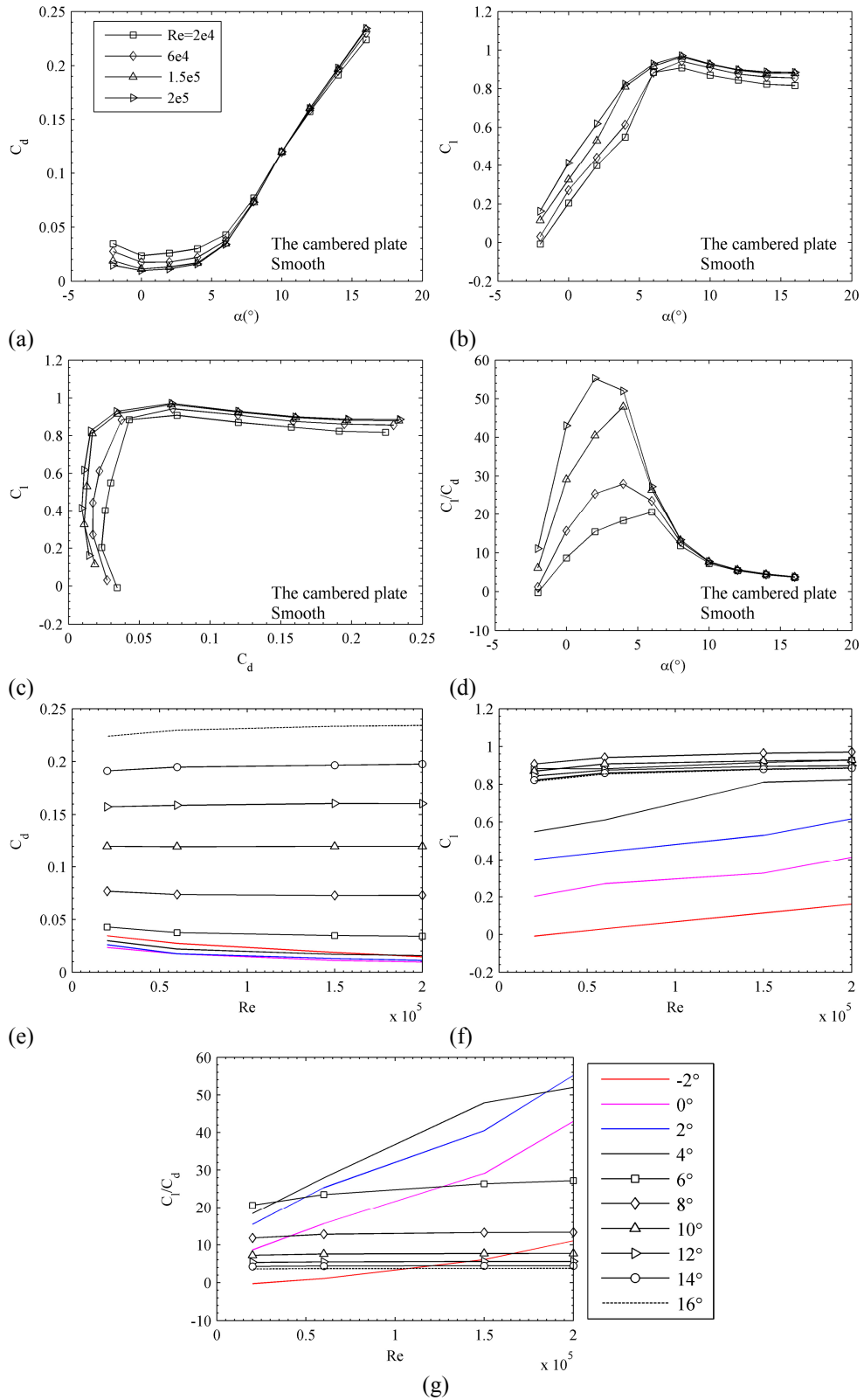
Fig. 6-16. Reynolds number effects on the smooth cambered plate
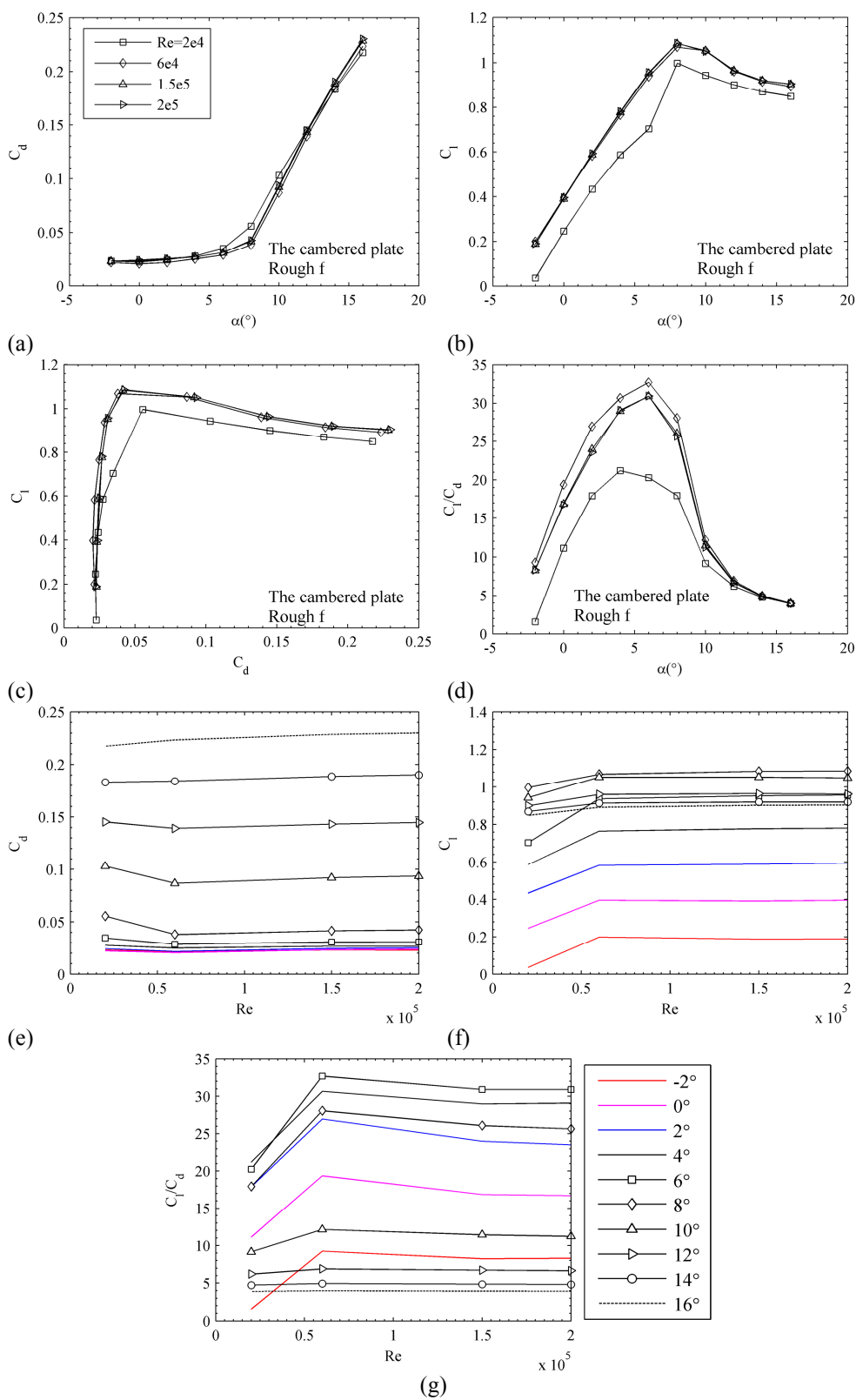
Fig. 6-17. Reynolds number effects on the rough cambered plate, *Rough f* condition

The observation above implies that, for a given aerofoil, an appropriate roughness height can only exist in a small range of Reynolds numbers, preferably at lower Reynolds numbers. The choice of roughness condition

116

should therefore take accounts of the design requirement of a given MAV. For example, if the vehicle is required to operate in a broad speed range and the fluctuation of performance is not desired, the *Rough f* condition may be used. If the vehicle is expected to fly around $Re = 6 \times 10^4$ and the performance near that low Reynolds number is of the most importance, the *Rough e* condition may be used.

6.5.2 Variation of Critical Reynolds Number for Different Roughness Conditions

The $Re_{crit,min}$ for the three aerofoils on smooth and rough aerofoils is obtained by checking the flow field at various Reynolds number, and the results are shown in Table 6-6. It is observed that the three types of aerofoil have distinct $Re_{crit,min}$. This difference can be the reason for their difference in lift and drag characteristics at low Reynolds numbers. It is also observed that, the roughness has the effects to decrease the $Re_{crit,min}$. In other words, the roughness can extend the operating speed range of a given MAV to lower speed. The aerofoil mostly benefited from the roughness effects is the thickest NACA 2415, indicating that thick aerofoils can also be employed at low Reynolds numbers, provided that a suitable roughness is applied.

Table 6-6 The comparisons of $Re_{crit,min}$

	NACA 0012		NACA 2415		The cambered plate	
	Smooth	Rough f	Smooth	Rough f	Smooth	Rough f
$Re_{crit,min}$	5×10^4	4×10^4	9×10^4	$<6 \times 10^4$	$<2 \times 10^4$	$<2 \times 10^4$

6.5.3 Comparison with McMaster and Henderson's diagram

The key factors denoting the flight performance, $C_l/C_{d,max}$ and $C_{l,max}$, are plotted against the variation of Reynolds number in Fig. 6-18 and Fig. 6-19. The data is plotted along with McMaster and Henderson's diagram[93], which provides an aerofoil data survey in a range of low Reynolds numbers. The roughness condition that provides the best performance at $Re = 2 \times 10^4$ or 6×10^4 is selected.

It is observed that, whatever the aerofoil, there is a "beneficial interval" for the Reynolds number, only within which the roughness introduces better $C_l/C_{d,max}$. The thickest NACA 2415 presents the largest interval, whereas the thinnest cambered plate presents the smallest interval.

The beneficial interval is also valid for $C_{l,max}$ for NACA 0012 and NACA 2415 aerofoils, whereas the $C_{l,max}$ for cambered plate is always improved. The NACA 0012 aerofoil presents the largest improvements on the $C_{l,max}$.

(a)

(b)

(c)
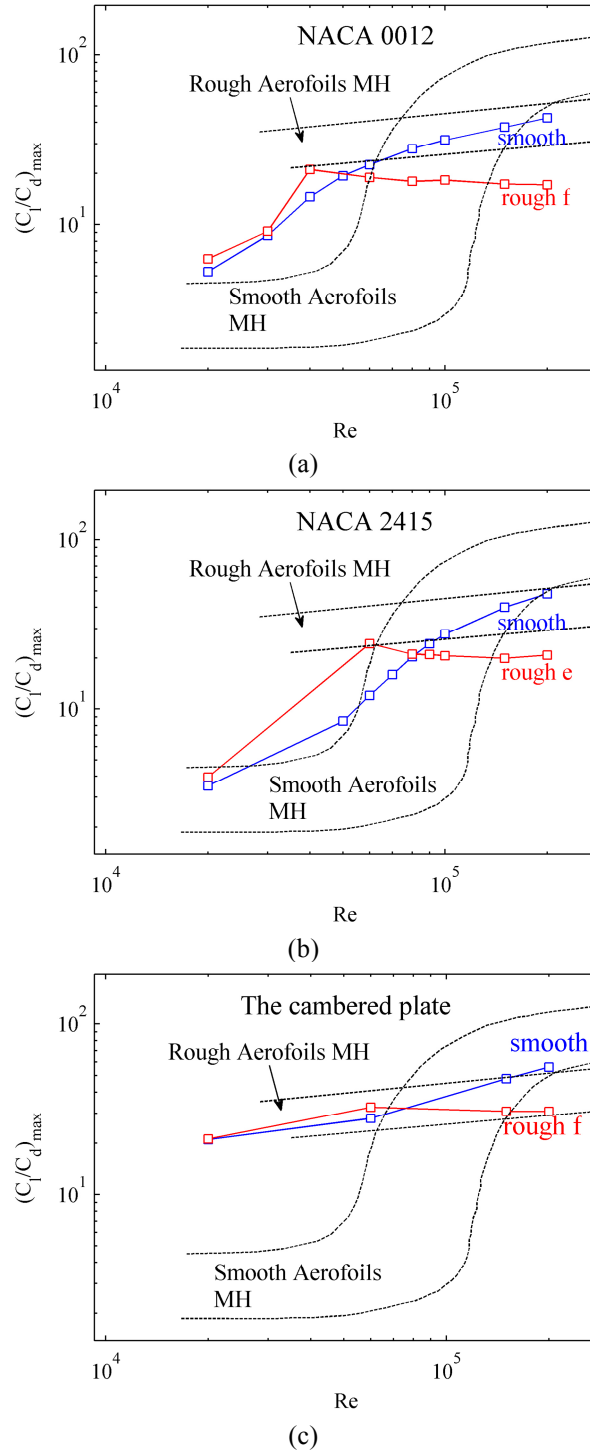
Fig. 6-18. Maximum lift to drag ratio comparisons, MH: McMaster and Henderson's survey[93]

(a)

(b)

(c)
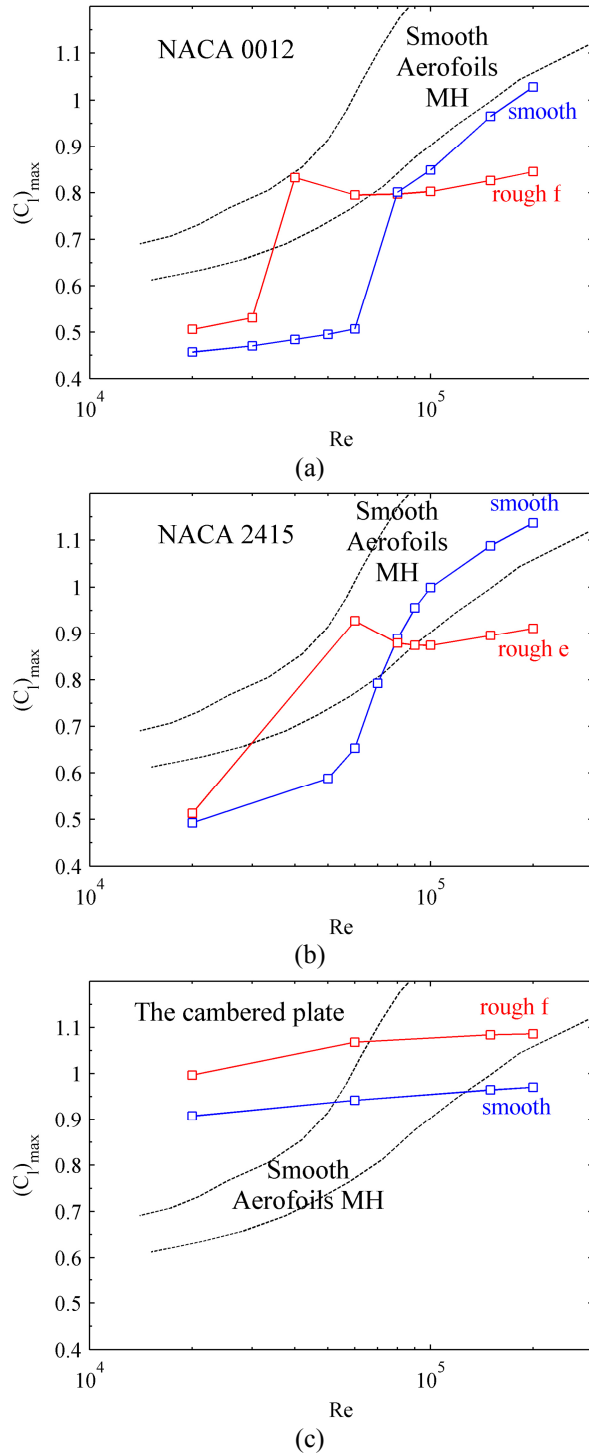
Fig. 6-19. Maximum lift comparisons, MH: McMaster and Henderson's survey[93]

The comparison between the simulated data and the diagram's data shows that the simulated data match the general trend for the smooth aerofoils while the data does not all fall inside the band. The sudden drop of the $C_l/C_{d,max}$ is not well-followed, even for the thickest NACA 2415 aerofoil. Possibly the selected data in the diagram demonstrates the worst situation or the possible change for other aerofoils.

For the rough aerofoils, the trend of the roughness is reproduced, although the data does not fall inside the band. Possibly the data selected for the diagram includes no data at lower Reynolds numbers to demonstrate the beneficial interval. The result from the simulations provides more information at the lowest Reynolds number. On the other hand, at higher Reynolds numbers, the diagram's data may demonstrate lesser roughness effects, because the degradation on very rough aerofoils can be more substantial.

The Reynolds numbers for the largest gain on $C_l/C_{d,max}$ and $C_{l,max}$ in Fig. 6-18 and Fig. 6-19 are interestingly found close to $Re_{crit,min}$ for NACA 0012 and NACA 2415 aerofoil. This may indicate that $Re_{crit,min}$ may be a simple tool to define the suitable Reynolds number for beneficial roughness effects. This should be applicable to aerofoils similar to NACA 0012 and NACA 2415, however not applicable to aerofoils similar to the thin cambered plate. For the cambered plate, there is no $Re_{crit,min}$, and the improvements on the $C_l/C_{d,max}$ is small.

6.6 Application of Roughness on Micro Air Vehicle

Among the literature reviewed, it is lack of the discussion on the application of the roughness on MAV design. Based on the results obtained, two applications are suggested as follows.

The first application is the aspect ratio of the wing. Most MAVs currently use low aspect ratio wings, with one purpose to increase the chord Reynolds number to reduce the parasite drag, and another purpose to ensure compactness and portability. However, reducing the aspect ratio increases the induced drag. It is possible to have a rough profile operates at lower Reynolds number without sacrificing the aerodynamic performance, meanwhile a higher aspect ratio wing has much less induced drag. An optimal combination of the roughness and wing's aspect ratio may exist. In such cases, a foldable wing or flexible wing design may be required to ensure the small size.

This idea should be possible for thick wings with moderate aspect ratios. The thick aerofoil is a good candidate, because it benefits the most from the

roughness with an appropriate roughness height. The use of thick aerofoils also provides the advantage for larger internal volume, which can be used to contain more battery or equipment. The Reynolds number selected for the operation must be within the beneficial interval.

The last application is the adaptive roughness for the flow control. As observed, a fixed roughness can only perform well in a narrow range of Reynolds numbers and incidences, so that an adaptive roughness is favoured. It can be deployed when necessary and changes according to the flow conditions. For example, for the NACA 0012 aerofoil at $Re = 6 \times 10^4$, it is preferable to have no roughness at lower incidences and high roughness at high incidences. In such way, the maximum lift can be improved without introducing detrimental effects at lower incidences. For another example, for the NACA 2415 aerofoil, it is preferable to have high roughness at lower Reynolds numbers and no roughness at higher Reynolds numbers. In such way, the lift and drag characteristics at lower Reynolds numbers can be improved without introducing the degradation at higher Reynolds numbers. The adaptive roughness may be realised by "flexible tuft". It can stand up on the surface for low dynamic pressure, making the surface rougher, and it can lay down for high dynamic pressure, making the surface smoother. This idea may be similar to the features of birds.

6.7 Conclusion

This work demonstrates an effort using the rough low Re SST model in the investigation for the roughness effects at low Reynolds numbers between 2×10^4 and 2×10^5. The rough aerofoils investigated are NACA 0012 aerofoil, NACA 2415 aerofoil and a cambered plate profile. The lift and drag characteristics on smooth and rough surfaces are compared for the roughness effects. Except for the drag reduction at $Re = 2 \times 10^4$, all trends of the roughness effects predicted are consistent with experimental data. A qualitative match to the aerofoil survey by McMaster and Henderson is also obtained[93]. The numerical results first observe the significant reduction of $C_l/C_{d,max}$ and $C_{l,max}$ at the even lower Reynolds number due to the roughness for moderate thick aerofoils.

The beneficial effects of the roughness are observed to be the reduction in

the drag, the increase in the lift, higher C_l/C_d, higher $C_{l,max}$, and higher $C_l/C_{d,max}$. The effects depend on the roughness effects on the separation.

The condition for the beneficial roughness effects is found to be influenced by the Reynolds number, the roughness height and the incidence. The appropriate Reynolds number is believed to be near the minimum critical Reynolds number. A beneficial interval is observed for all aerofoils. The roughness height is required to be appropriate at the suitable Reynolds numbers. The empirical relationships may provide an initial guess. The incidence relates to the separation type on the upper surface. Higher incidences are more likely to obtain beneficial effects. The elimination of the separation bubble reduces the lift for most cases at low incidences.

The beneficial effects on the three aerofoils are found to be different, while the NACA 0012 aerofoil and the NACA 2415 aerofoil show some similarity. The NACA 2415 aerofoils can have the largest improvements on $C_l/C_{d,max}$. The NACA 0012 can have the largest improvements on $C_{l,max}$. The cambered plate is different to the other two, because it has no minimum critical Reynolds number. The improvements on $C_l/C_{d,max}$ is small, while the improvements on $C_{l,max}$ is always possible at the Reynolds numbers studied.

Two possible applications of the roughness on MAV design are proposed. Firstly, the application may combine the high aspect ratio wing with rough thick aerofoils. The higher aspect ratio wing has less induced drag, while the rough aerofoil has less profile drag than the smooth ones. The thick aerofoil is particularly of interest for its largest benefit on the $C_l/C_{d,max}$ due to the roughness. The thick aerofoils also increase the internal capacity, allowing more battery and equipment to store. Once a thick aerofoil is chosen, the Reynolds number in the operation must be within the beneficial interval. The second application refers to the adaptive roughness for the flow control. The idea is to use the roughness for better performance only when necessary, avoiding detrimental effects.

Chapter 7 Investigation of Roughness Effects on an MAV Platform

The investigation of the roughness effects is conducted on the MAV platform developed in the author's research group. The rough surfaces are also simplified to sand grains, which are realisable using sandpapers. The roughness conditions and Reynolds numbers are explored for the beneficial roughness effects. The roughness is applied to the wing, or also to the fuselage.

7.1 Mesh

7.1.1 Geometry and Design Condition

Table 7-1 summarises the design condition. The wing-fuselage configuration for the MAV platform is investigated. Fig. 7-1 shows the corresponding geometry.

Table 7-1. The description of the design condition

C_L	Cruise speed	Reference wing area	Reynolds number	Mean aerodynamic chord
0.35	10m/s	0.09m^2	157000	0.23m
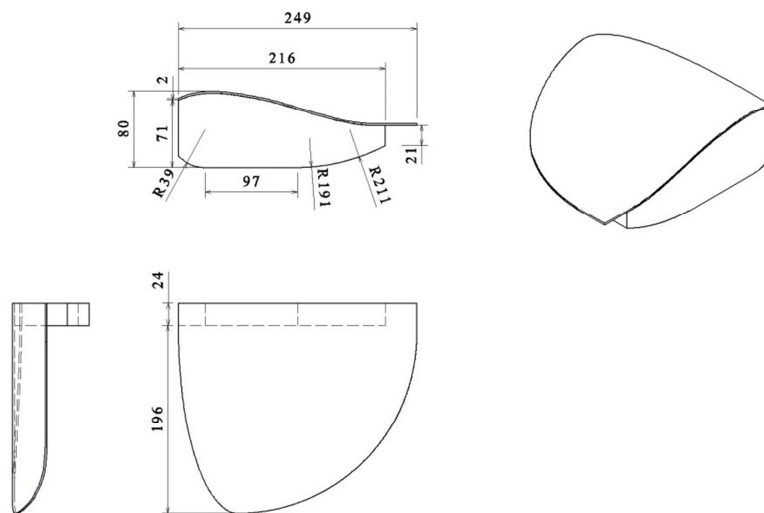
Fig. 7-1. The wing-fuselage geometry

7.1.2 Mesh Design and Sensitivity

The mesh uses multi-block structured mesh. In the planform, the leading and trailing edges of the wing shrink into one point at the wingtip. The surface mesh topology for this shape uses the C-type, as show in Fig. 7-2b. It is suitable

for a good control of mesh spacing on this shape. Fig. 7-2a shows the mesh with a single block. It can be seen the mesh elements are highly skewed around the marked circle.

To resolve the boundary layer, the appropriate mesh topology can be H-type or O-type. An H-type mesh is relatively easy to implement while an O-type mesh is better for reducing the number of elements. The wing-fuselage configuration uses H-type. The mesh spacing normal to the solid surfaces ensure $y^+<1$, checked after the simulations, and the growth rate is between 1.1 and 1.2. Fig. 7-3 shows H-type boundary layer mesh on the symmetry plane.

The wake region after the simulated geometry is split into the near wake region and the far wake region. The near wake region uses a lower growth ratio for mesh spacing and the far wake region uses a higher growth ratio to save the total number of mesh elements. There is no clear identification for under-resolving the near wake, checked after the simulations.
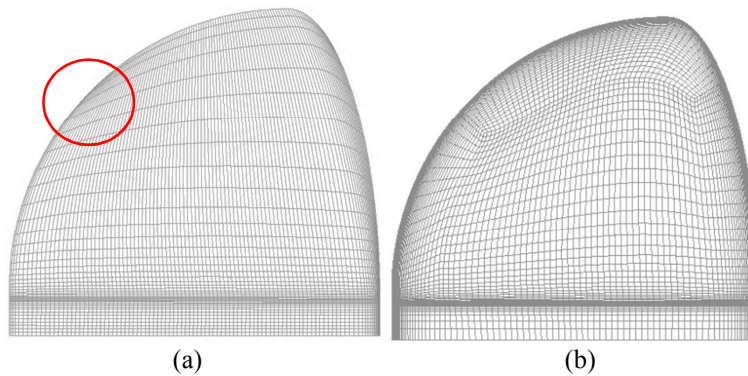
(a)   (b)
Fig. 7-2. Mesh topology for the wing, (a) a single block, (b) C-type block
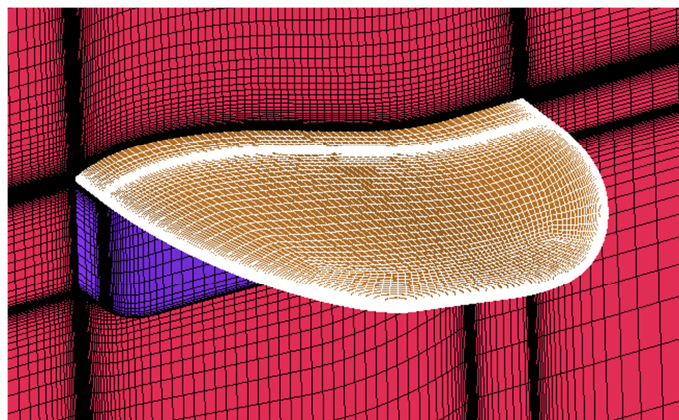
Fig. 7-3. Surface mesh for the wing-fuselage configuration

Table 7-2 shows the mesh sensitivities. The mesh is refined by a

refinement factor of 1.3 in each coordinate direction. It can be seen the highest change due to mesh is no more than 2%, and this is satisfactory.

Table 7-2. Mesh sensitivity on smooth and rough surfaces, V_∞ = 10m/s

	Mesh elements	$\alpha = 0^o$ Smooth	$\alpha = 0^o$ $h_s = 500\mu m$	$\alpha = 14^o$ Smooth	$\alpha = 14^o$ $h_s = 500\mu m$
C_l	2.6M	0.3482	0.3534	0.7136	0.7113
	6M	0.3556	0.3586	0.7039	0.7098
C_d	2.6M	0.0700	0.0782	0.3173	0.3179
	6M	0.0684	0.0764	0.3153	0.3165
C_l/C_d	2.6M	5.0	4.5	2.2	2.2
	6M	5.2	4.7	2.2	2.2

7.2 Investigation of Beneficial Roughness Effects

Two efforts are conducted to investigate the beneficial roughness effects, i.e., searching for a suitable roughness condition and searching for a suitable Reynolds number.

7.2.1 Roughness Effects for the case with the Rough Wing

The simulations are performed with various roughness heights ranging from 100μm to 1mm at design condition (V_∞ = 10m/s). The roughness is applied only to the wing. Fig. 7-4 shows the result for h_s = 100μm. Fig. 7-5 shows the result for h_s = 1mm. At the design lift condition, the roughness introduces more drag, more lift and lower lift to drag ratio. At higher incidences, the increase in the lift and the reduction in the drag are observed for low roughness heights. For example the case h_s = 100μm, at high incidences larger than 14º, an average increase by 0.4% in the lift is observed, and at α = 15º, the reduction in the drag is 0.1%. Nevertheless these beneficial effects are negligible. When the roughness height becomes larger, no beneficial effects on lift to drag ratio are observed. At α = 15º, the previous beneficial effects becomes even detrimental, i.e., the drag increases.

The roughness height h_s = 100μm is selected because it may be a safe lower limit for the roughness to take effects. This is based on admissive roughness height result in Chapter 6, see Table 6-3. The Reynolds number based on the mean chord for design condition is 1.6×10^5, so that this surface is on the verge of demonstrating noticeable roughness effects.

(a)

(b)

(c)

(d)
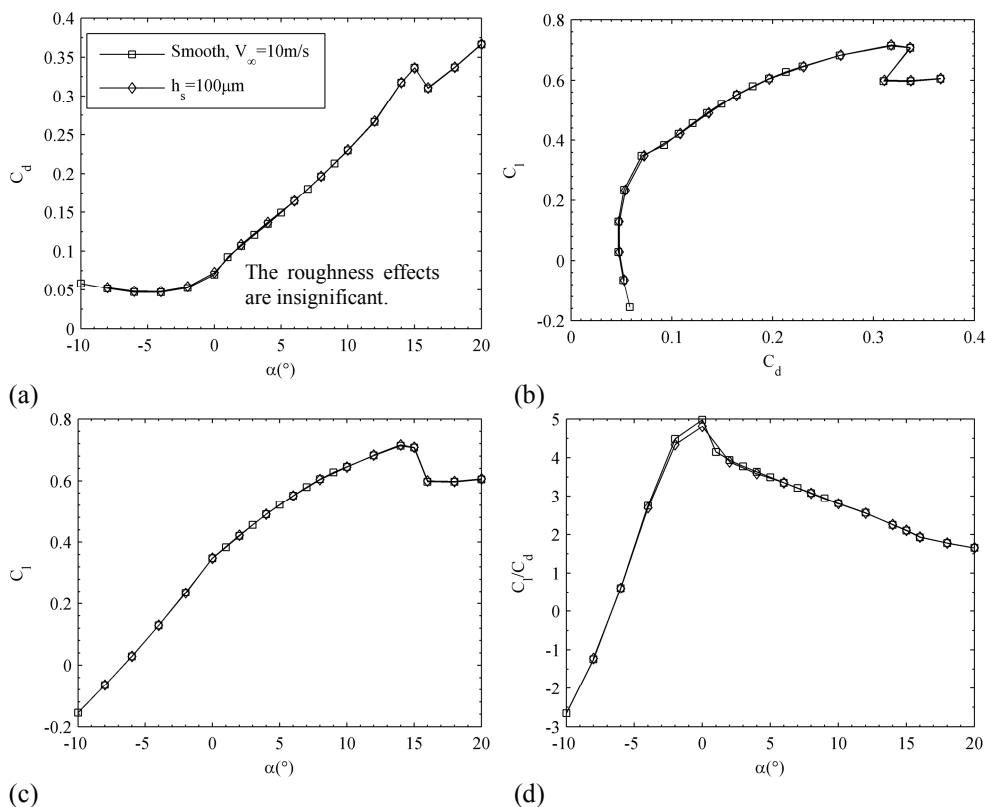
Fig. 7-4. Lift and drag, $V_\infty = 10$m/s, $h_s = 100$µm

(a)

(b)

(c)

(d)
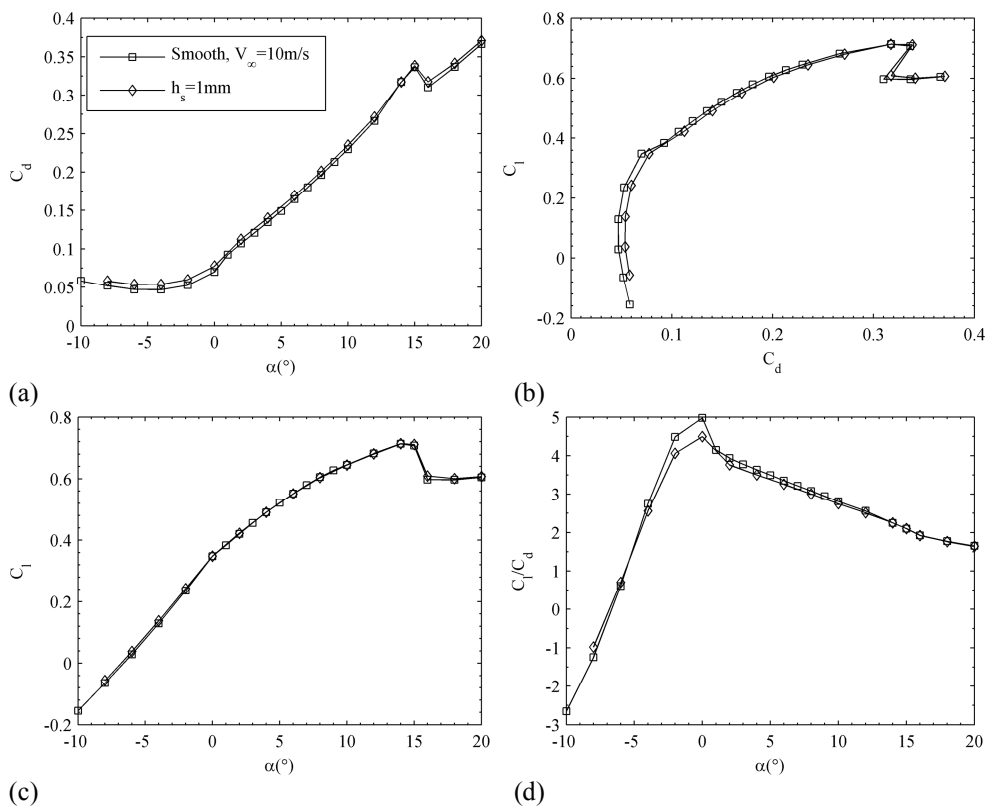
Fig. 7-5. Lift and drag, $V_\infty = 10$m/s, $h_s = 1$mm

The lift and drag are divided into pressure and skin friction components to investigate the detailed roughness effects, as shown in Table 7-3. At $\alpha = 0°$, i.e.,

the design lift condition, the lift is slightly enhanced by less than 0.1% (negligible), whereas the drag is increased by 3.6%. It can be seen that both C_{dp} and C_{df} increase and the total rise is more contributed by C_{df}. The lift to drag ratio is reduced by 3.4% as a result. This means the aerodynamic performance at the design lift condition is degraded by a small amount. The reason for the increase in the pressure drag is related to the fuselage, as discussed in the next section.

Table 7-3. The comparison on lift and drag coefficients at the design lift

	$V_\infty = 10\text{m/s}, \alpha = 0°$	
	Smooth	$h_s = 100\mu\text{m}$
C_l	0.3482	0.3484
C_{lp}	0.3499	0.3506
C_{lf}	-0.0017	-0.0021
C_d	0.0700	0.0725
C_{dp}	0.0620	0.0629
C_{df}	0.0080	0.0095
C_l/C_d	5.0	4.8

7.2.2 Roughness Effects for the Case with Both Rough Wing and Fuselage

The roughness is also applied on the fuselage to investigate the fuselage effects. The selected roughness height is $h_s = 500\mu\text{m}$ and the condition simulated is at the design lift. The detailed result for the lift and drag components are presented in Table 7-4. It is found that, the case with both rough wing and fuselage has lower drag than the case with rough wing only, leading to a better lift to drag ratio. The case with both rough wing and fuselage still has a higher drag than the case for the smooth surface. This is primarily resulted from the excessive skin friction drag.

The results of the flow field are presented to explain the change in the pressure drag, as shown in Fig. 7-6 and Fig. 7-7. In Table 7-4, the result of the pressure drag shows the fuselage has less drag when it is rough. This corresponds to the change in Fig. 7-7 from b to c, e to f, and h to i. It can be seen that the separation area on the bottom surface of the fuselage reduces, as well as the separation near the conjunction between fuselage and the wing's lower surface near the maximum camber. The rough fuselage case still has a larger separation area near the conjunction between the fuselage and the wing

than the smooth case. The pressure drag is still higher as a result.

Table 7-4. Lift and drag coefficient components, $V_\infty = 10\text{m/s}$, design lift

		Smooth	$h_s = 500\mu\text{m}$ (rough wing only)	$500\mu\text{m}$ (both rough wing and fuselage)
Wing	C_l	0.3482	0.3484	0.3483
and	C_{lp}	0.3499	0.3508	0.3509
fuselage	C_{lf}	-0.0017	-0.0023	-0.0027
	C_d	0.0700	0.0775	0.0763
	C_{dp}	0.0620	0.0641	0.0621
	C_{df}	0.0080	0.0134	0.0142
	C_l/C_d	5.0	4.5	4.6
Fuselage	C_l	-0.0234	-0.0251	-0.0230
	C_{lp}	-0.0225	-0.0242	-0.0219
	C_{lf}	-0.0009	-0.0009	-0.0012
	C_d	0.0265	0.0272	0.0276
	C_{dp}	0.0253	0.0259	0.0255
	C_{df}	0.0012	0.0013	0.0021
Wing	C_l	0.3716	0.3735	0.3713
	C_{lp}	0.3724	0.3750	0.3728
	C_{lf}	-0.0008	-0.0015	-0.0015
	C_d	0.0435	0.0504	0.0487
	C_{dp}	0.0366	0.0383	0.0365
	C_{df}	0.0068	0.0121	0.0121

The result in Table 7-4 also shows the wing has less pressure drag when the fuselage becomes rough. Referring back to Fig. 7-7 again, the separation on the upper surface of the wing near the quarter-chord location reduces, as well as the main separation near the rear. This explains for the reduction. Additionally, it can be seen that, the smaller separation for the case with both rough wing and fuselage only leads to a slight reduction (0.0001) in the pressure drag than that for the smooth case. The reason may be obtained from the pressure contour in Fig. 7-6. On the upper surface of the wing, the low pressure area near the leading edge reduces when the wing becomes rough, resulting in a loss of the suction.
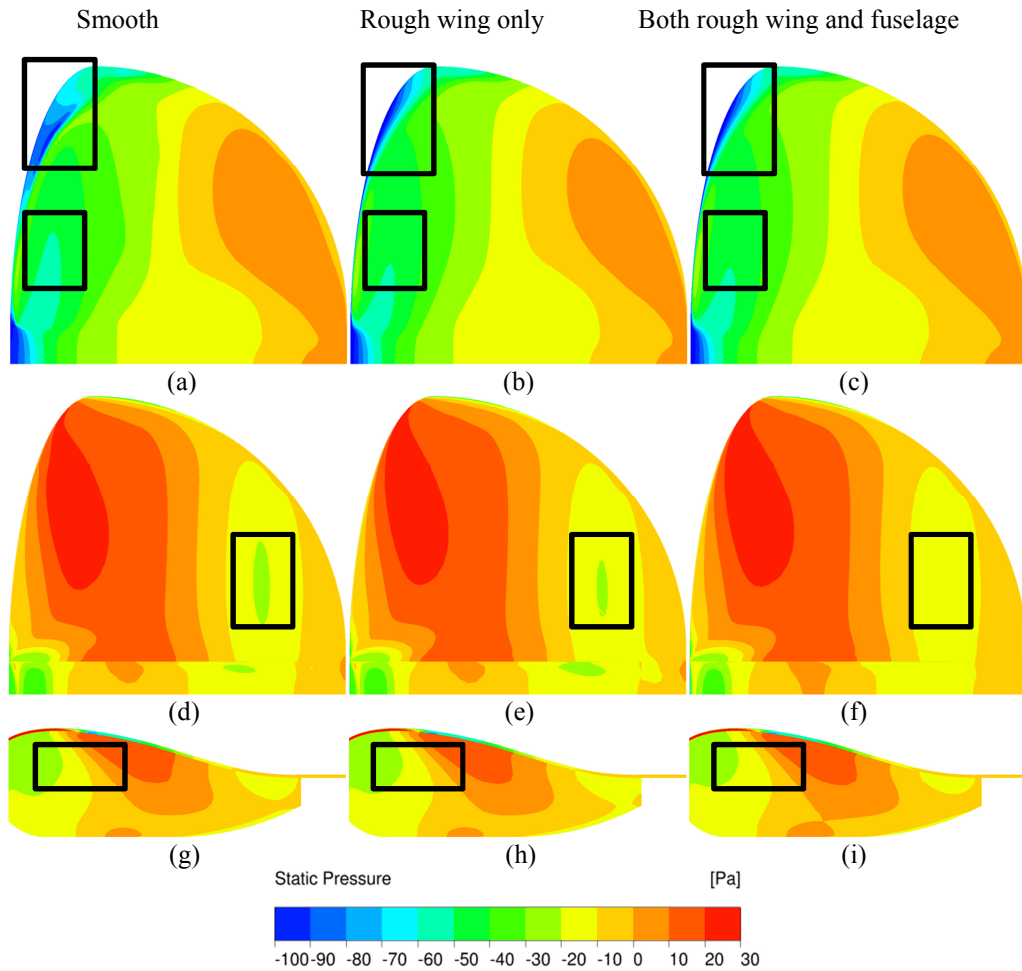
Fig. 7-6. The comparisons on the pressure contour, $V_\infty = 10$m/s, $h_s = 500$μm, $C_l \approx 0.3482$, top view: (a), (b), (c), bottom view: (d), (e), (f), side view: (e), (f), (g)

In summary, the roughness on the fuselage also affects the total roughness effects. The rough fuselage reduces the separation on itself and the separation near the conjunction between the wing and the fuselage. A rough fuselage is beneficial. In addition, this 500μm roughness condition is just able to reduce the pressure drag of the wing. At lower roughness heights, this reduction is less likely to occur. At higher roughness heights, the skin friction drag is more likely to be higher. This shows that it is impossible to find a suitable roughness height to reduce the total drag at the design lift condition.
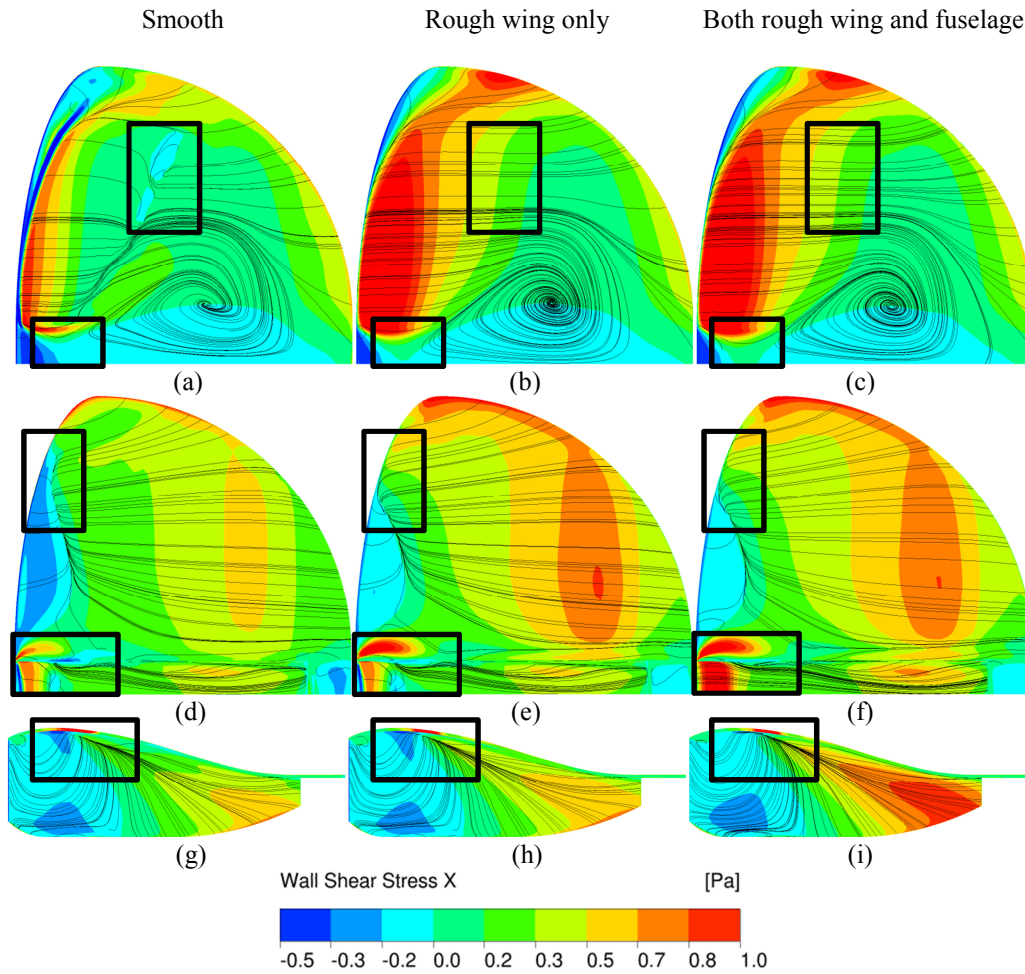
Fig. 7-7. The comparisons on the contour of X wall shear stress with surface streamlines, $V_\infty = 10$m/s, $h_s = 500$μm, $C_l \approx 0.3482$, top view: (a), (b), (c), bottom view: (d), (e), (f), side view: (e), (f), (g)

7.2.3 Roughness Effects at Lower Reynolds Numbers

The second effort aims to find a suitable Reynolds number. Based on the result obtained in Chapter 6, the cambered plate profile may be similar to the thin wing of the MAV platform, and the previous result shows lower Reynolds numbers or flight speeds may be preferable. One simulation at the lowest possible flight speed 7.1m/s ($Re = 1.1 \times 10^5$) is performed with $h_s = 500$μm. Fig. 7-8 shows the result. The flight speed is determined just above the minimum horizontal flight speed, calculated using a conservative $C_{l,max} = 0.7$. The roughness beneficial effects is an increase in $C_{l,max}$ by 1.3% at $\alpha = 14°$. At this incidence, C_d increases by 0.3%, and C_l/C_d shows an increase by 1.6%. These effects are small, nevertheless more substantial than those at higher flight speeds. Table 7-5 includes the pressure and skin friction component of C_l and C_d. It can be seen that the reduction in C_{dp} overcomes the increase in C_{df}. At

lower Reynolds numbers the beneficial effects may be more substantial. However, a redesign of the MAV platform is required because this is already the lowest possible speed.

The results obtained generally matches the findings for the cambered plate, although a low aspect ratio wing investigated here should include three dimensional effects of the flow.

(a)   (b)

(c)   (d)
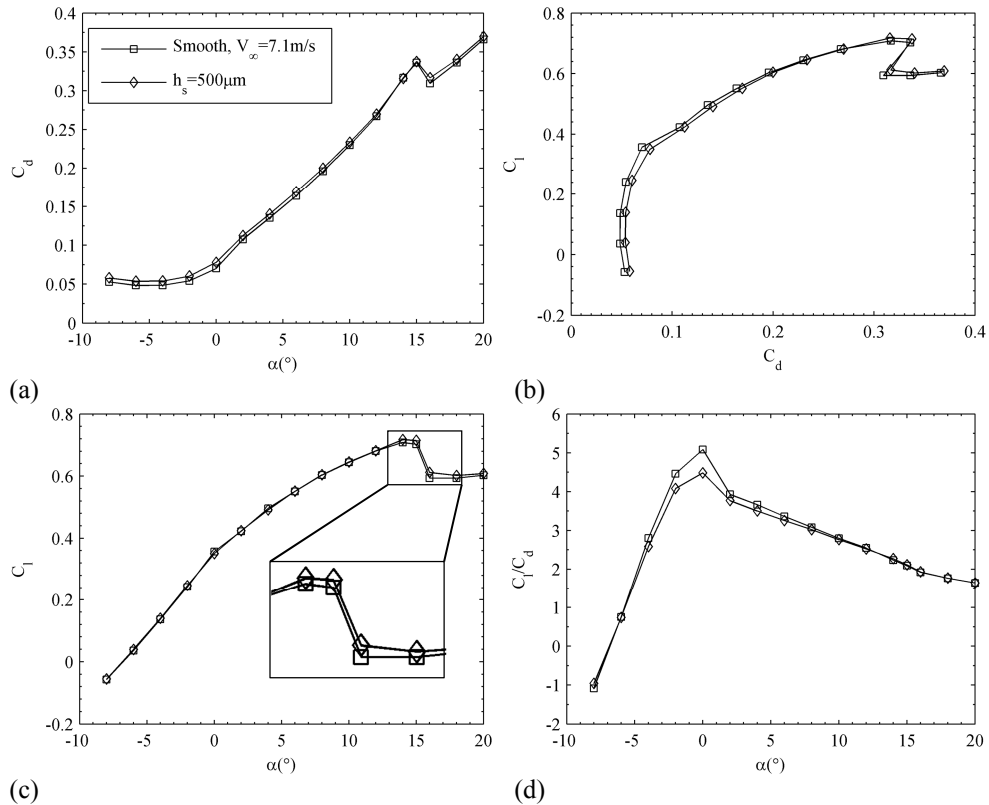
Fig. 7-8. Lift and drag, V_∞ = 7.1m/s, h_s = 500µm

Table 7-5. The comparison on lift and drag coefficients at lower Reynolds number

	V_∞ = 7.1m/s, α = 14º	
	Smooth	h_s = 500µm
C_l	0.7080	0.7173
C_{lp}	0.7105	0.7205
C_{lf}	-0.0025	-0.0032
C_d	0.3166	0.3157
C_{dp}	0.3116	0.3096
C_{df}	0.0050	0.0061
C_l/C_d	2.2	2.3

7.3 Conclusion

In the efforts to find a notable beneficial roughness condition, the investigations are performed with various roughness heights and Reynolds

numbers. At the design lift condition, the result shows the roughness reduces the lift to drag ratio. At high incidences, the roughness can increase $C_{l,max}$ for low roughness heights, although the beneficial effects are found to be negligibly small. At the lowest possible Reynolds number, more beneficial effects on $C_{l,max}$ and C_l/C_d are obtained at high incidences. The improvements are still small at an order of O(1%).

The fuselage also plays a role in the roughness effect. When the roughness is only applied on the wing, the separation on the fuselage increases. This leads to an increase in the pressure drag. When the roughness is also applied to the fuselage, the separation area reduces. However it is still larger than that for the smooth surface. The separation on the upper surface of the wing and the separation near the conjunction between the fuselage and the wing are also reduced. Although the wing's pressure drag reduces due to lesser separation area, the increase in skin friction drag overwhelms the reduction.

The range of the roughness heights and Reynolds numbers in this investigation is sufficiently broad for the MAV platform investigated. A suitable fuselage shape that causes less interference drag and less flow separation, or a dedicated roughness condition for the fuselage, can be the directions for future improvements on the aerodynamics. In addition, future considerations on the roughness condition may aim at reducing the large separation on the top of the aft fuselage. The guiding principle is to reduce more pressure drag than the increase in the skin friction drag at all times.

Chapter 8 Conclusion

8.1 Conclusion and Contribution

This work investigates: 1) the simulation for smooth surfaces (transition models), 2) the simulation for rough surfaces (roughness models including transition), 3) the roughness effects for rough aerofoils, and 4) the roughness effects on an MAV platform at low Reynolds numbers. The investigation on the simulation for smooth surfaces compares the capability of low Re SST, γ-Re_θ SST and low Re DDES-SST models, with the comparisons to the experiment. The investigation on the simulation for rough surfaces compares the capability of rough low Re SST and γ-Re_θ SST models, also with the comparisons to the experiment. The roughness model uses the equivalent sand grain roughness method. The following 4 paragraphs provide the detailed response to the *Objective A* defined in Chapter 1.

For the flow on a smooth aerofoil, the two RANS models show a similar prediction on the lift and drag. The predictions in the lift and drag are within 10% difference from the experiment in a range of incidence. On the NACA 2415 aerofoil at $Re = 1 \times 10^5$, the range of incidence is between $2^\circ \le \alpha \le 8^\circ$ for the low Re SST model, and between $4^\circ \le \alpha \le 8^\circ$ for the γ-Re_θ SST model. The larger the effects of separation or bubble are, the larger the difference between the experiment and the prediction is. A similar behaviour of the models can be also found for the smooth NACA 0012 aerofoil at $Re = 1.5 \times 10^5$.

The two RANS models also have a capability of predicting bubbles on the NACA 2415 aerofoil at $Re = 1 \times 10^5$. However, an exact match to the experiment is not obtained. At $\alpha = 4^\circ$, the two models predicts bubbles shorter than the experimental one. The difference between the prediction and the experiment becomes large when the incidence increases. At $\alpha = 12^\circ$, the bubble predicted starts from a much more upstream location. At $\alpha = 15^\circ$, no bubble is predicted. Although in above cases, the two models show a similar behaviour, a difference between the two models exist at $\alpha = 8^\circ$.

The DDES model with a low Re correction (page 40, Eq 3-39~Eq 3-46) is

133

compared with the two RANS models and the experiment on the smooth NACA 2415 aerofoil at $Re = 1 \times 10^5$ for α = 4º and 12º. The DDES model only performs well and predicts the best lift at α = 12º. Also at α = 12º, the DDES model predicts the periodic change in the flow field, as well as detailed eddies responsible for the transition. The DDES model only predicts a time-averaged bubble with a similar location and size as comparable to the two RANS models. The low Re correction is important for the DDES model to have these capabilities. Because of an inaccurate prediction of the bubble, the agreement on the pressure distribution between the experiment and the prediction (time-averaged) is also inaccurate.

For the rough NACA 0012 aerofoil at $Re = 1.5 \times 10^5$, the two rough RANS models show a different capability. Only the rough low Re SST model predicts the correct trend of the roughness effects. The roughness induced transition is not predicted by the γ-Re_θ SST model, resulting in a wrong trend of prediction in the lift and drag. The rough low Re SST model is therefore used for subsequent investigations for the roughness effects. The following 5 paragraphs provide the detailed response to the *Objective B* defined in Chapter 1.

The investigation on the roughness effects on rough aerofoils is performed between 2×10^4 and 2×10^5. Three aerofoils are investigated, including NACA 0012 aerofoil, NACA 2415 aerofoil and a cambered plate profile. Under different combinations of Reynolds number, roughness height, incidence and aerofoils, the roughness effects on the lift and drag are different. The following examples demonstrate beneficial roughness effects under appropriate combinations of aforementioned parameters. The maximum lift coefficient can be improved. For example, the $C_{l,max}$ for the NACA 0012 aerofoil at $Re = 6 \times 10^4$ can be improved approximately from 0.7 to 0.85. The maximum lift to drag ratio can be improved. For example, the $C_l/C_{d,max}$ for the NACA 2415 aerofoil at $Re = 6 \times 10^4$ can be improved approximately from 12 to 24.

The important findings are summarised as follows for providing guidance of the appropriate usage of the roughness. (1) An appropriate Reynolds number must be selected at first. For all three aerofoils under a given roughness

condition, there is a beneficial range in the Reynolds number, in which the $C_l/C_{d,max}$ and $C_{l,max}$ can be improved. Fig. 6-18 and Fig. 6-19 provide the details. The investigation suggests for aerofoils similar to NACA 0012 and NACA 2415, the minimum critical Reynolds number is always within the beneficial range. Therefore Reynolds numbers close to this number can be attempted at the beginning. For aerofoils like the thin cambered plate, the $C_{l,max}$ can be improved at all Reynolds numbers investigated, whereas the improvement on $C_l/C_{d,max}$ can be not considerable. (2) Generally, at very low Reynolds number, larger roughness height is preferable. At moderate Reynolds number, for example within the beneficial range, a moderate roughness height is preferable. The appropriate value can be determined from the results under different roughness heights. (3) The flow fields at different incidences are different, as well as the roughness effects. Table 6-4 and Table 6-5 provide the details. Generally, at low incidences (e.g., 0°~4°), when a separation forms near trailing edge, it is preferable to use roughness to eliminate the separation. At moderate incidences before stall (e.g., 4°~8° or 10°), it is only preferable to use roughness to reduce or eliminate the bubble and the separation after the bubble at the same time. At higher incidences, stalled or post-stalled, it is preferable to use roughness to delay the separation point. In all cases, the reduction in the pressure drag must overcome the rise in the skin friction drag to have a reduction in the total drag. Above general cases provide higher lift to drag ratio due to the roughness.

The investigation of rough aerofoils suggests possible applications of the roughness. For example, a high aspect ratio wing using rough thick aerofoils. The induced drag is reduced from the higher aspect ratio, and the profile drag is compensated through the roughness. The thick aerofoils can also enlarge the internal capacity for more battery and equipment. For another example, an adaptive roughness for the flow control. The idea is to use the roughness for better performance only when beneficial effects can be obtained.

The roughness effects are further investigated on the MAV platform as 3D cases with low aspect ratio wings. The roughness heights and the Reynolds numbers are altered for the beneficial effects. Using a thin wing profile, the roughness improves the maximum lift, which is consistent with the result of 2D

cambered plate profile. However, it is found no improvements on the lift to drag ratio at the design lift condition. The reduction in the pressure drag is small (only on the wing), whereas the increase in the skin friction drag is excessive. Based on the experience on the rough aerofoils in Chapter 6, the flight Reynolds number for the MAV may need to be reduced to have more beneficial effects (better $C_{l,max}$, $C_l/C_{d,max}$, and $C_l/C_{d,cruise}$). This may be realised by increasing the wing's aspect ratio.

It is also found that the wing-fuselage integration influences the roughness effect. It is preferable to have both rough wing and fuselage, rather than a rough wing alone. The rough fuselage can reduce the separation around itself, resulting in the reduction in the pressure drag.

In summary:

(1) In response to the *Objective A*, based on the models' behaviour on the test cases, it is believed that the models compared demonstrate capabilities on the prediction of bubbles, accurate lift and drag on smooth surfaces. However, this is only obtained in a limited range of incidence. The accurate simulation at all incidences is still a challenging task. For the even more challenging tasks on the rough surfaces, the rough low Re SST model is only safe to be used to obtain the trend of roughness effects.

(2) The low Re correction (page 40, Eq 3-39~Eq 3-46) demonstrates a great modelling capability, whenever incorporated to the SST turbulence model, DDES framework or the roughness model. Within such a simple correction, laminar separation bubble, roughness induced transition and low Reynolds number effects can be reasonably modelled.

(3) In response to the first part of the *Objective B*, the systematic investigation on rough aerofoils provides more understanding of the roughness effects, especially at very low Reynolds numbers. The results are useful to obtain the general trend of the roughness effects. The guidance and suggestions summarised should be useful for the application of roughness on MAV design.

(4) In response to the second part of the *Objective B*, the investigation on the MAV platform shows the roughness on the wing can have no substantially beneficial effect. MAV design with a higher aspect ratio wing, i.e., lower

Reynolds numbers based on the mean chord, or with a better designed wing-fuselage conjunctions that induce less separations, may benefit more from the roughness.

8.2 Suggestions for Future Work

Future work is suggested as follows:

(1) 3D low Re separation bubble flow validation

This is the extended comparison of low Re SST and γ-Re_θ SST models on 3D flows. Some work has already been done on lift and drag comparison, see Appendix D-2. However, the accuracy on the bubble location is unknown. Future work requires better mesh and more detailed experiment for comparisons.

(2) Wind tunnel experiment on the MAV platform

This will enhance the current work. It remains unclear about the real separation bubble on 3D wings on the MAV, and thus an experiment can be beneficial to understand both the flow and the capability of the simulations. The experiment can consider both smooth and rough surfaces. For the experiment on realistic rough surfaces, it can be very interesting to characterise the equivalent roughness height, and to provide insights for proper simulation of realistic surfaces. Some work has been done, see Appendix D-1 and Appendix D-3. Future work requires refinement.

(3) Improvements on the aerodynamic design for the MAV platform

This is inspired from the roughness effects study, and not of the concern in current thesis. The roughness is shown to be difficult to improve the aerodynamic performance substantially, so that the only way left is to improve the design. Appendix D-4 provides the preliminary result on the comparison between wing, wing-fuselage and full aircraft configuration, which may be helpful for better understanding on the aerodynamic performance of the MAV and for future design improvement. Another aspect of Appendix D-4 is the comparison between low Re SST and γ-Re_θ SST models. It is interesting to note the γ-Re_θ SST model has the difficulty to reach steady state convergence for 3D cases. A companion experiment may be of great value to validate these results

and to obtain more understandings of the models. The last work might be continued is the attempt on the roughness bump. The preliminary result indeed shows drag reductions, however as aforementioned, the potential is not expected to be substantial. The roughness bump might be just an appropriate measure for aerodynamic fixing, not for better design. The future work on the aerodynamic design for the MAV is expected to investigate optimal wing planform, wing-fuselage integration, control surface integration, etc.

(4) Model improvements

This refers to the improvements on low Re SST, γ-Re$_\theta$ SST and DDES models, as well as their roughness models. Although the results presented in Chapter 4 and Chapter 5 provide some knowledge sufficient for current investigations, it is interesting to gain a more complete understanding. The overall plan should try various RANS transition models and various DDES models on a number of test cases. The planned RANS transition models for future will at least include low Re $k - \omega$, γ-Re$_\theta$ SST, and Catalano and Tognaccini[68]. The planned DDES model can consider incorporating other known RANS transition models. The planned test cases will at least include SD7003[129], cambered plates and flat plates[127], low aspect ratio wings[130], wing-propeller interference[41], and full MAV[131].

For all of the variants of SST models used, the F_2 blending function may be improved according to Catalano and Tognaccini[68]. However, their proposal requires the user to input a Reynolds number, and the usage may be limited. For further improvements on the low Re SST model with the simplicity maintained, an intermittency factor may be incorporated with the empirical correlation for turbulent spot production for separation induced transition. For the γ-Re$_\theta$ SST model, the transition onset and transition length correlation for separation bubbles may be incorporated. For DDES models, the switching function for RANS and LES modes should be improved. It might be also necessary for some calibration on the model constants. For the roughness model, the first suggestion is on the near wall mesh convergence, although it is sufficient for the investigation presented in this work. The convergence affects the rigorousness of the model, and it is expected to require substantial work. The second

suggestion is the roughness induced transition for the γ-Re$_θ$ SST model. Other than transition correlations for low freestream turbulence, the related blending function and limiters might be also improved.

Reference

[1]Mueller, T. J., "Overview of Micro-Air-Vehicle Development," *Introduction to the Design of Fixed-Wing Micro Air Vehicles Including Three Case Studies*, edited by Mueller, T. J., Kellogg, J. C., Ifju, P. G., and Shkarayev, S. V., American Institute of Aeronautics and Astronautics, Reston, VA, USA, 2007, pp. 1–38.

[2]Amadori, K., Lundstrom, D., and Krus, P., "Automated Design and Fabrication of Micro-air Vehicles," *Proceedings of the Institution of Mechanical Engineers, Part G: Journal of Aerospace Engineering*, Vol. 226, 2011, pp. 1271–1282.

[3]Cosyn, P., and Vierendeels, J., "Numerical Investigation of Low-Aspect-Ratio Wings at Low Reynolds Numbers," *Journal of Aircraft*, Vol. 43, No. 3, 2006, pp. 713–722.

[4]Garmann, D. J., Visbal, M. R., and Orkwis, P. D., "Comparative Study of Implicit and Subgrid-scale Model Large-eddy Simulation Techniques for Low-Reynolds Number Airfoil Applications," *International Journal for Numerical Methods in Fluids*, Vol. 71, 2013, pp. 1546–1565.

[5]Hrishikeshavan, V., Black, J., and Chopra, I., "Design and Performance of a Quad-Shrouded Rotor Micro Air Vehicle," *Journal of Aircraft*, Vol. 51, No. 3, 2014, pp. 779–791.

[6]Michelson, R. C. R., "Overview of Micro Air Vehicle System Design and Integration Issues," *Encyclopedia of Aerospace Engineering*, John Wiley & Sons, Ltd, 2010, pp. 1–12.

[7]Benedict, M., Jarugumilli, T., Lakshminarayan, V., and Chopra, I., "Effect of Flow Curvature on Forward Flight Performance of a Micro-Air-Vehicle-Scale Cycloidal-Rotor," *AIAA Journal*, Vol. 52, No. 6, 2014, pp. 1159–1169.

[8]Boutilier, M. S. H., and Yarusevych, S., "Separated Shear Layer Transition over an Airfoil at a Low Reynolds Number," *Physics of Fluids*, Vol. 24, No. 8, 2012, pp. 084105–1 – 084105–23.

[9]Barbarino, S., Bilgen, O., Ajaj, R. M., Friswell, M. I., and Inman, D. J., "A Review of Morphing Aircraft," *Journal of Intelligent Material Systems and Structures*, Vol. 22, No. 9, 2011, pp. 823–877.

[10]Bilgen, O., "A Novel Unmanned Aircraft with Solid-State Control Surfaces: Analysis and Flight Demonstration," *52th AIAA/ASME/ASCE/AHS/ASC*

Structures, Structural Dynamics, and Materials Conference, AIAA 2011-2071, Denver, Colorado, 2011.

[11]Vos, R., Barrett, R., Breuker, R. De, and Tiso, P., "Post-Buckled Precompressed Elements: a New Class of Control Actuators For Morphing Wing UAVs," *Smart Materials and Structures*, Vol. 16, No. 3, 2007, pp. 919–926.

[12]Mueller, T. J., Kellogg, J. C., Ifju, P. G., and Shkarayev, S. V., *Introduction to the Design of Fixed-Wing Micro Air Vehicles : Including Three Case Studies*, American Institute of Aeronautics and Astronautics, New York, 2007.

[13]Schmitz, F. W., *Aerodynamics of the Model Airplane, Part 1, Airfoil Measurements*, NASA-TM-X-60976, 1967.

[14]Hooker, R. W., *The Aerodynamic Characteristics of Airfoils as Affected by Surface Roughness*, NACA-TN-457, 1933.

[15]Kraemer, K., *Airfoil Profiles in a Critical Reynolds Number Region*, NASA-TT-F-14959, 1973.

[16]Lyon, C. A., Broeren, A. P., Giguère, P., Gopalarathnam, A., and Selig, M. S., *Summary of Low-Speed Airfoil Data, Vol. 3*, SoarTech Publications, Virginia Beach, VA, USA, 1998, pp. 102–105, 107–109, 164–187.

[17]Althaus, D., *Profilpolaren für den Modellflug: Windkanalmessungen an Profilen im kritischen Reynoldszahlbereich, Band 2*, Neckar-Verlag VS-Villingen, Germany, 1985, pp. 32–36, 154–168.

[18]Carmichael, B. H., *Low Reynolds Number Airfoil Survey, Volume 1*, NASA-CR-165803-Vol-1, 1981.

[19]Mueller, T. J., Torres, G. E., and Srull, D. W., "Elements of Aerodynamics, Propulsion, and Design," *Introduction to the Design of Fixed-wing Micro Air Vehicles: Including Three Case Studies*, edited by Mueller, T. J., Kellogg, J. C., Ifju, P. G., and Shkarayev, S. V., AIAA Education Series, AIAA, Reston, VA, USA, 2006, pp. 39–107.

[20]Tani, I., "Low-speed Flows Involving Bubble Separations," *Progress in Aerospace Sciences*, Vol. 5, 1964, pp. 70–103.

[21]Schmitz, F. W., *The Aerodynamics of Small Reynolds Numbers*, NACA TM-75815, 1980.

[22]Schmitz, F. W., *Aerodynamik des Flugmodells*, 6th ed. ed., Verlag W Zuerl Steinebach, Germany, 1975.

[23]Gaster, M., *The Structure and Behaviour of Laminar Separation Bubbles*, Aeronautical Research Council RM 3595, London, England, 1969.

[24]Horton, H. P., *A Semi-Empirical Theory for the Growth and Bursting of Laminar Separation Bubbles*, Aeronautical Research Council, CP 1073, London, England, 1969.

[25]Meara, M. M. O., and Thomas J. Mueller, "Laminar Separation Bubble Characteristics on an Airfoil at Low Reynolds Numbers," *AIAA Journal*, Vol. 25, No. 8, 1987, pp. 1033–1041.

[26]Marxen, O., Lang, M., and Rist, U., "Vortex Formation and Vortex Breakup in a Laminar Separation Bubble," *Journal of Fluid Mechanics*, Vol. 728, 2013, pp. 58–90.

[27]Burgmann, S., Brücker, C., and Schröder, W., "Scanning PIV Investigation of the Laminar Separation Bubble on a SD7003 Airfoil," *Experiments in Fluids*, Vol. 41, No. 2, 2006, pp. 319–326.

[28]Zhang, W., Hain, R., and Kähler, C. J., "Scanning PIV investigation of the laminar separation bubble on a SD7003 airfoil," *Experiments in Fluids*, Vol. 45, No. 4, 2008, pp. 725–743.

[29]Malkiel, E., and Mayle, R. E., "Transition in a Separation Bubble," *Journal of Turbomachinery*, Vol. 118, No. 4, 1996, pp. 752–759.

[30]Serna, J., and Lázaro, B. J., "The Final Stages of Transition and the Reattachment Region in Transitional Separation Bubbles," *Experiments in Fluids*, Vol. 55, No. 4, 2014, p. 1695.

[31]Brinkerhoff, J. R., and Yaras, M. I., "Interaction of Viscous and Inviscid Instability Modes in Separation–bubble Transition," *Physics of Fluids*, Vol. 23, No. 12, 2011, p. 124102.

[32]Lin, J. C. M., and Pauley, L. L., "Low-Reynolds-number Separation on an Airfoil," *AIAA Journal*, Vol. 34, No. 8, 1996, pp. 1570–1577.

[33]Batill, S. M., and Mueller, T. J., "Visualization of Transition in the Flow over an Airfoil Using the Smoke-Wire Technique," *AIAA Journal*, Vol. 19, No. 3, 1981, pp. 340–345.

[34]Mueller, T. J., "The Influence of Laminar Separation and Transition on Low Reynolds Number Airfoil Hysteresis," *Journal of Aircraft*, Vol. 22, No. 9, 1985, pp. 763–770.

[35]Simoni, D., Ubaldi, M., and Zunino, P., "Experimental Investigation of Flow Instabilities in a Laminar Separation Bubble," *Journal of Thermal Science*, Vol. 23, No. 3, 2014, pp. 203–214.

[36]Mayle, R. E., "The 1991 IGTI Scholar Lecture: The Role of Laminar-Turbulent Transition in Gas Turbine Engines," *Journal of Turbomachinery*, Vol. 113, No. 4, 1991, pp. 509–536.

[37]Mueller, T. J., and Batillt, S. M., "Experimental Studies of Separation on a Two-Dimensional Airfoil at Low Reynolds Numbers," *AIAA Journal*, Vol. 20, No. 4, 1982, pp. 457–463.

[38]Zhou, Y., and Wang, Z. J., "Effects of Surface Roughness on Separated and Transitional Flows over a Wing," *AIAA Journal*, Vol. 50, No. 3, 2012, pp. 593–609.

[39]Brinkerhoff, J. R., and Yaras, M. I., "Direct Numerical Simulations of Transitional Separation-Bubble Development in Swept-Blade Flow Conditions," *Journal of Turbomachinery*, Vol. 135, No. 4, 2013, p. 041006.

[40]Chen, Z. J., Qin, N., and Nowakowski, a. F., "Three-Dimensional Laminar-Separation Bubble on a Cambered Thin Wing at Low Reynolds Numbers," *Journal of Aircraft*, Vol. 50, No. 1, 2013, pp. 152–163.

[41]Makino, F., and Nagai, H., "Propeller Slipstream Interference with Wing Aerodynamic," *AIAA SciTech 52nd Aerospace Science Meeting*, AIAA 2014-0744, Maryland, USA, 2014, pp. 1–12.

[42]Arena, A., and Mueller, T., "Laminar Separation, Transition, and Turbulent Reattachment near the Leading Edge of Airfoils," *AIAA Journal*, Vol. 18, No. 7, 1980, pp. 747–753.

[43]Hatman, A., and Wang, T., "A Prediction Model for Separated-flow Transition," *Journal of Turbomachinery*, Vol. 121, No. 3, 1999, pp. 594–602.

[44]Walker, G. J., "The Role of Laminar-Turbulent Transition in Gas Turbine Engines: A Discussion," *Journal of Turbomachinery*, Vol. 115, No. 2, 1993, pp. 207–216.

[45]McAuliffe, B. R., and Yaras, M. I., "Transition Mechanisms in Separation Bubbles Under Low- and Elevated-Freestream Turbulence," *Journal of Turbomachinery*, Vol. 132, No. 1, 2010, p. 011004.

[46]Schlichting, H., and Gersten, K., *Boundary-Layer Theory*, 8th ed., Springer, Berlin, 2000, pp. 526–532, 420, 436, 440.

[47]White, F. M., *Viscous Fluid Flow*, 2nd ed., McGraw-Hill, New York, 1991, pp. 335–392.

[48]Windte, J., Scholz, U., and Radespiel, R., "Validation of the RANS-simulation of Laminar Separation Bubbles on Airfoils," *Aerospace Science and Technology*, Vol. 10, No. 6, 2006, pp. 484–494.

[49]Stuart, J. T., "Nonlinear Stability Theory," *Annual Review of Fluid Mechanics*, Vol. 3, No. 1, 1971, pp. 347–370.

[50]Smith, A. M. O., and Gamberoni, N., *Transition, Pressure Gradient and Stability Theory*, Report No. ES 26388, Douglas Aircraft Company, CA, USA, 1956.

[51]Van Ingen, J. L., *A Suggested Semi-empirical Method for the Calculatio of the Boundary Layer Transition Region*, Report V.T.H.-74, Department of Aeronautical Engineering, Technological University, Delft, Holland, 1956.

[52]Lian, Y., and Shyy, W., "Laminar-Turbulent Transition of a Low Reynolds Number Rigid or Flexible Airfoil," *AIAA Journal*, Vol. 45, No. 7, 2007, pp. 1501–1513.

[53]Radespiel, R., Windte, J., and Scholz, U., "Numerical and Experimental Flow Analysis of Moving Airfoils with Laminar Separation Bubbles," *AIAA Journal*, Vol. 45, No. 6, 2007, pp. 1346–1356.

[54]Windte, J., Radespiel, R., Scholz, U., and Eisfeld, B., "RANS Simulation of the Transitional Flow Around Airfoils at Low Reynolds Numbers for Steady and Unsteady Onset Conditions," *Specialists Meeting on Enhancement of NATO Military Flight Vehicle Performance by Management of Interacting Boundary Layer Transition and Separation*, RTO-MPAVT-111-P-03, Prague, Czech Republi, 2004, pp. 1–20.

[55]Cebeci, T., Chen, H. H., and Leej, P., "Calculation of Three-Dimensional Low Reynolds Number Flows," *Journal of Aircraft*, Vol. 31, No. 3, 1994, pp. 564–571.

[56]Stock, H. W., "eN Transition Prediction in Three-Dimensional Boundary Layers on Inclined Prolate Spheroids," *AIAA Journal*, Vol. 44, No. 1, 2006, pp. 108–118.

[57]Wilcox, D. C., "A Model for Transitional Flows," *AIAA 15th Aerospace Science Meeting*, AIAA 77-126, Los Angeles, CA, 1977.

[58]Fu, S., and Wang, L., "RANS Modeling of High-speed Aerodynamic Flow Transition with Consideration of Stability Theory," *Progress in Aerospace Sciences*, Vol. 58, 2013, pp. 36–59.

[59]Menter, F. R., Langtry, R., and Völker, S., "Transition Modelling for General Purpose CFD Codes," *Flow, Turbulence and Combustion*, Vol. 77, No. 1-4, 2006, pp. 277–303.

[60]Menter, F. R., Langtry, R. B., Likki, S. R., Suzen, Y. B., Huang, P. G., Völker, S., and Völker, S., "A Correlation-Based Transition Model Using Local Variables—Part I: Model Formulation," *Journal of Turbomachinery*, Vol. 128, No. 3, 2006, pp. 413–422.

[61]Langtry, R. B., Menter, F. R., Likki, S. R., Suzen, Y. B., Huang, P. G., and Völker, S., "A Correlation-Based Transition Model Using Local Variables—Part II: Test Cases and Industrial Applications," *Journal of Turbomachinery*, Vol. 128, No. 3, 2006, p. 423.

[62]Langtry, R. B., and Menter, F. R., "Correlation-Based Transition Modeling for Unstructured Parallelized Computational Fluid Dynamics Codes," *AIAA Journal*, Vol. 47, No. 12, 2009, pp. 2894–2906.

[63]Zhang, X., and Gao, Z., "Numerical Discussions on Complete Empirical Correlation in Langtry's Transition Model," *Applied Mathematics and Mechanics*, Vol. 31, No. 5, 2010, pp. 575–584.

[64]Medida, S., and Baeder, J., "Role of Improved Turbulence and Transition Modeling Methods in Rotorcraft Simulations," *AHS 69th Annual Forum,* Phoenix, Arizona, USA, 2013.

[65]Pasquale, D. Di, Rona, A., and Garrett, S. J., "A Selective Review of CFD Transition Models," *39th AIAA Fluid Dynamics Conference*, AIAA 2009-3812, San Antonio, Texas, USA, 2009, pp. 1–10.

[66]Wilcox, D. C., "Simulation of Transition with a Two-Equation Turbulence Model," *AIAA Journal*, Vol. 32, No. 2, 1994, pp. 247–255.

[67]Tang, L., "Reynolds-Averaged Navier–Stokes Simulation of Low-Reynolds-Number Airfoil Aerodynamics," *Journal of Aircraft*, Vol. 45, No. 3, 2008, pp. 848–856.

[68]Catalano, P., and Tognaccini, R., "Turbulence Modeling for Low-Reynolds-Number Flows," *AIAA Journal*, Vol. 48, No. 8, 2010, pp. 1673–1685.

[69]Catalano, P., and Tognaccini, R., "RANS Analysis of the Low-Reynolds Number Flow Around the SD7003 Airfoil," *Aerospace Science and Technology*, Vol. 15, No. 8, 2011, pp. 615–626.

[70]Probst, A., Radespiel, R., and Rist, U., "Linear-Stability-Based Transition Modeling for Aerodynamic Flow Simulations with a Near-Wall Reynolds-Stress Model," *AIAA Journal*, Vol. 50, No. 2, 2012, pp. 416–428.

[71]Mayle, R. E., and Schulz, A., "The Path to Predicting Bypass Transition," *Journal of Turbomachinery*, Vol. 119, No. 3, 1997, pp. 405–411.

[72]Walters, D. K., and Cokljat, D., "A Three-Equation Eddy-Viscosity Model for Reynolds-Averaged Navier–Stokes Simulations of Transitional Flow," *Journal of Fluids Engineering*, Vol. 130, No. 12, 2008, p. 121401.

[73]Batten, P., Goldberg, U., Peroomian, O., and Chakravarthy, S., "Recommendations and Best Practice For the Current State of the Art in Turbulence Modelling," *International Journal of Computational Fluid Dynamics*, Vol. 23, No. 4, 2009, pp. 363–374.

[74]Rumsey, C., Reif, B. P., and Gatski, T., "Arbitrary Steady-State Solutions with the K-ε Model," *AIAA Journal*, Vol. 44, No. 7, 2006, pp. 1586–1592.

[75]Spalart, P. R., and Rumsey, C. L., "Effective Inflow Conditions for Turbulence Models in Aerodynamic Calculations," *AIAA Journal*, Vol. 45, No. 10, 2007, pp. 2544–2553.

[76]Rumsey, C. L., "Apparent Transition Behavior of Widely-used Turbulence Models," *International Journal of Heat and Fluid Flow*, Vol. 28, No. 6, 2007, pp. 1460–1471.

[77]Rumsey, C. L., and Spalart, P. R., "Turbulence Model Behavior in Low Reynolds Number Regions of Aerodynamic Flowfields," *AIAA Journal*, Vol. 47, No. 4, 2009, pp. 982–993.

[78]Langtry, R. B., "A Correlation-Based Transition Model using Local Variables for Unstructured Parallelized CFD codes," PhD Thesis, Institut für Thermische

Strömungsmaschinen und Maschinenlaboratorium, Universität Stuttgart, Germany, 2006.

[79]Chen, Z. J., and Qin, N., "Planform Effects for Low-Reynolds-Number Thin Wings with Positive and Reflex Cambers," *Journal of Aircraft*, Vol. 50, No. 3, 2013, pp. 952–964.

[80]Counsil, J. N. N., and Boulama, K. G., "Validating the URANS Shear Stress Transport Model γ-Re for Low-Reynolds-number External Aerodynamics," *International Journal for Numerical Methods in Fluids*, Vol. 69, No. 8, 2011, pp. 1411–1432.

[81]Counsil, J. N. N., and Goni Boulama, K., "Low-Reynolds-Number Aerodynamic Performances of the NACA 0012 and Selig–Donovan 7003 Airfoils," *Journal of Aircraft*, Vol. 50, No. 1, 2013, pp. 204–216.

[82]Magagnato, F., Pritz, B., and Gabi, M., "Comparison of DES and LES on the Transitional Flow of Turbine Blades," *Advances in Hybrid RANS-LES Modelling*, edited by Peng, S.-H., and Haase, W., Springer Berlin Heidelberg, 2008, pp. 212–221.

[83]Alam, M. F., Walters, D. K., and Thompson, D. S., "A Transition-Sensitive Hybrid RANS / LES Modeling Methodology for CFD Applications," *51st AIAA Aerospace Sciences Meeting including the New Horizons Forum and Aerospace Exposition*, AIAA 2013-0995, Grapevine, TX, USA, 2013, pp. 1–13.

[84]Fujii, K., "Role of RANS, Hybrid and LES for Wing Flow Simulations at Relatively Low Reynolds Numbers," *Progress in Hybrid RANS-LES Modelling*, edited by Fu, S., Haase, W., Peng, S.-H., and Schwamborn, D., Springer Berlin Heidelberg, 2012, pp. 45–57.

[85]Sørensen, N. N., Bechmann, A., and Zahle, F., "3D CFD Computations of Transitional Flows Using DES and a Correlation Based Transition Model," *Wind Energy*, Vol. 14, 2011, pp. 77–90.

[86]Gross, A., and Fasel, H. F., "Hybrid Turbulence Model Simulations of Internal and External Flows," *AIAA SciTech 52nd Aerospace Science Meeting*, AIAA 2014-1448, 2014, pp. 1–30.

[87]Arvidson, S., Davidson, L., and Peng, S.-H., "Hybrid RANS-LES Modeling Using a Low-Reynolds-Number k − ω Based Model," *AIAA SciTech 52nd Aerospace Science Meeting*, AIAA 2014-0225, Maryland, USA, 2014, pp. 1–22.

[88]Gopalarathnam, A., Broughton, B. a., Mcgranahan, B. D., and Selig, M. S., "Design of Low Reynolds Number Airfoils with Trips," *Journal of Aircraft*, Vol. 40, No. 4, 2003, pp. 768–775.

[89]Kellogg, J. C., "Case Study: Micro Tactical Expendable Rigid-Wing Micro Air Vehicle," *Introduction to the Design of Fixed-wing Micro Air Vehicles: Including Three Case Studies*, edited by Mueller, T. J., Kellogg, J. C., Ifju, P. G., and Shkarayev, S. V., AIAA Education Series, AIAA, Reston, VA, USA, 2006, p. 177.

[90]Bloch, D. R., and Mueller, T. J., "Effects of Distributed Grit Roughness on Separation and Transition on an Airfoil at Low Reynolds Numbers," *4th Applied Aerodynamics Conference*, AIAA 86-1788, 1986, pp. 152–161.

[91]Huebsch, W. W., Gall, P. D., and Hamburg, S. D., "Dynamic Roughness as a Means of Leading-Edge Separation Flow Control," *Journal of Aircraft*, Vol. 49, No. 1, 2012, pp. 108–115.

[92]Zhang, Y., Igarashi, T., Hu, H., Introduction, I., and Student, U., "Experimental Investigations on the Performance Degradation of a Low-Reynolds-Number Airfoil with Distributed Leading Edge Roughness," *49th AIAA Aerospace Sciences Meeting including the New Horizons Forum and Aerospace Exposition*, AIAA 2011-1102, Orlando, FL, USA, 2011, pp. 1–18.

[93]McMasters, J. H., and Henderson, M. L., "Low Speed Single Element Airfoil Synthesis," *Technical Soaring*, Vol. 6, No. 2, 1980, pp. 1–31.

[94]Simons, M., *Model Aircraft Aerodynamics*, 4th ed., Special Interest Model Books, Ltd., Dorset, UK, 1999, pp. 99, 125–126, 240.

[95]Schlichting, H., *Boundary layer thoery*, 7th ed., McGraw-Hill, New York, 1979, pp. 615–623, 540–542, 743.

[96]Feindt, E. G., "Untersuchungen über die Abhängigkeit des Umschlages laminar- turbulent von der Oberflächenrauhigkeit und der Druckverteilung," Dissertation Brauschweig, 1956.

[97]Nikuradse, J., *Law of Flow in Rough Pipes*, NACA TM-1292, 1950.

[98]Eça, L., and Hoekstra, M., "Numerical Aspects of Including Wall Roughness Effects in the SST k–ω Eddy-Viscosity Turbulence Model," *Computers & Fluids*, Vol. 40, No. 1, 2011, pp. 299–314.

[99]Knopp, T., Eisfeld, B., and Calvo, J. B., "A New Extension for k-ω Turbulence Models to Account for Wall Roughness," *International Journal of Heat and Fluid Flow*, Vol. 30, No. 1, 2009, pp. 54–65.

[100]Dirling, R. B., "A Method for Computing Roughwall Heat Transfer Rates on Reentry Nosetips," *AIAA 8th Thermophysics Conference*, AIAA 73-763, 1963.

[101]Bradshaw, P., "A Note on 'Critical Roughness Height' and 'Transitional Roughness,'" *Physics of Fluids*, Vol. 12, No. 6, 2000, pp. 1611–1614.

[102]Wilcox, D. C., *Turbulence Modeling for CFD*, 3rd ed., DCW Industries, La Cãnada, California, USA, 2006, pp. 192–210.

[103]Hellsten, A., and Laine, S., "Extension of k–ω Shear-Stress Transport Turbulence Model for Rough-Wall Flows," *AIAA Journal*, Vol. 36, No. 9, 1998, pp. 1728–1729.

[104]Apsley, D., "CFD Calculation of Turbulent Flow with Arbitrary Wall Roughness," *Flow, Turbulence and Combustion*, Vol. 78, No. 2, 2007, pp. 153–175.

[105]Stripf, M., Schulz, A., Bauer, H.-J., and Wittig, S., "Extended Models for Transitional Rough Wall Boundary Layers With Heat Transfer---Part II: Model Validation and Benchmarking," *Journal of Turbomachinery*, Vol. 131, No. 3, 2009, p. 31017.

[106]Elsner, W., and Warzecha, P., "Modeling of Rough Wall Boundary Layers with an Intermittency Transport Model," *TASK Quarterly*, Vol. 14, No. 3, 2010, pp. 271–282.

[107]Elsner, W., and Warzecha, P., "Numerical Study of Transitional Rough Wall Boundary Layer," *Journal of Turbomachinery*, Vol. 136, No. 1, 2013, p. 011010.

[108]Dassler, P., Kožulović, D., and Fiala, A., "Transport Equation for Roughness Effects on Laminar - Turbulent Transition," *The 15th International Conference on Fluid Flow Technologies*, Conference on Modelling Fluid Flow (CMFF' 12), Budapest University of Technology and Economics, Budapest, Hungary, 2012, p. 8.

[109]Langel, C. M., Chow, R., van Dam, C. P., Maniaci, D., Ehrmann, R. S., and White, E. B., "A Computational Approach to Simulating the Effects of Realistic Surface Roughness on Boundary Layer Transition," *52nd Aerospace Sciences Meeting*, 2014, pp. 1–16.

[110]Bons, J. P., and Christensen, K. T., "A Comparison of Real and Simulated Surface Roughness Characterizations," *37th AIAA Fluid Dynamics Conference and Exhibit*, AIAA 2007-3997, Miami, FL, USA, 2007, pp. 1–27.

[111]Pailhas, G., Touvet, Y., and Aupoix, B., "Effects of Reynolds Number and Adverse Pressure Gradient on a Turbulent Boundary Layer Developing on a Rough Surface," *Journal of Turbulence*, Vol. 9, No. 43, 2008, pp. 1–24.

[112]Rhie, C. M., and Chow, W. L., "Numerical Study of the Turbulent Flow Past an Airfoil with Trailing Edge Separation," *AIAA Journal*, Vol. 21, No. 11, 1983, pp. 1525–1532.

[113]Chen, Z. J., and Przekwas, A. J., "A Coupled Pressure-based Computational Method for Incompressible/compressible Flows," *Journal of Computational Physics*, Vol. 229, No. 24, 2010, pp. 9150–9165.

[114]Menter, F. R., Kuntz, M., and Langtry, R., "Ten Years of Industrial Experience with the SST Turbulence Model," *Turbulence Heat and Mass Transfer 4*, edited by Hanjalic, K., Nagano, Y., and Tummers, M., Begell House, Inc, 2003, pp. 625–632.

[115]Gritskevich, M. S., Garbaruk, A. V., Schütze, J., and Menter, F. R., "Development of DDES and IDDES Formulations for the k-ω Shear Stress Transport Model," *Flow, Turbulence and Combustion*, Vol. 88, No. 3, 2011, pp. 431–449.

[116]Ioselevich, V. A. Pilipenko, V. N., "Logarithmic Velocity Profiles for Fow of a Weak Polymer Solution Near a Rough Surface," *Soviet Physics Doklady*, Vol. 18, 1974, pp. 790–796.

[117]Menter, F., Ferreira, J. C., Esch, T., and Konno, B., "The SST Turbulence Model with Improved Wall Treatment for Heat Transfer Predictions in Gas Turbines," *Proceedings of the International Gas Turbine Congress*, IGTC2003-TS-059, Gas Turbine Society of Japan, Tokyo, 2003, pp. 1–7.

[118]Langtry, R., and Menter, F., *Overview of Industrial Transition Modelling in CFX*, ANSYS CFX, 83624 Otterfing, Germany, 2006.

[119]*ANSYS® FLUENT Academic Research, Release 14.0, ANSYS FLUENT Theory Guide*, ANSYS, Inc., 2011, p. 84.

[120]Pimenta, M. M., Moffat, R. J., and Kays, W. M., *The Turbulent Boundary Layer: An Experimental Study of the Transport of Momentum and Heat with the*

Effect of Roughness, Report HMT-21, The Office of Naval Research, USA, 1975.

[121]Stripf, M., Schulz, A., and Wittig, S., "Surface Roughness Effects on External Heat Transfer of a HP Turbine Vane," *Journal of Turbomachinery*, Vol. 127, No. 1, 2005, p. 200.

[122]Genç, M. S., Karasu, İ., and Hakan Açıkel, H., "An Experimental Study on Aerodynamics of NACA2415 Aerofoil at Low Re Numbers," *Experimental Thermal and Fluid Science*, Vol. 39, 2012, pp. 252–264.

[123]Chakroun, W., Al-Mesri, I., and Al-Fahad, S., "Effect of Surface Roughness on the Aerodynamic Characteristics of a Symmetrical Airfoil," *Wind Engineering*, Vol. 28, No. 5, 2004, pp. 547–564.

[124]Chakroun, W. M., Abdel-Rahman, A. A., and Taylor, R. P., "Effect of Surface Roughness on Flow Over a Circular Cylinder and Flapped Aerofoil," *ASME Fluids Engineering Division Conference*, FED-Vol. 237, No. 2, 1996, pp. 845–853.

[125]Ferrer, E., and Munduate, X., "CFD Predictions of Transition and Distributed Roughness over a Wind Turbine Airfoil," *47th AIAA Aerospace Sciences Meeting Including The New Horizons Forum and Aerospace Exposition*, AIAA 2009-269, Orlando, FL, USA, 2009, pp. 1–13.

[126]Roache, P. J., *Fundamentals of Verification and Validation*, 3rd ed., Hermosa publications, Socorro, New Mexico, USA, 2009, pp. 450–452.

[127]Pelletier, A., and Mueller, T. J., "Low Reynolds Number Aerodynamics of Low-Aspect-Ratio, Thin/Flat/Cambered-Plate Wings," *Journal of Aircraft*, Vol. 37, No. 5, 2000.

[128]Xia, Y., Bilgen, O., and Friswell, M. I., "The Effect of Corrugated Skins on Aerodynamic Performance," *23rd International Conference on Adaptive Structures and Technologies*, ICAST2012, Nanjing, China, 2012, pp. 1–11.

[129]Ol, M. V, McAuliffe, B. R., Hanff, E. S., Scholz, U., and Kähler, C. J., "Comparison of Laminar Separation Bubble Measurements on a Low Reynolds Number Airfoil in Three Facilities," *35th AIAA Fluid Dynamics Conference and Exhibit*, AIAA 2005-5149, Toronto, Ontario Canada, 2005, pp. 1–11.

[130]Torres, G., and Mueller, T., "Low Aspect Ratio Wing Aerodynamics at Low Reynolds Numbers," *AIAA Journal*, Vol. 42, No. 5, 2004, pp. 865–873.

[131]Khambatta, P., Ukeiley, L., Tinney, C., Stanford, B., and Ifju, P., "Flow Characteristics of a Three-dimensional Fixed Micro Air Vehicle Wing," *38th AIAA Fluid Dynamics Conference and Exhibit*, AIAA 2008-3820, FL, USA, 2008, pp. 1–16.

[132]Kuo, C.-M., "Adaptive Micro Air Vehicle Design," PhD Thesis, University of Sheffield, Sheffield, England, 2007.

[133]Aupoix, B., and Spalart, P. R., "Extensions of the Spalart–Allmaras Turbulence Model to Account for Wall Roughness," *International Journal of Heat and Fluid Flow*, Vol. 24, No. 4, 2003, pp. 454–462.

Appendix A Supplement Glossary

Some important technical terms used in the thesis are clarified. The list of glossary is presented as follows:

1. "Resolving" and "modelling"
2. Laminar Separation Bubble
3. Low Reynolds number turbulence model
4. Wall functions and enhanced wall functions
5. Universal law-of-the-wall for rough walls

"Resolving" and "modelling"

When mentioning the flow is modelled, it implies a certain flow details are modelled by a model. The flow details cannot be seen through post-processing.

When mentioning the flow is resolved, it implies a certain flow details are not modelled. The flow details can be seen through post-processing.

"Simulation" is a term with a broad meaning, involving resolving and modelling.

Laminar Separation Bubble

It is found a bubble can reattaches without transition, see Figure 35, pp. 26 in Van Dyke, An Album of Fluid Motion, The Parabolic Press, Stanford, CA, USA, 2003. This happens at $Re = 1\times10^4$. At higher Reynolds number, that is not expected to happen. Such flow is out of the scope of this thesis.

This thesis does not distinguish "laminar separation bubble", "separation bubble", and "bubble". When mentioning any of these three, the same thing (bubble) is referred to. In Chapter 6, "LE bubble" and "TE bubble" only refers to the relative location of a bubble, either relatively close to the leading edge or relatively close to the trailing edge. The two terms are not referred to any new types of bubble or related flow. In addition, "separation" refers to open separation, fundamentally different to the "separation bubble". Similarly, "LE separation" and "TE separation" only refers to the relative location of the separation.

Low Reynolds number turbulence model

In RANS turbulence modelling, when a model is called "low Reynolds number model", it must be capable of resolving near wall flows, using a fine near wall mesh, e.g., $y^+ < 1$. This is also mentioned as low Reynolds number RANS models in some literature. The low Re SST model in this thesis can resolve the near wall, and a low Re correction is used for transition modelling.

The disagreement on the capability of low Re models might due to the difference between $k - \varepsilon$ model and $k - \omega$ model. In a historical context, $k - \varepsilon$ model gained popularity before $k - \omega$ model, and the near wall model or wall functions was required. In the words by Wilcox[66], $k - \omega$ model showed a remarkable advance in transition modelling as compared to $k - \varepsilon$ model. Some review papers on the transition models believe low Re models has very limited capability of transition modelling. For $k - \varepsilon$ model, that view may be appropriate, however for $k - \omega$ model, that view is definitely inappropriate.

Wall functions and enhanced wall functions

It may cause confusion when mentioning these two terms together, however they are the standard usage in the documentation of FLUENT software. Wall functions are referred usually when the turbulence model is incapable of resolving near wall flow and thus a model is required. In the case for enhanced wall function, the name "automatic wall treatment" may be more appropriate, because the model in fact realises an automatic switch between resolving and modelling the near wall flow based on the near wall mesh spacing.

Universal law-of-the-wall for rough walls

A discrepancy of the definition of ΔB in the transitional region across open literature is found. FLUENT's code uses h_s^+ from 2.25 to 90, whereas other code may use 5 to 70 (e.g. Eça[98] and ANSYS CFX® Academic Research, Release 14.0). The different practice follows "technical roughness" (see Schlichting[46], Eqn. 17.39, pp.529). The discrepancy is resulted from different correlations on the ΔB profile in the transitional rough region, i.e. Nikuradse's

sand grain and Colebrook's "industrial roughness" (see the difference in the transitional region of the function $C^+(k_s^+)$ and $C_r^+(k_s^+)$ in Fig. 17.8 in Schlichting[46], pp.528). Bradshaw[101] made a critical comment on the discrepancy, pointing out that Nikuradse's sand grain is a very special case, as compared to the real life roughness.

Appendix B CFD Technique

B-1 Pre-processing

The pre-processing for a CFD procedure usually includes the preparation of the geometry and the mesh. If the geometry is an aerofoil, coordinate points can be used to generate geometry. For NACA aerofoils, analytic expression is available. For other aerofoils, especially for low Reynolds number aerofoils, the "UIUC Airfoil Data Site" by University of Illinois is strongly recommended. Other than aerofoil coordinates, wind tunnel data may be available. The web site is http://aerospace.illinois.edu/m-selig/ads/coord_database.html. It is well-maintained by the applied aerodynamics group at University of Illinois, USA, led by prof. Michael Selig. He is a distinguished scholar for low Reynolds number aerodynamics. The 3D MAV geometry used is prepared via computer aided design software.

All the mesh is generated in the ICEM CFD program, which is distributed along with the ANSYS package. The structure mesh generator is substantially used in the current work. In the experience, the structured mesh requires block splitting. This takes the majority of the time for the mesh design, especially when the geometry is complex, such as the full aircraft configuration for MAV. The time for the operation is not great. After the block splitting is done, substantial time is required to fine tune the distribution of mesh points. The more blocks, the more time is required. The mesh smoother for structured mesh is found not easy to use. The default setting for model tolerance of the minimum feature is found always insufficient for external flow problems. A large farfield is usually used, and the aircraft's geometrical detail is very small compared to the whole domain. Lastly, in most occasions, the cause for not generating the correct mesh is due to the erroneous settings on the association and the distribution of mesh point. Re-association and alteration on the distribution should troubleshoot the problem.

B-2 The Usage of FLUENT

FLUENT is a comprehensive CFD solver for fluid dynamic problems, which comes with the ANSYS package. In the experience, the software is easy

to pick up. The journal script is powerful for automating the solution process.

During the time for this study, a dedicated MATLAB script is written to generate the FLUENT script for polar curve calculations. The script makes new directories for each incidence, and modifies the FLUENT script according to the incidence. This procedure saves tremendous time and avoids human involved mistakes. The script also automates the job submission on computing clusters.

It is found a new turbulence model is difficult to implement using FLUENT's user defined function. Substantial work and experience are required beforehand.

The parallel efficiency is found not great. For a 2-3 million mesh, the experience shows 4~8 cores is an acceptable choice. Choosing more cores tends to waste the computing resources. Besides, the data file contains much redundant variables than the primary velocity, pressure, and turbulence variables. This asks for a very high storage requirement for the post-processing of unsteady results. The DDES result presented in the main text requires approximately 2 Gigabytes (2.6 million mesh, binary and compressed data) for individual files. A full storage from 2000 time step to 8000 more time step requires 12 Terabytes disk space, and this is for only one simulation. More simulations at different incidences, inlet condition and other settings will lead to an enormous requirement of disk spaces.

B-3 Post-processing

The primary post-processing tools are MATLAB, CFD-Post and Tecplot. Similar to the MATALB script written for generating FLUENT script, a dedicated script is written to plot lift curves, drag curves, etc. This procedure saves tremendous time for data processing and figure production.

CFD-Post is a flow visualisation tool that is also available in ANSYS package. The experience shows, it is much simpler and easier to pick up whilst powerful, as compared to another similar tool Tecplot. Especially for the macro script, no prior knowledge is required, and all processes are recordable. This work substantially relies on CFD-Post for 3D post-processing. The best use for

Tecplot may be for the process that requires mathematical operations, such as the averaging used for the DDES result. The script language is powerful although some programming knowledge is required.

Appendix C The Specification for the MAV Platform

The MAV design used in this thesis was published in Kuo[132]. The main components are a propeller to generate thrust and yawing control (i.e., vector thrust), a fuselage carrying electronic components, a low aspect ratio Zimmerman planform wing to provide the lift, a vertical tail to provide yaw stability, and a piece of elevators of no-end-gap design located in the rear of the wing. The main material is Depron foam for the wing and the tail, and white foam for the fuselage. The wing is reinforced by two carbon rods. The wing, fuselage, and tail are glued together. The propeller is connected to the motor via a gear box and the motor is connected to the fuselage via a wooden structure. The actuation is servo. The design is intended for low cost construction and using commercial off-shelf material/component. The prototype flew. Fig. A-1 shows the geometry, and main specifications are shown in Table A-1.

Table A-1. The MAV specification

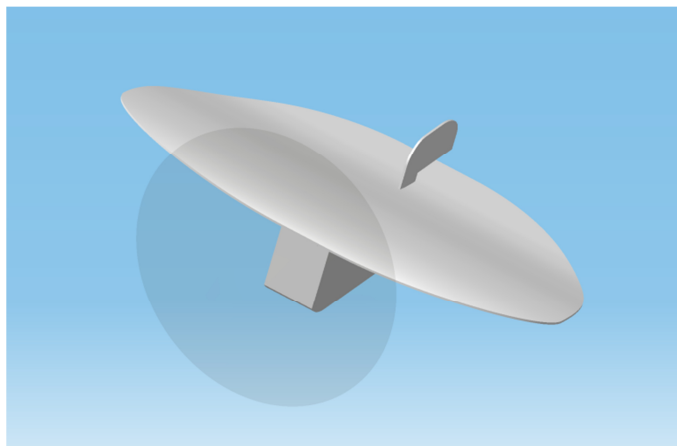|	
Weight	200g
Wing area	$0.09m^2$
Cruise speed	10m/s
Mean chord	0.23m
Span	0.44m
Cruise C_l	0.35
Endurance	20 min
x_{CG} (from the leading edge of the root chord)	0.043m

Fig. A-1 The MAV geometry

Appendix D Supplement Investigation

Some investigations are conducted during the time for the doctorate study. Although for time reason they are insufficiently refined to put into the main text, they are expected to be a good start for the future work.

D-1 Estimation of Equivalent Roughness Height of Foam Surface

The MAV prototype uses foam as the construction material. The fuselage is covered with clear tapes for connection and it is relatively smooth, whereas the foam surface on the wing is exposed to the flow. The foam surface is apparently different from the smooth surface, therefore it is of practical importance to know its influence on the aerodynamic performance. To estimate this influence, a surface roughness test is performed and an equivalent sand grain roughness height is characterised. Then the simulation can be made based on this height. The roughness test was conducted in the Tribology lab in the University of Sheffield.

D-1-1 Method

The realistic rough surface is characterised by an equivalent sand grain height. A surface roughness test is performed at first, and then the Dirling's correlation is used to estimate the equivalent height.

The test is conducted on a Mitutoyo surface roughness tester. The used software is Surfpack-SV version 1.3. The primary setup is listed in Table A-2. The tested sample is a Depron foam sheet that is used for the wing construction. It is clipped into a wing shape and placed horizontally on a stand. When the stylus moves on the surface, it measures the roughness height and simultaneously delivers the data to the software for processing. The sample is tested in chordwise and spanwise orientation, and various locations, either in the centre part or near the edge. Fig. A-2 shows a test setup in streamwise orientation. The final roughness height representing the sample is the averaged value of these locations. This height is the value of the geometrical roughness height for γ-Re$_\theta$ SST model.

The relationship used to link real surfaces and the equivalent sand grain surfaces is the Dirling's correlation that is frequently cited in literature, after Aupoix and Spalart[133]:

$$h = \alpha h_s \tag{A-1}$$

$$\alpha = \begin{cases} 60.95 \Lambda^{-3.78} & \text{if } \Lambda < 4.915 \\ 0.0072 \Lambda^{1.9} & \text{if } \Lambda > 4.915 \end{cases} \tag{A-2}$$

$$\Lambda = \frac{L}{h} \left(\frac{A_s}{A_p} \right)^{\frac{4}{3}} \tag{A-3}$$

where h is the mean roughness height that measured from the roughness measurement, Ra. L is the mean distance between roughness elements, $L = \sqrt{S/N}$, i.e. the root square of a given area over the number of roughness elements. A_s is the surface area projected on a plane normal to the flow direction, and A_p is the windward surface area.

D-1-2 Equivalent Sand Grain Roughness Characterisation

A series of surface roughness tests is conducted to determine the mean roughness height with respect to the centreline (Ra). Fig. A-3 shows two samples of the roughness profile. It is found that the mean roughness height is smaller in the chordwise orientation than that in the spanwise orientation. The averaged value is used.

The estimated surface roughness characteristics are shown in Table A-3, and $h_{s,eq}$ is estimated according to the Dirling correlation mentioned in Section D-1-1. The determination of S/N is difficult. Several samples of tested profiles are examined, and then an averaged value is estimated. For the two samples presented in Fig. A-3, 6 and 23 elements are estimated respectively. The determination on $(A_s/A_p)^{4/3}$ is even more difficult. A similar practice is followed as in Pailhas et al.,[111] and a same value of 2 is adopted. This gives $h_{s,eq}$ a value of $53\mu m$, and this value is likely to be underestimated. As a conservative estimation, $h_{s,eq}$ is eventually estimated between $50\mu m$ and $100\mu m$.

D-1-3 Remark

It is suspicious that the estimation may be of large uncertainty. A

photograph of the surface may be very useful to provide the estimation of the roughness height.

Table A-2. Surfpack-SV setup

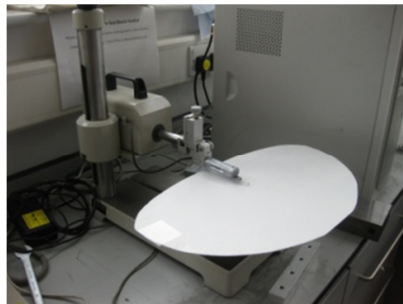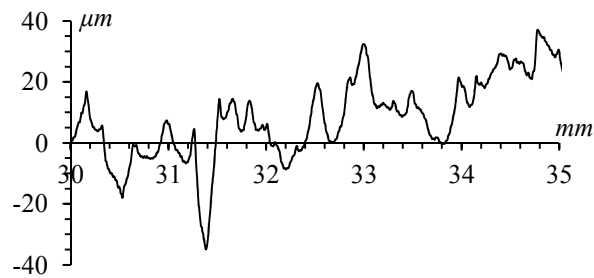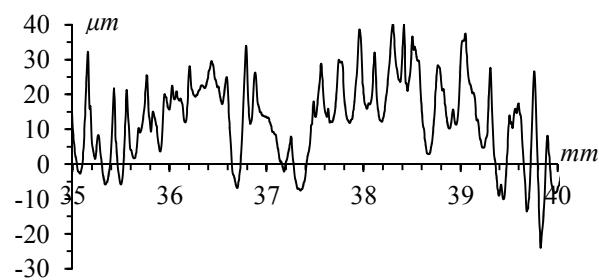| Options	Settings
test profile	P - profile
measuring speed	2 mm/s
measuring length	50mm
measured points	15875
compensate	inclination all

Fig. A-2 Surface roughness test setup

(a) spanwise

(b) chordwise

Fig. A-3 Sample roughness profiles in a given length

Table A-3. Surface roughness characteristics estimation

h (μm)	S/N (mm² /grains)	l	$(A_s/A_p)^{4/3}$	Λ	α	h_s(μm)
12.816	25/198	0.355	2	4.327	0.24	50-100

D-2 Simulation on Cambered Plate Profile and Wing

These two simulations use a number of turbulence models. The results are compared to the experiment by Pelletier and Mueller[127]. The cambered plate profile is simulated at $Re = 6\times10^4$ and 1.4×10^5. In addition to low Re SST (kwsst) and γ-Re$_\theta$ SST (tsst) models, $k - k_l - \omega$ (kklw) model is included. The result on $Re = 1.4\times10^5$ only has the data by the γ-Re$_\theta$ SST model. The cambered wing is a wing with an aspect ratio of 6 using the cambered plate profile. The mesh is not descent and no mesh sensitivity result is available. There is yet a conclusion drawn.

(a)

(b)
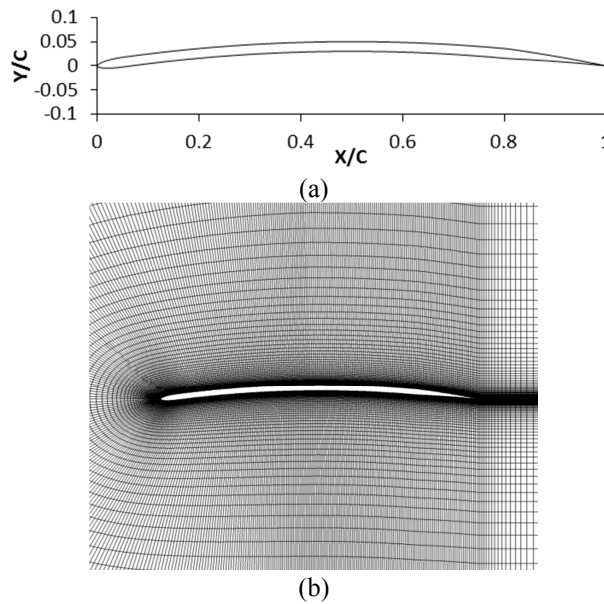
Fig. A-4 (a) The cambered plate geometry, (b) mesh

Table A-4. Grid independence of the cambered plate

Mesh elements	α	C_l	C_d	C_m
coarse	4	0.6655	0.0224	-0.0852
30248	7	0.9640	0.0564	-0.0764
	12	0.9322	0.1634	-0.1235
medium	4	0.6540	0.0223	-0.0826
66982	7	0.9593	0.0555	-0.0751
	12	0.9367	0.1627	-0.1210
fine	4	0.6546	0.0223	-0.0827
135584	7	0.9595	0.0552	-0.0752
	12	0.9354	0.1621	-0.1202

Table A-5. Lift and drag results

(a)

(b)

(c)
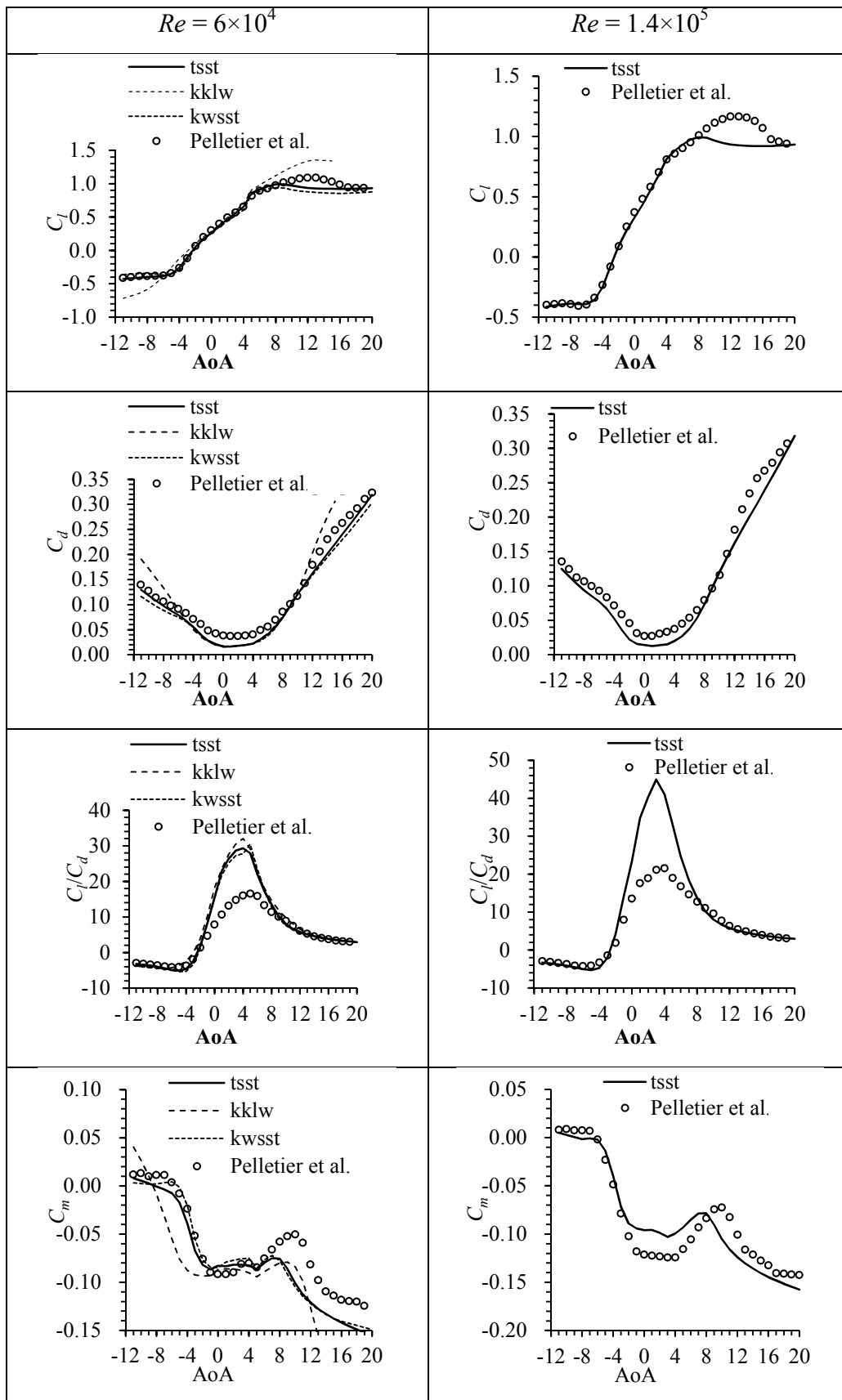
Fig. A-5 (a) The mesh for the wing, (b) lift comparisons, (c) drag comparisons

Experiment: Pelletier and Mueller[127], error bar is provided from the experiment
CFD1: pressure based solver, SIMPLE algorithm
CFD2: pressure based coupled solver, 2nd order accuracy
CFD3: pressure based coupled solver, 1st order accuracy
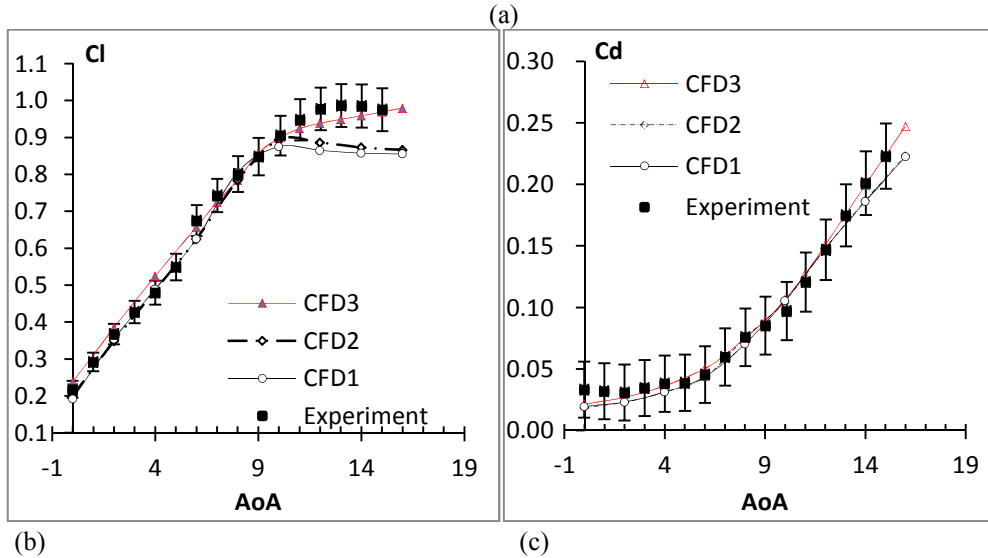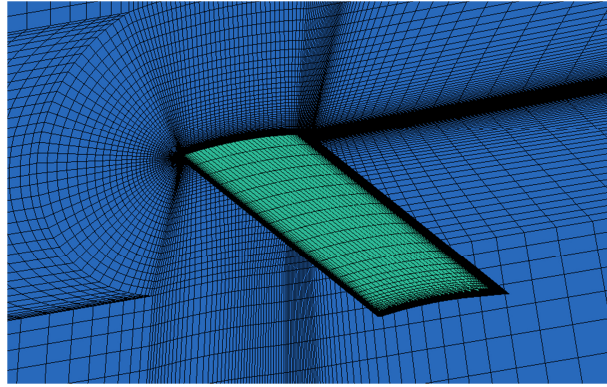
D-3 Wind Tunnel Experiment

An experiment was performed between September 2013 and February 2014. Due to lack of maintenance of the wind tunnel, the uncertainty of the force measurement was believed to be large, and the wind speed did not match the design condition. The measurements were performed on foam, plywood and various sand papers surfaces. The simulation used a full MAV configuration, i.e., with the vertical tail, and the wind speed the wind tunnel could achieve. A few roughness heights were selected for the roughness simulations, instead of estimating the equivalent roughness height for the sand papers.

The results are available in Ligas, T., Surface Roughness Effects on Micro Air Vehicle Aerodynamics at Low Reynolds Number, Master dissertation, Department of Aerospace Engineering, University of Sheffield, Sheffield, 2014. The main findings are:

(1) The lift and drag comparison only receives a qualitatively match between the simulation and the experiment. It is unclear whether the inaccuracy on the model or the wind tunnel inflow turbulence causes the discrepancy.

(2) The trend for roughness is the improved lift post stall, and this is confirmed from both experiments and simulations.

Tomaz Ligas participated in the manufacture of the model and all experimental measurements. He conducted the measurement for the use of his master dissertation. Jamie Booth and Karl A Rotchel provided the support on the fuselage manufacturing in the workshop of the department of mechanical engineering. Danial G Sturge provided the instructions on the use of the wind tunnel and the force measurement system. Dr Wenhua Wu provided useful suggestion for the design of the experiment and the model. Dr Robert J Howell arranged the time slot and provided information for using the facilities. Drs Timothy J Swait and Austin D Lafferty manufactured a sample of composite wing. Barry Johnson at foamwings.co.uk manufactured the template for the wing manufacturing. All the assistance is gratefully acknowledged.

D-4 Additional Simulation on the MAV platform

A comparative simulation between wing, wing-fuselage and full aircraft configuration is attempted, including the comparison between low Re SST and γ-Re$_\theta$ SST models. It is found that the calculations using the γ-Re$_\theta$ SST model are difficult to fully converge to steady state, and unsteady calculations are not accomplished due to a lack of time. Lift and drag, aerodynamic centre, pressure and skin friction results are compared. The variation on aerodynamic force due to incomplete convergence is not substantial. The flow field is clearly unsteady (vortex shedding was found). There is yet a conclusion drawn. Nevertheless, it is believed better design on wing and fuselage conjunction is desired, because the wing-fuselage configuration degrades maximum lift to drag ratio from 8 to 5 (37.5% reduction!).

Another attempted simulation is the roughness bump. The preliminary result provides no mesh sensitivity and the result for only one design. The result shows a reduction in separation area and a drag reduction.
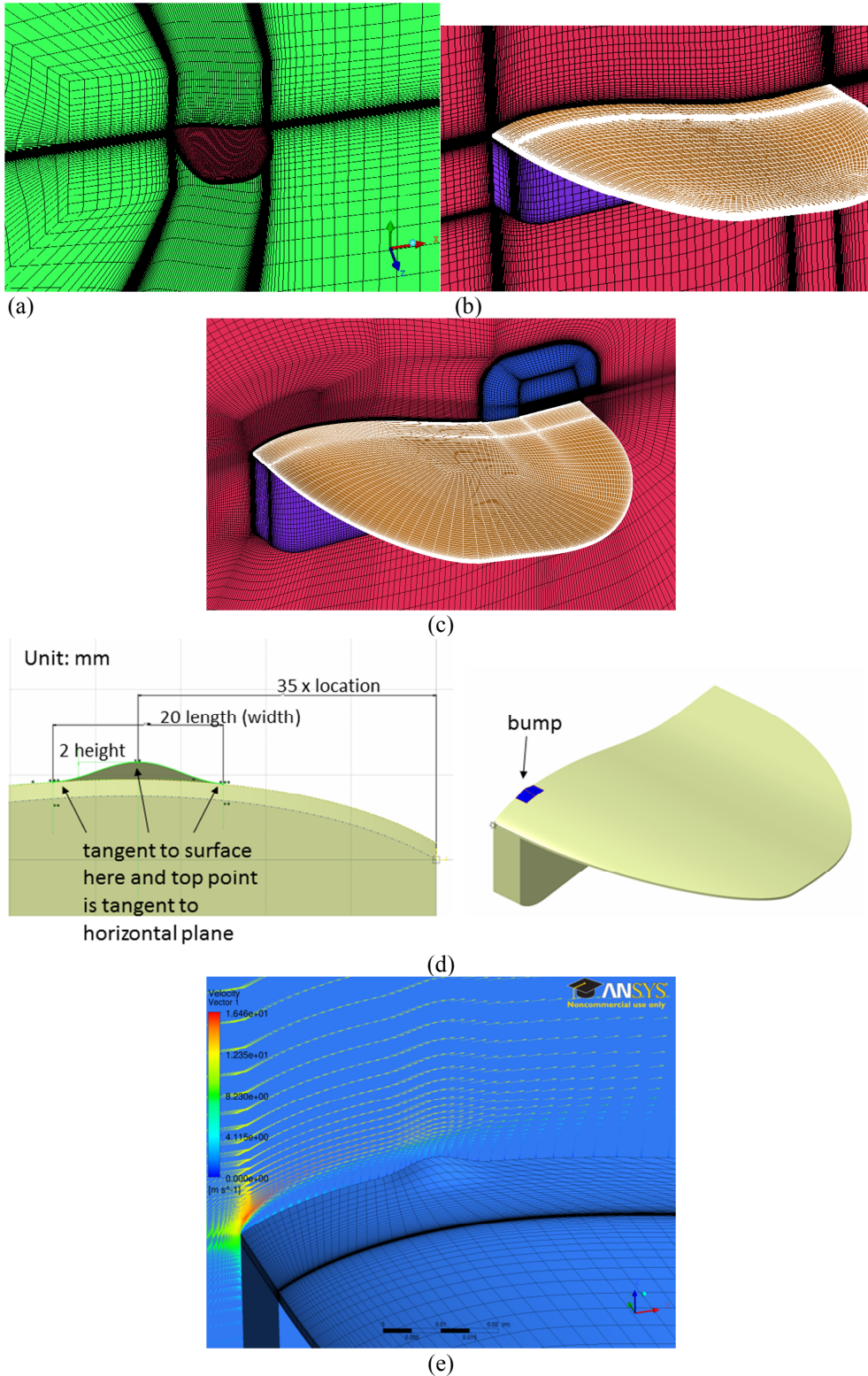
(a)

(b)

(c)

(d)

(e)

Fig. A-6 The mesh for (a) wing, (b) wing-fuselage, (c) full aircraft configurations, (d) the bump design, (e) the bump mesh with velocity vectors

Table A-6. Mesh sensitivity, low Re SST, $V_\infty = 10$m/s

	Wing				Wing-fuselage			
	$\alpha = 0^\circ$		$\alpha = 14^\circ$		$\alpha = 0^\circ$		$\alpha = 14^\circ$	
Mesh elements	1.8M	4M	1.8M	4M	2.6M	6M	2.6M	6M
C_L	0.3854	0.3874	0.6930	0.6815	0.3482	0.3556	0.7136	0.7039
C_D	0.0460	0.0465	0.2674	0.7355	0.0700	0.0684	0.3173	0.3153
C_L/C_D	8.4	8.3	2.6	2.6	5.0	5.2	2.2	2.2

	Full aircraft			
	$\alpha = 0^\circ$		$\alpha = 14^\circ$	
Mesh elements	2.9M	6.7M	2.9M	6.7M
C_L	0.3418	0.3420	0.7098	0.7050
C_D	0.0801	0.0804	0.3186	0.3155
C_L/C_D	4.3	4.3	2.2	2.2

Table A-7. Mesh sensitivity, γ-Re$_\theta$ SST, $V_\infty = 10$m/s

	Wing				Wing-fuselage			
	$\alpha = 0^\circ$		$\alpha = 14^\circ$		$\alpha = 0^\circ$		$\alpha = 14^\circ$	
Mesh elements	1.8M	4M	1.8M	4M	2.6M	6M	2.6M	6M
C_L	0.3947	0.3955	0.7355	0.7344	0.3564	0.3554	0.7416	0.7036
C_D	0.0500	0.0502	0.2783	0.2750	0.0681	0.0672	0.3244	0.3207
C_L/C_D	7.9	7.9	2.7	2.7	5.2	5.3	2.3	2.3

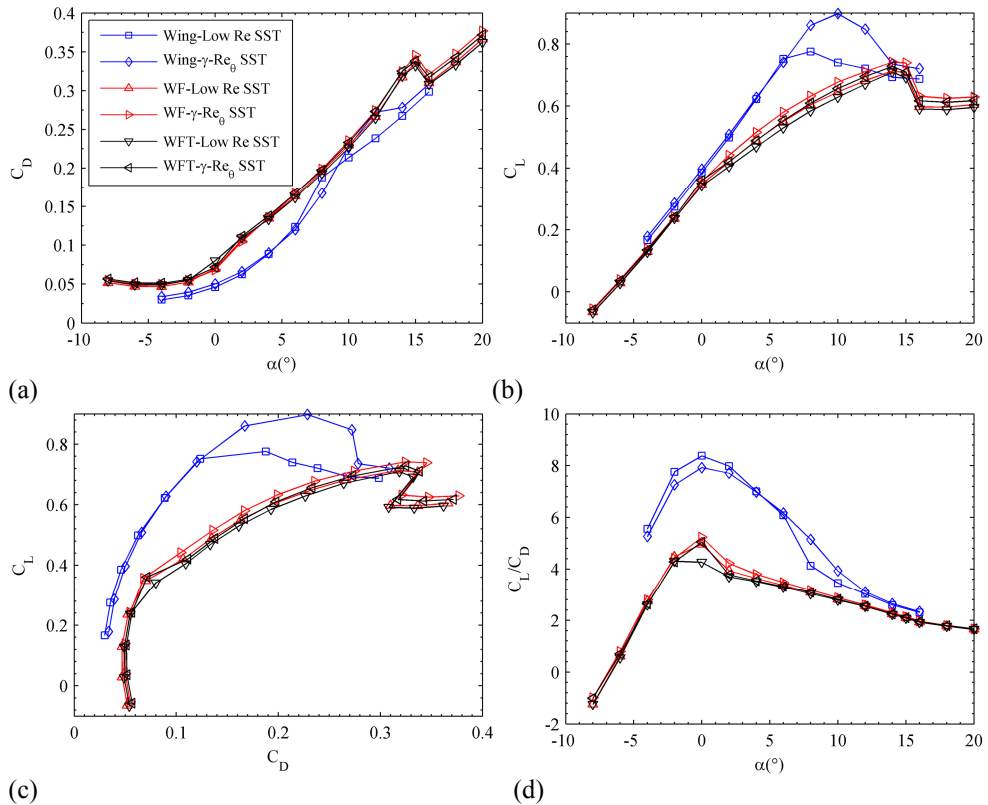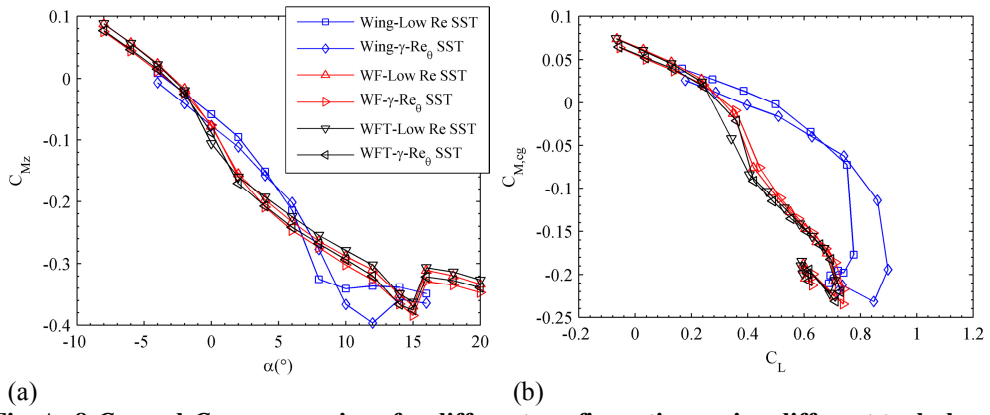|	Full aircraft			
	$\alpha = 0^\circ$		$\alpha = 14^\circ$	
Mesh elements	2.9M	6.7M	2.9M	6.7M
C_L	0.3607	0.3600	0.7282	0.7229
C_D	0.0715	0.0712	0.3251	0.3211
C_L/C_D	5.0	5.1	2.2	2.3

(a) (b) (c) (d)

Fig. A-7 C_L, C_D, C_L/C_D comparison for different configurations using different turbulence models, WF: wing-fuselage configuration, WFT: full aircraft configuration

(a)   (b)

Fig. A- 8 C_{Mz} and $C_{M,cg}$ comparison for different configurations using different turbulence models, WF: wing-fuselage configuration, WFT: full aircraft configuration

Table A-8. The lift centre $\bar{x}_{ac}$ at $\alpha = 0^o$

	Wing	Wing-fuselage	Full aircraft
Low Re SST	0.30	0.51	0.57
γ-Re$_\theta$ SST	0.31	0.46	0.52

Low Re SST γ-Re$_\theta$ SST

$\alpha = -2^o$

Unsteady

$\alpha = 4^o$

Unsteady

$\alpha = 10^o$

Static Pressure   [Pa]
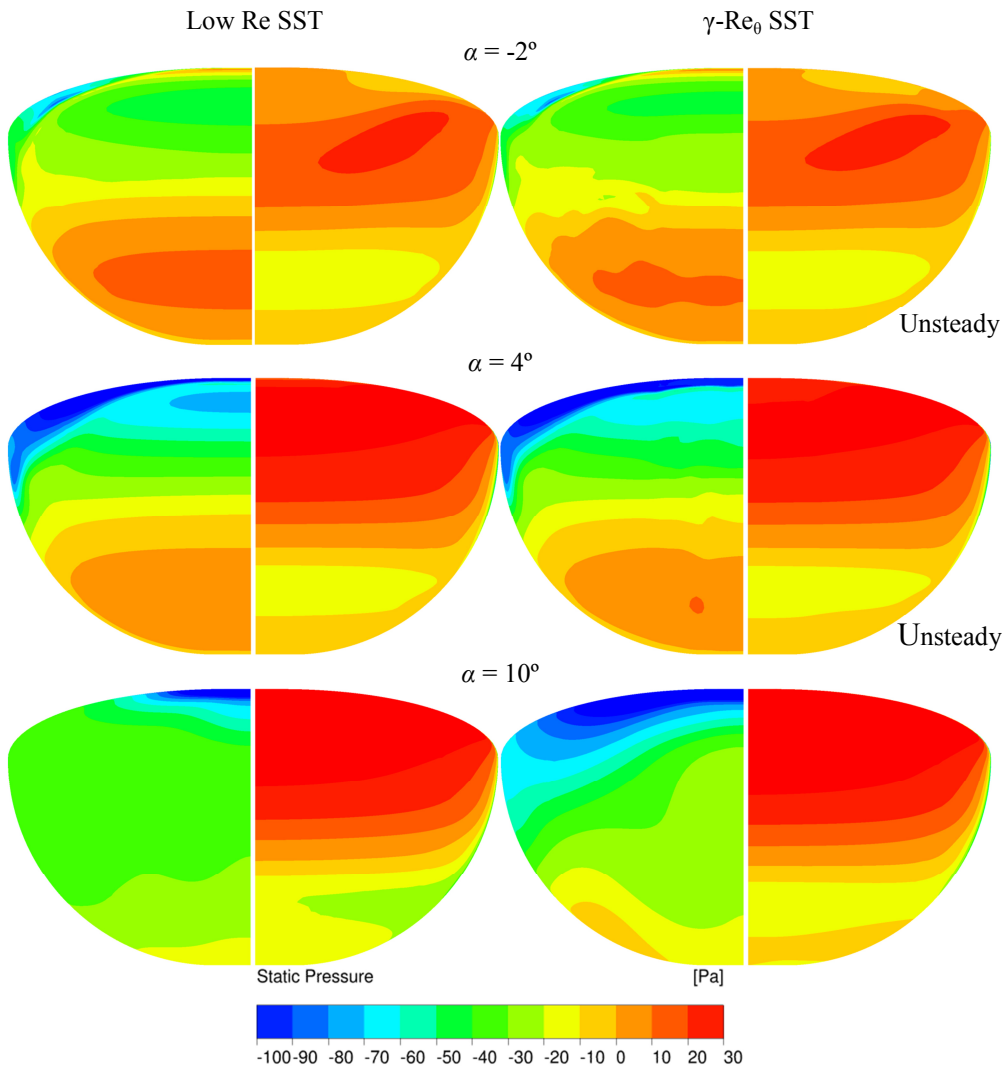
Fig. A-9 Pressure contour comparisons on the wing

Low Re SST   γ-Re_θ SST

$\alpha = -2°$

Unsteady

$\alpha = 6°$

Unsteady

$\alpha = 14°$

Static Pressure   [Pa]

-100 -90 -80 -70 -60 -50 -40 -30 -20 -10 0   10 20 30

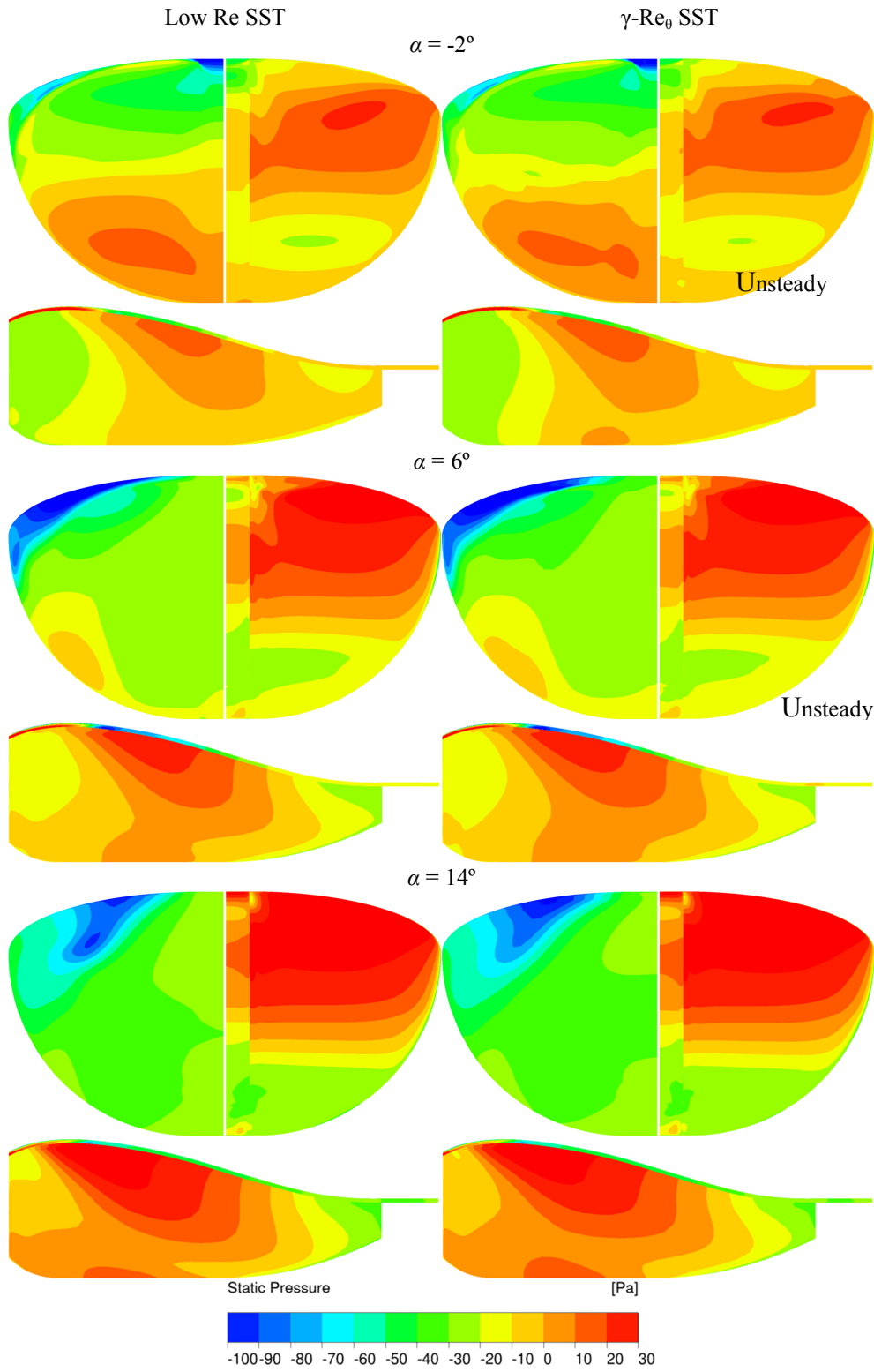**Fig. A-10 Pressure contour comparisons on the wing-fuselage configuration**
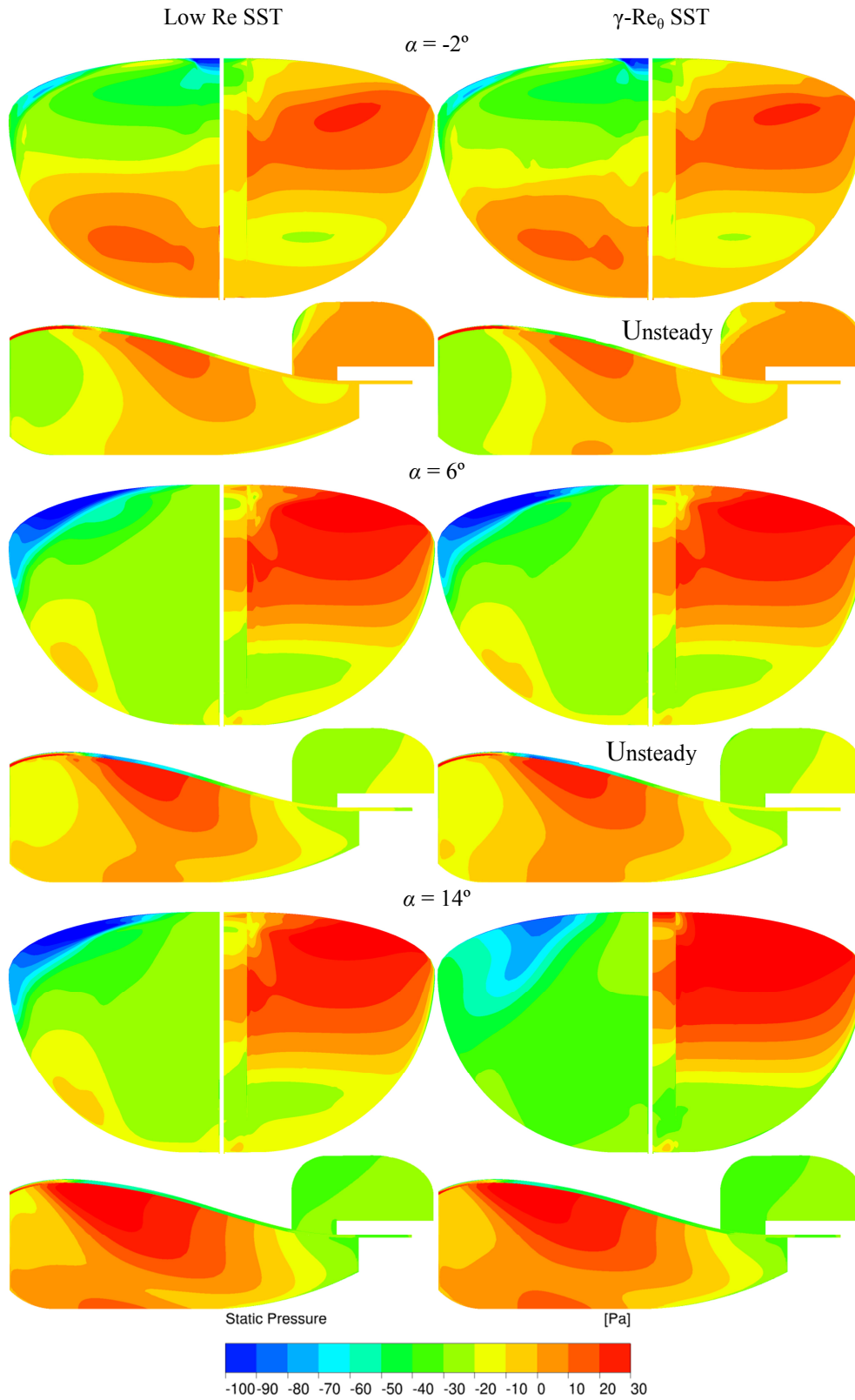
Fig. A-11 Pressure contour comparisons on the full aircraft configuration
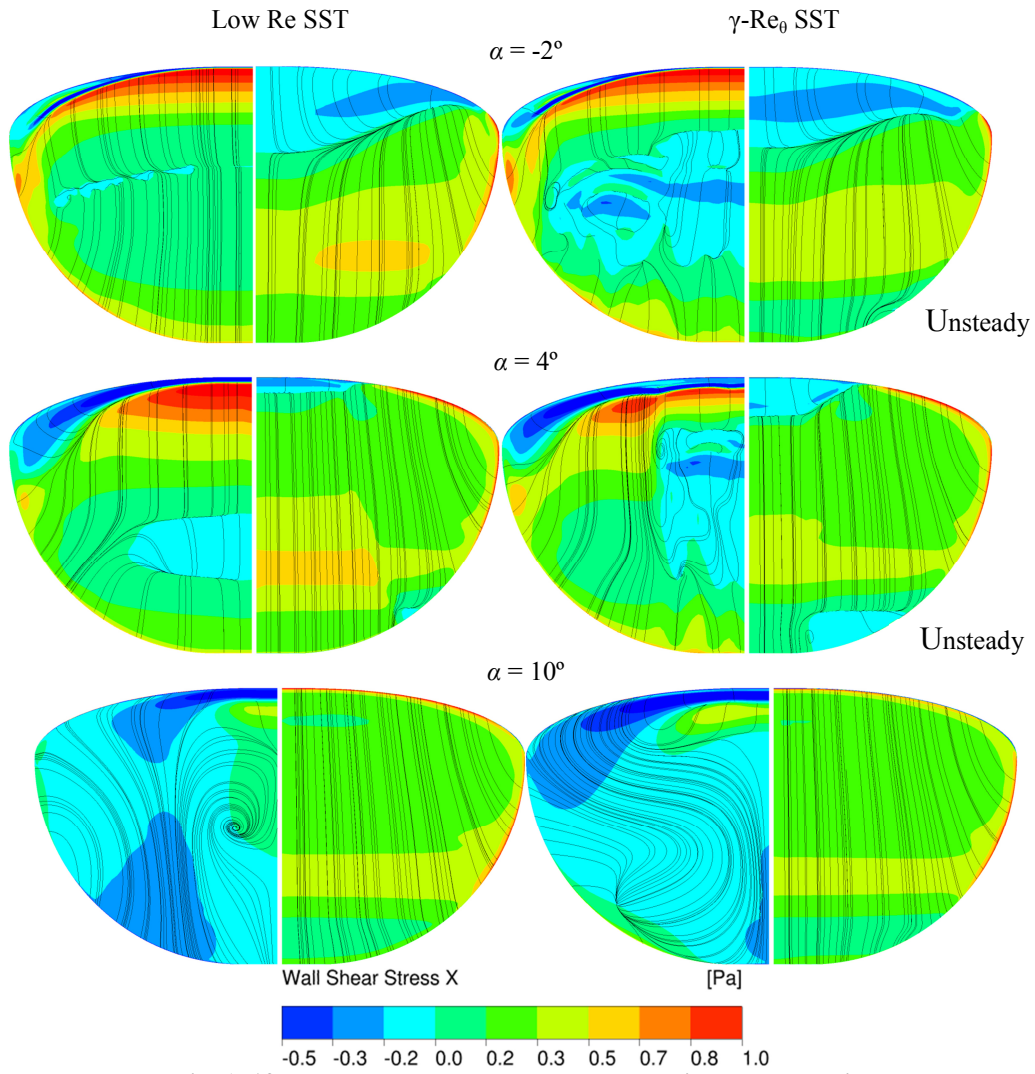
Low Re SST   γ-Re$_\theta$ SST

α = -2º

α = 4º

Unsteady

α = 10º

Unsteady

Wall Shear Stress X   [Pa]

-0.5 -0.3 -0.2 0.0 0.2 0.3 0.5 0.7 0.8 1.0

Fig. A-12 X wall shear stress contour comparisons on the wing

Results

With bump   Without bump

Wall Shear X
Contour 1
3.000e+00
2.500e+00
2.000e+00
1.500e+00
1.000e+00
5.000e-01
0.000e+00
-5.000e-01
-1.000e+00
-1.500e+00
-2.000e+00
[Pa]

Center Separation
area decreases in
width.
Side Separation
area increases.

Drag reduction is
due to pressure
drag reduction.

0   0.050   0.100 (m)
   0.025   0.075

	Cl	Clp	Clf	Cd	Cdp	Cdf
Without bump	0.3482	0.3499	-0.0017	0.0700	0.0620	0.0080
With bump	0.3498	0.3515	-0.0017	0.0689	0.0608	0.0081
Reduction	-0.5%			-1.6%		

Fig. A-13 The roughness bump results

Low Re SST   γ-Re$_\theta$ SST

$\alpha = -2^o$

Unsteady

$\alpha = 6^o$

Unsteady

$\alpha = 14^o$

Wall Shear Stress X   [Pa]

-0.5 -0.3 -0.2 0.0 0.2 0.3 0.5 0.7 0.8 1.0
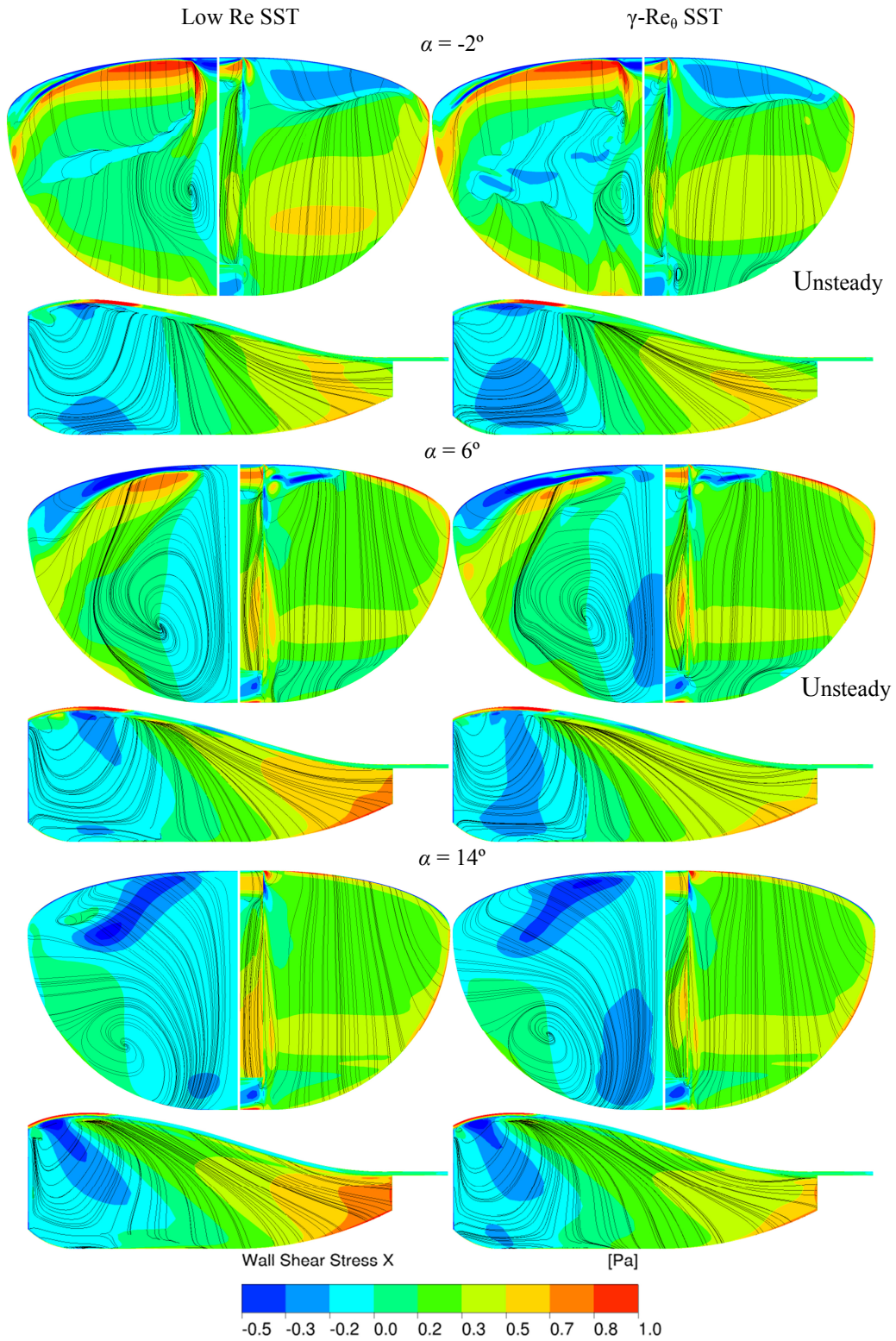
Fig. A-14 X wall shear stress contour comparisons on the wing-fuselage configuration

Low Re SST γ-Re$_\theta$ SST

$\alpha = -2^\circ$

Unsteady

$\alpha = 6^\circ$

Unsteady

$\alpha = 14^\circ$

Wall Shear Stress X [Pa]
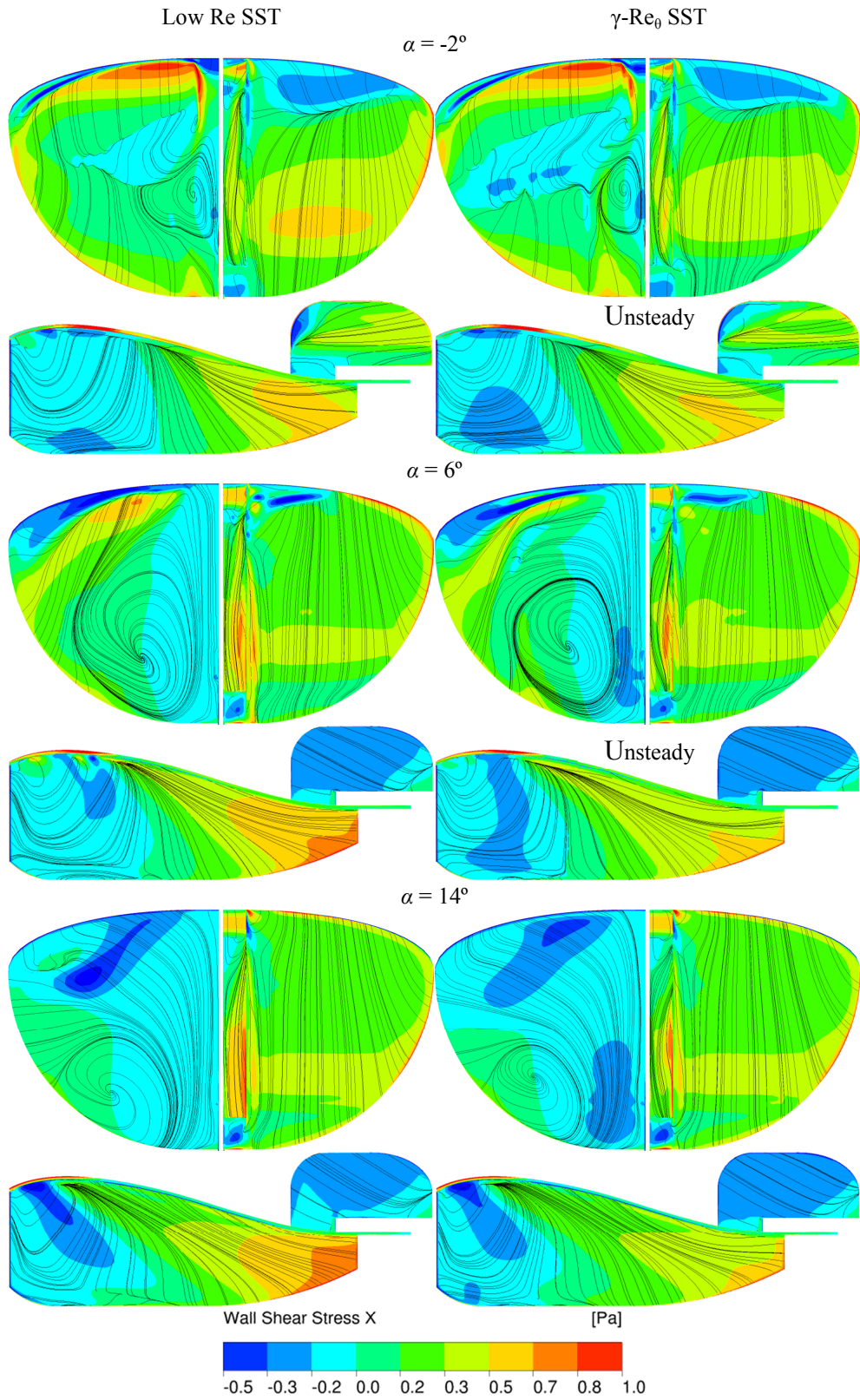
-0.5 -0.3 -0.2 0.0 0.2 0.3 0.5 0.7 0.8 1.0

Fig. A-15 X wall shear stress contour comparisons on the full aircraft configuration